

Summer 2010

Mitigation of chloride and sulfate based corrosion in reinforced concrete via electrokinetic nanoparticle treatment

Kunal Kupwade-Patil
Louisiana Tech University

Follow this and additional works at: <https://digitalcommons.latech.edu/dissertations>



Part of the [Civil Engineering Commons](#), and the [Mechanical Engineering Commons](#)

Recommended Citation

Kupwade-Patil, Kunal, "" (2010). *Dissertation*. 397.
<https://digitalcommons.latech.edu/dissertations/397>

This Dissertation is brought to you for free and open access by the Graduate School at Louisiana Tech Digital Commons. It has been accepted for inclusion in Doctoral Dissertations by an authorized administrator of Louisiana Tech Digital Commons. For more information, please contact digitalcommons@latech.edu.

NOTE TO USERS

Page(s) missing in number only; text follows. The manuscript was microfilmed as received.

9

This reproduction is the best copy available.

UMI[®]

**MITIGATION OF CHLORIDE AND SULFATE
BASED CORROSION IN REINFORCED
CONCRETE VIA ELECTROKINETIC
NANOPARTICLE TREATMENT**

by

Kunal Kupwade-Patil, M.S.

A Dissertation Presented in Partial Fulfillment
of the Requirements for the Degree
Doctor of Philosophy

COLLEGE OF ENGINEERING AND SCIENCE
LOUISIANA TECH UNIVERSITY

August 2010

UMI Number: 3429511

All rights reserved

INFORMATION TO ALL USERS

The quality of this reproduction is dependent upon the quality of the copy submitted.

In the unlikely event that the author did not send a complete manuscript and there are missing pages, these will be noted. Also, if material had to be removed, a note will indicate the deletion.



UMI 3429511

Copyright 2010 by ProQuest LLC.

All rights reserved. This edition of the work is protected against unauthorized copying under Title 17, United States Code.



ProQuest LLC
789 East Eisenhower Parkway
P.O. Box 1346
Ann Arbor, MI 48106-1346

LOUISIANA TECH UNIVERSITY

THE GRADUATE SCHOOL

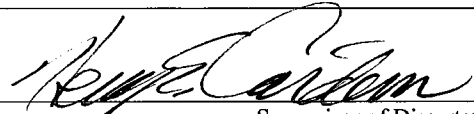
05-06-2010

Date

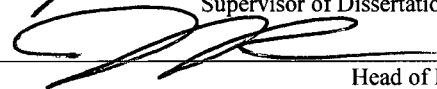
We hereby recommend that the dissertation prepared under our supervision
by Kunal Kupwade-Patil

entitled Mitigation of Chloride and Sulfate based Corrosion in Reinforced Concrete via
Electrokinetic Nanoparticle Treatment

be accepted in partial fulfillment of the requirements for the Degree of
Doctor of Philosophy



Supervisor of Dissertation Research

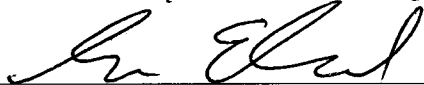


Head of Department

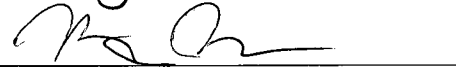
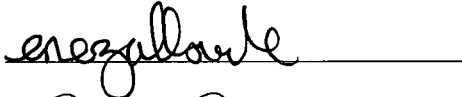
Mechanical Engineering

Department

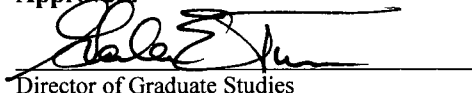
Recommendation concurred in:



Advisory Committee

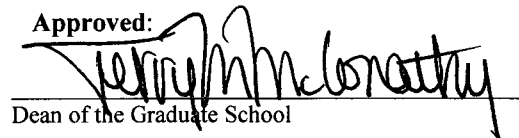


Approved:

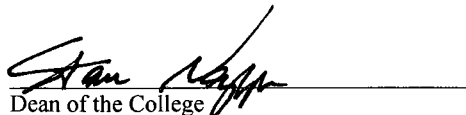


Director of Graduate Studies

Approved:



Dean of the Graduate School



Dean of the College

ABSTRACT

Concrete is a porous material which is susceptible to the migration of highly deleterious species such as chlorides and sulfates. Various external sources, including sea salt spray, direct seawater wetting, deicing salts and chlorides can contaminate reinforced concrete. Chlorides diffuse into the capillary pores of concrete and come into contact with the reinforcement. When chloride concentration at the reinforcement exceeds a threshold level it breaks down the passive oxide layer, leading to chloride induced corrosion. The application of electrokinetics using positively charged nanoparticles for corrosion protection in reinforced concrete structures is an emerging technology. This technique involves the principle of electrophoretic migration of nanoparticles to hinder chloride diffusion in the concrete. The return of chlorides is inhibited by the electrodeposited assembly of the nanoparticles at the reinforcement interface.

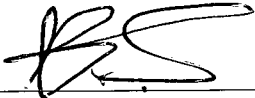
This work examined the nanoparticle treatment impact on chloride and sulfate induced corrosion in concrete. Electrokinetic Nanoparticle (EN) treatments were conducted on reinforced cylindrical concrete, rectangular ASTM G109 specimens that simulate a bridge deck and full scale beam specimens. EN treatment to mitigate external sulfate attack in concrete was performed on cylindrical concrete specimens. Corrosion results indicated lower corrosion potentials and rates as compared to the untreated specimens. Scanning electron

microscopy (SEM) showed a dense microstructure within the EN treated specimens. Chemical analysis (Raman spectroscopy, X ray-diffraction, and Fourier transform infrared spectroscopy FTIR) showed the presence of strength enhancing phases such as calcium aluminate hydrate (C-A-H) and increased amounts of calcium silicate hydrate (C-S-H) within the EN treated specimens. Strength and porosity results showed an increase in strength and a reduction in porosity among the EN treated specimens. EN treatment acted as a protective barrier that formed primarily at the reinforcement surface where it inhibited the ingress of chlorides. When applied to sulfate attack, EN treatment was found to extract sulfate ions. This treatment also reduced porosity and increased concrete strength. The strength increases were limited by the accumulation of spallation damage that was accrued during the sulfate exposure period of the work. This demonstrated that treatment for sulfate attack was best suited to early stages of degradation or as a preventive measure.

APPROVAL FOR SCHOLARLY DISSEMINATION

The author grants to the Prescott Memorial Library of Louisiana Tech University the right to reproduce, by appropriate methods, upon request, any or all portions of this Dissertation. It is understood that "proper request" consists of the agreement, on the part of the requesting party, that said reproduction is for his personal use and that subsequent reproduction will not occur without written approval of the author of this Dissertation. Further, any portions of the Dissertation used in books, papers, and other works must be appropriately referenced to this Dissertation.

Finally, the author of this Dissertation reserves the right to publish freely, in the literature, at any time, any or all portions of this Dissertation.

Author  _____

Date 07/15/2010

To my parents and brother

Dr. Vijay Kupwade, Dr. Saraswati Kupwade and Harsh Kupwade-Patil

To my advisor and mentor

Dr. Henry Cardenas

TABLE OF CONTENTS

ABSTRACT	iii
LIST OF TABLES.....	xi
LIST OF FIGURES	xiii
ACKNOWLEDGEMENTS	xxi
CHAPTER 1 INTRODUCTION	1
1.1 Problem.....	2
1.2 Objective	3
1.3 Approach.....	4
1.4 Overview	7
CHAPTER 2 BACKGROUND	10
2.1 Theory of Electrokinetics.....	10
2.1.1. Particle Suspensions	11
2.1.2 Electrophoresis	12
2.1.3 Zeta Potential	13
2.1.4 Electroosmosis.....	15
2.2 Concrete and Portland Cement.....	16
2.2.1 Concrete Strength	17
2.2.2 Pore Structure Characteristics	19
2.2.3 Calcium Silicate Hydrate (C-S-H)	21
2.2.4 Interfacial Transition Zone (ITZ).....	23
2.3 Transport Mechanism in Concrete	25
2.4 Durability of Concrete.....	26
2.5 Corrosion Mechanism of Reinforced Concrete.....	30
2.6 Diffusion of Chloride in Concrete.....	32
2.7 Service Life of Structures	34
2.8 Corrosion Cracking Process.....	35
2.9 Sulfate Attack in Concrete.....	37
2.10 Repair and Rehabilitation Techniques	41
2.10.1 Cathodic Protection.....	42
2.10.2 Electrochemical Chloride Extraction (ECE)	44
2.10.3 High Performance Concrete.....	45
2.10.4 Corrosion Inhibitors.....	46
2.10.5 Coatings, Sealers and Durable Reinforcement.....	47

	2.10.6 Electrokinetic Nanoparticle (EN) Treatment.....	49
	2.11 Evaluation Techniques	51
	2.11.1 Visual Inspection.....	52
	2.11.2 Half Cell Potential Measurements.....	53
	2.11.3 Polarization Resistance and Tafel Plot Technique	54
	2.11.4 Electrochemical Impedance Spectroscopy (EIS)	56
	2.11.5 Macrocell Techniques	60
CHAPTER 3	PROCEDURE.....	63
	3.1 Mix Design and Curing	63
	3.2 Electrokinetic Nanoparticle (EN) Treatments.....	68
	3.2.1 EN Treatment Setup on Young and Mature RC Cylinder	69
	3.2.2 EN Treatment on ASTM G109 Specimens.....	70
	3.2.3 EN Treatment on Reinforced Concrete Beams	72
	3.2.4 EN Treatment and Sulfate Extraction	74
	3.3 Electrochemical Measurements.....	76
	3.3.1 Corrosion Potential	76
	3.3.2 Corrosion Rate Measurements.....	77
	3.3.3 EIS Measurements	78
	3.4 Strength Tests	79
	3.5 SEM/BSE Specimen Analysis.....	81
	3.6 Microstructure Characterization	82
	3.7 Porosity Measurements	83
	3.8 Simulated Pore Fluid	83
CHAPTER 4	RESULTS AND DISCUSSION	85
	4.1 EN Treatment on Young and Mature RC Specimens	85
	4.1.1 Corrosion Potential and Corrosion Rates	86
	4.1.2 Chloride Diffusion Coefficients.....	90
	4.1.3 Corrosion Product, Porosity and Strength Analysis ..	92
	4.1.4 Chloride Content Analysis	96
	4.1.5 Microstructural Analysis	97
	4.1.6 FTIR and Raman Spectra Analysis.....	101
	4.1.7 XRD Analysis.....	102
	4.1.8 Summary of Findings for Young and Mature RC Specimens	104
	4.2 EN Treatment of ASTM G109 Specimens	105
	4.2.1 Corrosion Potential	106
	4.2.2 Corrosion Rates	108
	4.2.3 Corrosion Plots.....	111
	4.2.4 Electrochemical Impedance Spectroscopy.....	113
	4.2.5 Visual and Corrosion Product Analysis	116
	4.2.6 SEM Analysis.....	120

4.2.7	Summary of ASTM G109 Simulated Bridge Deck Specimens	122
4.3	EN Treatment of Reinforced Concrete Beams.....	123
4.3.1	Corrosion Potential and Corrosion Rates	124
4.3.2	Chloride Contents	129
4.3.3	Mercury Induced Porosimetry (MIP)	130
4.3.4	SEM/BSE Analysis	134
4.3.5	Raman Spectroscopy	140
4.3.6	FTIR Spectral Analysis.....	143
4.3.7	X-Ray Diffraction (XRD) Analysis.....	145
4.3.8	Summary of the Beam Specimen Work	146
4.4	Sulfate Attack in Concrete	147
4.4.1	Sulfate Exposure Results	148
4.4.2	Compressive Strength and Porosity Results.....	150
4.4.3	Microstructural Analysis	154
4.4.4	Raman Spectral Analysis.....	159
4.4.5	FTIR Analysis	160
CHAPTER 5	CONCLUSION AND FUTURE WORK	168
5.1	EN Treatment on Young and Mature Concrete.....	168
5.2	EN Treatment on ASTM G109 Specimens	169
5.3	EN Treatment on Reinforced Concrete Beams	169
5.4	EN Treatment to Mitigate Sulfate Attack in Concrete.....	170
5.5	Overall Conclusion Regarding EN Treatment.....	171
5.6	Future Work.....	172
APPENDIX A	MERCURY INTRUSION POROSIMETRY (MIP)	173
APPENDIX B	CHLORIDE CONTENT MEASUREMENTS	180
APPENDIX C	pH MEASUREMENT IN CONCRETE.....	183
APPENDIX D	CORROSION PRODUCT ANALYSIS.....	185
APPENDIX E	EN TREATMENT ON BEAMS	187
APPENDIX F	ADDITIONAL IMAGES ON SULFATE ATTACK	193
APPENDIX G	ATOMIC FORCE MICROSCOPY (AFM).....	198
APPENDIX H	EQUIPMENT USED FOR MICROSTRUCTURAL ANALYSIS	200
APPENDIX I	DATA OF YOUNG AND MATURE CONCRETE	205
APPENDIX J	DATA OF ASTM G109 SPECIMENS	208

APPENDIX K ENERGY DISPERSIVE SPECTRUM ANALYSIS..... 211
REFERENCES..... 215

LIST OF TABLES

Table 1.1 List of publications incorporated into dissertation	8
Table 2.1 Composition of ordinary Portland cement (Adapted from Mindess et al., 2005, p. 21)	17
Table 2.2 Classification of pore sizes (Adapted from Aligizaki, 2006, p.13 and from Mindess et al., 2005, pp.75-76)	21
Table 2.3 Chemical notations and formulae of monosulfate, gypsum and ettringite (Skalny et al., 2001, p.20)	39
Table 2.4 Condition surveying methods for corrosion in concrete (Adapted from Broomfield, 1997, p.26)	52
Table 2.5 Guidelines for evaluating reinforcement corrosion in concrete (ASTM C 876-91)	54
Table 2.6 Units of Faraday's constant (Adapted from ASTM G102, 1999).....	55
Table 3.1 Type I Portland cement composition	64
Table 3.2 Batch composition	64
Table 3.3 Chemical composition of cement.....	67
Table 3.4 Material setup for reinforced concrete beam	67
Table 3.5 Material setup, curing and mix proportions	68
Table 3.6 Schedule of EN treatments for young and mature concrete	69
Table 3.7 Composition of high-alkali simulated pore fluid.....	84
Table 4.1 Interpretation of corrosion current density with corrosion (Adapted from Broomfield, 1997)	89
Table 4.2 Strength, porosity and corrosion analysis	95

Table 4.3 Guidelines for chloride-ion penetrability based on the charge passed as per ASTM C 1202	112
Table 4.4 Guidelines for evaluating the severity of corrosion	127
Table 4.5 Porosity results using MIP and WLR methods.....	132
Table 4.6 Compressive strength and porosity analysis	152
Table 4.7 Typical pore diameter ranges for concrete materials.....	152
Table I.1 Corrosion potential data.....	206
Table I.2 Diffusion coefficients of young and mature reinforced concrete	207
Table I.3 Chloride content data	207
Table J.1 Corrosion rate measurements on control specimens.....	209
Table J.2 Corrosion rate measurements on EN Treated specimens	209
Table J.3 Total corrosion data of the control specimens	210
Table J.4 Total corrosion data of the EN Treated specimens.....	210

LIST OF FIGURES

Fig 1.1 Fundamental concept of nanoparticle transfer.....	2
Fig 1.2 Experimental plan of EN treatment on chloride exposed specimens.....	5
Fig 1.3 Experimental plan of EN treatment on sulfate exposed specimens.....	6
Fig 2.1 Particles undergoing Brownian motion	11
Fig 2.2 Schematic representation of zeta potential (Adapted from Zetasizer Nanoseries Manual, 2004, p.16.2)	13
Fig 2.3 Schematic diagram of double layer (Adapted from Crow, 1994, p.80) ..	15
Fig 2.4 Flow chart showing the factors influencing the concrete strength (Adapted from Mehta and Monteiro, 2006, p.67)	18
Fig 2.5 Pore structure in concrete.....	20
Fig 2.6 Illustration of wall effect phenomena in ITZ (Adapted from Scrivener et al., 2004, p.412)	24
Fig 2.7 Idealized model of transfer process within concrete (Adapted from Hearn and Figg, 2001, p.329)	26
Fig 2.8 Flow chart illustrating the causes for deterioration of concrete (Adapted from Mehta and Monteiro, 2006, p.131)	28
Fig 2.9 The breakdown of the passive layer and recycling of chlorides.....	30
Fig 2.10 Variation of chloride concentration values with distance from the exposed surface (Adapted from Poulsen and Mejlbro, 2006, p.69)	34
Fig 2.11 Chloride corrosion deterioration process for a low permeable reinforced concrete structures when exposed to sea saltwater (Adapted from Weyers, 1998, p.446)	35

Fig 2.12 Two paths leading to corrosion-cracking process (Adapted from Liu and Weyers, 1998, p. 679).....	37
Fig 2.13 Flow chart showing the non-destructive methods for rehabilitation of corroded reinforced concrete	42
Fig 2.14 Layout of the impressed current cathodic protection (CP) system (Adapted from Scannell et al., 1996, p.4-24)	43
Fig 2.15 Schematic diagram of electrochemical chloride extraction (ECE) (Adapted from Bertolini et al., 2004, p.364)	45
Fig 2.16 Schematic representation of different types of surface coatings (Adapted from Bentur et al., 1998, p.124).....	49
Fig 2.17 Alumina coated silica nanoparticle	50
Fig 2.18 A schematic illustration of the corrosion potential measurement of reinforced concrete (Adapted from Bentur et al. 1998, p.77)	54
Fig 2.19 Tafel plot exhibiting log current versus relative potential (Adapted from Al-Tayyib and Khan, 1998)	56
Fig 2.20 Argand diagram or complex plane (Adapted from Barsoukov and Macdonald, 2005, p.6)	57
Fig 2.21 Equivalent circuit model used to determine the linear polarization resistance (R_p) from EIS (Adapted from Kelly et al. 2002, p.135)	59
Fig 2.22 Typical Nyquist plot for a hardened cement paste (Adapted from Cardenas 2002, p.26)	59
Fig 2.23 ASTM G109 Specimen simulating the formation of macrocell.....	61
Fig 2.24 Measurement of macrocell current density (Adapted from Mohammed et al. 1999, p.156).....	62
Fig 3.1 Front view of the reinforced cylindrical concrete specimen	65
Fig 3.2 Schematic diagram of ASTM G109 specimens	66
Fig 3.3 EN treatment on cylindrical reinforced concrete	70
Fig 3.4 Circuit diagram for ECE and EN treatment of G109 specimens	71

Fig 3.5 Circuit diagram during electrochemical chloride (ECE) and electrokinetic nanoparticle (EN) treatment	73
Fig 3.6 Circuit diagram for sulfate extraction and EN treatment	75
Fig 3.7 Measurement of half-cell potential.....	77
Fig 3.8 Corrosion rate measurement setup	78
Fig 3.9 Schematic setup for EIS measurement	79
Fig 3.10 Schematic setup of splitting tensile test.....	80
Fig 4.1 Corrosion potential of young and mature reinforced concrete	87
Fig 4.2 Corrosion current densities using LPR method on young and mature specimens.....	88
Fig 4.3 Chloride diffusion through pore wall	89
Fig 4.4 Chloride diffusion coefficients using electrochemical Impedance spectroscopy (EIS) for young and mature concrete	91
Fig 4.5 Concept of chloride diffusion into capillary pores.....	92
Fig 4.6 Front view of the mature un-cracked EN treated cylindrical specimens and cracked controls.....	93
Fig 4.7 Corrosion product coverage areas measured on steel bars taken from control specimens and EN treated specimens of mature concrete	94
Fig 4.8 Corrosion product coverage areas measured on steel bars taken from control specimens and EN treated specimens of young concrete	94
Fig 4.9 Variation of chloride contents with distance from the reinforcement.....	96
Fig 4.10 A. Ettringite in the presence of calcium hydroxide of mature concrete. B. Ettringite needles in the mature concrete specimens	98
Fig 4.11 Morphology of untreated specimens compared to EN treated specimens that exhibited a more dense morphology.....	98

Fig 4.12 Backscattered electron image (BSE) of a young EN treated specimen. Brighter regions indicate C-S-H mixed with calcium carbonate.....	99
Fig 4.13 Backscattered electron image (BSE) of a young control specimen showing degradation and EDS spectrum.....	100
Fig 4.14 Presence of dicalcium aluminate hydrate (C_2AH_8) on young EN treated specimens	100
Fig 4.15 Magnified image showing striated needles of dicalcium aluminate hydrate (C_2AH_8)	100
Fig 4.16 Fourier transform infrared spectroscopy (FTIR) of EN treated and control specimens.....	102
Fig 4.17 XRD data of EN treated and control specimens	104
Fig 4.18 Corrosion potential plot of reinforced G109 specimens at different stages of the treatment.....	107
Fig 4.19 Corrosion current densities (I_{corr}) of control specimens	109
Fig 4.20 Corrosion current densities of EN treated specimens.....	109
Fig 4.21 Corrosion rates of control (A) and EN (B) treated specimens.....	110
Fig 4.22 Mass loss rate of the top and bottom bars of control and EN treated specimens	111
Fig 4.24 Total corrosion plot in terms of charge of coulomb for EN treated specimens	113
Fig 4.23 Total corrosion plot in terms of charge of coulombs for control specimens	112
Fig 4.25 Nyquist plot of control specimens.....	114
Fig 4.26 Nyquist plot of EN treated specimens.....	115
Fig 4.27 Resistivity spectra of $\log Z$ versus frequency (Hz).....	115
Fig 4.28 Phase versus log of frequency	116

Fig 4.29 A.Top view of a cracked control and an un-cracked EN Treated specimen, B. EN treated specimens, and C. Cracked control specimens	117
Fig 4.30 Digital image of top bars of controls and EN treated specimens	118
Fig 4.31 Digital image of bottom bars of controls and EN treated specimens .	118
Fig 4.32 Corrosion product analysis of EN treated and controls of bottom and top rebars.....	119
Fig 4.33 Control specimens (cracked specimen) and EN treated specimens showing dense microstructure	121
Fig 4.34 EN treated specimens depicting a microstructure of C-S-H.....	121
Fig 4.35 (A) Corrosion products in the form lepidocrocite, (B) Magnified image of corrosion products, (C) pores present in the control specimens and (D) Magnified image of corrosion products	122
Fig 4.36 Corrosion potential data of reinforced concrete specimens.....	125
Fig 4.37 Comparative plot of corrosion current density (I_{corr}) for EN Treated, ECE and Controls	127
Fig 4.38 Comparative plot of polarization resistance (R_p) for EN treated, ECE and Controls	128
Fig 4.39 Chloride content values with the distance away from the reinforcement.....	130
Fig 4.40 Mercury induced porosimetry (MIP) curves on powdered concrete adjacent to the rebar.....	131
Fig 4.41 MIP curves on the powdered concrete two inches away from the rebar	131
Fig 4.42 Concept of positive nanoparticles and negative ions into the capillary pore	133
Fig 4.43 Imprints of corrosion products at the rebar/concrete interface for EN Treated and controls.....	135
Fig 4.44 A: Presence of lepidocrocite which is exhibited as flowery structures. B: Magnified image of lepidocrocite on the control at R/C interface.....	135

Fig 4.45 A:Lepidocrocite crystals depicting flowery pattern outside the pores. B: Presence of lepidocrocite crystals present in the inner layer of the pores.....	135
Fig 4.46 A:Cotton ball structures demonstrating the semicrystalline phase of goethite, B: Magnified image of goethite cotton ball	136
Fig 4.47 A: EN treated specimens indicating formation of stable trigonal calcite B: Control depicting sandwiched layer of unstable hexagonal calcium hydroxide (CH) crystals.....	137
Fig 4.48 Backscattered electron (BSE) image of control (A and B), EN treated (C) and ECE specimen (D)	138
Fig 4.49 Quantitative EDS analysis of EN Treated specimen of $0.65 \text{ (l/m}^2\text{)}$	139
Fig 4.50 Quantitative EDS analysis of EN treated specimen of $0.33 \text{ (l/m}^2\text{)}$	139
Fig 4.51 Quantitative EDS analysis of EN treated specimen of $0.16 \text{ (l/m}^2\text{)}$	139
Fig 4.52 EDS analysis of ECE treated specimen	140
Fig 4.53 EDS analysis of the polished untreated control	140
Fig 4.54 Raman spectroscopy of EN Treated ($0.65, 0.33$ and 0.16 l/m^2) and control specimens.....	141
Fig 4.55 Raman spectra of simulated pore fluid (SMP) with alumina coated silica and excess calcium hydroxide	143
Fig 4.56 FTIR spectra of SMP mixed with alumina coated silica and colloidal alumina	144
Fig 4.57 FTIR spectra of EN treated specimens and untreated control.....	145
Fig 4.58 XRD analysis of powdered concrete of beam specimens.....	146
Fig 4.59 Damage due to sodium sulfate exposure	149
Fig 4.60 Sulfate induced expansion during the initial exposure applied to 12 specimens over a course of 4 weeks.....	149
Fig 4.61 Influence of sodium sulfate exposure on compressive strength	150
Fig 4.62 Pore size distributions using mercury intrusion porosimetry (MIP)	153

Fig 4.63 SEM micrograph of gypsum and ettringite.....	156
Fig 4.64 SEM micrograph of ettringite needles demonstrating porous volume	156
Fig 4.65 BSE image and EDAX micrograph of epoxy impregnated sulfate exposed and EN treated specimen indicating pores.....	157
Fig 4.66 Raman spectroscopy of EN treated specimen depicting sulfate, carbonation and C-S-H phase	160
Fig 4.67 FTIR transmittance spectra of sulfate exposed, untreated control and EN treated specimen	161
Fig 4.68 FTIR spectra of alumina-coated silica with colloidal alumina mixed with simulated pore fluid	162
Fig A. 1 Schematic setup of MIP (Adapted from Aligizaki, 2006, p.62).....	175
Fig A. 2 Forces inside a capillary pore (Adapted from Aligizaki 2006, p.66).....	177
Fig A. 3 Critical and threshold pore diameter (Adapted from Aligizaki, 2006, p.74).....	179
Fig D. 1. Schematic layout of corrosion products on the reinforcement.....	186
Fig E. 1. Configuration of EN treatment on beams	188
Fig E. 2 EN treated (A and B) and control reinforcements (C and D)	189
Fig E. 3. EN treated and control rebar/concrete interface.....	190
Fig E. 4. Efflorescence observed on the EN treated specimens.....	190
Fig E. 5. EN treated and control reinforcements after strength test.....	191
Fig E. 6 Sponge and titanium mesh used for EN treatment.....	192
Fig F. 1 Sodium sulfate crystal on sulfate exposed specimen	194
Fig F. 2 Magnified image of the sodium sulfate crystal.....	194
Fig F. 3 C-S-H II in the form of flakes on the EN treated specimens	195

Fig F. 4 Type II C-S-H in the form of honeycomb flakes within EN Treated specimen.....	195
Fig F. 5 Pores within the control specimens.....	196
Fig F. 6 Micro-cracks within control specimens.....	196
Fig F. 7 Concrete specimen cast in epoxy.....	197
Fig F. 8 Degradation in the form of color change on sulfate control	197
Fig G. 1 AFM image of C-S-H gel.....	199
Fig G. 2 (a) AFM Image C-S-H gel (topography), (b) Change in amplitude.....	199
Fig H. 1 Hitachi S-4800 field emission scanning electron microscope.....	201
Fig H. 2 X-ray diffraction analysis (D8 Advance Bruker AXS Inc).....	201
Fig H. 3 Raman Spectrometer (Raman Systems, Woburn, MA)	202
Fig H. 4 Mattson Genesis II Fourier transform Infrared Spectroscopy (FTIR) ..	202
Fig H. 5 Alpha beta grinder used for polishing concrete (Buehler, Lake Bluff, IL).....	203
Fig H. 6 Vacuum impregnation using castable vacuum system (Buehler, Lake Bluff, IL).....	203
Fig H. 7 Mercury Intrusion porosimetry (Auto Pore 9500, Micromeritics, Inc, Norcross GA)	204
Fig K. 1 EDS spectrum with element mapping	212
Fig K. 2 EDS spectrum with element mapping of SiK, SK, CaK, LaCa, LaSiCa and LaS.....	213
Fig K. 3 EDS spectrum with element mapping of LaAl and LaMg	214

ACKNOWLEDGEMENTS

I am indebted to Dr. Henry E. Cardenas for providing me with his constant guidance, support and encouragement. Synergetic discussions with him aided me to overcome various difficulties during this project. I also express my sincere gratitude and appreciations to the members of my advisory committee, Dr. Luke Lee, Dr. Sven Eklund, Dr. Erez Allouche, Dr. Hisham Hegab, Dr. Daniela Mainardi and Dr. Jinko Kanno. I would like to thank Dr. Galen Turner and Dr. Ramu Ramachadran for the college of engineering and science fellowship. I thank Dr. Luz Marina Calle from the Kennedy Space Research Center, NASA for her support and guidance during my project work. I would like to express my gratitude to Dr. Karen Xu and Dr. Alfred Gunasekaran for helping me with the X-ray diffraction and SEM work. I would like to thank Dr. Sidney Sit and Dr. Stephanie Tully-Dartez for their assistance in the MIP test. I am in debt to my research colleagues Kanielle Gordon, Anupam Joshi, Harish Venkateshaiah and Oner Moral. I would like to express my gratitude to Mr. Ray McKinney Jr. and Mr. Jimmy Cook for giving me access to the machine shop laboratory facilities. I would like thank Mrs. Julia Hardie from the Department of English for proofreading and English editing. I am extremely thankful for the encouragement and support provided by my friends namely Pritam Karulkar, Raunak Patil, and Pranjal Bhatia. I am grateful to the support of Anirvan Sircar during my doctoral

work. My appreciations and thanks are due to all my family and my roommates. Last but not least, I am forever indebted to my father, Dr. Vijay Kupwade, mother, Dr. Sarawati Kupwade and brother, Harsh Kupwade-Patil for fortifying my dreams and aspirations.

CHAPTER 1

INTRODUCTION

This work deals with the application of electrokinetics, using positively charged nanoparticles for corrosion protection in reinforced concrete structures. This technique involves the principle of electrophoretic migration of nanoparticles to hinder chloride diffusion in the concrete. The re-entry of the diffused chlorides is inhibited by the electrodeposited assembly of the nanoparticles at the rebar interface, as shown in Figure 1.1. Concrete is also susceptible to degradation due to the ingress of deleterious species, such as sulfates which are commonly referred to as a sulfate attack.

The aim of this investigation was to analyze the effect of electrokinetic nanoparticle (EN) treatment on chloride and sulfate induced corrosion. Insertion of charged nanoparticles was done using an applied electric field. The corrosion potential and corrosion rates of the steel reinforcement, microstructural, chemical and porosity analysis were conducted during this study. The effect of EN treatment on strength was also investigated during this study.

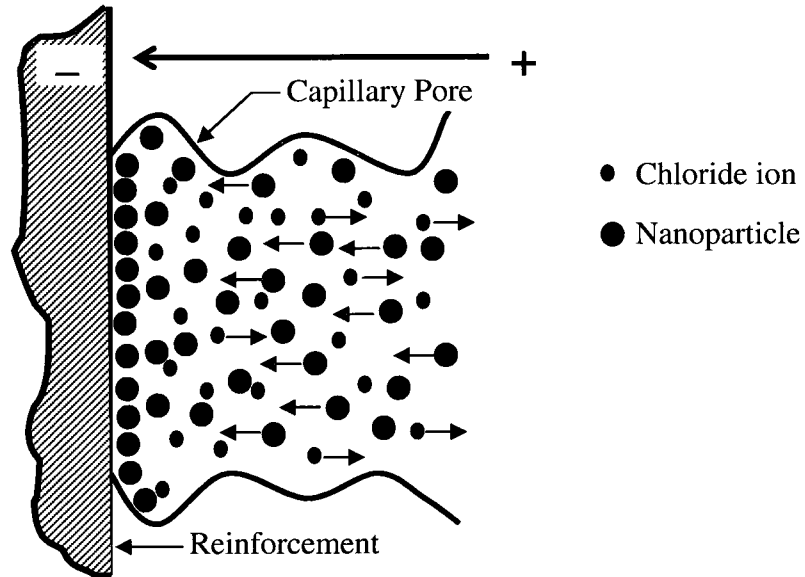


Fig 1.1 Fundamental concept of nanoparticle transfer

1.1 Problem

Concrete is a highly porous material which is susceptible to the migration of highly deleterious species such as chlorides and sulfates (Mindess et al., 2003). Reinforcement corrosion in concrete due to the ingress of these species is a serious durability issue in the civil infrastructure industry (Bentur et al., 1998). Billions of dollars are spent to rehabilitate the corroded infrastructure using various repair techniques. This work addresses an \$8 billion national infrastructure repair problem (Koch et al., 2002). Corrosion of reinforcement occurs when the rebar in concrete is exposed to chlorides either leached from the concrete ingredients or migrated in from the surrounding environment (Mehta and Monteiro, 2006). Various external sources, including sea salt spray, direct sea water wetting, deicing salts and brine tanks, harbor chlorides that can enter reinforced concrete. Chlorides diffuse into the capillary pores of concrete and

come into contact with the reinforcement (rebar). When the chloride concentration at the rebar exceeds a threshold level, it breaks down the passive oxide layer of the rebar, leading to chloride induced corrosion.

An alternate method of initiation of corrosion is due to absorption of CO_2 . Calcium hydroxide, which exists as one of the primary constituents in concrete, reacts with the carbonic acid to form calcium carbonate. This process is called carbonation. The carbonation of concrete, the application of chloride deicing salts, and the increased use of concrete in marine environments all facilitate reinforcement corrosion. Reinforcement corrosion leads to a reduction of rebar cross sections, delamination and spalling of concrete cover and loss of the bond between the rebar and concrete. This causes cracking, reduction in strength and finally the failure of the structure (Shamsad, 2003). Various methods are used to prevent reinforcement corrosion of new structures, including epoxy coated rebar, overlays, membranes, and inhibitors mixed into the batch (Broomfield, 1997). Electrochemical chloride extraction (ECE) and cathodic protection are some of the existing techniques used as repair strategies against corroded reinforced concrete structures.

1.2 Objective

The objective of this work was to mitigate both reinforcement corrosion and sulfate induced corrosion in concrete using Electrokinetic Nanoparticle (EN) treatment. The intent was to improve the durability of concrete by using nanoparticles as a pore blocking agent. It was anticipated that these particles would result in a dense microstructure at the rebar/concrete interface that would

provide a barrier against chloride penetration. In the sulfate attack, it was anticipated that the particles would provide a reduction in porosity that would provide a recovery of strength and removal of sulfates.

1.3 Approach

Electrokinetic nanoparticle (EN) treatment was conducted using 24-nm alumina coated silica nanoparticles. The effectiveness of the EN treatment to mitigate reinforcement corrosion in concrete was evaluated using three different sizes of specimens, as shown in the experimental flow chart (refer to Figure 1.2). EN treatment was applied initially to three inch diameter by six inch length reinforced cylindrical concrete specimens. ASTM G109 specimens, which simulate a bridge deck, were also subjected to EN treatment followed by the treatment application to full length beams specimens. The cylindrical specimens were categorized as mature and young concrete. The details of the treatment are discussed in Section 3.2 of the procedure section. The specimens were subjected to electrochemical chloride extraction (ECE) concurrent with EN treatment. ECE is a process involving the removal of chlorides from reinforced concrete structures by electrokinetic ion migration (Elsener et al., 1993). Chemical, porosity, strength and microstructure analysis was conducted on the untreated controls, ECE and EN treated specimens as shown in Figure 1.2.

EN treatment was also used as a remedy to mitigate degradation in concrete in the form of sulfate attack (refer to Figure1.3). Sulfate attack is a form of deterioration of concrete accompanied by microstructural expansion and loss

of strength due to the ingress of high sulfate content into the pores of the concrete (Neville, 2004).

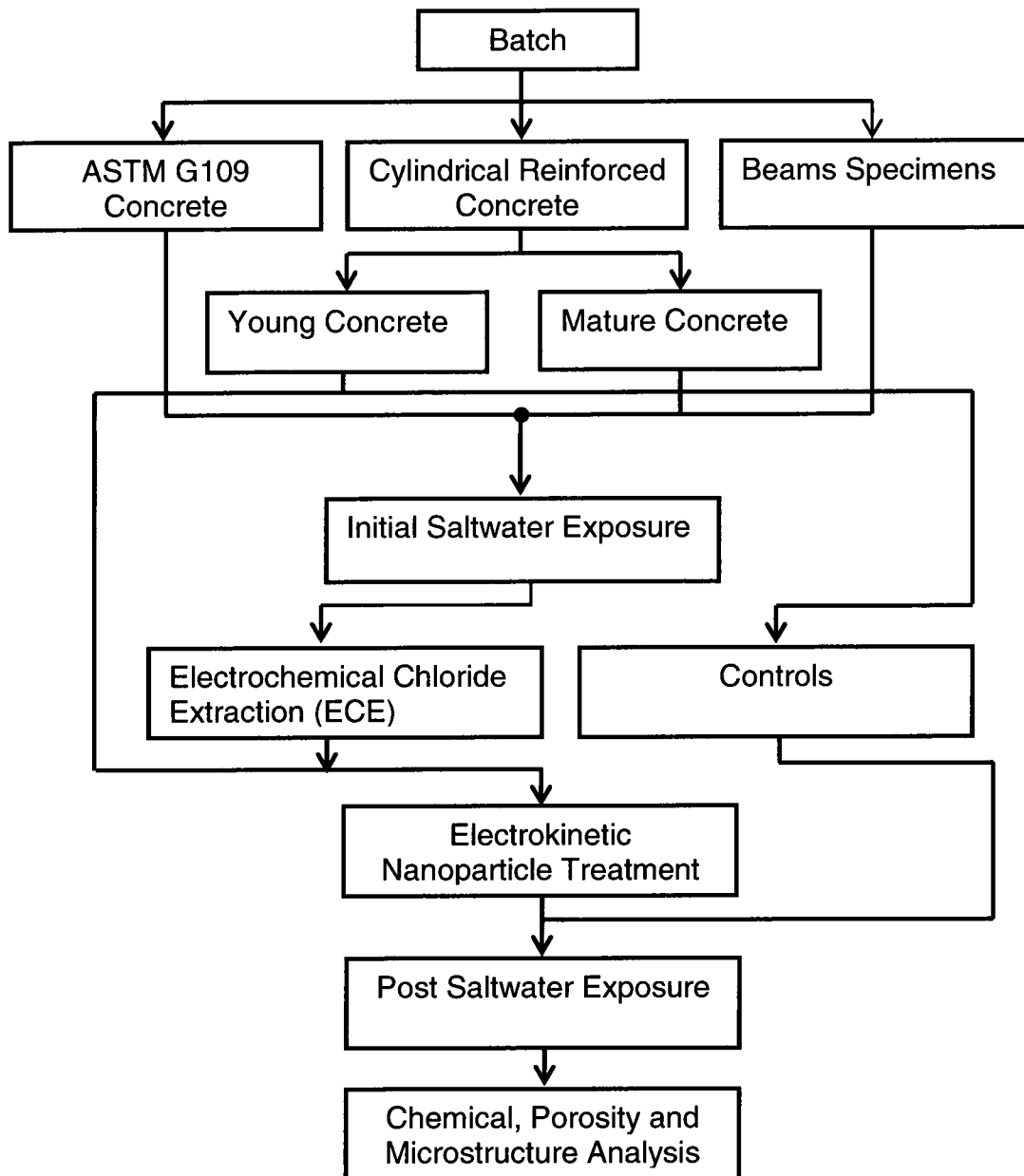


Fig 1.2 Experimental plan of EN treatment on chloride exposed specimens

Cylindrical concrete specimens were subjected to initial sulfate exposure followed by length change and compression strength evaluation or testing. Sulfates were extracted from some specimens followed by EN treatment. Chemical, porosity and microstructural analysis were conducted on all the specimens as shown in Figure 1.3.

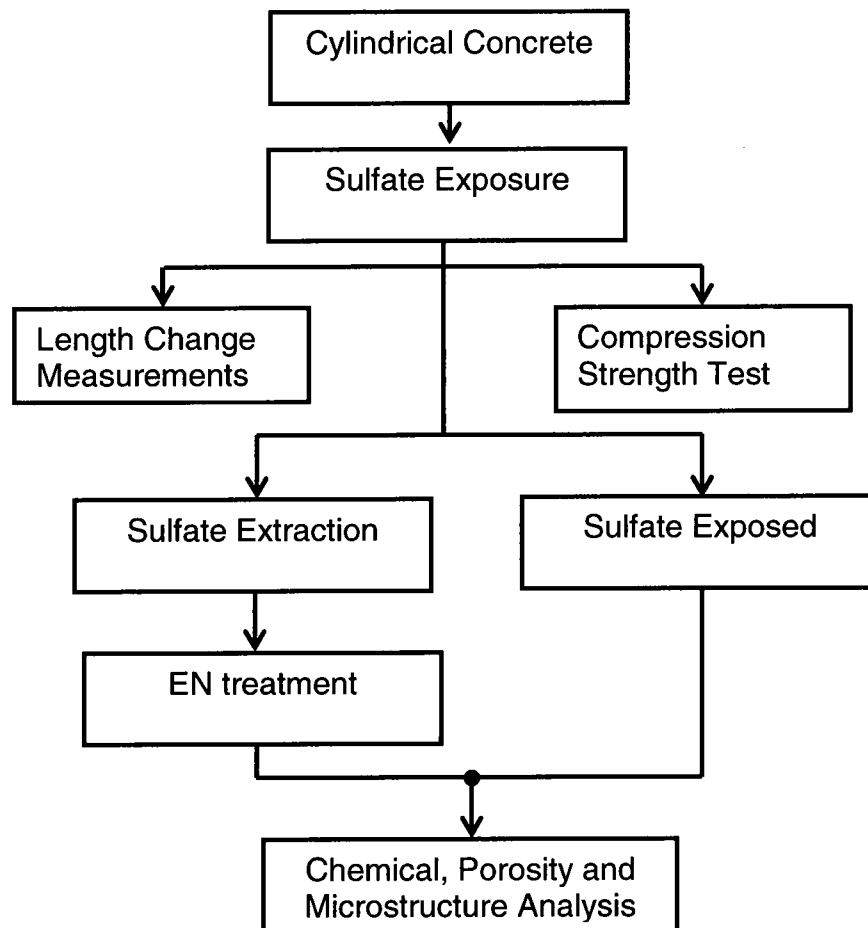


Fig 1.3 Experimental plan of EN treatment on sulfate exposed specimens

1.4 Overview

This dissertation provides a brief background (Chapter Two) on the theory of electrokinetics and its processes in Section 2.1. This section also deals with chemistry of Portland cement and concrete. Degradation of structures due to corrosion and sulfate attack in concrete is discussed in Sections 2.4 to 2.8. Existing repair techniques used to mitigate reinforcement corrosion is shown in Section 2.9. Concepts such as half cell potential measurements, corrosion rate measurements (Linear polarization resistance and Tafel plot), and application of electrochemical impedance spectroscopy for corrosion analysis are discussed in Section 2.10.

Chapter Three primarily highlights the procedure for EN treatment on three different specimen geometry configurations. EN treatment was conducted on reinforced cylindrical concrete specimens, ASTM G109 specimens that simulate a bridge deck and full length beam specimens (refer to Sections 3.2.1 to 3.2.4). It was prudent in terms of cost to evaluate the small scale specimens. The cylindrical specimens were the most cost effective to examine an initial proof of the principle. Full length beams were used to explore scale up issues for specimens that represent the size challenges of actual field conditions. Electrochemical techniques, measurement of strength tests, microstructural and porosity analysis are discussed in this section. The results section consisted of studies published by the author. The outline of the published work is shown in Table 1.1.

Table 1.1 List of publications incorporated into dissertation

Section	Authors	Title	Publications	Place/Year
4.1	Cardens, H; Kupwade-Patil, K.; and Eklund,S.	Corrosion mitigation in mature reinforced concrete using nanoscale pozzolan deposition	Second international conference on sustainable construction materials and technologies	Ancona, Italy, 2010
4.2	Kupwade-Patil, K.; and Cardenas, H.	Corrosion mitigation in concrete using electrokinetic injection of reactive composite nanoparticles	Proceeding of 53 international conference on advancement of material and process engineering	Long Beach, CA, 2008
4.3	Kupwade-Patil, K.; Gordon, K.; Xu, K.; Moral, O.; Cardenas, H.; and Lee, L.	Corrosion mitigation in concrete beams using electrokinetic nanoparticle treatment	Proceedings on Excellence in Concrete Construction through Innovation	London, UK, 2008
4.4	Kupwade-Patil, K.; and Cardenas, H.	Composite nanoparticle treatments for mitigation of sulfate attack in concrete	Proceeding of 53 international conference on advancement of material and process engineering	Long Beach, CA, 2008

CHAPTER 2

BACKGROUND

Sections 2.1 to 2.15 provide information regarding the fundamental properties that affect reinforcement corrosion in concrete. These sections cover characteristics of concrete strength, the corrosion mechanism, the concrete cracking process and review of the electrochemical repair techniques for corroded reinforced concrete structures.

2.1 Theory of Electrokinetics

Electrokinetics refers to the motion of charges in fluids under the influence of an electric field (Delgado, 2002). The main types of electrokinetic transport can be classified into ionic conduction, electrophoresis and electroosmosis. Ionic conduction is the motion of ions through water as induced by an electric field (E). Electrophoresis can be attributed to the motion of suspended micro or nanoparticles through liquid as induced by an electric field. The bulk flow of the liquid through a porous material as induced by an electric field is known as electroosmosis.

2.1.1. Particle Suspensions

Solid particles can be suspended in liquid (Bockris and Reddy, 1970; King et al, 1972). Consider the motion of a solid particle in a liquid as shown in Figure 2.1. The random movement of the particle is Brownian motion. It is due to collisions between the particles and fluid molecules in which they are suspended. As long as the particles are not too large, or do not collide and stick together, Brownian motion remains more influential than the gravitational force that could otherwise pull it down out of suspension. The suspension is a chemical mixture in which one phase of matter is dispersed uniformly throughout another.

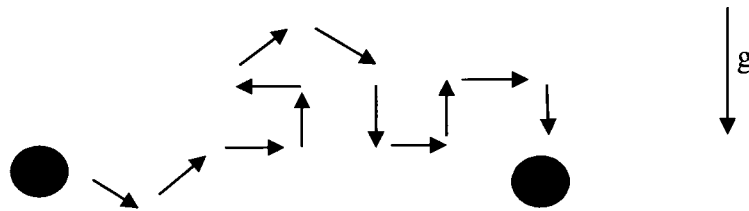


Fig 2.1 Particles undergoing Brownian motion

The factors influencing the stability of the particles are temperature, particle size and particle concentration. At high temperatures, collision frequency is higher, hence the stability of the particles is lower. Collision induced agglomerations and just simply large particle sizes tend to be pulled by gravity. Small particles have more surface area, allowing more chances to collide and stick together (agglomeration). The particle concentration also predicts the effect of stability. Higher particle concentration leads to more collisions, allowing less stability. Particle surface charge can also help with the stability by causing repulsion, which helps avoid collision.

2.1.2 Electrophoresis

The motion of suspended particles using an electric field is known as electrophoresis (Schwarz et al., 2004; Delgado, 2002; Masliyah and Bhattacharjee, 2006). When an electric field is applied across a conducting liquid, the charged particle moves toward the oppositely charged electrode. The viscous forces acting on the particle tends to oppose the electrical force. These two opposing forces reach equilibrium, thus causing the particle to move with constant velocity. The velocity of the particle per unit of electric field is known as the electrophoretic mobility (U). The electrophoretic mobility of a particle is defined as follows

$$U \text{ (Mobility)} = \frac{\text{Velocity}}{\text{Electric Field}} = \frac{v \text{ (m/sec)}}{E \text{ (Volts/m)}} \quad [1]$$

The mobility of the charged particle depends on the strength of the electric field, viscosity of the medium, zeta potential and the dielectric constant of the medium. Henry's law relates the electrophoretic mobility to the zeta potential (ζ)

$$U = \frac{2 \varepsilon \xi f(kr)}{3\eta} \quad [2]$$

where ε = dielectric constant, ξ = zeta potential, $f(kr)$ = Henry's function, and η = viscosity. The Henry's function is a correction factor depending on the product of k , which is the Debye-Huckel parameter, and r is the particle radius. A constant value of 1.5 is usually adopted for $f(ka)$ and this is referred to as the Smoluchowski approximation (Schwarz et al., 2004; Delgado, 2002).

2.1.3 Zeta Potential

A key feature in transport is the net charge possessed by the particle in the suspension (Cardenas, 2002; Schwarz et al., 2004). The net charge developed on the particle influences the ions surrounding the interfacial region, causing an increased concentration of counter ions near the surface as shown in Figure 2.2. The interfacial region exists in a system which possesses a large ratio of surface area to volume like porous bodies with pores on a micro or nano size levels.

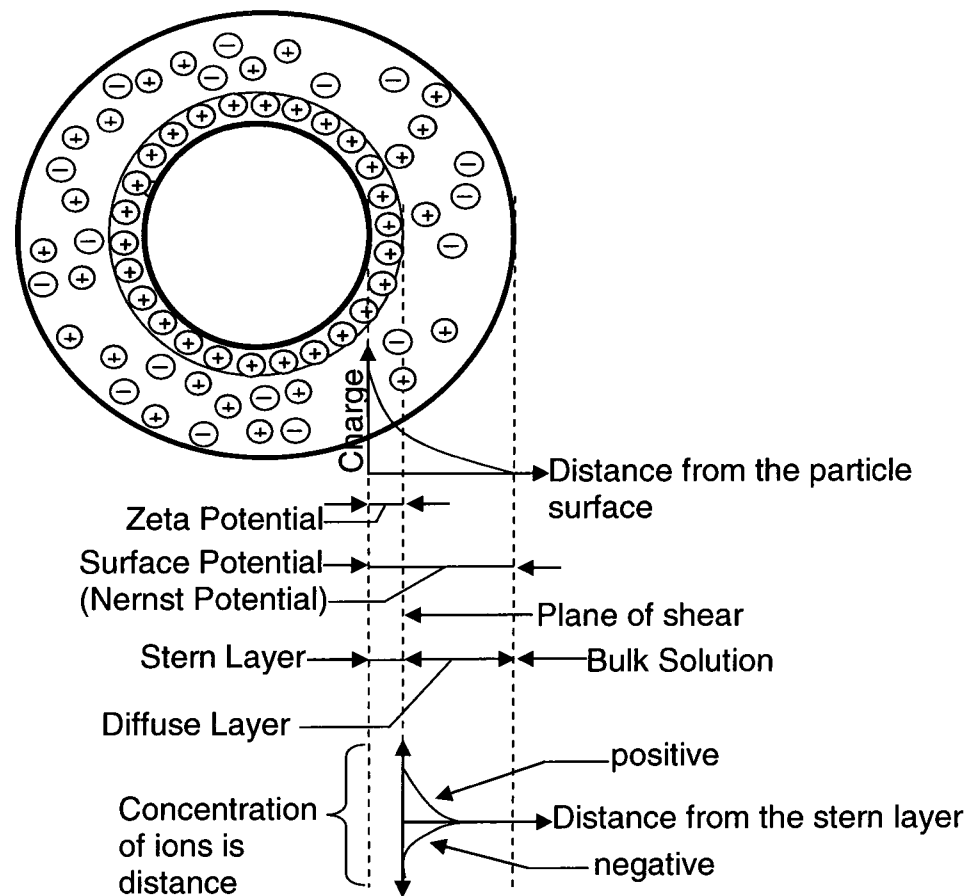


Fig 2.2 Schematic representation of zeta potential (Adapted from Zetasizer Nanoseries Manual, 2004, p.16.2)

The counter ions possess an opposite charge as compared to the particle. Oppositely charged ions approach the counter ion layer (stern layer). This forms a double layer surrounding each particle.

The inner region is called the stern layer in which the ions are strongly bound, and in the diffuse region (the outer layer) they are loosely attached. The double layer originates when an object (solid particle or porous body) comes in contact with a liquid (Lyklema, 1995). The charge on the surface consists of the first layer, while the double layer has parallel layers of charges (refer to Figure 2.3). The diffuse layer has unbound ions in fluid (sol or colloid) due to the influence of the electric field. In the diffuse layer, the ions and particles form a semi-stable entity. The ions move in succession with the particle, but the ions are prohibited from entering the slipping plane (hydrodynamic shear), and the potential that exists at the boundary is called the zeta potential (ζ). The slipping plane segregates the moving fluid from the fluid that remains coupled to the surface (Schwarz et al., 2004; Delgado, 2002). Therefore, zeta potential can be defined as the electrical potential in the plane which separates the mobile and immobile sections of the double layer.

The stability of the colloidal system can be predicted by the magnitude of the zeta potential. The particles that possess less negative or positive zeta potential tend to repel each other and prevent the particles from coming together. The factors affecting the zeta potential are pH, conductivity and concentration.

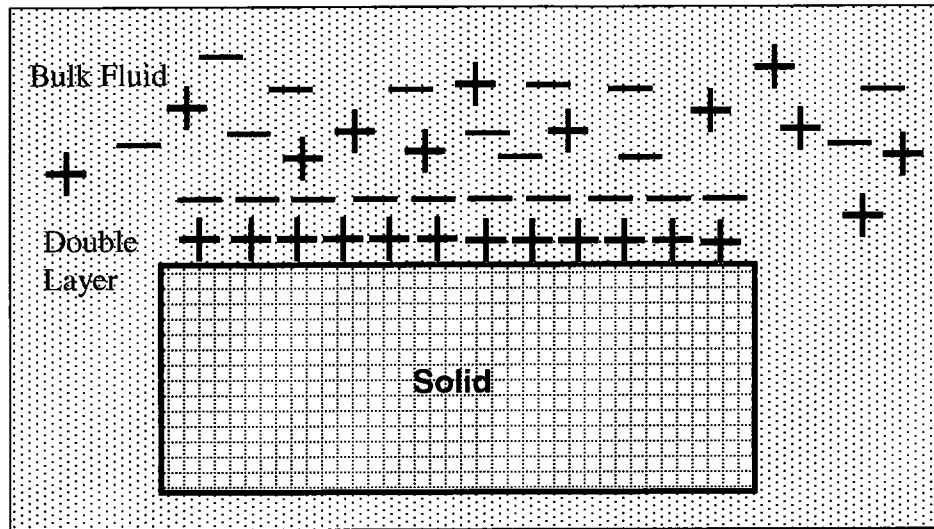


Fig 2.3 Schematic diagram of double layer (Adapted from Crow, 1994, p.80)

2.1.4 Electroosmosis

The bulk flow of liquid through a charged porous material under the influence of the electric field is known as electroosmosis (Glasstone, 2008; Sorenson, 1999). This electric field, when applied on the pore wall, generates forces which are exerted on both sides of the double layer. The forces include the electroosmotic force and the frictional force between the liquid layer and the pore wall. The electric field helps the sol particles to move with an electroosmotic velocity (v_{EO}) with the double layer.

$$v_{EO} = \frac{\varepsilon \zeta E}{4\pi\eta} \quad [3]$$

where η , ζ and ε are the viscosity of the solution, zeta potential of the particle and the dielectric constant. E is the applied electric field. The electroosmotic velocity can be modified when applied to a capillary pore of the concrete, Equation 3 was modified by (Cardenas and Struble, 2008)

$$v_{EO} = \frac{A F r^2 \Delta E}{8 \eta l} \quad [4]$$

where A = fluid concentration of the pore wall, F = Faraday's constant, r = pore radius, l = pore length, η = absolute viscosity of fluid and ΔE = applied electric potential.

The volume (V) of the solution when a current density I is applied per unit time and per unit area is given by

$$V = \frac{\epsilon \zeta I}{4 \pi \eta \bar{\kappa}} \quad [5]$$

where $\bar{\kappa}$ is the specific conductance of the particle solution filling the pores.

2.2 Concrete and Portland Cement

Concrete consists of coarse material (coarse or fine gravel, sand and crushed stone) embedded in matrix material (cement or binder) and forms a composite material (Mindess et al., 2003, Mehta and Monteiro, 2006; Odler, 2000). Cement can be defined as a powdered inorganic material that, when mixed with appropriate amounts of water, yields a suspension that converts to a solid body at an ambient temperature. Portland cement is made from hydraulic cements consisting of calcium silicates. The name Portland cement was derived from the Portland stone which was found at the Isle of Portland in Dorset, England (Mindess et al., 2003). The typical composition of Type I Portland cement is shown in Table 2.1. Portland cements undergo chemical reactions called hydration, which leads to hardening. There are five types of Portland cement, namely ASTM Type I, Type II, Type III, Type IV and Type V.

Table 2.1 Composition of ordinary Portland cement (Adapted from Mindess et al., 2005, p. 21)

Chemical Name	Chemical Formula	Shorthand Notation
Tricalcium silicate	$3\text{CaO} \cdot \text{SiO}_2$	C_3S
Dicalcium silicate	$2\text{CaO} \cdot \text{SiO}_2$	C_2S
Tricalcium aluminate	$3\text{CaO} \cdot \text{Al}_2\text{O}_3$	C_3A
Tetracalcium aluminoferrite	$4\text{CaO} \cdot \text{Al}_2\text{O}_3 \cdot \text{Fe}_2\text{O}_3$	C_4AF
Calcium sulfate dehydrate (gypsum)	$\text{CaSO}_4 \cdot 2\text{H}_2\text{O}$	$\text{C}\bar{\text{S}}\text{H}_2$

Type I Portland cement is commonly used in civil infrastructure because of early strength gain and low cost (Mindess et al., 2003). This type of cement is also used when concreting at low temperatures (Mehta and Monteiro, 2006). Type II Portland cements are also used commonly but also provides moderate sulfate resistance. Type III Portland cements gain double the early strength as compared to Type I and are used when early strength gain is required. When low heat of hydration is required, Type IV cements are usually used. This type of cement can prevent thermal cracking.

2.2.1 Concrete Strength

Concrete can be divided into three types, namely low-strength concrete (< 20 MPa or 3000 psi), moderate strength concrete (20- 40 MPa or 3000 to 6000 psi) and high-strength concrete (> 40 MPa or > 6000 psi). Factors influencing the strength of the concrete are shown in Figure 2.4.

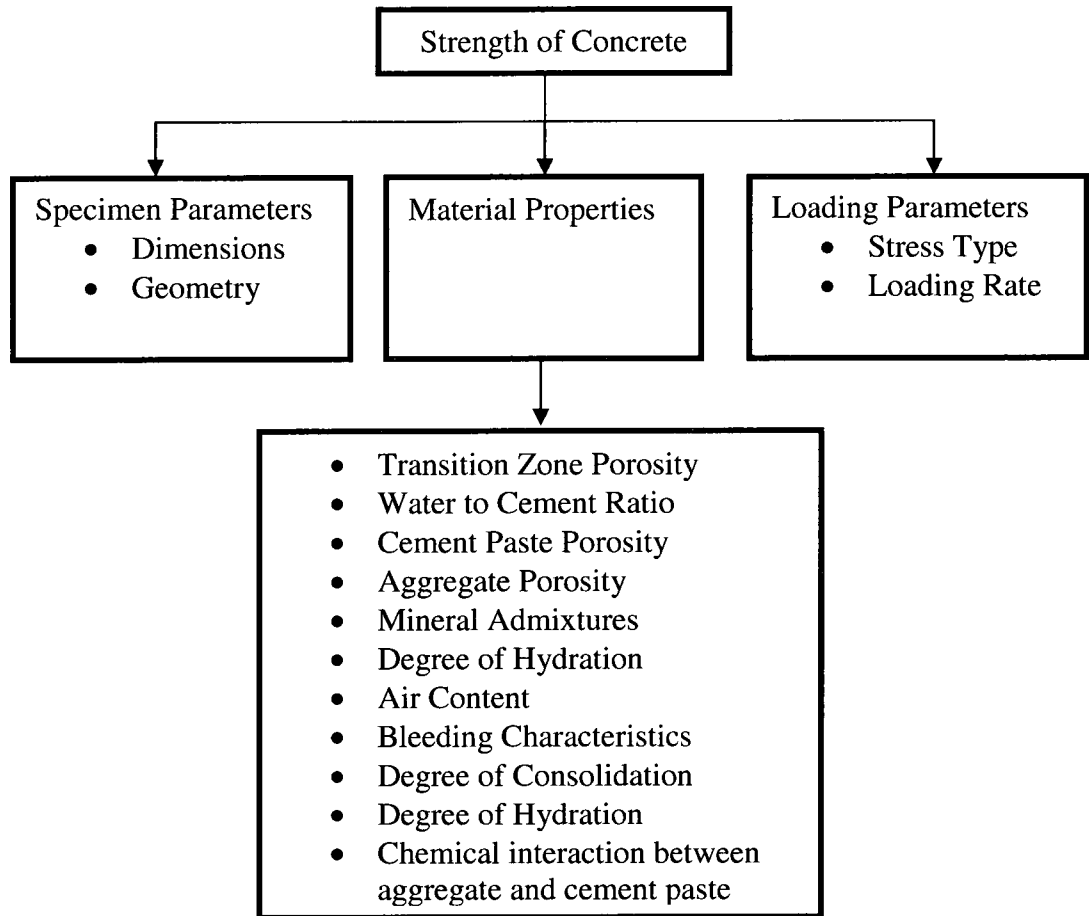


Fig 2.4 Flow chart showing the factors influencing the concrete strength (Adapted from Mehta and Monteiro, 2006, p.67)

In the laboratory, the compressive strength of concrete is measured by the uniaxial compression test as per ASTM C 469. Specimen dimensions in terms of the height/diameter ratio of cylindrical specimens are considered a standard for the compression test (Mindess et al., 2003). As the ratio of the specimen height to diameter increases, the strength will be lowered. Other factors affecting the compressive strength of concrete are water to cement ratio, porosity, batch composition, admixtures, degree of compaction and conditions of curing. The relationship between the strength of the material (concrete) and porosity is given by

$$S = S_0 e^{-kp} \quad [6]$$

where S = strength of the material, S_0 = intrinsic strength at zero porosity, k = constant, p = porosity.

2.2.2 Pore Structure Characteristics

Pore structure analysis is essential to understand pore volume, surface area of the pore, shape and connectivity of the pore (Aligizaki, 2006; Mindess et al., 2003). Parameters such as porosity, hydraulic radius, specific surface area, threshold diameter and pore size distribution are commonly used to characterize pores. Porosity can be defined as the ratio of total pore volume in the bulk material (V_p) to the bulk volume of the material (V_b) in mm^3 .

$$\epsilon = \frac{V_p}{V_b} \times 100 \quad [7]$$

The pore sizes can be defined by measuring the geometric parameter such as the hydraulic radius (Aligizaki, 2006). The hydraulic radius (r_h) of a pore can be predicted by the ratio of a cross sectional area of the pore (V_p) to the perimeter of the pore cross section (A_s) in mm. The hydraulic radius not only provides information on regular pores but also the irregular pores.

$$r_h = \frac{V_p}{A_s} \quad [8]$$

Pores can be classified as gel, pores, capillary, hallow-shell pores and air voids (refer to Figure 2.5). Gel pores primarily originate inside the hydration products and are dominant between the liquid phase and anhydrous cement grains (Aligizaki, 2006; Mindess et al., 2003). Gel pores range from 0.5 to 3 nm and posses strong affinity for water molecules. Studies have shown that

microstructural models have been able to predict strength using gel and capillary pores. Capillary pores exist in the unfilled zones which are not filled by the solid components of the hydrated cement paste. The water to cement ratio and the degree of hydration affect the capillary porosity of the cement paste. The volume of the C-S-H hydration product gel is not sufficient to fill the space available between reacting grains of cement when the water to cement ratio is above 0.34, thus forming the capillary pore. Capillary pores are irregular in shape and lie in the range of 2 nm to 10 μm .

Unstable cement hydration sometimes leads to void space (hollow shells), which originates within the inner boundary of the hydrating cement grains (Aligizaki, 2006). A size range of (1-15 μm) is exhibited by these void spaces. Entrapped or entrained air voids originate during the batching of concrete. These voids are mostly spherical in shape and range from 50 μm to 3 mm. Air voids can affect strength but generally not permeability.

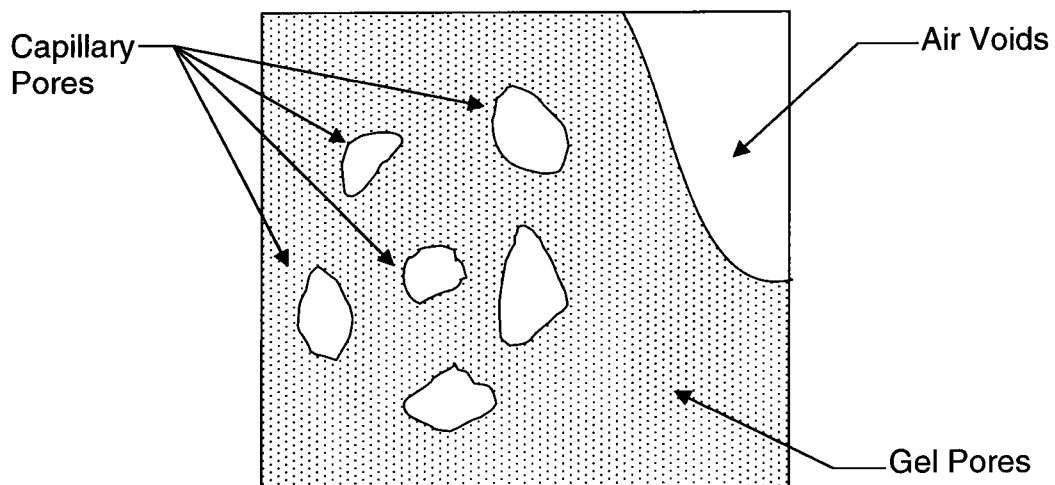


Fig 2.5 Pore structure in concrete

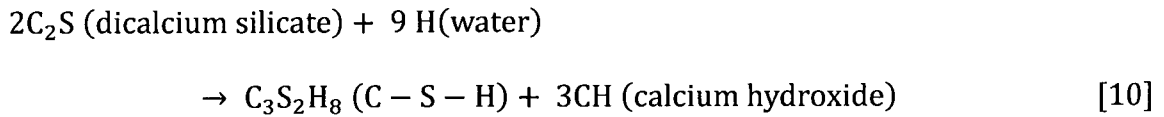
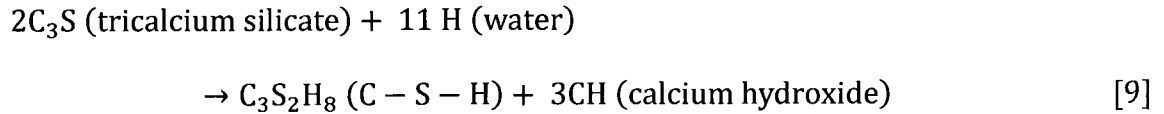
The characterization of pore sizes plays an important role in accessing the type and extent of damage due to various degradation processes (Aligizaki, 2006). Pore size can be classified as micropores, mesopores and macropores, as shown in Table 2.2.

Table 2.2 Classification of pore sizes (Adapted from Aligizaki, 2006, p.13 and from Mindess et al., 2005, pp.75-76)

Designation	Diameter Range	Pore Type	Characteristics	Properties Affected
Micropore	Up to 2 nm	Gel pores	<ul style="list-style-type: none"> • Strongly adsorbed water • Structural water involved in bonding. 	Shrinkage and Creep
Mesopore	2 nm to 50 nm	Capillary pores	<ul style="list-style-type: none"> • Large surface tension forces generated 	Permeability, Strength and Shrinkage
Macropore	Greater than 50 nm	Capillary pores	<ul style="list-style-type: none"> • Behaves as a bulk water 	Permeability, diffusivity

2.2.3 Calcium Silicate Hydrate (C-S-H)

The hydration products of Portland cement primarily can be characterized as calcium hydroxide $[Ca(OH)_2]$ and C-S-H (calcium silicate hydrate) gel and comprises 50-60% of the volume of solids in a completely hydrated cement paste (Mindess et al., 2003). The hydration reaction of tricalcium silicate (C_3S) and diacalcium silicate (C_2S) with water leads to the formation of C-S-H, as shown in Equations 9 and 10.



where H = H₂O (Water)

The typical composition of C-S-H gel in concrete structures is 3CaO·2SiO₂· 2H₂O. The calcium to silicate ratio varies from 1.5 to 2.0 (Taylor, 1997). This phase is strongly related to the strength of concrete. C-S-H can be detected and characterized by X-Ray diffraction (XRD), Fourier Transform Infra-red spectroscopy (FTIR), Raman Spectroscopy, Scanning electron microscopy (SEM) and Energy dispersive spectroscopy (EDS). Studies have shown that the microstructure of C-S-H involves a crystalline fiber like-structure and sometimes a reticular network (Odler, 2000). Diamond classified C-S-H gel into four morphological types, namely Type I, Type II, Type III and Type IV (Diamond, 1976). Type I is predominantly prominent at an early stage of hydration and possess fibers up to 2 μm long. Type II is usually observed under a SEM as foils of honeycomb flakes. Older pastes or mature concrete paste are obtained as inner products of hydration. Homogenous fine grain morphology was observed as C-S-H within the pore diameter ranging less than 10 nm (Richardson, 1999). Techniques such as transmission electron microscopy (TEM), atomic force microscopy (AFM), nuclear magnetic resonance (MNR) spectroscopy, small angle X-ray scattering (SAXS) and small angle neutron scattering (SANS) are used to characterize the nano-nature of C-S-H (Winslow and Diamond, 1974;

Thomas et al., 1999; Yang et al., 1990). Recent research has shown that a triboindenter is used to analyze the nano-mechanical properties of C-S-H (Mondal et al., 2008). These techniques are used to measure the mass density and composition of solid nanoscaled C-S-H in cement. Calcium hydroxide at nanoscale has been quantified using Neutron and X-ray scattering. It was found that calcium hydroxide can co-exist with C-S-H (Allen et al., 2007). C-S-H gel was found to be much stronger when not exposed to drying.

2.2.4 Interfacial Transition Zone (ITZ)

The porosity of the concrete is influenced by the nature of the cement matrix and also the interfacial transition zone (ITZ) between the matrix and coarse or fine aggregate (Mehta and Monteiro, 2006). The ITZ is a thin zone of the cement paste surrounding the aggregate particles and is typically in the range of 20 – 40 μm (Scrivener et al., 2004; Basheer et al., 2000). This region is most easily detected by backscatter electron imaging of polished samples.

The ITZ can be found surrounding cement grains and is a bulk characteristic of the cement paste (Brandt, 2009; Scrivener et al., 2004). ITZ originates from the wall effect of the cement grains against an aggregate surface, as shown in Figure 2.6. A flat solid aggregate wall in contact with cement grains would disrupt the normal packing pattern of the grains leading to a new transition zone. This disruption of the parent zone leads to higher porosity and smaller particles in the transition zone.

Bond strength between the aggregates particles and the paste is affected by the ITZ (Mehta and Monteiro, 2006).

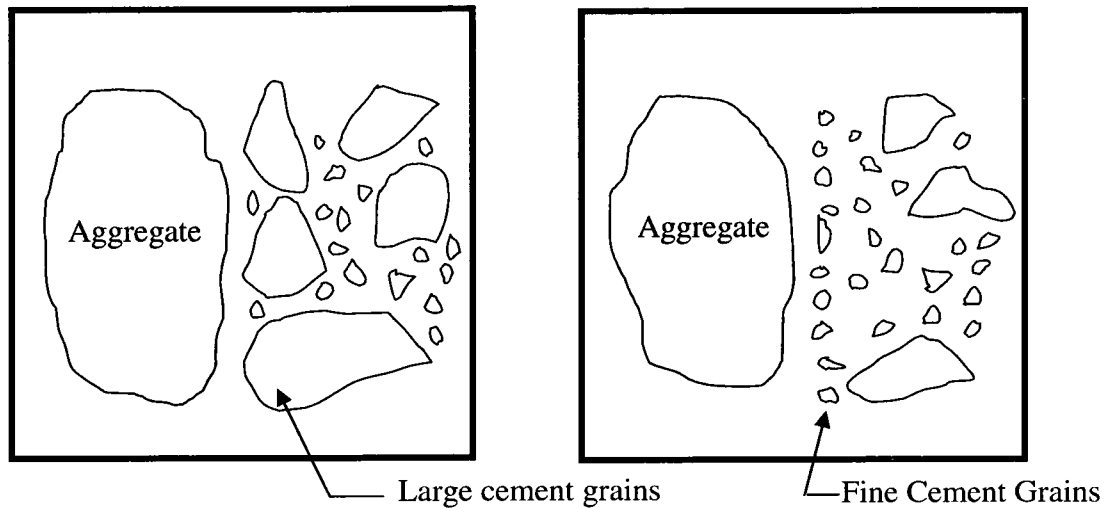


Fig 2.6 Illustration of wall effect phenomena in ITZ (Adapted from Scrivener et al., 2004, p.412)

This strength in turn depends on the smoothness or roughness characteristics of the aggregate, the degree of bleeding and the chemical bonding between the paste and the aggregate. The ITZ has less resistance to cracking, and thus suffers debonding between the aggregate and the cement paste. This leads to a reduction in strength. The water to cement ratio is higher in the ITZ zone than in the bulk paste (Nemati and Gardoni, 2005). The wall effect leads to a layer of 15 μm of ITZ around each aggregate, which is susceptible to absorption of water. This in turn reduces the water content in the bulk paste. Partial substitution of admixtures (silica fume) by weight of cement can lead to effective methods of improving the ITZ (Mindess et al., 2006; Mitsui et al., 1994). The silica fume eliminates pores in the ITZ, making the structure homogenous. The mineral admixtures help reduce porosity by converting the calcium hydroxide to C-S-H.

2.3 Transport Mechanism in Concrete

The mechanism of transport in concrete depends on adsorption, vapor diffusion, ionic diffusion, liquid assisted vapor transfer and saturated liquid flow, as shown in Figure 2.7 (Hearn and Figg, 2001; Ramachandran and Beaudoin, 2002). Adsorption is a driving force which initiates the suction of fluid into the capillary pores. As relative humidity approaches zero, the hydrophilic nature of the cement will lead to adsorption of water. As relative humidity increases, the local surface adsorption energy decreases since the water molecules have become limited. The adsorption process is followed by intrusion of water vapor. The molecular diffusion of water vapor is governed by Fick's first law (Hearn and Figg, 2001; Cardenas, 2002).

$$Q = -K_v A \frac{dp}{dx} \quad [11]$$

where Q = transport rate of vapor (m^3/s), K_v = Diffusion coefficient of vapor (m/s), A = cross sectional area (m^2), and $\frac{dp}{dx}$ = pressure gradient of vapor (m/m).

The non-uniform pore widths in concrete lead to formation of menisci at the neck of the pores (Hearn and Figg, 2001). Menisci are also dependent on the relative humidity (RH). An increase in RH causes the increase in pore size widths, which also initiates the formation of menisci. The non-uniformity of the pores leads to the condensation at the pressure side (upstream meniscus) and evaporation at the low pressure side (downstream meniscus). This situation initiates a short circuit and causes moisture transfer.

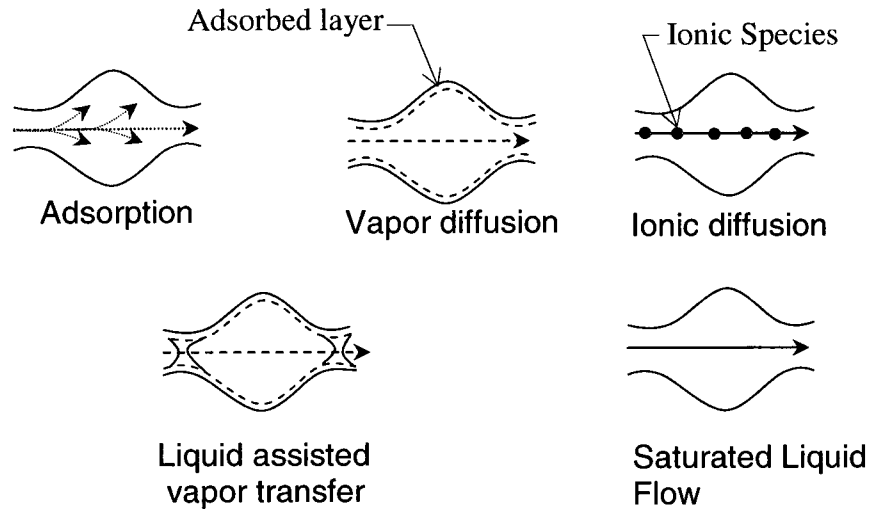


Fig 2.7 Idealized model of transfer process within concrete (Adapted from Hearn and Figg, 2001, p.329)

At the saturation stage, the fluid transport is dominated by the viscosity of the fluid and pressure gradient (Hearn and Figg, 2001; Ramachandran and Beaudoin, 2002). Darcy's law provides a relationship between these two parameters. This law also introduces a term known as permeability of concrete. The ease with which the fluid passes into the concrete structure under the influence of pressure differential is known as permeability of concrete.

$$D = \frac{\mu}{\rho g} K \quad [12]$$

where D = permeability (m^2), μ = viscosity (Pa.s), g = gravitational acceleration ($9.81 m^2/s$), K = coefficient of permeability (m^2/s).

2.4 Durability of Concrete

Concrete as a material is generally considered to be strong and durable. Concrete is strong in compression and weak in tension. The structure is given tensile strength by steel reinforcement. The effectiveness of the reinforced

concrete structure depends on the mechanical bond between the reinforcement and the concrete. Deterioration in concrete can arise due to the ingredients used in the concrete mix and also due to the external agents like chlorides and sulfates (Mays, 1990). The classification of various causes of deterioration in concrete is illustrated in Figure 2.8. The causes are grouped into two categories; one cause is surface wear and the other is cracking (Mehta and Gerwick, 1982). Mass loss by surface wear includes abrasion, erosion and cavitation. Abrasion can be referred to as wear of pavements due to excessive vehicular loads. Erosion in concrete takes place due to the abrasion action of fluid flow. This occurs commonly in spillways, canal linings, and water (or sewage) pipes. Cavitation takes place when surface irregularities or a sudden change in direction takes place in rapidly flowing water. In one notable example, Glen Canyon Dam located in Arizona) suffered from cavitation damage due to surface irregularities combined with a high flow rate.

Physical cracking can be divided into three categories: volume change, structural loading and exposure to extreme temperatures. Volume changes take place due to the environmental conditions, such as marine water exposure and loss of moisture by evaporation (Mindess et al., 2006). Crystallization of salts leads to corrosion when sufficient quantities of these are dissolved. The salts ingress into the concrete and crystallize in the pores and are concentrated due to cycles of wetting and evaporation.

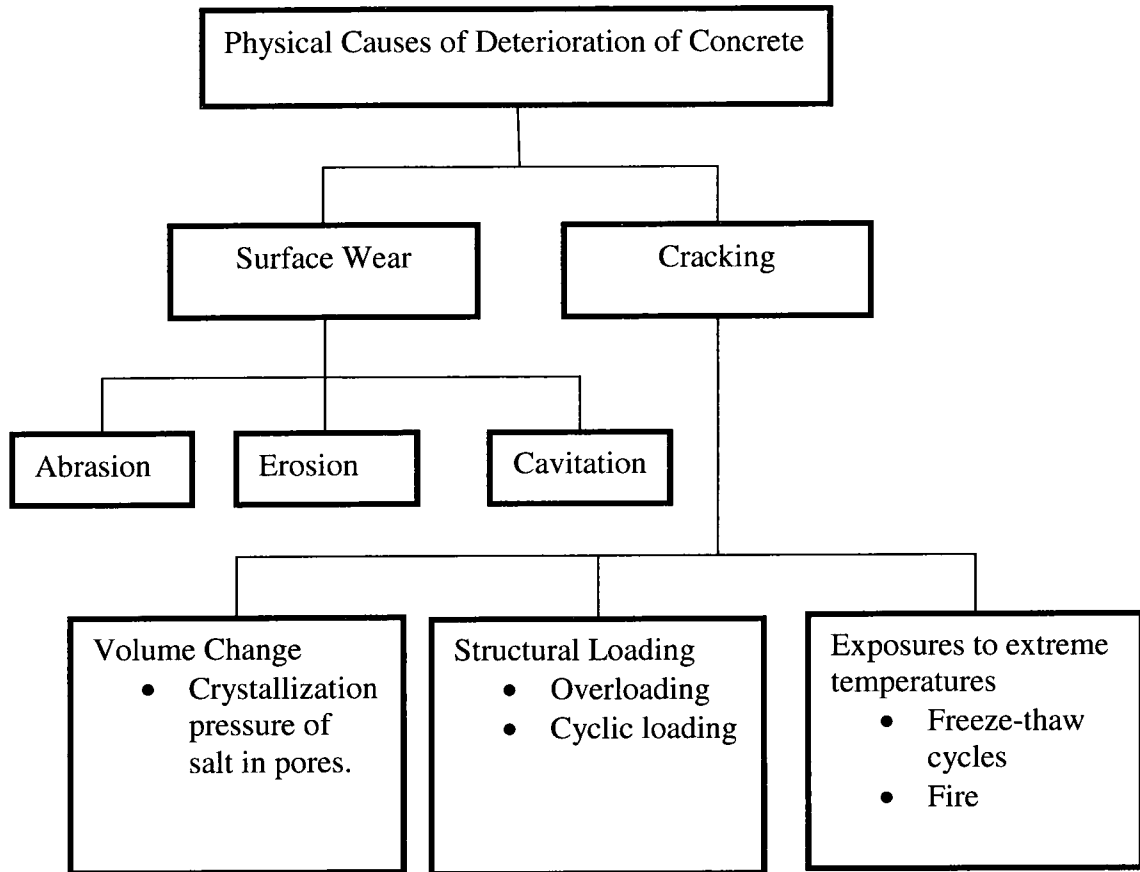


Fig 2.8 Flow chart illustrating the causes for deterioration of concrete (Adapted from Mehta and Monteiro, 2006, p.131)

This cyclic evaporation process will cause the salts to build up and eventually lead to cracking, once the threshold limit is exceeded (Neville, 1996). The solution to prevent this problem is the usage of a low water to cement ratio, and thus a low permeability concrete which inhibits moisture evaporation. The sealing of concrete can also inhibit both the moisture ingress and evaporation.

When concrete is subjected to constant load and low relative humidity, it leads to drying shrinkage and drying creep (Mehta and Monteiro, 2006). If the total strain of the concrete is higher than the elastic strain, it leads to free shrinkage strain or drying shrinkage. Drying shrinkage is caused by the

withdrawal of water from concrete in an unsaturated environment (Neville, 1996). The volume change of dried concrete is not equal to the volume of water withdrawn. In the initial stage, loss of water takes place, causing negligible shrinkage called free shrinkage. Parameters affecting free shrinkage in concrete are water to cement ratio and the aggregate content (Wiegrink et al., 1996; Yang et al., 2000). A reduction in water to cement ratio helps in mitigating free shrinkage in concrete. The volume shrinkage is the evaluation of strain on load-free reinforced concrete. Basic creep can be defined as the application of constant stress on a concrete specimen when subjected to 100 % relative humidity. The concrete specimen subjected to constant load without drying leads to dry creep. Some of the factors affecting drying shrinkage and creep are concrete mix proportions, curing of concrete, w/c ratio, aggregate shape and concrete admixtures (calcium chloride, granulated blast furnace slag and pozzolans).

Porous materials, such as concrete, are susceptible to severe damage due to frost attack (Mindess et al., 2006). In cold climates, as the temperature drops below 0°C, the water inside the cement paste does not freeze immediately. Large numbers of pores are present in the cement paste and water inside the pores does not freeze immediately. The freezing temperature depends on the pore-diameter. An increase in the concentration of solute in the liquid adjacent to the freezing location is due to the nucleation of pore solution. Osmotic pressure will draw water from the higher concentration of the pore solution and cause the cracks in the surrounding cement paste.

2.5 Corrosion Mechanism of Reinforced Concrete

The alkaline nature of concrete leads to elevated pH, thus causing a passive layer on the reinforcement, protecting it from corrosion (Broomfield, 1997; Bentur, 1997). Carbonation and chloride attack are the two processes which can change the passive chemical environment in concrete and lead to corrosion as shown in Figure 2.9. The carbon dioxide is absorbed in the pore fluid from the atmosphere. This carbon dioxide reacts with water forming carbonic acid as shown in Equation 13. The carbonic acid reacts with the calcium hydroxide present in the cement paste forming calcium carbonate (refer to Equation 14). The abundant calcium hydroxide reacts and precipitates carbonic acid, decreasing the pH level below the threshold (pH = 11) and causing corrosion.

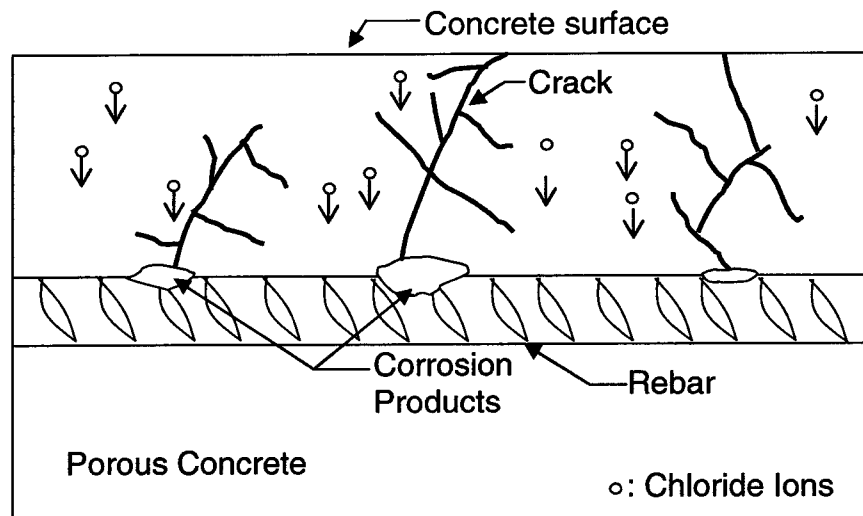
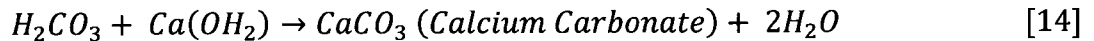
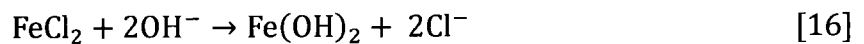


Fig 2.9 The breakdown of the passive layer and recycling of chlorides

Due to the porous nature of concrete, it is susceptible to the migration of deleterious species such as chlorides (Broomfield, 1997). Various external sources, including sea salt spray, direct sea water wetting, deicing salts and contaminated aggregates, can be sources of chlorides that can enter reinforced concrete. Chlorides diffuse into the capillary pores of the concrete and come into contact with the rebar. The protective oxide layer adsorbs chloride ions leading to the formation of ferrous chloride ($FeCl_2$) as shown in Equation 15 (Ahmad, 2006). The ferrous chloride reacts with the moisture to form ferrous hydroxide [$Fe(OH)_2$] rust (white green precipitate).



These oxides absorb oxygen as they undergo volume changes and induce tension in the surrounding concrete causing cracking. The free chloride ions are not consumed in the corrosion process and are continuously recycled (Jones, 1995). For this reason, many concrete repairs continue to suffer from corrosion because the repair failed to reduce the chloride content of the structure. With the chlorides eliminated, or at least reduced in concentration as compared to the pH, the life of the structure is significantly extended (Johansen, 1995). ASTM allowed chloride threshold level percentages as per mass of cement are 0.10 for acid soluble chlorides and 0.08 for water soluble chlorides in reinforced concrete (ASTM C1152, 2002).

2.6 Diffusion of Chloride in Concrete

Fick's second law of diffusion can be used to predict the penetration of chloride ions into porous concrete (Poulsen and Mejlbro, 2006). It is given by,

$$\frac{\partial C}{\partial t} = -D_c \left(\frac{\partial^2 C}{\partial x^2} \right) \quad [17]$$

where C = chloride concentration, x = depth, t = time, D_c = chloride diffusion coefficient.

The diffusion constant D_c is a function of temperature since the ambient temperatures also influences diffusion (Poulsen and Mejlbro, 2006). In the northern states, the capillary pores are frozen for several months, which will affect the diffusion efficiency. Diffusion constants are also dependent on the pore size distribution and porosity. Highly porous structures exhibit higher diffusion rates because diffusion through air or water is faster than through the solid matrix. The solution using the LIGHTCON model applied to Fick's law for a constant chloride boundary condition is as follows (Poulsen and Mejlbro, 2006):

Applying the following boundary conditions:

$$D = D_0 \text{ for } x \geq 0 \text{ and } t \geq 0 \quad [18]$$

$$\frac{\partial C}{\partial t} = D_0 \frac{\partial^2 C}{\partial x^2} \text{ for } x > 0, t > 0 \quad [19]$$

$$C(x, t) = C_i \text{ for } x \geq 0 \text{ and } t = 0 \quad [20]$$

$$C(x, t) = C_o \text{ for } x \geq 0 \text{ and } t \geq 0 \quad [21]$$

One possible solution using these boundary conditions is

$$C(x, t) = C_i + (C_o - C_i) \operatorname{erfc} \left(\frac{0.5x}{\sqrt{D_0 t}} \right) \quad [22]$$

where, D_0 is the achieved diffusion coefficient, C = Chloride concentration at time t and at depth x , C_i = initial chloride concentration, C_o = Constant chloride content.

Chloride content (C_o) can be determined using ASTM C 1152, and the diffusion constant can be predicted using Equation 20. This equation can also be used to develop a profile of chloride contents (C_o) at various depths (x) starting from the concrete cover surface to the rebar/concrete interface (refer to Figure 2.10). In most cases, the chloride content is at a maximum at the cover surface and decreases towards the rebar (Hooton et al., 2002).

An alternative method for estimating chloride diffusion coefficients at each point on the chloride profile (refer to Figure 2.10) can be estimated using Equation 23 (Prezzi et al., 1996). As the concrete porosity decreases (η) for distances less than x , the chloride concentration increases from 'x' to the exposed concrete surface.

$$C = \frac{C_{dry\ concrete} \times \gamma_{dry\ concrete}}{\rho \times n} \quad [23]$$

where C = chloride concentration per weight of water (%), $C_{dry\ concrete}$ = chloride content per weight of dry concrete (%), $\gamma_{dry\ concrete}$ = concrete unit weight (kg/m^3), and n = concrete porosity.

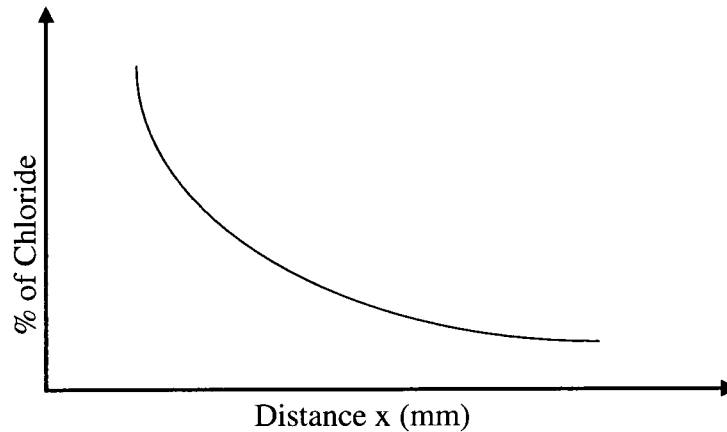


Fig 2.10 Variation of chloride concentration values with distance from the exposed surface (Adapted from Poulsen and Mejlbro, 2006, p.69)

2.7 Service Life of Structures

The service life of concrete structures consists of an initiation and a propagation period (Maage et al., 1996). The time of exposure between when the chlorides have penetrated the concrete cover and the chloride content within the vicinity of the rebar is high enough to start corrosion is known as the initiation period. The propagation period is the time from which the rebar starts to corrode until a critical chloride limit has been reached. The parameters governing the service life are corrosion threshold limits, the chloride diffusion constants for initiation of corrosion, properties of concrete, and the distance of the reinforcing bar from the concrete cover (Weyers, 1998). The chloride deterioration process exhibits an initial diffusion period of 15 years for relatively low permeability concrete, when subjected to sea salt exposure before corrosion initiation starts, as shown in Figure 2.11. The initiation period is followed by reinforced concrete corrosion for an average period of 5 years, leading to severe cracking and spalling of concrete and finally leading to failure of the structure.

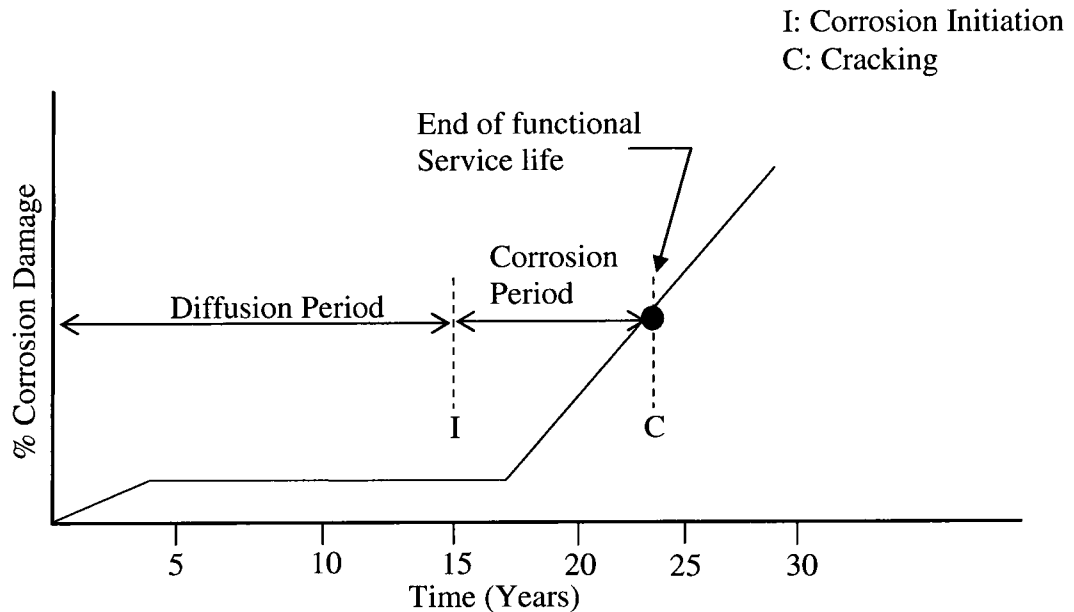


Fig 2.11 Chloride corrosion deterioration process for a low permeable reinforced concrete structures when exposed to sea saltwater (Adapted from Weyers, 1998, p.446)

2.8 Corrosion Cracking Process

Corrosion induced cracking is a significant phenomenon in studying the service life of the structures. Various researchers have developed equations for predicting the weight of metal loss due to cracking and the total amount of corrosion products formed due to cracking (Li et al., 2008; Liu 1996). Farady's law shows that metal weight loss is directly proportional to the corrosion current.

$$W_{\text{loss}} = kIt \quad [24]$$

where W_{loss} = metal weight loss, k = electrochemical equivalent constant (g/amp-sec), I = current (Amps) and t = time (sec).

As noted earlier, chloride ions have the potency to destroy the passive film and thus permit the metallic iron to oxidize to form ferrous ions (Weyers, 1998). These ions react to produce hydrated ferric oxide. The reaction products

expand in free space (the surface of the reinforcement). Corrosion products start accumulating in the free space, and internal stresses start developing. The concrete matrix surrounding the free space reacts by developing tensile stress. Once this stress exceeds the tensile strength of the concrete it said to equal to the critical amount of corrosion products (W_{crit}). The W_{crit} is responsible for cracking the concrete, as shown in Figure 2.12.

Corrosion can be initiated physically due to cyclic loading (Liu and Weyers, 1998). This loading initiates stress in the concrete, leading to initial cracking as shown in Figure 2.12. The cracked reinforced concrete structure suffers from severe cracking and becomes susceptible to deleterious species like chlorides and sulfates. Diffusion of these species into the initially cracked concrete leads to the corrosion initiation. This stage is followed by the propagation period and failure of the structure.

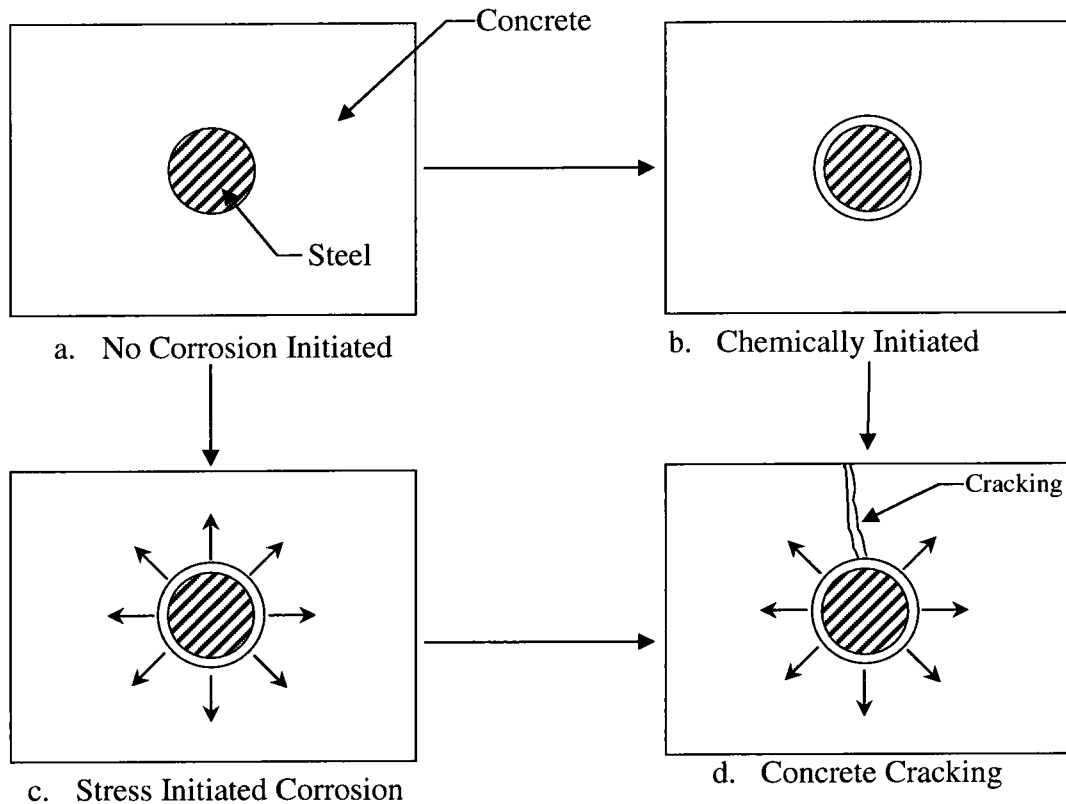
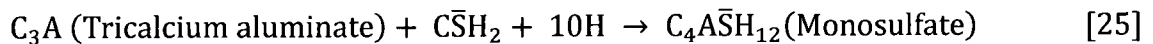


Fig 2.12 Two paths leading to corrosion-cracking process (Adapted from Liu and Weyers, 1998, p. 679)

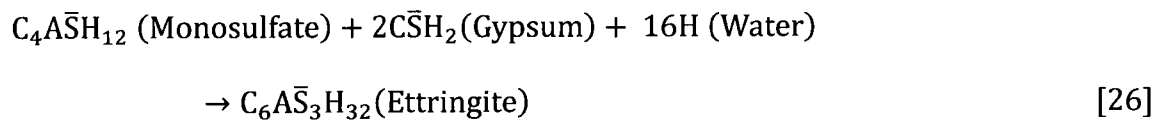
2.9 Sulfate Attack in Concrete

Concrete is susceptible to ingress of sulfate ions, which initiates the formation of ettringite and causes deterioration of concrete (Skalny et al., 2001). Sulfate attack is caused predominantly by the presence of sodium sulfate, calcium sulfate or magnesium sulfate in soils or waters that come into contact with concrete. After sulfate ions enter the concrete, calcium sulfate (gypsum) is produced by the reaction of these ions with the calcium hydroxide that is resident within concrete. The calcium sulfate then reacts with tricalcium aluminate to form ettringite (Shazali et al., 2006; Mehta, 2000; Neville, 2006). Ettringite forms long hexagonal needles that push the cement apart as they grow, causing tensile

stress, expansion, and cracks (Rasheeduzzafar et al., 1994). The damage caused by a sulfate attack may take the form of macro and micro cracking, spalling, delamination, increased permeability, volume expansion and leaching. In general, ettringite formation is not problematic as long as it occurs only during the initial hydration of the cement paste. During initial hydration, the gypsum in the Portland cement reacts with C_3A , forming monosulfate as follows

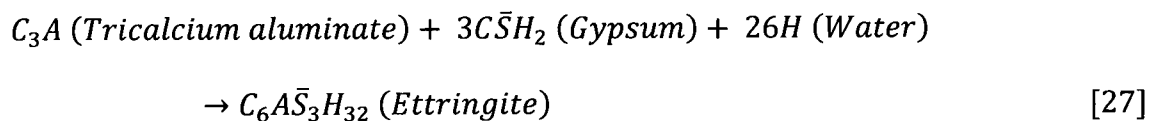


If excess gypsum is available after this reaction, then it can react with monosulfate to convert it to ettringite as follows (refer to Table 2.3 for chemical notations).



It has been reported that not all types of ettringite are expansive. Structures known to support significant expansion are clusters of spherulite ettringite needles, each of dimensions $(10 \times 0.5 \mu m)$ (Ghafoori and Mathis, 1997).

During hydration of Portland cement, ettringite formation takes place due to the reaction between tricalcium aluminate and calcium sulfate as follows



The best scenario is when all sources of ettringite, such as C_3A and monosulfate, are converted prior to the set. If residuals of C_3A or monosulfate persist after the concrete has set, the structure could then be considered susceptible to attack if sulfates become available (Skalny et al., 2001).

Table 2.3. Chemical notations and formulae of monosulfate, gypsum and ettringite (Skalny et al., 2001, p.20)

Chemical Name	Chemical Formula	Shorthand Notation
Monosulfate	$Ca_4Al_2(OH)_{12} \cdot SO_4 \cdot 6H_2O$	$C_4A\bar{S}H_{12}$
Calcium sulfate dihydrate (Gypsum)	$CaSO_4 \cdot 2H_2O$	$C\bar{S}H_2$
High-sulfate calcium sulfoaluminate hydrate (Ettringite)	$[Ca_3Al(OH)_6 \cdot 12H_2O]_2 \cdot (SO_4)_3 \cdot 2H_2O$	$C_6A\bar{S}_3H_{32}$

where $C = CaO$, $\bar{S} = SO_3$, $A = Al_2O_3$, $H = H_2O$

Deterioration due to sulfate attack depends on the sulfate ion concentration. For example, an attack becomes significant when the sodium sulfate content in the pores exceeds 1% (Li et al., 1996; Mehta, 1983). Extremely high sodium content in the pore solution can lead to U-phase formation. U-phase ($4CaO \cdot 0.9Al_2O_3 \cdot 1.1SO_3 \cdot 0.5Na_2O \cdot 16H_2O$) usually occurs when sodium is added to the fresh concrete mix. U-phase is observed commonly in cement-stabilized wastes that contain high amounts of sodium sulfate. This leads to damage of concrete, as it undergoes transformation into ettringite.

Various researchers have examined the formation of gypsum and its effects (Skalny et al., 2001; Li et al., 1996; Monterio and Kurtis, 2003; Kurtis et al., 2000; Corr et al., 2001; Bentur and Cohen, 1987). An increase in calcium hydroxide content in concrete may increase the amount of gypsum formed when the structure is exposed to sulfates. Bing and Cohen found that formation of gypsum may cause significant expansion even when formation of ettringite is excluded (Bing and Cohen, 2000). Under appropriate conditions with a high

degree of gypsum super saturation in the pore fluid, the crystallization pressure may be sufficient to generate expansion of the hardened cement paste.

Various indicators are used for analyzing the severity of sulfate attack. These include changes in length, mass, compressive strength, flexural strength, modulus of elasticity and cracking (ASTM C 1012- 95 a; Boyd and Mindess, 2004; Naik et al., 2006). A reduction in compressive strength is one of the main parameters for evaluating the effects of sulfate attack on concrete. Compressive strength decreases as the presence of voids increases. The water to cement ratio is also a vital aspect to consider when predicting sulfate resistance. As water to cement (w/c) ratio and C_3A content increases the time to failure, as determined by expansion of cement paste, decreases. Reliability analyses have indicated that the w/c ratio is more influential than the C_3A content for predicting degradation due to sulfate attack.

Use of sulfate resistant cement (Type V) and admixtures of pozzolans with Type I or II are some of the preventive formulations against sulfate attack (Skalny et al., 2001; Mehta and Monteiro, 2006). The Type V cement limits the tricalcium aluminate content, which is a primary constituent/reactant for ettringite formation. Studies have indicated that at 0.75 w/c ratio, Type V, cement performs better than Type I. These types of findings have shown that Type V cements generally are not sensitive to w/c ratio when compared to Type I and Type II cements. Young and others observed that sulfate attack thus can be prevented by reducing the C_3A content and by using a low w/c ratio (Cohen and Bentur, 1988; Cohen and Mather, 1991). Another approach for mitigating sulfate

attack has been the use of pozzolanic admixtures. Selected fly ash and silica fume admixtures are used to increase the sulfate resistance in concrete (Tikalsky and Carrasquillo, 1993). The pozzolans react with calcium hydroxide so that it is no longer available for reaction with sulfate ions.

2.10 Repair and Rehabilitation Techniques

Structures are rehabilitated using a number of common strategies in the civil infrastructure industry. The procedures for rehabilitation are based on the cause and extent of the damage. The following flow chart indicates some of the rehabilitation methods against corrosion in reinforced concrete (refer to Figure 2.13). Sections 2.12.1 to 2.12.4 examine the principles of cathodic protection, electrochemical chloride extraction, corrosion inhibitors, coatings, sealers and coated reinforcement.

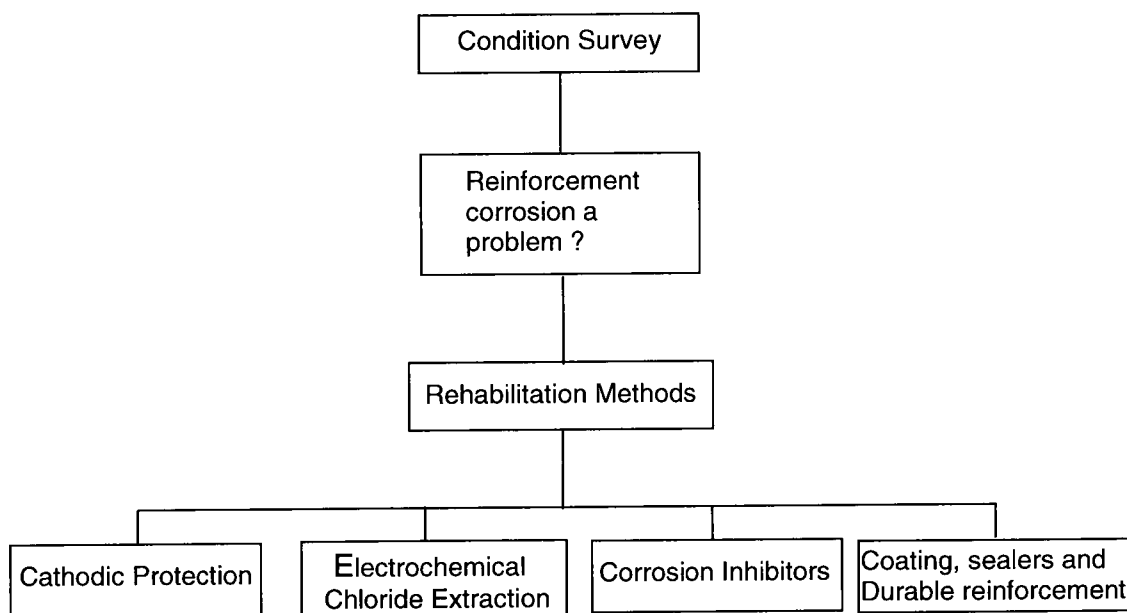


Fig 2.13 Flow chart showing the non-destructive methods for rehabilitation of corroded reinforced concrete

2.10.1 Cathodic Protection

Cathodic protection (CP) is a rehabilitation technique used to mitigate reinforcement corrosion in concrete (Bertolini et al., 2004). Cathodic and anodic sites exist on the corroded reinforcement. Corrosion takes place at the anodic sites, to counteract this CP is used. A power supply forces the corroded rebar to act as a cathode. CP which utilizes an external source of current to suppress the surface corrosion current. In the impressed current method, an external electrode is introduced into the concrete or the conductive media surrounding it and is connected to a current rectifier as shown in Figure 2.14. A low voltage direct current is applied from a corrosion resistant anode material (Example: titanium mesh), through the concrete and to the reinforcement. The direct current is applied by a rectifier which converts it from the ac to dc and keeps the

reinforcing rebar as the cathode. Another method of cathodic protection is galvanic cathodic protection (GCP). This principle is based on dissimilar metal corrosion. In this technique, a metal (e.g., zinc) is connected to the reinforcement and will corrode readily while protecting the reinforcing steel. Unlike impressed current CP, no external power source is needed with GCP and relatively little maintenance is required.

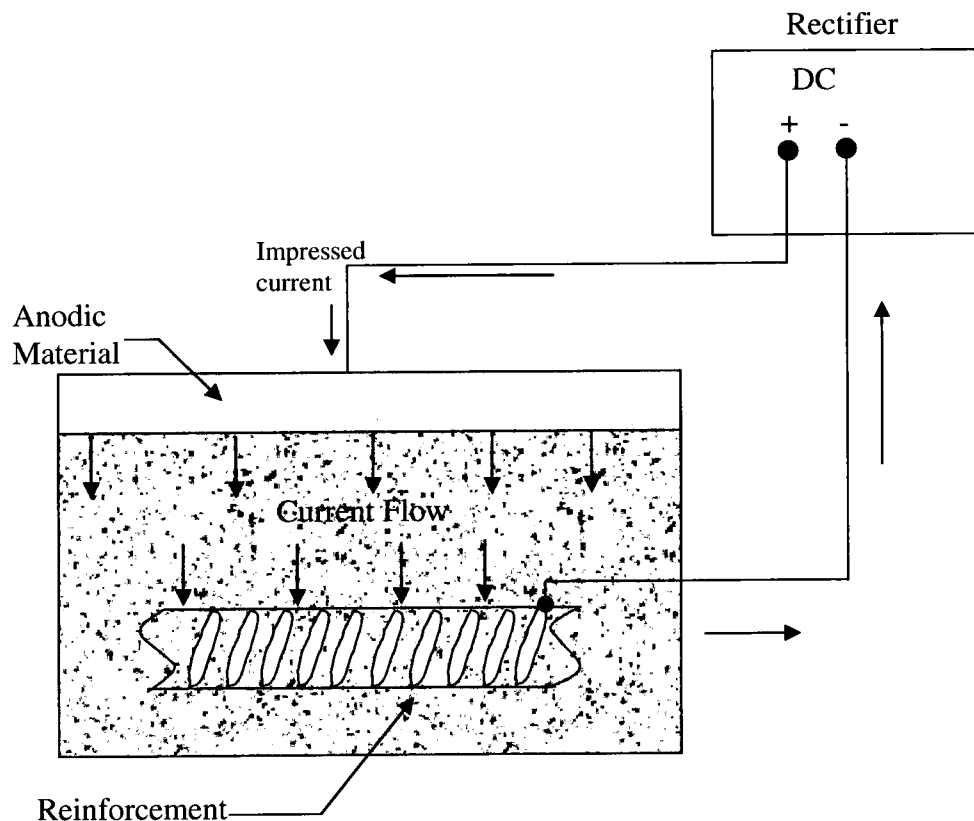


Fig 2.14 Layout of the impressed current cathodic protection (CP) system
(Adapted from Scannell et al., 1996, p.4-24)

Some advantages of CP are that it works at high chloride levels, provides uniform treatment and is not limited to specific locations. Chloride ions are driven away from the reinforcement while hydroxyl ions are drawn toward the

reinforcement and provide additional protection. The sacrificial anodes have a finite life and are consumed over time.

2.10.2 Electrochemical Chloride Extraction (ECE)

Electrochemical chloride extraction (ECE) or desalination involves the application of an electric current for removal of chlorides from contaminated reinforced concrete (Fajardo et al., 2006; Siegwart et al., 2005; Castellote et al., 2000). This process involves the application of direct current between the cathode (reinforcement) and a temporary anode (titanium mesh) on the outer surface of the concrete (refer to Figure 2.15). The anodic mesh is surrounded by a pond of tap water or saturated calcium hydroxide solution or other alkaline liquid. Under the influence of the electric field, positive ions such as oxides of sodium, potassium and calcium move toward the cathode, while negative ions (such as chlorides) to the anode. A maximum current density of 1 A/m^2 is continuously applied, usually for a period of 6-12 weeks.

After the application of ECE, the chlorides are removed from the reinforced concrete (Siegwart et al., 2005; Castellote et al., 2000). The ECE process leads to significant chloride removal, within 1 inch bar diameter of the reinforcement. Continuous generation of hydroxyl ions assists in restoring the passivity to the reinforcement. The rate of chloride extraction depends on the amount of chloride present and the permeability of the concrete. It also depends on the service environment, and the depth and amount of reinforcement. Chloride extraction generally removes up to 40% of the chlorides. Only the free

ions in the pore solution are extracted, while bound chloride ions are still left in the concrete (Orellan et al., 2004).

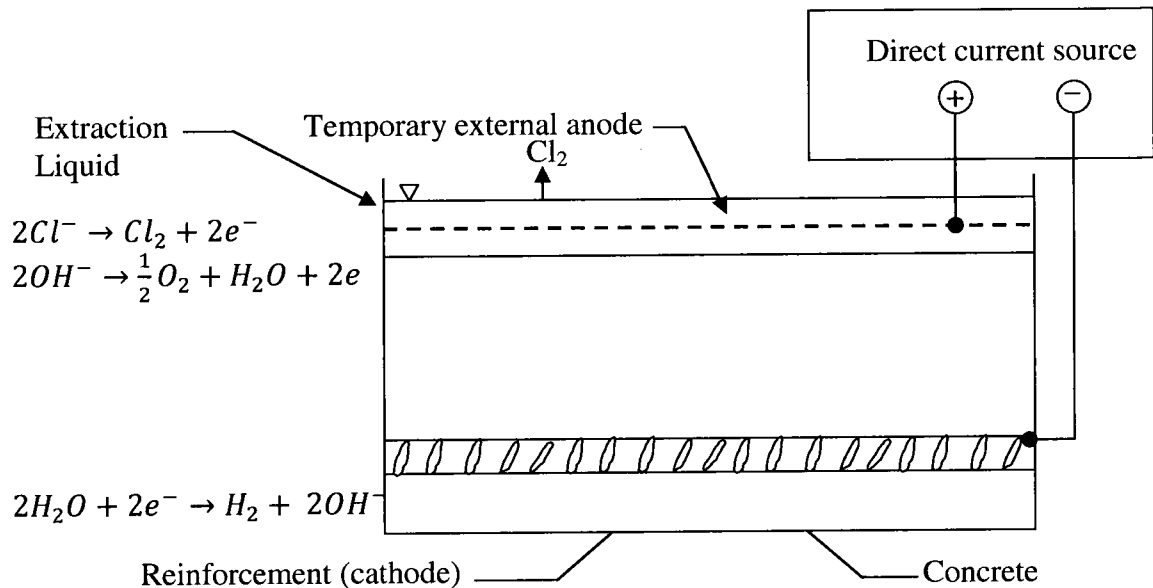


Fig 2.15 Schematic diagram of electrochemical chloride extraction (ECE)
(Adapted from Bertolini et al., 2004, p.364)

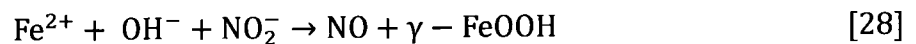
2.10.3 High Performance Concrete

Structures in the vicinity of high chloride environments are built with high performance concrete (HPC) (Neville, 1996; Mindess et al., 2003; Mehta and Monteiro, 2006). Common ingredients used in HPC are aggregate, Portland cement Type I, Portland cement Type III for early strength gain and 5-15% silica fume substitution of cement, in combination with superplasticizer to minimize the w/c ratio. The silica fume helps to grade down the pore volume by filling the space between the particles and the aggregate. The superplasticizer helps to disperse the cement grains to achieve a dense cement matrix and also enhances workability. The dense nature of the concrete prevents the ingress of

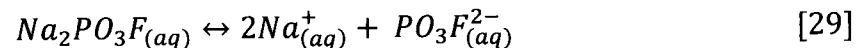
chlorides and also exhibits relatively high electrical resistivity. The low w/c ratio characteristic of HPC helps the concrete to gain high strength and low permeability. HPC's are used as a measure of protection against chloride attack and carbonation, the alkali silica reaction, and freeze-thaw damage.

2.10.4 Corrosion Inhibitors

A corrosion inhibitor is a chemical substance that suppresses reinforcement corrosion in concrete (Bentur et al., 1998; Broomfield, 1997). Inhibitors can be applied as a concrete admixture during mixing and can be applied to hardened concrete by drilling and injection. These chemicals influence the anodic or cathodic reactions of corrosion, leading to a significant reduction in degradation. Commonly used corrosion inhibitors are nitrite, monofluorophosphate (MSP) and alkanolamine (Ngala et al., 2003). Nitrite (an anodic inhibitor) is generally cast into the mix to delay the initiation of corrosion. Nitrites combine with ferrous ions Fe^{2+} ions, leading to a stable ferric oxide,



Monofluorophosphate (MFP) is a surface applied inhibitor which undergoes a dissociation in aqueous solution as shown in the Equation,



The $PO_3F_{(aq)}^{2-}$ ion acts as a inhibitor by providing a protective, passive film against reinforcement corrosion. Studies have shown that MFP slows the corrosion rates on carbonated reinforced concrete specimens (Nagla, 2003). During the carbonation process, MFP was also found to react with calcium

hydroxide and calcium carbonate, forming fluoroapatite minerals. These minerals have been found to resist freeze-thaw damage in concrete.

The factors that influence migrating inhibitor effectiveness are uniform application of inhibitor on the surface and the permeability of concrete, which allows inhibitor penetration (Bentur et al., 1998; Broomfield, 1997). Drawbacks include non-uniform distribution of inhibitor across the corroded reinforcement, the ability to suppress severe corrosion and ineffectiveness to protect the reinforcement from long term corrosion. A lack of knowledge of the inhibitor (whether it penetrates and reaches the steel reinforcement) is a major concern.

2.10.5 Coatings, Sealers and Durable Reinforcement

In recent times, the construction industry has used a wide range of reinforcement designs in the construction industry which, have complicated the issue of durability of concrete. In some cases the reinforcement has been coated with zinc to provide protection by acting as a sacrificial barrier coating (Broomfield, 1997; Belaid et al., 2001; Andrade et al., 2001). Hot dipping, spraying, electrodeposition and diffusion are some of the methods used for coating the zinc onto the rebar. The effectiveness of the galvanized coating depends on the layer of thickness of the coating and the pH in the pore solution. The threshold value of pH of 13.3 is considered to be in the protective zone of zinc coating.

Another technique commonly used in construction is epoxy coating of steel (Bentur, 1998; Treece and Jirsa, 1989). The stainless steel (reinforcement) is pre-cleaned, and an epoxy coating is applied by fusion bonding to the surface.

The intent of this technique is to provide a coating thickness of $200 \pm 50 \mu\text{m}$ to prevent the access of aggressive species. This coating also acts as an insulator, preventing electrical conductivity. Epoxy resins provide chemical resistance against acids, alkalis and solvents. The disadvantages of epoxy coating includes severe corrosion at coating defects, including low thickness area and bending of coated bars, leading to cracks where corrosion can be accelerated (Peterman et al., 1999; Hester et al., 1993). Some epoxy formulations can cause shrinkage strains at the rebar/concrete interface, leading to coating cracking in the concrete. The effectiveness of the coating decreases if pin hole defects (holidays) in the coating reach a frequency of six locations per meter, causing the degradation of coating on the rebar.

Long term protection of concrete is possible using concrete surface treatments (Bentur, 1998; Treece and Jirsa, 1989). Pore liners, pore blockers and film formers are commonly used surface treatments. Pore liners like silicone compounds which arrange themselves along the capillary pores of the concrete are shown in Figure 2.16. These liners are water repellent but are susceptible to the entry of water vapor. Liquid silicates or liquid silicofluorides are pore blocking agents that are used in concrete (Bentur, 1998). They react with calcium hydroxide to form calcium silicate hydrates (C-S-H). Organic resins like styrene butadiene and polymethyl methacrylate are applied to form in situ polymeric chains inside the pore. Organic polymers bind mechanically with the Portland cements by penetrating some distance into the capillary pores of the hardened cement paste (Odler, 2000). A polymer can be mixed with fresh cement paste,

forming a cementitious polymeric system. Prior to polymer impregnation, the pore should be emptied and water must be removed using air drying or heating above 100 °C of temperature. The impregnating liquid is placed in a chamber on the concrete element. Air pressure up to 50-100 kPa is applied to impregnate the polymer inside the pores of the concrete (Odler, 2000). Parameters such as viscosity of the treatment liquid and the network of the pore system, impact the effectiveness of polymer impregnation. The impregnation of a polymer into the pores of the concrete increases its strength, while simultaneously attaining corrosion and frost resistance.

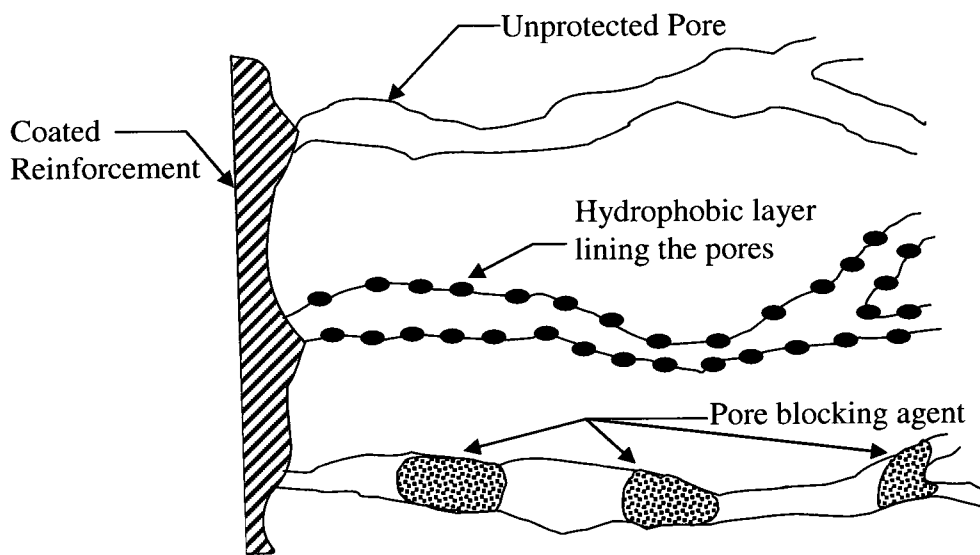


Fig 2.16 Schematic representation of different types of surface coatings
(Adapted from Bentur et al., 1998, p.124)

2.10.6 Electrokinetic Nanoparticle (EN) Treatment

Electrokinetic nanoparticle (EN) treatment involves the injection of nanoparticles into concrete or hardened cement paste, in order to achieve

reduction in permeability and increases in strength (Cardenas and Struble, 2006; Cardenas, 2002; Kupwade-Patil, 2007; Cardenas et al., 2007). In one study the permeability was reduced by a factor of three, when 20 nm silica particles and 2 nm alumina particles were transported into the cement paste using a weak electric field (Cardenas 2002). The alumina coated silica possessed a positive charge with a 20 nm silica core surrounded by 2 nm alumina particles as shown in Figure 2.17. A model was developed that predicted the rate of penetration via EN treatment under the influence of electrophoresis, electroosmosis and hydraulic flow (Cardenas and Struble, 2008).

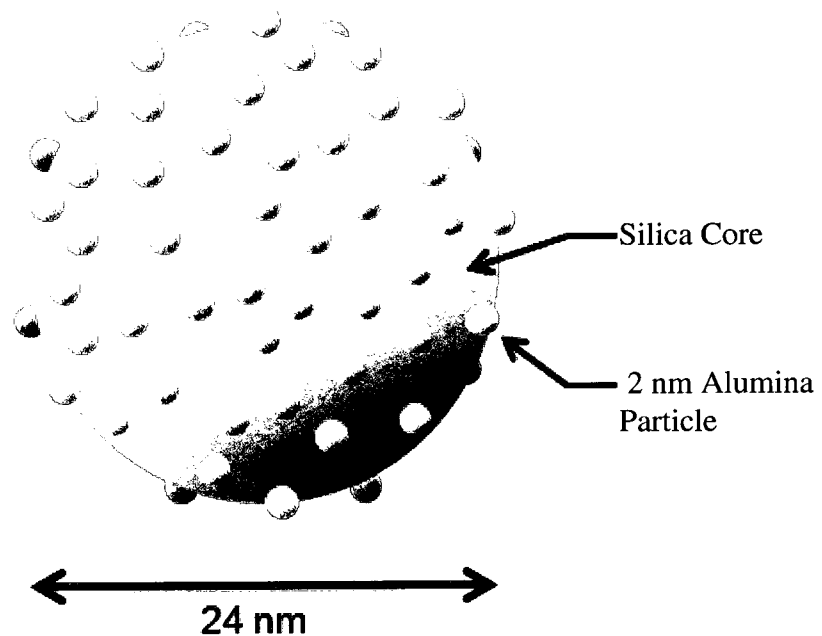


Fig 2.17 Alumina coated silica nanoparticle

Pozzolanic nanoparticles were used as a pore blocking agents to mitigate reinforcement corrosion in concrete (Kupwade-Patil, 2007; Cardenas and

Kupwade-Patil, 2007). Cylindrical reinforced concrete specimens were subjected to initial saltwater exposure followed by electrochemical chloride extraction (ECE) and electrokinetic nanoparticle (EN) treatment. The EN treated specimens showed a 25% increase in strength and an, 11% decrease in porosity as compared to the control specimens. EN treatment was effective in reducing the magnitude of the corrosion potential associated to reinforcement corrosion.

2.11 Evaluation Techniques

Electrochemical techniques are useful in examining the corrosion behavior of reinforcement in concrete (Roy et al., 1993). These measurement techniques include non-destructive testing methods (NDT), which can be used to detect the corrosion of reinforcement over time. Techniques commonly used for corrosion detection in the field are shown in Table 2.4 (Broomfield, 1997). Some of these methods include the measurement of corrosion potential, linear polarization resistance (LPR), electrochemical impedance spectroscopy (EIS), cyclic polarization, and macrocell techniques (ASTM G109 and ASTM STP 1056).

Table 2.4 Condition surveying methods for corrosion in concrete (Adapted from Broomfield, 1997, p.26)

Measurement Technique	Detection Area	Skill set required	Approximation speed
Visual	Surface defects	General	$1m^2s^{-1}$
Chloride content using titration	Chloride induced corrosion	General	10 minutes (laboratory facility required)
Corrosion Potential	Corrosion risk/ state of steel reinforcement	General/specialist	5 s per reading
Linear Polarization Resistance	Corrosion rate/ Corrosion current density	General/specialist	5-30 min per reading (depending on the type of potentiostat used)
Resistivity	Corrosion risk	General/specialist	20 s per reading
Permeability	Diffusion rate	Specialist	5 min per reading (laboratory facility require)
Impact/ Ultrasonics	Defects in concrete	Specialist	2 min per reading
Petrography (Microstructural characterization)	Condition in concrete	Specialist	Laboratory access required

2.11.1 Visual Inspection

Visual inspection is the primary method for investigating the corroded concrete structure and the reinforcement (Bentur, 1997). The visual analysis should consist of specimen identification, type of environmental exposure, location and specimen geometry (ASTM G 33-99). The color of the corroded area of the specimen should be recorded. The area of the discoloration should

be measured as a percentage of the overall surface area. The surface texture of the specimen should be examined for lustrous, semi-lustrous, matte, graining and pebbly areas. Blistering, peeling, cracking, checking, rust, tubercles, nodules and pits are the common local surface irregularities observed on corroded reinforcement. Specimen mass and thickness loss should also be recorded if encountered and compared to the original state of the specimen.

2.11.2 Half Cell Potential Measurements

The half cell potential method is widely used for analysis of reinforcement corrosion in bridge decks (Grantham, 1993; Roberge, 2007; Talbot, 2007). The corroding metal exhibits a steady potential, which is known as the corrosion potential ($E_{\text{corrosion}}$). The corrosion potential gives an indication as to whether the anodic and cathodic corrosion currents are equal. In this method reference electrode is introduced into the corrosive medium. The potential is measured using the voltage difference between the reference electrode and the working electrode (reinforcement). The reference electrode must be properly maintained and periodically compared to a primary reference electrode. A high input impedance voltmeter is required so that it is capable of reading 1mV resolution and a range up to 5V. A schematic diagram demonstrating the corrosion potential measurement is shown in Figure 2.18 (ASTM C 876-91).

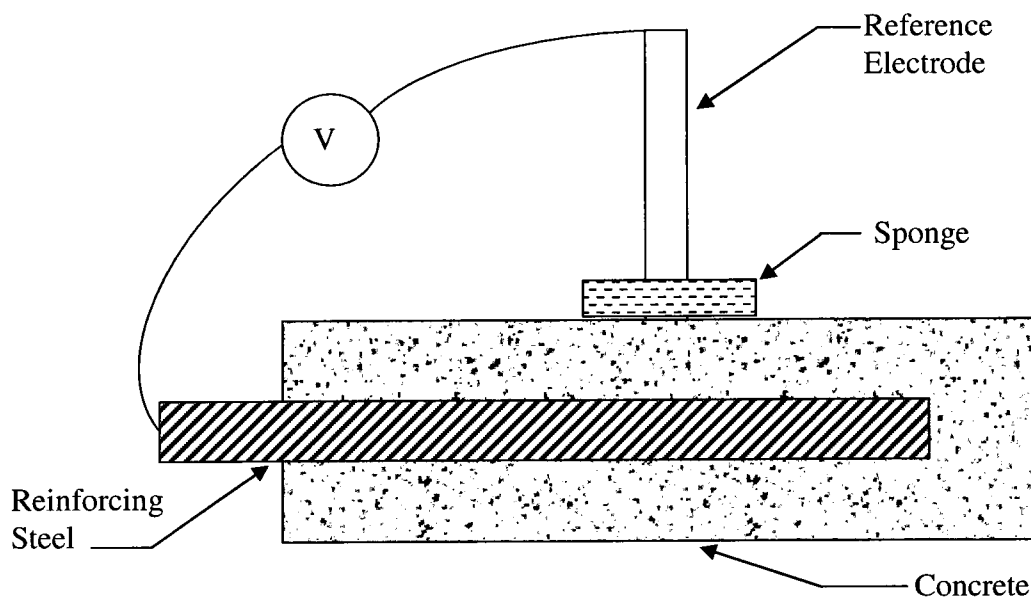


Fig 2.18 A schematic illustration of the corrosion potential measurement of reinforced concrete (Adapted from Bentur et al., 1998, p.77)

In order for the measurement to be made, the reinforcement is connected to the positive end of the voltmeter and the reference electrode is connected to the common input of the voltmeter. The corrosion activity evaluation of reinforcing steel in concrete is shown in Table 2.5.

Table 2.5 Guidelines for evaluating reinforcement corrosion in concrete (ASTM C 876-91)

Half-cell potential reading vs Cu/CuSO ₄	Corrosion Activity
Less negative than -0.200V	90 % probability of no corrosion
Between -0.200 V and -0.350 V	an increasing probability of corrosion
More negative than -0.350 V	90 % probability of corrosion

2.11.3 Polarization Resistance and Tafel Plot Technique

Stern-Geary developed a theoretical relationship between a metal freely corroding potential (ΔE), current density (ΔI) and corrosion rate (CR) (Kelly et

al., 2002; ASTM G102) Ohm's law was used to define the polarization resistance (R_p) which is the slope of corrosion potential versus current density. The Stern-Geary equation relates the current density (I_{corr}) to the linear polarization resistance (R_p),

$$I_{corr} \left[\frac{\mu A}{cm^2} \right] = \frac{\beta_a \beta_c \left[\frac{mV}{decade} \right]}{2.3(\beta_a + \beta_c) R_p [ohm \ cm^2]} \quad [30]$$

where β_a = Anodic Tafel Curve Slope (mV/decade), β_c = Cathodic Tafel Curve Slope (mV/decade), R_p = Polarization resistance (ohm cm^2),

The calculated value of corrosion current density (I_{corr}) and Faraday's constants are shown in Table 2.6. These values are used in the calculation of corrosion rate (CR) and mass loss rate (MR), which are given by

$$CR = \frac{K_1 \cdot I_{corr} \cdot EW}{\rho}, \text{ and} \quad [31]$$

$$MR = K_2 \cdot I_{corr} \cdot EW \quad [32]$$

where K_1 and K_2 = Faraday's Constant ($K_1 = mpy \ g/\mu A \ cm$), ($K_2 = mg \ cm^2/\mu A \ dm^2 \ d$), $d = \text{day}$, I_{corr} = Corrosion current density ($\mu A/cm^2$), EW = Equivalent Weight (g/equiv) $\rho = \text{Density (g/cm}^3\text{)}$

Table 2.6 Units of Faraday's constant (Adapted from ASTM G102, 1999)

Penetration Rate	I_{corr} (Unit)	K1	Units of K1
Mpy	$\mu A/cm^2$	0.1288	mpy g/ $\mu A \ cm$
mm/yr	$\mu A/cm^2$	3.27×10^{-3}	mm g/ $\mu A \ cm_y$

In the Tafel plot technique, the polarization curves for the anodic and cathodic reactions are obtained by applying potentials (approximately 300 mV) away from the corrosion potential and recording the current. A logarithmic plot of current density ($\log i$) versus potential is generated. This plot of potential versus measured current is known as the Tafel plot (see Figure 2.19). The slopes obtained from the linear regions are referred to as the Tafel constants. The intersection of the linear regions of the anodic and cathodic curves correspond to E_{corr} and I_{corr} . The value of I_{corr} is used to calculate the corrosion rate as shown in Equation 30.

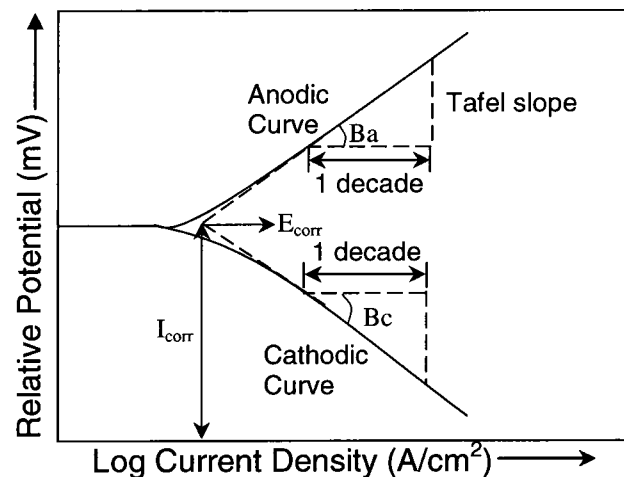


Fig 2.19 Tafel plot exhibiting log current versus relative potential (Adapted from Al-Tayyib and Khan, 1998)

2.11.4 Electrochemical Impedance Spectroscopy (EIS)

Impedance spectroscopy is a popular methods of characterizing many electrical properties of materials (Barsoukov and Macdonald 2005). Electrical impedance $Z(\omega)$ is defined as a vector

$$Z(\omega) = \frac{V(\omega)}{I(\omega)} \quad [33]$$

The complex plane plot or Argand diagram consists of real and imaginary components as shown in Figure 2.20. The following definitions can be predicted

$$Z(\omega) = Z'(\omega) - jZ''(\omega), \quad j = \sqrt{-1} \quad [34]$$

$$Z'(\omega) = |Z| \cos \theta \quad [35]$$

$$Z''(\omega) = |Z| \sin \theta \quad [36]$$

$$\theta = \tan^{-1} \left(\frac{Z''}{Z'} \right) \quad [37]$$

$$|Z| = \sqrt{(Z')^2 + (Z'')^2} \quad [38]$$

where $Z'(\omega)$ and $Z''(\omega)$ are the real and imaginary components of the impedance in ohm, $|Z|$ is the modulus of real and imaginary components and θ is the phase angle.

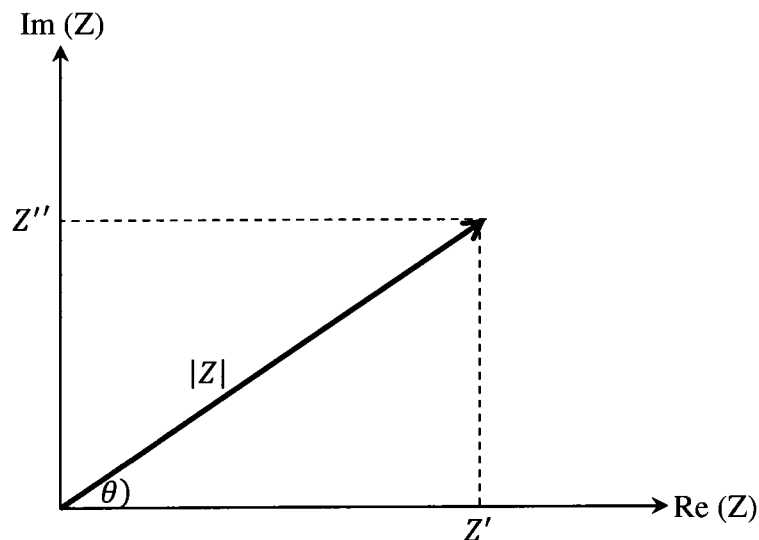


Fig 2.20 Argand diagram or complex plane (Adapted from Barsoukov and Macdonald, 2005, p.6)

The linear polarization resistance (LPR) can be calculated using equivalent circuit analysis (Ramachandran and Beaudoin, 2002; Kelly et al., 2002). The EIS method is mostly conducted in the frequency domain. The common circuit model used for analysis of three parameters, the polarization resistance (R_p), the solution resistance (R_s) and the double layer capacitance (C_{dl}), which is formed when an electrochemical interface exists as shown in Figure 2.21.

Corrosion characteristics can also be studied by plotting the log of frequency versus the phase angle (Bode plot), the frequency versus modulus of impedance $|Z|$ and the real versus imaginary components of impedance as seen in the Nyquist plot (Zhang et al., 2001). The resistivity modulus versus frequency becomes flatter with increasing corrosion rates while the phase angle drops with increase in corrosion rates when plotted against frequency. The arc diameter tends to decrease with corrosion rates, as seen in a standard Nyquist plot as shown in Figure 2.22. The Nyquist plot consists of the bulk resistance (R_b) which is related to the axis intercept and is considered one of the most reliable part of the electrochemical impedance spectroscopy parameters (Cardenas, 2002; Christensen et al., 1994).

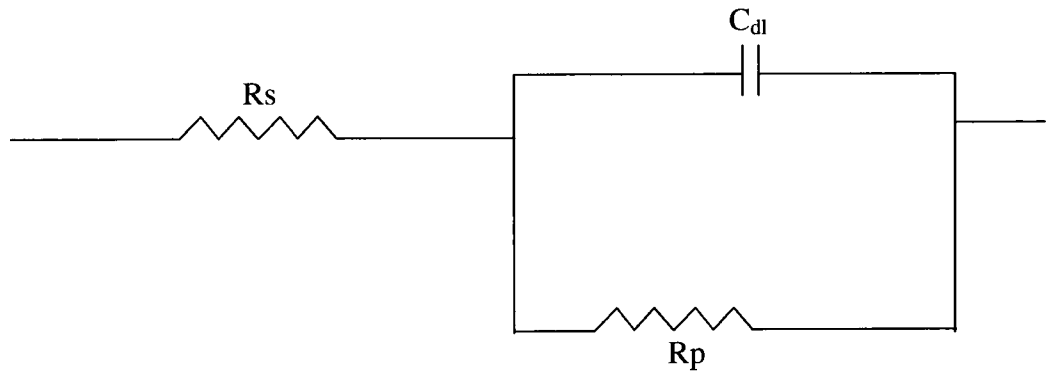


Fig 2.21. Equivalent circuit model used to determine the linear polarization resistance (R_p) from EIS (Adapted from Kelly et al., 2002, p.135)

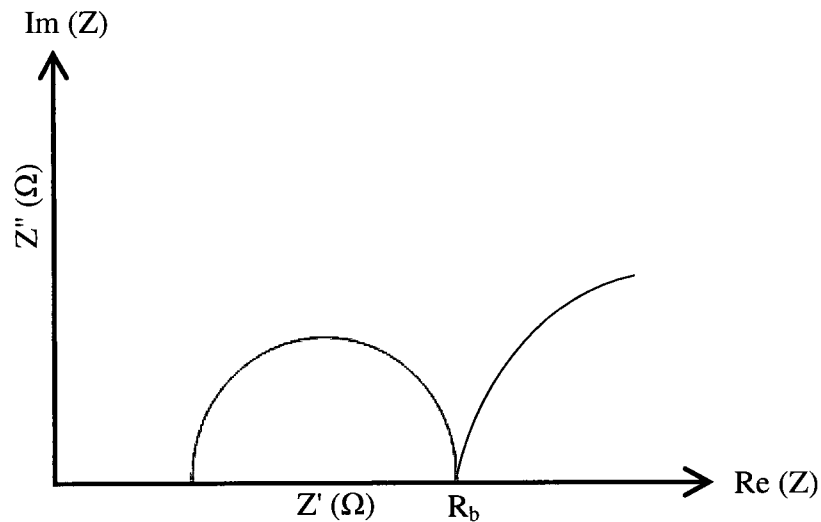


Fig 2.22. Typical Nyquist plot for a hardened cement paste (Adapted from Cardenas 2002, p.26)

The bulk material conductivity is calculated by,

$$\sigma = \frac{AR_b}{L} \quad [39]$$

where σ = bulk conductivity, L = length over which current flows during measurement, A = cross-sectional area through which the current flows during the measurement. The other loop demonstrates that the reinforcement in steel is corroding (Dhouibi-Hachani et al.,1996; Marcus and Mansfeld, 2005). Greater

the length of the loop, indicates higher corrosion. The linear polarization resistance (R_p) for the corroding reinforcement in concrete can be calculated by Equation 40 using the data from the Nyquist plot (refer to Figure 2.20)

$$R_p = \frac{Z' - R_s}{1 - \omega C |Z''|} \quad [40]$$

where R_p = Polarization resistance, Z' = real part of impedance, Z'' = imaginary part of impedance, R_s = solution resistance, resonance frequency(ω) = $2\pi f$, and C = capacitance.

As the value of the polarization resistance (R_p) increases the corrosion current density (I_{corr}) decreases, as shown in Equation 28. A decrease in I_{corr} indicates lower corrosion rates, as per Equation 29. EIS can also be used as a tool in interpreting the corrosion rates of the reinforcement.

2.11.5 Macrocell Techniques

ASTM G109 specimens which simulate a bridge deck are shown in Figure 2.23. The reinforced concrete specimens consist of a top rebar and two bottom rebars. A chloride pond is located about 1 inch from the rebar (ASTM G109). Chlorides diffuse into the concrete and accumulate, leading to a chloride concentration cell (Elsener, 2002; Mohammed and Hamada, 2007; Mohammed et al, 2001). The chloride contaminated structures lead to macrocell corrosion with corroding local anode (top rebars) and a non-corroding cathode (bottom rebars). The high chloride concentration in the vicinity of the top anodic rebar causes a change in corrosion potential, and a potential difference between top and bottom rebars leads to a macrocell formation.

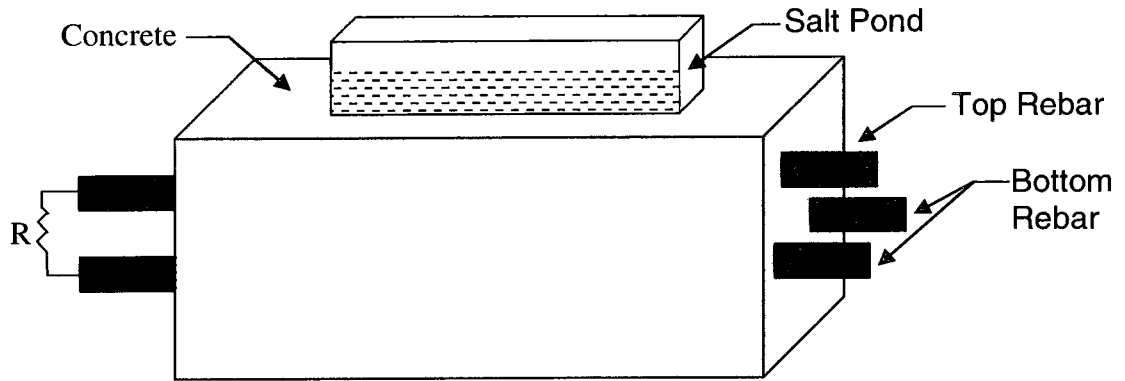


Fig 2.23 ASTM G109 Specimen simulating the formation of macrocell

Macrocell corrosion measurement is done by calculating the voltage drop across the 100Ω resistor (R) (ASTM G109, Ramachandran and Beaudoin, 2002). This voltage (V) drop is used to calculate the corrosion current (I) by using Ohm's law given by,

$$I = \frac{V}{R} \quad [41]$$

The macrocell current density is calculated by

$$I_{\text{mac}} = \frac{I_0 - I_i}{A} \quad [42]$$

where I_{mac} is the macrocell current density in $\mu\text{A}/\text{cm}^2$, I_0 and I_i are the output and input flow of electrons in the reinforcement in μA and A is the surface area of the steel element in cm^2 (refer to Figure 2.24). A positive value for I_{mac} indicates the anodic state while a negative value means that it is cathodic.

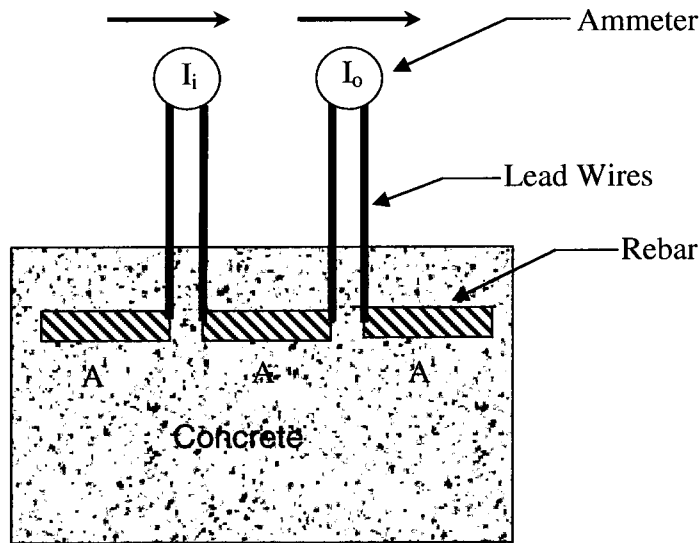


Fig 2.24 Measurement of macrocell current density (Adapted from Mohammed et al., 1999, p.156)

The charge passed through the reinforced concrete specimen can be used to predict the chloride ion permeability (ASTM C 1202). The total current (I_j) is measured from the voltage (V_j) developed between the anodic and cathodic reinforcement that are separated by the 100Ω resistor (refer to Figure 2.23).

$$I_j = \frac{V_j}{100} \quad [43]$$

The total coulombs of corrosion current (TC) in coulombs is shown by,

$$TC_j = TC_{j-1} + \left[(t_j - t_{j-1}) \times \left(\frac{i_j + i_{j-1}}{2} \right) \right] \quad [44]$$

where TC = total coulombs of corrosion current, t_j = time in seconds at which the measurement of macrocell current occurred, i_j = macrocell current (amps) at time (t_j).

CHAPTER 3

PROCEDURE

The work initiated in this section focused on the application of electrokinetic nanoparticle (EN) treatment on concrete cylinders, ASTM G109 specimens, and full length reinforced concrete beams. In another case EN treatment was applied to mitigate sulfate attack. Corrosion measurements were conducted using half cell potentials, linear polarization resistance and electrochemical impedance spectroscopy (EIS). Microstructure was studied using scanning electron microscopy, X-ray diffraction, Fourier transform infrared spectroscopy and Raman spectral analysis. Pore structure was examined using mercury induced porosimetry (MIP). The following sections describe the procedures used in this study.

3.1 Mix Design and Curing

The mix design for cylindrical, ASTM G109 specimens and beams were developed as per ACI 211.1. Portland Type I cement, fine aggregate and water constituted the primary ingredients of the mix. Arkansas pea gravel and silica sand were obtained from TXI Inc., Ruston, LA. The cement and batch composition used is listed in Table 3.1 and Table 3.2. Batching was done as per ASTM C 192 and C 195.

Table 3.1 Type I Portland cement composition

Compound	SiO ₂	Al ₂ O ₃	Fe ₂ O ₃	CaO	MgO	SO ₃
Concentration (%)	20.50	5.21	1.71	62.63	3.83	3.08

After the concrete was poured, the electrodes were inserted using mold covers equipped with guide holes to accurately place and secure each electrode. After 24 hours of initial curing, the specimens were demolded and placed in lime water for a period of 7 days at approximately 20°C. The top surface of each cylinder was coated with masonry sealant (Dry Lock Masonry sealant, United Gilsonite Labs, Jacksonville, IL). Five minute epoxy (Devcon Scientific, Riviera Beach, FL) was applied to exposed sections of the carbon steel to prevent atmospheric corrosion. After a week of limewater cure, the specimens were immersed in saltwater solution.

Table 3.2 Batch composition

Materials	Water	Gravel	Cement	Sand
Weight lb (kg)	18.5 (8.3)	93.5 (42.4)	36.5 (16.5)	56.5(25.6)

Both young and mature cylindrical reinforced concrete specimens were cast six inch high by three inch in dia. The design of the specimen is shown in Figure 3.1. The elemental composition of the 1018 carbon steel was of C= (0.14-0.2) %, Mn = (0.6-0.9)%, S= 0.05% max, P = 0.04% and Fe = (98.81-99.26)%. The electrode dimensions were 300 mm (12 in) in length and 6 mm (0.2 in) in diameter. Fresh concrete was poured as per ASTM C192. Each cylindrical specimen consisted of 3.2 lb (1.45 kg) of concrete.

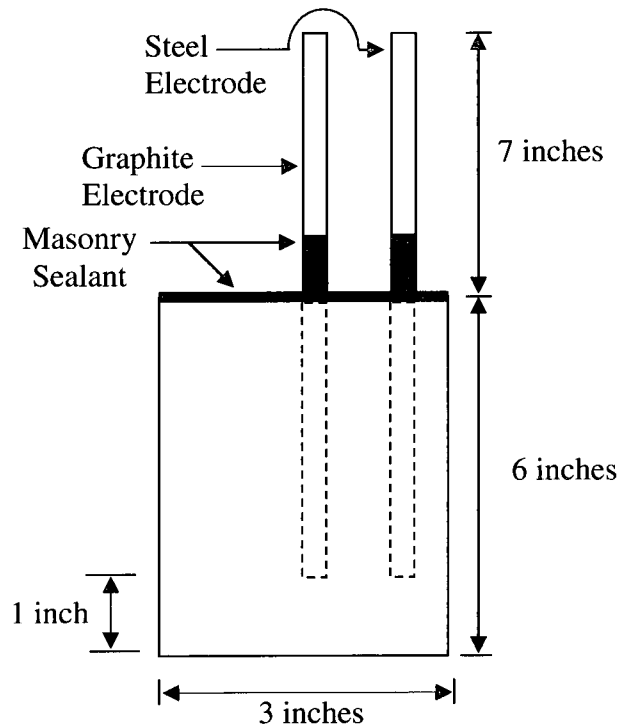


Fig 3.1 Front view of the reinforced cylindrical concrete specimen

ASTM G109 specimens were cast using Portland cement Type I. The reinforcement (rebars) was 0.4 in (10 mm) in diameter and 15 in (381 mm) in length, as shown in Figure 3.2. Concrete specimens were 280 mm (11 in) in length, 115 mm (4.5 in) in width and 150 mm (6 in) in depth. These specimens were prepared as per ASTM C 192M. Plexiglass dams of 75 mm (3 in) wide by 6 in (150 mm) long, and 75 mm (3 in) height were sealed using silicone caulk on the top of the specimens.

Reinforced concrete beams (length: 1.98 m (78 in), width: 0.17 m (6.6 in), length: 0.18 m (7.0 in)) were cast using Portland cement Type I (refer to Table

3.3). All beams had two No. 4 (12.7 mm (0.5 in) diameter) rebars and two No.6 (19 mm (0.7in) diameter) rebars as longitudinal reinforcement.

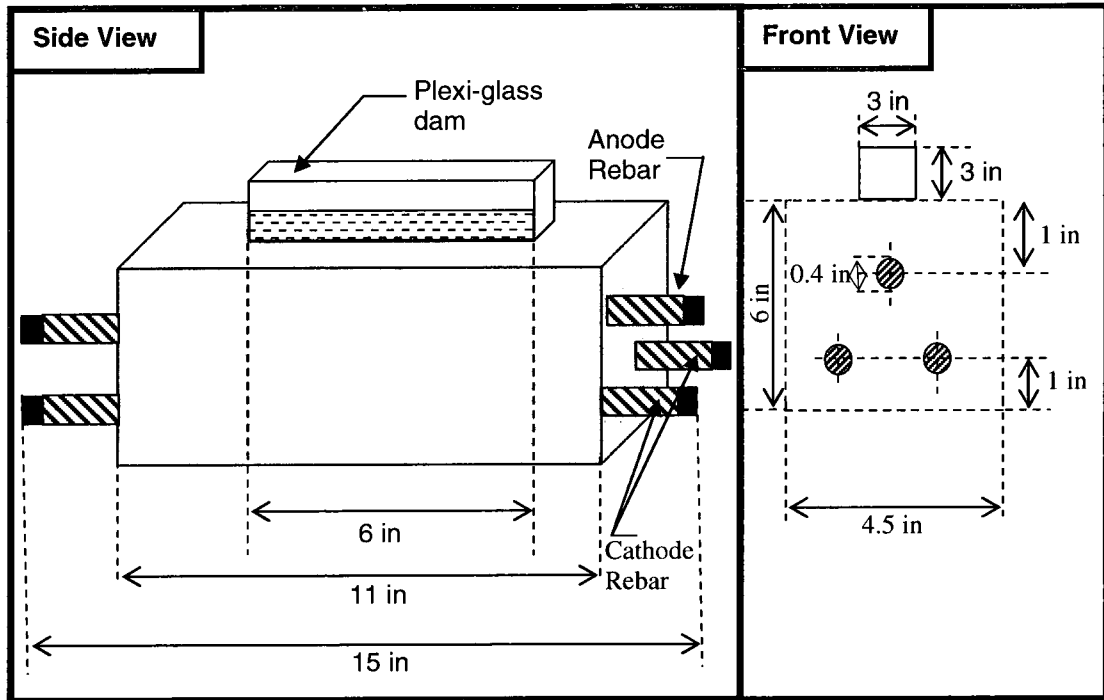


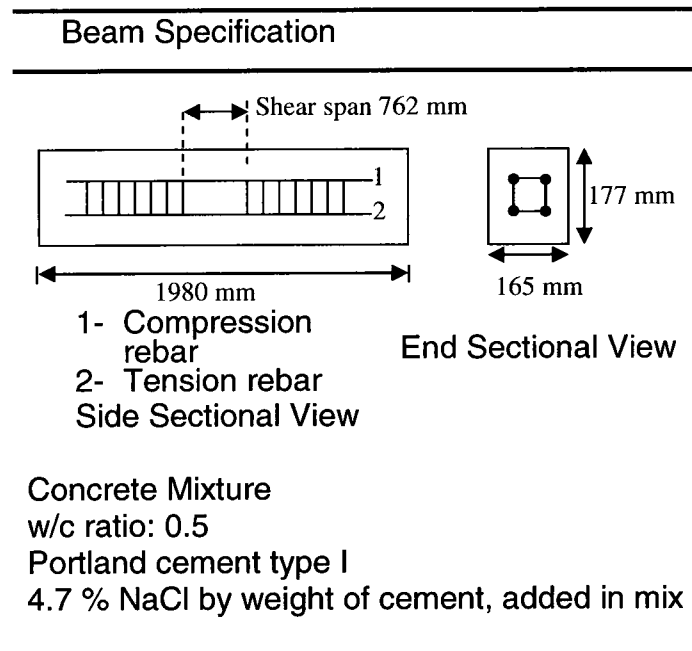
Fig 3.2 Schematic diagram of ASTM G109 specimens

No. four bars acted in compression, while the No. six bars were in tension. Commercially available stirrups (9.5 mm (0.4 in) diameter) were used to form the rebar cages of each beam. The shear reinforcement stirrups were placed 102 mm (4.0 in) apart throughout each beam. Cement composition and properties of the concrete are shown in Table 3.3. Specimen set-up, curing conditions and concrete mixture details are summarized in Table 3.4. Sodium chloride (NaCl) was added to the mix in order to simulate the use of beach sand.

Table 3.3 Chemical composition of cement

Chemical	Al ₂ O ₃	Fe ₂ O ₃	SO ₃	C ₃ A	CO ₂	CaCO ₃	CaO	SiO ₂
Wt %	4.5	3.7	2.7	6.0	1.2	2.9	64	24

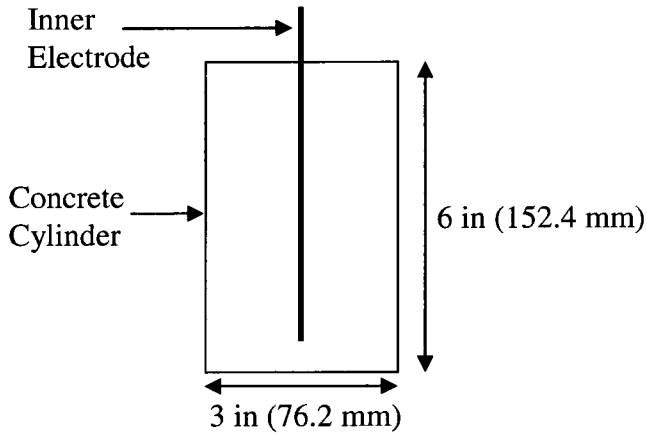
Table 3.4 Material setup for reinforced concrete beam



The effect of sulfate attack was studied using cylindrical concrete specimens. Cylindrical concrete specimens approximately 150 mm (6 inch) in length by 76 mm (3 inch) in diameter were fabricated using a mix design in accordance with ACI 211.1 (see Table 3.5). The concrete mix was prepared as per ASTM C192 with a w/c ratio of 0.5. Mixed-metal oxide coated titanium wire electrodes (Corrpro, Medina, OH) of 127 mm (5 inches) in length were cast into the centers of each specimen. The specimens were limewater cured for 7 days at 23⁰C. A 35.5 g/l solution of reagent grade anhydrous sodium sulfate was

prepared for specimen immersion. As specified by ASTM C 1012, a solution/specimen volume ratio of 4/1 was maintained for the immersion of the specimens at a 23⁰C. The sulfate solution was refreshed weekly, coinciding with length change measurements.

Table 3.5 Material setup, curing and mix proportions

Concrete Cylinders	
1. Specimen set up	
2. Concrete Mixture	<ul style="list-style-type: none"> - w/c ratio 0.5 - Portland cement type 1 - Arkansas Pea gravel 93.5 lb - Sand (TXI, Ruston, LA) 56.5 lb - aggregate size < 0.375 in - fineness modulus of sand 2.71
3. Curing Conditions	<ul style="list-style-type: none"> - 7 days of lime water curing - 23⁰C

3.2 Electrokinetic Nanoparticle (EN) Treatments

Electrokinetic Nanoparticle (EN) treatments were conducted on chloride and sulfate exposed cylindrical specimens. EN treatment was also conducted on full length beam specimens with three different treatment dosages.

3.2.1 EN Treatment Setup on Young and Mature RC Cylinder

Both young and mature cylindrical reinforced concrete specimens were cast six inches high by three inches in dia. using Type I Portland cement. Young specimens (freshly batched concrete) were subjected to seven days of EN treatment using a current density of one A/m^2 . These specimens were then subjected to 36 months of wet and dry saltwater exposure, as shown in Table 3.6. The wet and dry cycle consisted of 14 days of 3.5% NaCl solution exposure (wet cycle) followed by lab air exposure for 14 days (dry cycle). Mature specimens were first subjected to one year of initial wet-dry saltwater exposure. After this period, chlorides were extracted from six specimens for 7 days followed by 7 days of EN treatment using alumina coated silica nanoparticles with a current density of 1 A/m^2 .

Table 3.6 Schedule of EN treatments for young and mature concrete

Specimen Type	Time (Years)		
	1	2	3
Mature Concrete	Saltwater Exposure	E N	Saltwater Exposure
Young Concrete	E N	Saltwater Exposure	
Controls (Young and Mature Concrete)	Saltwater Exposure		

The circuit used for EN treatment is shown in Figure 3.3. The positive pole of the power supply was connected to the titanium ring surrounding the reinforcement, and the negative pole was connected directly to the 1018 steel

rebar. After EN treatment, the specimens were subjected to two years of 14-day, wet-dry, saltwater exposure cycles as shown in Table 3.6.

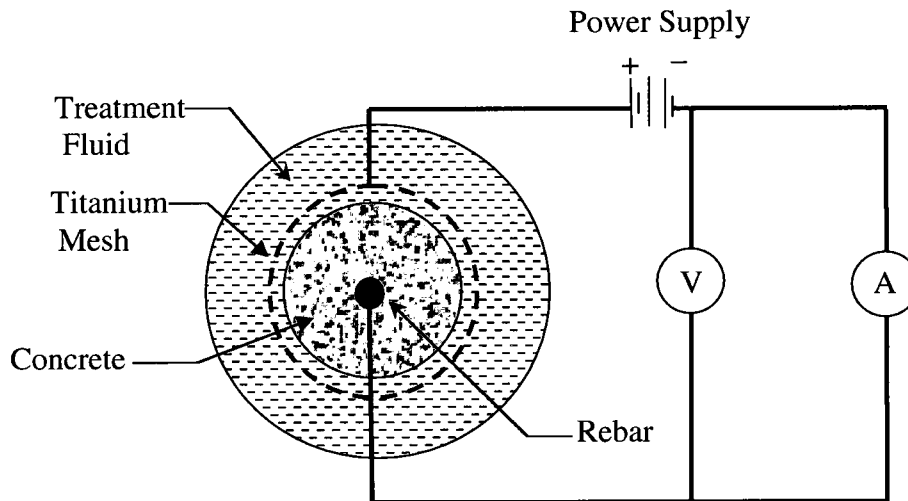


Fig 3.3 EN treatment on cylindrical reinforced concrete

3.2.2 EN Treatment on ASTM G109 Specimens

Rectangular reinforced concrete specimens (280 x 150 x 115 mm) were prepared using rebar that was 10 mm in diameter and 360 mm in length (ASTM G109 2003). Type I Portland cement was used with water to cement (w/c) ratio of 0.5. The anodic (upper) and cathodic (lower) bars were placed longitudinally one inch from the top and bottom of the specimen. Approximately 200 mm of rebar was exposed outside the test specimens as per ASTM G109. Plexiglass dams (75 x 150 x 75 mm) for saltwater exposure were placed on top of each specimen. Epoxy sealer of Type III and Grade I was used to seal the glass dams to the specimens. An NaCl solution was prepared by combining three parts sodium chloride in 97 parts water by mass and loaded into the plastic dams. A loose fitting plastic cover was used to minimize atmospheric evaporation. A

relative humidity of $50 \pm 5\%$ was maintained during the experiment. Specimens were subjected to eight weeks of initial saltwater exposure. Thereafter, wet-dry cycles consisted of seven days of saltwater exposure (wet cycle) followed by vacuuming off the solution and allowing the specimens to dry for seven days (dry cycle). Cycles of wet-dry exposure were applied prior to the application of ECE and EN treatments. ECE was conducted using sodium hydroxide solution and deionized water for 14 days. The circuit used for ECE and EN treatment of the specimens is shown in Figure 3.4. NaOH solution was placed into the tub containing the specimen and into the plexiglass dam that was mounted on top. Care was taken to avoid liquid contact with the rebar. Care was taken to avoid liquid contact with the rebar. The negative pole of the power supply was connected to the rebar while the positive terminal was connected to the titanium mesh, which was placed both inside the plexiglass dam and beneath the specimen.

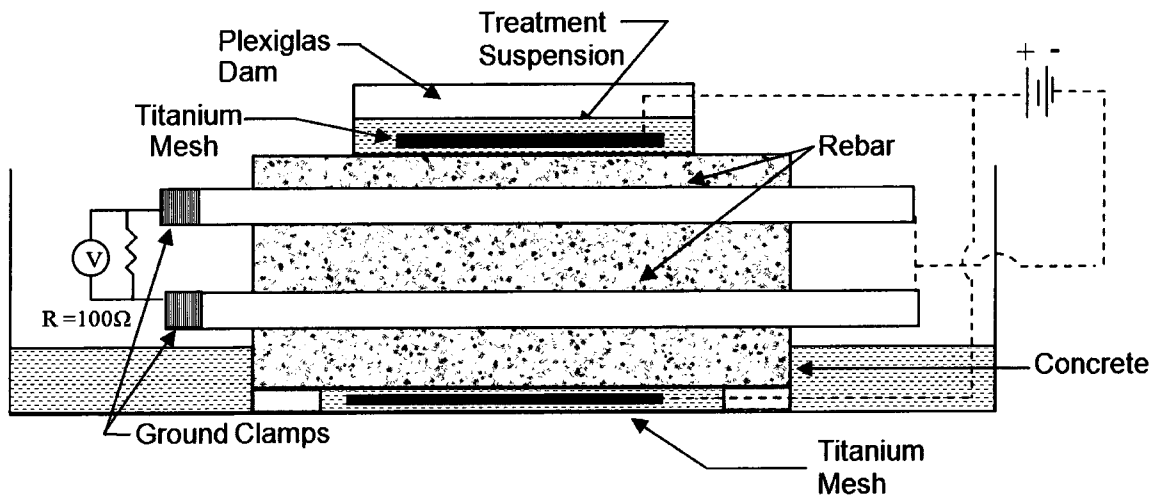


Fig 3.4 Circuit diagram for ECE and EN treatment of G109 specimens

The 14 days of ECE was followed by EN treatment for a period of six weeks. The EN treatment fluid was discarded and replaced every two days. Post treatment saltwater exposure of 240 days (~34 weeks) was conducted on all the specimens.

Alumina coated silica was the nanoparticle used for the EN treatment. The nanoparticle was 24 nm in size, with a 20 nm silica interior surrounded by a two nanometer layer of alumina particles. The acetate stabilized particles were maintained in a 12% particle volume suspension. The nanoparticle suspension was loaded at the top (Plexiglass dam) and at the bottom of the specimen. These particles were expected to drift through the pores of the specimen and toward the rebar while the chloride ions drifted away from the rebar, toward the titanium mesh, and thus out of the concrete.

3.2.3 EN Treatment on Reinforced Concrete Beams

Initial saltwater exposure was conducted for 12 weeks on eight specimens by placing the beams in NaCl (3.5 wt %) immersion. Two beams were not subjected to initial saltwater exposure and were lime water cured as untreated controls. The other six specimens were subjected to ECE and EN treatments at the end of the initial saltwater exposure. The treatment circuit for both the ECE and EN treatments are shown in Figure 3.5. Mixed metal oxide titanium mesh was wrapped along the base and sides, serving as the external electrode. The mesh was in between the sponge and the plexiglass. This was covered by a plexiglass outershell. The treatment liquid was circulated using an aquarium

pump along the sponge between the plexiglass and the beam. A constant current density of one A/m^2 was maintained.

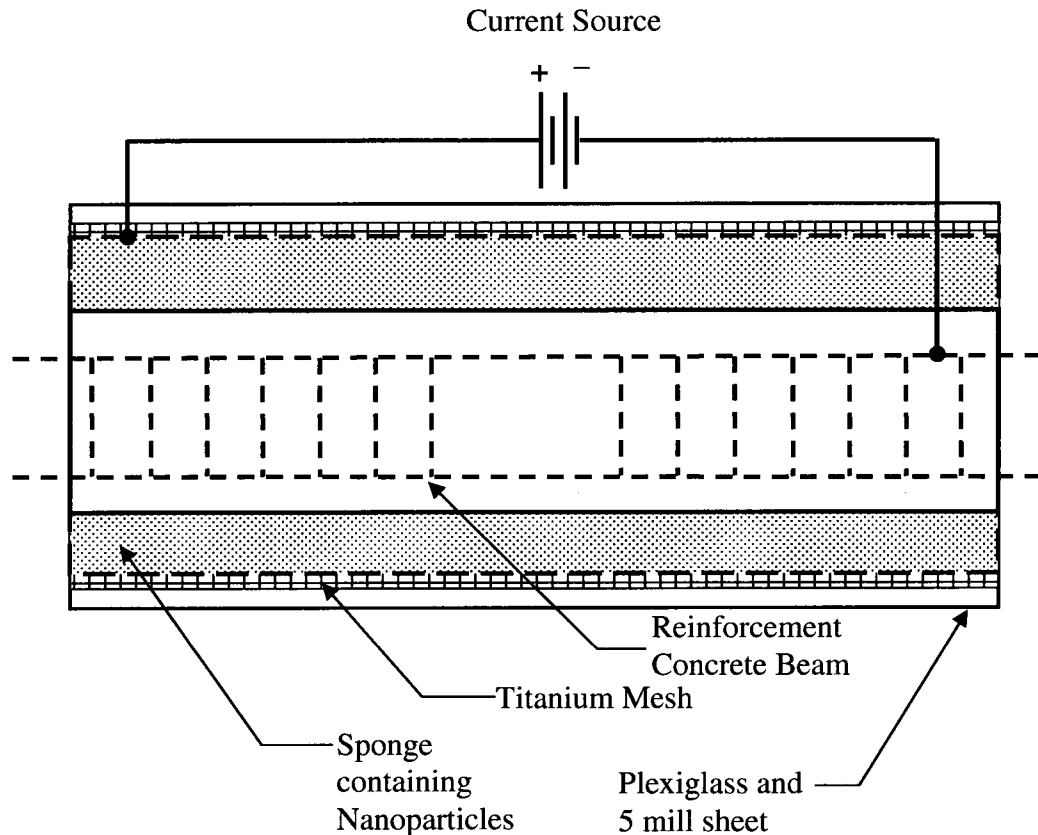


Fig 3.5 Circuit diagram during electrochemical chloride (ECE) and electokinetic nanoparticle (EN) treatment

The positive pole of the power source was connected to the titanium mesh, and the negative terminal was connected directly to the concrete reinforcement. Six specimens were subjected to ECE for two weeks followed by six weeks of EN treatment. Two of the specimens were subjected to ECE for all eight weeks at selected dosages. The treatment dosages used on the beams were 0.16 l/m^2 , 0.33 l/m^2 and 0.65 l/m^2 (liters of particles delivered per meter square of beam length). During EN treatment, the electric field drew

nanoparticles from the fluid flowing through the sponge and drove them into the pores of the concrete. At the end of six weeks all treatments were discontinued and all the specimens were subjected to 24 weeks of post saltwater exposure. Corrosion potential and corrosion rate measurements were recorded periodically during the study.

3.2.4 EN Treatment and Sulfate Extraction

The cylindrical test specimens were exposed to sodium sulfate solution for a period of 30 days. Six additional specimens were maintained in lime water as control specimens with no sulfate exposure. Following the 30 day period, sulfate ions were extracted from the test specimens for 14 days using the treatment circuit shown in Figure 3.6. The positive pole of the power supply was connected to the outer electrode (mixed-metal oxide coated titanium wire) and the negative pole was connected to the inner wire electrode. The electrode at the center acted as a cathode while the sulfate solution in which the specimen was placed acted as an electrolyte. The applied current density was 1 A/m^2 as calculated over the outside surface area of the cylinder. The voltage was intended to drive the sulfate ions out of each specimen and toward the outer electrode. The outer electrode was a single loop of the same type of titanium wire that was configured to surround the exterior surface of the specimen.

Following the 7-day sulfate extraction, EN treatment was carried out for an additional 7 days. The nanoparticle used was 24 nm in size with a 20-nm silica interior surrounded by a layer of two nanometer alumina particles.

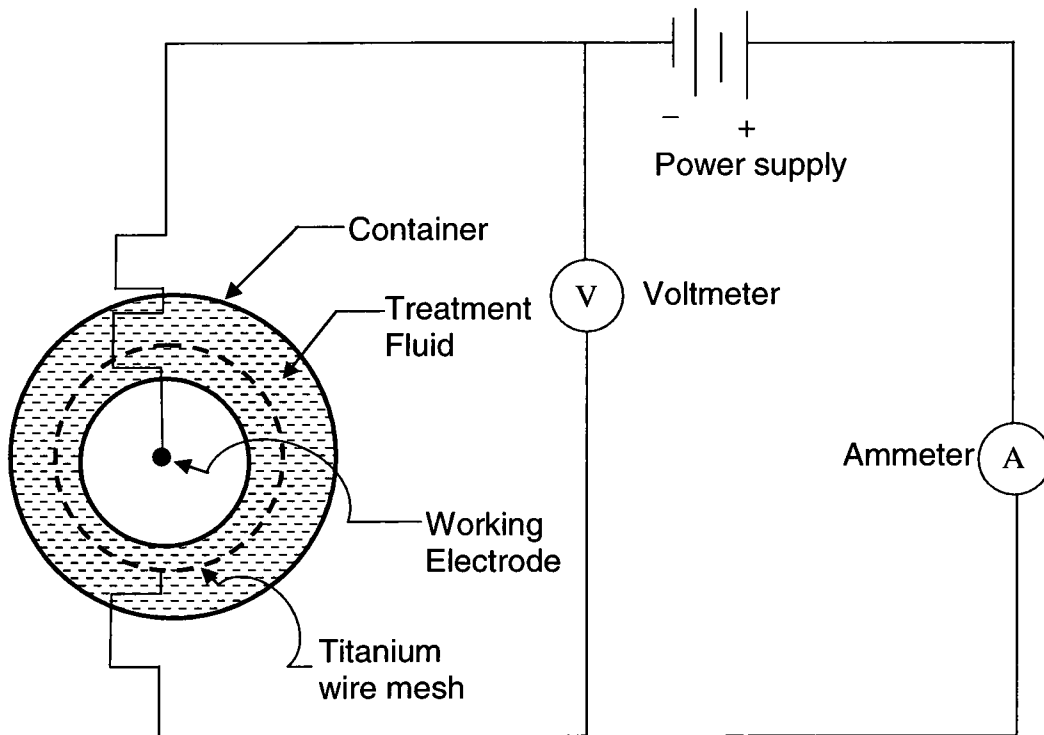


Fig 3.6 Circuit diagram for sulfate extraction and EN treatment

The particles were maintained in a 12% volume particle suspension that was acetate stabilized. The specimens were placed in a tank of the alumina-coated silica suspension (Nalco Chemicals, Naperville, IL) and treatment was conducted as per the circuit shown in Figure 3.6. Alumina-coated silica particles possess a positive charge and were expected to drift into the pores of the specimen toward the cathode. At the same time, the negatively charged sulfate ions were expected to drift toward the anode (external titanium wire electrode). Length change measurements were taken to the nearest 0.025 mm (0.001 inch) in accordance with ASTM C1012. The compression test was done in accordance with ASTM C 684-99. The inner electrode was trimmed flush with the top of the specimen prior to compression strength testing.

3.3 Electrochemical Measurements

Electrochemical monitoring techniques are useful in accessing the behavior of reinforcement corrosion in concrete. Corrosion measurements used in this study included corrosion potential, corrosion rates and electrochemical impedance spectroscopy (EIS).

3.3.1 Corrosion Potential

Half cell potential measurements were measured as per ASTM C 876-91. A copper-copper sulfate half cell reference electrode (manufactured by Tinkor and Rasor Inc., San Gabriel, CA) was used to measure the corrosion potential. The measurement setup is shown in Figure in 3.7. The corrosion potential was measured relative to the reference electrode and sponge using a multimeter (Gardner Bender, Milwaukee, WI). The corrosion potentials were recorded to the nearest 0.01 V.

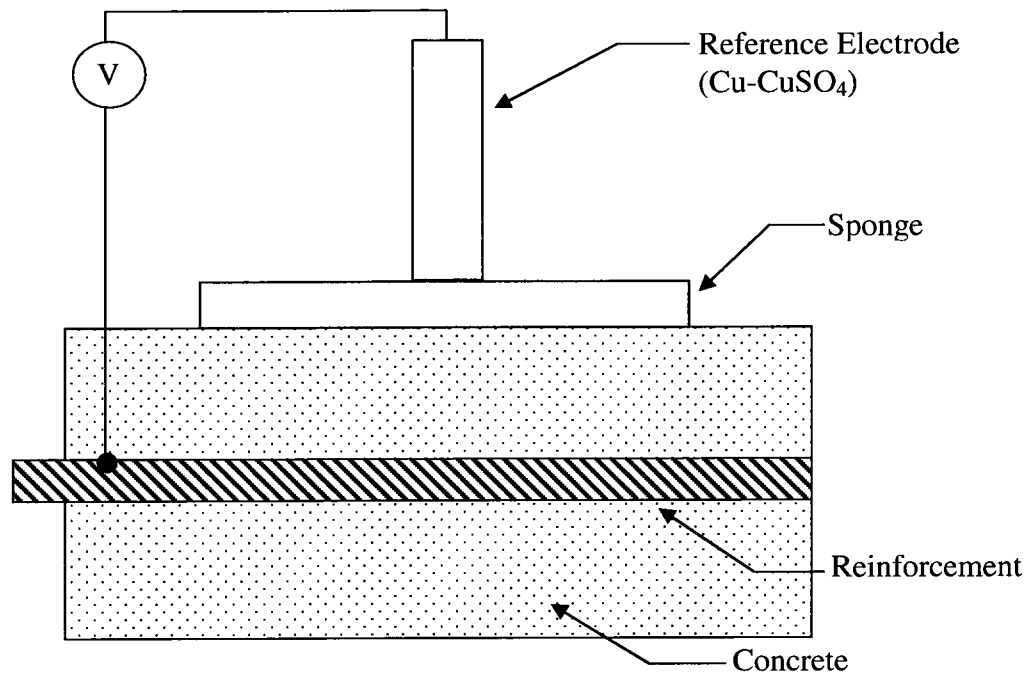


Fig 3.7 Measurement of half-cell potential

3.3.2 Corrosion Rate Measurements

The electrochemical polarization scans were taken using a Solartron potentiostat (model no 1287) manufactured by Roxboro Group Company (UK). The schematic layout of the setup for measuring corrosion rates is shown in Figure 3.8. The scans were taken in the range of -25 mV to + 25 mV at a scan rate of 0.2 mV/sec. The duration of each scan was seven to eight minutes. A plot of current versus potential was generated. The slope of potential versus current density at the origin of this plot is known as the polarization resistance (R_p). This can be related to the Stern-Geary relationship to find the corrosion current density (i_{corr}) (Jones, 1995). The IR drop was corrected using ($R_p = R - R_\Omega$) where R is the total resistance measured by the polarization resistance scan and R_Ω is the concrete resistance.

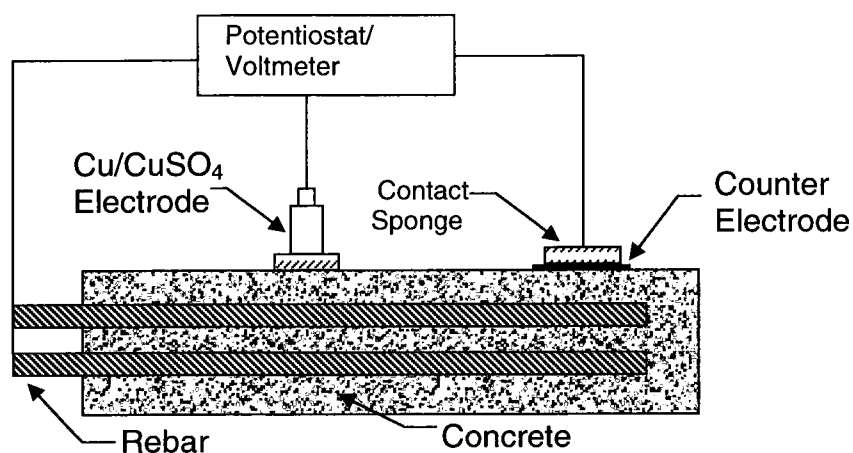
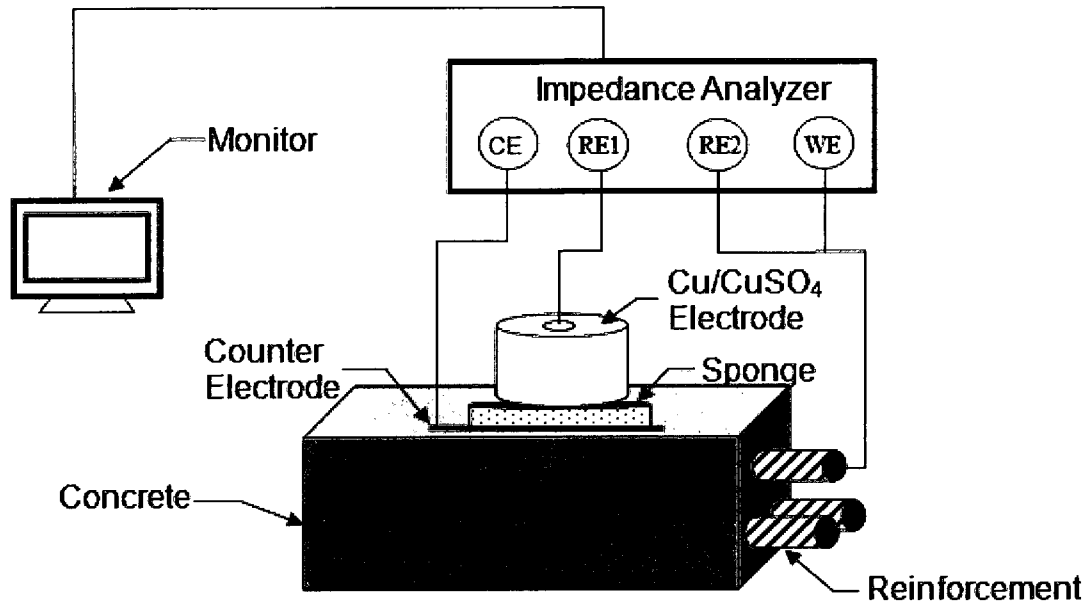


Fig 3.8 Corrosion rate measurement setup

The surface area, equivalent weight and density of steel were 60.70 cm^2 , 25.50 gm and 8.0 gm/cm^3 respectively. I_{corr} was calculated using Equation 30. The resulting value of I_{corr} was used to calculate the corrosion rate (CR) and mass loss rate (MR), which was derived from the Faraday's law as shown in Equations 31 and 32.

3.3.3 EIS Measurements

The schematic representation of the electrochemical impedance spectroscopy (EIS) set up is shown in Figure 3.9. The titanium was used as a counter electrode, while Cu/CuSO₄ was used as a reference electrode. The reinforcement was connected to the working electrode using cables on the impedance analyzer.



CE: Counter Electrode, RE: Reference Electrode, WE: Working

Fig 3.9 Schematic setup for EIS measurement

The measurements were taken using the sweep frequency mode of a Solartron SI 1260 impedance/ gain-phase analyzer, (Slough, Berkshire, UK). The measurements were taken as per ASTM G106 standards. The potential was set to 0. The sweep was conducted from a frequency range of 0.1 Hz (initial) to 10000 Hz (final) and a amplitude of 10 mV. Real impedance versus imaginary impedance (Nyquist plot), frequency versus impedance magnitude (bode plot) and frequency versus phase angle were plotted with Z-view software. Equivalent circuit analysis using Z-view software (manufactured by Scribner Associates, Inc) was used for calculating diffusion coefficients.

3.4 Strength Tests

Indirect tensile and compression tests were conducted on cylindrical reinforced concrete specimens. The splitting tensile test and the compression

test were conducted as per ASTM C 496-96 and C 873 respectively. These tests were used to compare the tensile strength of the EN treated specimens to the control specimens.

For the tensile test method consisted of the application of a diametrical compressive force distributed along the length of the cylinder at a rate of 150 psi/min until failure. The schematic layout of the setup is shown in Figure 3.10. The loading induces a transverse tensile stress on the vertical diametrical plane of the specimen. The maximum applied load P was used to calculate the splitting tensile strength (T) as per (ASTM C-496-96)

$$T = \frac{2P}{\pi Ld} \quad [45]$$

where L is the length and d is the diameter of the cylindrical concrete specimen.

The compression strength tests were performed as per ASTM C 873. The cylinders were capped before testing as per ASTM C 192-90a and the rate of loading was (50 psi/s).

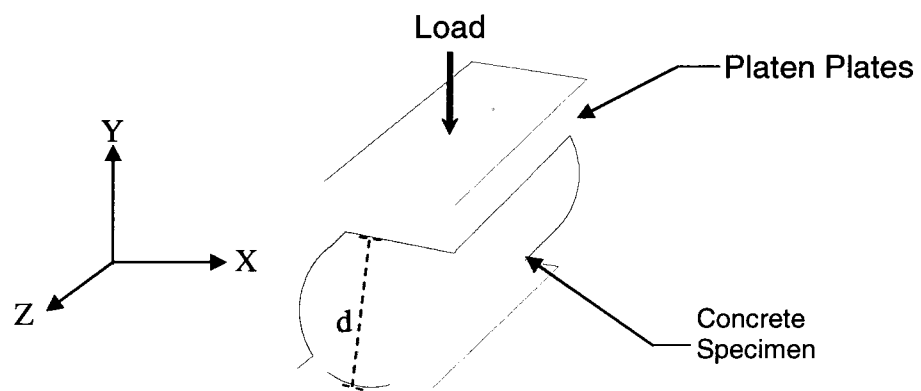


Fig 3.10 Schematic setup of splitting tensile test

3.5 SEM/BSE Specimen Analysis

Vacuum impregnation using an epoxy resin was conducted to fill the capillary pores of the concrete. A Buehler castable vacuum system (Lake Bluff, IL) was used to perform the vacuum impregnation. Oven dried concrete specimens were immersed in an epoxy solution (Epo-color, fast cure epoxy resin, model No. 638-500690 manufacture by Buehler, Lake Bluff, IL) and mixed with dye. The pressure was increased to 12.5 Psi, and the vacuum was released, forcing the epoxy solution to enter into the capillary pores. The epoxy was cured at a temperature of 65°C and this was followed by the polishing process.

Polishing was conducted using 60, 120, 150, 320, 600, 800 and 1200 grit size papers with the model Alpha-Beta Polisher (manufactured by Buehler, Lake Bluff, IL). Micro-polishing was conducted with Buehler polishing-cloths ranging from 3-0.02 μm . These cloths were the ULTRA-PAD: 3 μm (for SiC removal), TEXMET 2000: 3 μm (for profile flattening), TRIDENT: 1 μm (for polishing), and the MICROCLOTH: 0.02 μm (for finishing). Polishing was conducted with a non-aqueous lubricant (propylene glycol) and with no particulate abrasives. After each polishing stage the specimens were rinsed with ethyl alcohol to remove loose material. Microstructural analysis was conducted using an Hitachi S-4800 field emission scanning electron microscope (FE SEM) (manufactured by Hitachi, Pleasanton, CA). Quantitative elemental analysis was done using the FE SEM EDAX with Genesis Microanalysis software from Ametek Inc., (Paoli, PA).

3.6 Microstructure Characterization

Microstructural characterization was conducted using Raman Spectroscopy, Fourier Transform Infrared Spectroscopy (FTIR) and X-ray diffraction. Raman Spectroscopy was performed on polished concrete samples using an R-3000HR Raman spectrometer (Raman Systems, Woburn, MA) with a 4 cm^{-1} resolution and 785 nm diode laser excitation through a fiber optic sampling probe. This analysis technique detects the changes in the frequency of laser light due to its interaction with the vibrational modes of chemical bonds. Raman Spectrometry has been shown in the literature to be useful for investigating C-S-H, which is a primary source of strength in concrete. It has also been found useful in identifying the variant forms of C-S-H such as jennite and tobermorite (Kirkpatrick et al., 1997). Additional characterization was conducted via Fourier Transform Infrared Spectroscopy (FTIR) using a Mattson Genesis II FTIR spectrometer, (manufactured by Mattson Genesis Inc., Middleton WI). Samples were ground sufficiently to pass a No.30 sieve and mixed with potassium bromide (KBr) in a ratio of 1:100. The mixture was compacted to provide a smooth test surface, then pressed into pellets for transmittance measurements. An attenuated total reflectance (ATR) correction factor was applied to remove background scatter from the spectrum to help distinguish the specific peaks. X-Ray diffraction on powdered samples was conducted using a Bruker model AXS X-ray diffractometer, (Billerica, MI).

3.7 Porosity Measurements

Porosity measurements were conducted on samples taken from compression test specimens. Powdered samples of 5-7g were ground to pass a No.30 sieve. These particles were collected and dried to obtain a porosity measurement via weight loss at 105°C. The initial weight of the sample was W_1 and the stabilized weight was represented by W_2 . Porosity in terms of percentage was calculated as per Equation 46.

$$\text{Porosity (\%)} = \frac{W_1 - W_2}{W_1} \times 100 \quad [46]$$

An additional study of pore structure was carried out using mercury intrusion porosimetry (MIP) with similarly powdered samples. MIP tests were carried out using a Micromeritics Autopore IV 9500. High pressure MIP was applied delivering a peak of 226 MPa.

3.8 Simulated Pore Fluid

To determine anticipated reaction products, nanoparticle suspensions were mixed with simulated concrete pore fluid. These mixtures, alumina-coated silica suspension in one case and colloidal alumina in the other, were prepared using high-alkali simulated pore fluid. The combination of chemicals used in preparing this pore fluid is shown in Table 3.7 (Cardenas 2002). Equal volumes of simulated pore fluid and nanoparticle suspensions were combined. These mixtures reacted to form precipitates. The precipitates were immersed in methanol (to supplant pore water) and decanted three times at 24-hour intervals. This was followed by xylene immersion and similar decanting to remove the

methanol. Oven drying at 105°C was conducted for 24 hours to remove the xylene. The sample was ground (as noted before in the porosity study) and subjected to FTIR analysis.

Table 3.7 Composition of high-alkali simulated pore fluid

Constituent / Source	Chemical Symbol	Concentration (mol/L)
Sodium hydroxide	NaOH	0.16
Potassium hydroxide	KOH	0.64
Calcium hydroxide	Ca(OH) ₂	0.002

CHAPTER 4

RESULTS AND DISCUSSION

Sections (4.1 to 4.5) illustrate the experimental results that were obtained for electrokinetic nanoparticle (EN) treatment on young and mature concrete, ASTM G109 specimens and reinforced concrete beams. EN treatment was also used to mitigate sulfate attack was also explored in Section 4.4.

The Section 4.1 was published by Cardenas, Kupwade-Patil, and Eklund, under the title “Corrosion mitigation in mature reinforced concrete using nanoscale pozzolan deposition” in the proceedings of the Second International Conference on Sustainable Construction Materials and Technologies, Ancona, Italy, June 2010. This work was conducted under the guidance of Dr. Henry Cardenas. Dr. Eklund helped the author conduct chemical analysis (FTIR).

4.1 EN Treatment on Young and Mature RC Specimens

Electrokinetic Nanoparticle (EN) treatments were employed to mitigate corrosion in reinforced concrete (Cardenas et al., 2010). In this approach, an electric field was used to drive pozzolanic nanoparticles through the capillary pores of concrete, directly to the reinforcement. The intent was to use the

nanoparticles as pore blocking agents to prevent the ingress of chlorides. Treatment effectiveness was examined for both freshly batched and relatively mature concrete. Cylindrical reinforced concrete specimens were subjected to EN treatment immediately after batching and then exposed to chlorides for a period of three years. The EN treated specimens exhibited a reduction in corrosion rates by a factor of 74 as compared to the untreated controls. Another set of specimens were subjected to chlorides for a period of one year prior to EN treatment application. Electrochemical Chloride Extraction (ECE) and EN treatments were performed on these mature specimens for one week. These specimens were placed back into saltwater exposure for an additional year. The mature controls exhibited severe corrosion cracking as compared to the mature treated specimens after one year of saltwater exposure. The corrosion rates were eight times that of the treated specimens. Microstructural and chemical analysis was conducted using Scanning Electron Microscopy (SEM), XRD and Fourier Transform Infrared Spectroscopy (FTIR). This study demonstrated that microstructural changes due to treatment were effective in mitigating reinforcement corrosion in both young and mature concrete. The following sections exhibit the results related to corrosion potential, corrosion rates, microstructure, strength and porosity analysis.

4.1.1 Corrosion Potential and Corrosion Rates

The corrosion potentials and corrosion rates of the reinforced concrete specimens are shown in Figures 4.1 and 4.2. Average corrosion potentials of -1500 mV and -1200 mV were observed for mature and young control specimens

respectively at the end of 1100 days of saltwater exposure. After saltwater exposure, the mature EN treated specimens demonstrated an average corrosion potential of -840 mV and the young specimens yielded -820 mV. The lower corrosion potentials exhibited by the EN treated specimens indicated a likelihood of less active corrosion as compared to the untreated controls.

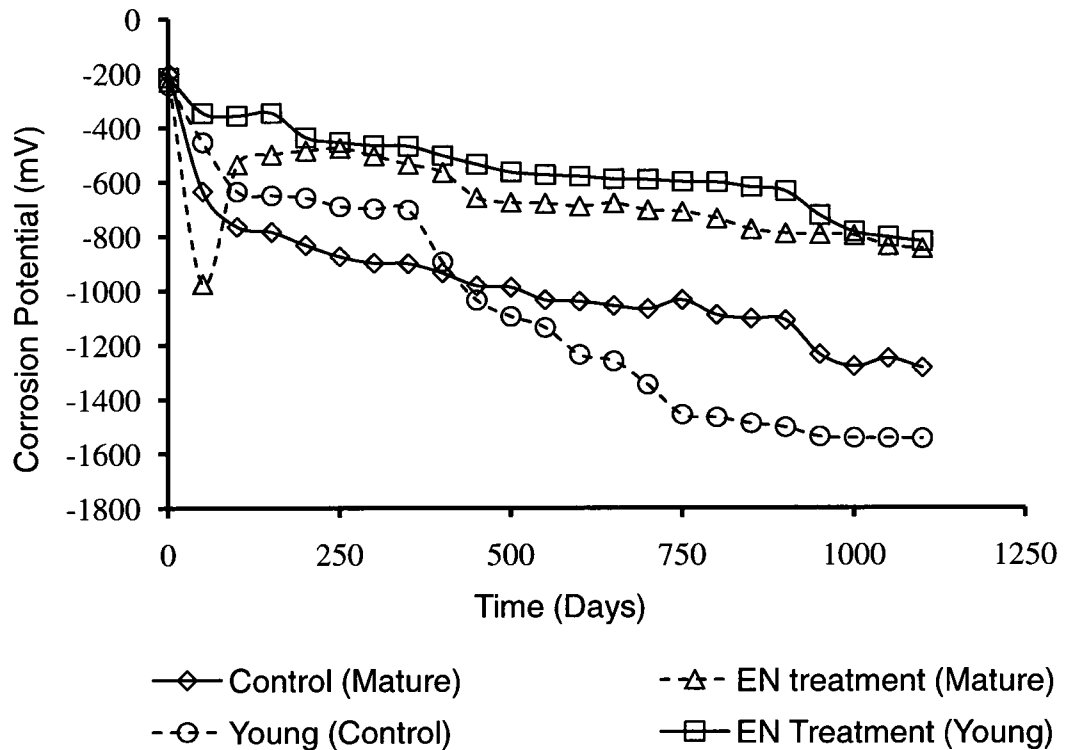


Fig 4.1 Corrosion potential of young and mature reinforced concrete

The corrosion current densities (I_{corr}) were measured following 250, 500, 750 and 1100 days of saltwater exposure, using the linear polarization resistance (LPR) technique (refer to Figure 4.2). Average I_{corr} values of $57 \mu A/cm^2$ and $1.3 \mu A/cm^2$ were observed in the young and mature controls respectively after 250 days of exposure, while the young and mature EN Treated specimens showed 0.2 and $0.7 \mu A/cm^2$ respectively.

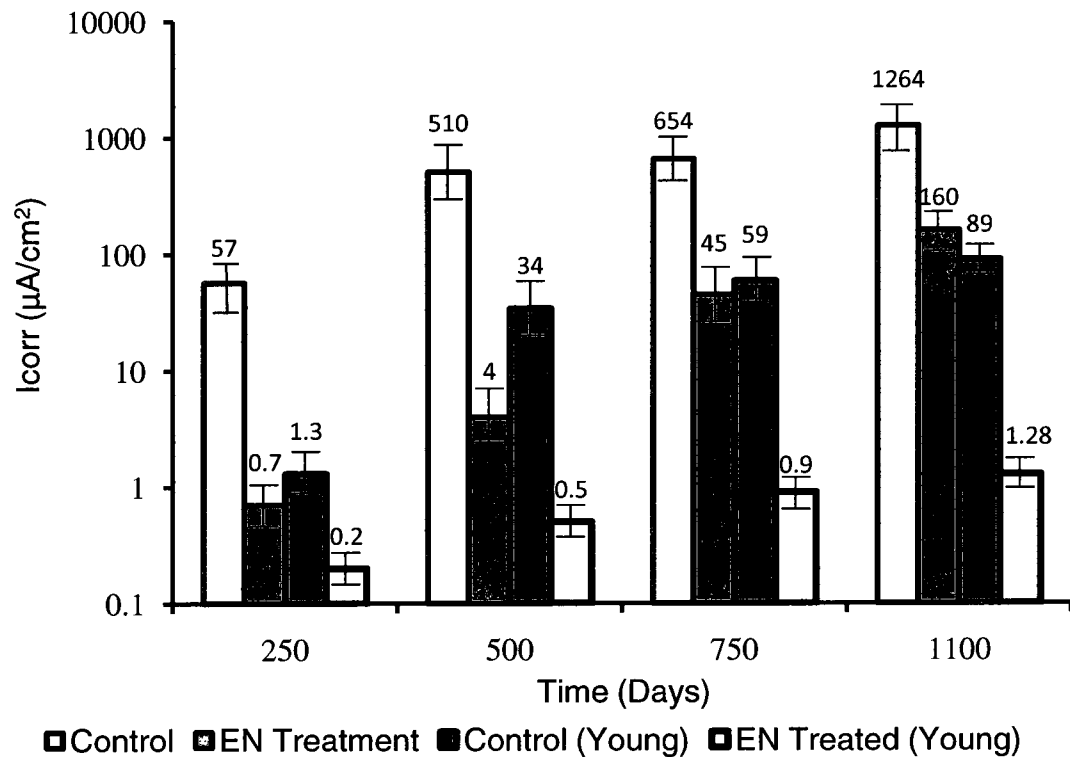


Fig 4.2 Corrosion current densities using LPR method on young and mature specimens

Comparison of the I_{corr} with the reference values of Table 4.1 shows that the reinforcement of the untreated controls was highly corroded as compared to the EN treated specimens which exhibited low to moderate corrosion. High I_{corr} values of 1264 and $89 \mu\text{A}/\text{cm}^2$ for the mature and young controls were significantly higher than the respective EN treated specimens (160 and $1.28 \mu\text{A}/\text{cm}^2$) at the end of 1100 days of exposure. These values indicate that the mature and young EN treated specimens exhibited lower corrosion rates by factor of 8 and 74 as compared to their respective untreated controls. The corrosion rates on the EN treated specimens were observed to increase in

course of the post salt water exposure. The chloride diffusion through the annulus of the pore wall when viewed theoretically is shown in Figure 4.3.

Table 4.1 Interpretation of corrosion current density with corrosion (Adapted from Broomfield, 1997)

Corrosion Current Density ($\mu\text{A}/\text{cm}^2$)	Corrosion
< 0.1	Negligible
0.1-0.5	Low
0.5-1.0	Moderate
> 1.0	High

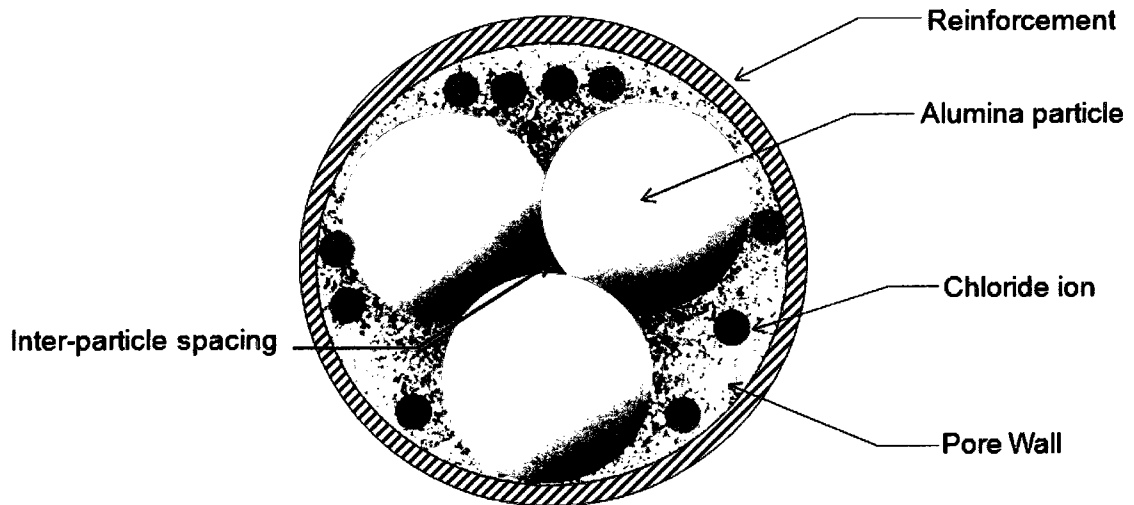


Fig 4.3 Chloride diffusion through pore wall

During EN treatment it was not likely that all the nanoparticles reacted with calcium hydroxide and got converted to C-S-H and C-A-H. The unreacted nanoparticles were able to bind together and act as a protective barrier against chloride diffusion. The 0.1 nm interparticle spacing between the nanoparticles inhibited the chloride migration (Kanno et al., 2009). It is conceivable that chlorides migrated through the annulus between the nanoparticles and the pore

wall, which could be the reason why the increase in corrosion among the EN treated specimens was observed. Studies have reported that indicate the effectiveness of chloride extraction was 40 % after seven weeks (Orellan et al., 1994). It is possible that non-extracted chlorides could have also caused the increase in corrosion rates observed among the EN treated specimens.

An increase in chloride content may also be due in part to the possibility of bound chlorides (Ann and Song, 2007). Chlorides are present as free and bound chlorides. Bound chlorides are interblended with the cement matrix, and are relatively immobile in nature. The chloride contents which are mobile and that can be extracted from the pore solution are known as free chlorides. The increase in chlorides can be associated with the release of bound chlorides due to the process of carbonation. Carbonation could have caused a rise of chloride contents, among the EN treated and control specimens.

4.1.2 Chloride Diffusion Coefficients

The chloride diffusion coefficients for reinforced concrete specimens are shown in Figure 4.4. Diffusion coefficients of $2.34 \times 10^{-14} \text{ m}^2/\text{s}$ (Young EN Treated), $6.50 \times 10^{-13} \text{ m}^2/\text{s}$ (Mature EN Treated), $2.30 \times 10^{-13} \text{ m}^2/\text{s}$ (Young Control) and $8.69 \times 10^{-12} \text{ m}^2/\text{s}$ (Mature Control) were observed. Bentur and others obtained a chloride diffusion coefficient for unprotected concrete (0.5 w/c ratio) of $1.63 \times 10^{-12} \text{ m}^2/\text{s}$ (Bentur et al., 1997). This diffusion coefficient was estimated to result in corrosion initiation in 17 years. This value was used in the current study as a bench mark for assessing chloride diffusion coefficients. The mature control specimens exhibited higher chloride diffusion coefficients as compared to

this benchmark level where as the young control specimens ($3.24 \times 10^{-12} \text{ m}^2/\text{s}$) did not exceed this benchmark until after 500 days of saltwater exposure. In contrast, the EN treated specimens exhibited significantly lower diffusion coefficients as compared to the benchmark, indicating that the nanoparticles would be expected to inhibit the re-entry of chlorides.

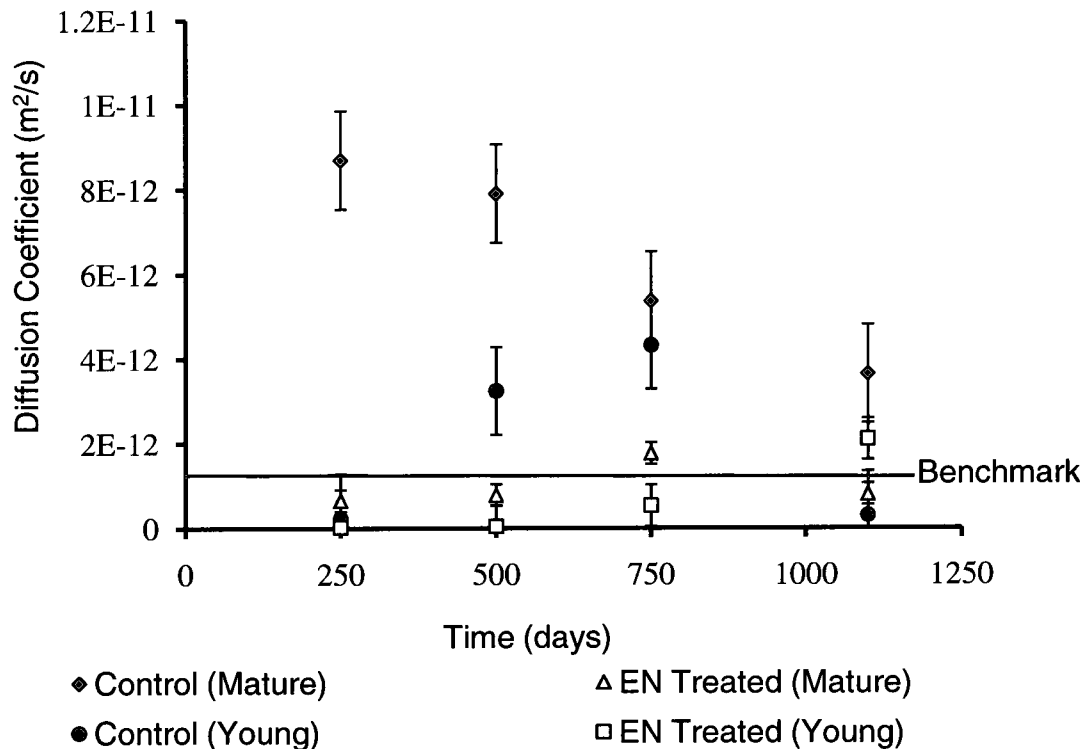


Fig 4.4 Chloride diffusion coefficients using electrochemical Impedance spectroscopy (EIS) for young and mature concrete

The capillary pores of the control specimens were empty and this susceptible to chloride diffusion as shown in Figure 4.5. Initially the chlorides diffuse rapidly and fill up the pore space. The diffusion efficiency decreases since the pores are already filled with the chloride ions, and over time it reaches

a threshold limit. At this limit, the chloride ions cannot diffuse as the pores are filled with chloride ions and thus inhibit further chloride ion migration.

An increase in the chloride diffusion coefficient was also observed among the EN treated specimens but was below the threshold limit of $1.63 \times 10^{-12} \text{ m}^2/\text{s}$ (Bentur et al., 1997).

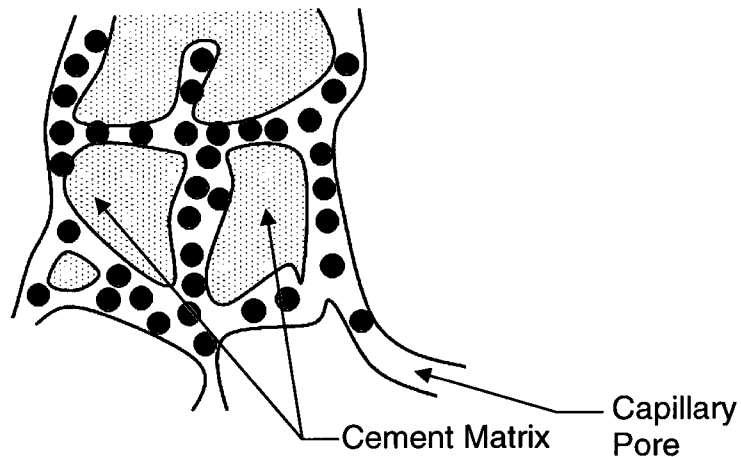


Fig 4.5 Concept of chloride diffusion into capillary pores

4.1.3 Corrosion Product, Porosity and Strength Analysis

The mature control specimens and EN treated specimens are shown in Figure 4.6 after 1100 days of saltwater exposure. The controls exhibited corrosion induced cracking whereas the EN treated specimens exhibited no signs of cracking. Images of the steel bars removed from the mature specimens after the splitting tensile test are shown in Figures 4.7 and 4.8. The mature EN treated specimens exhibited corrosion products covering an average of 14% of their surfaces while the control specimens showed an average corrosion product coverage of 99% (refer to Figure 4.7). Young EN treated concrete exhibited a

0.3% corrosion product coverage (see Figure 4.8). In comparison, the young untreated controls had a corrosion product coverage that averaged 96 %. Based on these observations, the EN treatment was found to inhibit the return of chlorides and significantly slowed the reinforcement corrosion rate in concrete. Results for splitting tensile strength, porosity, pH and corrosion rates are shown in Table 4.1. The mature EN treated specimens exhibited a 50% increase in strength while the young EN treated specimens showed a 14% increase in strength as compared to their respective controls.

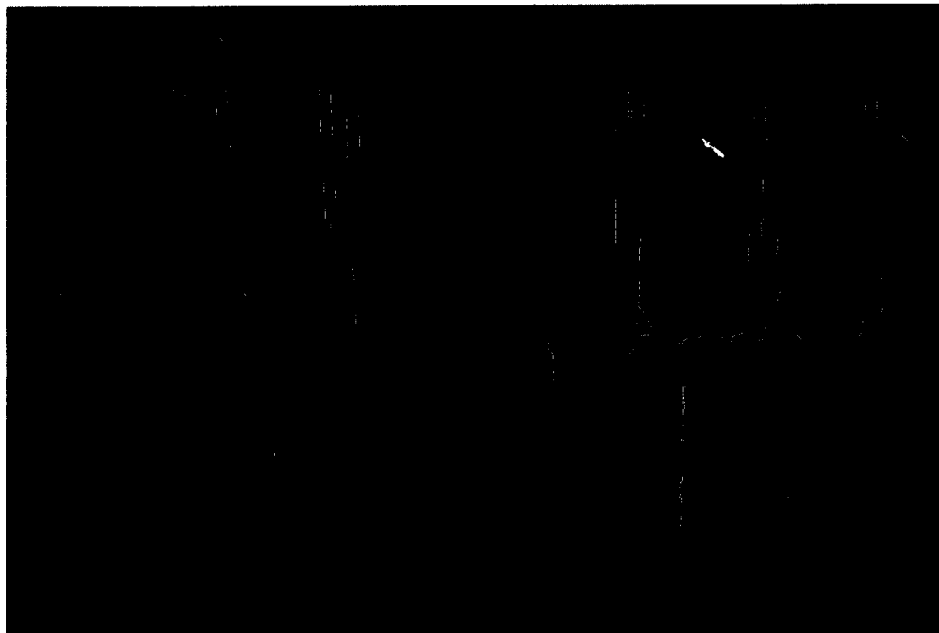


Fig 4.6 Front view of the mature un-cracked EN treated cylindrical specimens and cracked controls

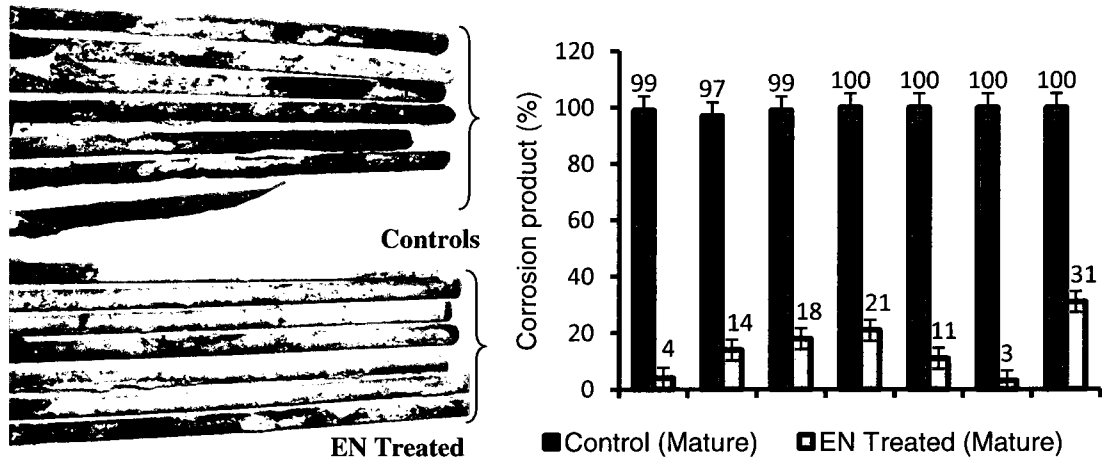


Fig 4.7 Corrosion product coverage areas measured on steel bars taken from control specimens and EN treated specimens of mature concrete

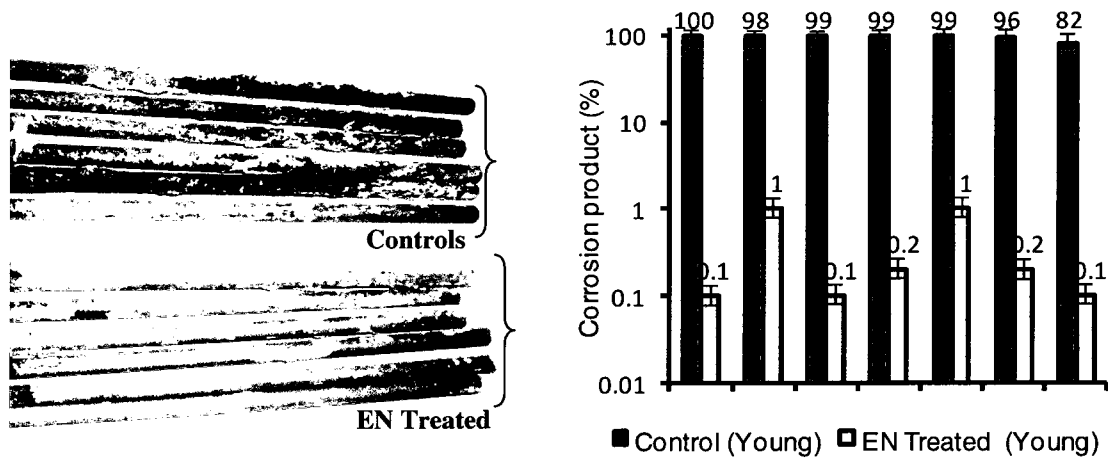


Fig 4.8 Corrosion product coverage areas measured on steel bars taken from control specimens and EN treated specimens of young concrete

The mature and young EN treated specimens exhibited 8% and 5% porosities respectively, while the controls exhibited respective values of 11 and 9%. The mature and young EN treated specimens yielded porosity reductions of 27% and 44% as compared to the untreated controls. pH values of 11.3 (mature) and 11.8 (young) were observed among the EN treated specimens. The controls

showed values of 8.1 (mature) and 8.4 (young). For comparison, the threshold pH value for corrosion initiation is 11.0 (Broomfield, 1997). This indicates that EN treatment was effective in keeping the pH value above the significant corrosion initiation limit, and hence slowing the carbonation process. The corrosion rates at the end of 1100 days of post treatment saltwater exposure are also shown in Table 4.2.

Table 4.2 Strength, porosity and corrosion analysis

Treatment Type	Strength (psi)	Porosity (%)	pH	Corrosion Covered Area (%)	Corrosion Rate (mpy)
Control (Mature)	263	11	8.1	99	517
EN Treated (Mature)	535	8	11.3	15	66
Control (Young)	583	9	8.4	96	37
EN Treated (Young)	680	5	11.8	0.3	0.5

The mature control and EN treated specimens exhibited high corrosion rates at the end of post treatment saltwater exposure period. These specimens were exposed to one year of wet-dry salt water exposure before receiving EN treatment. It is conceivable that the relatively short duration of the treatment was probably insufficient to remove enough chlorides needed for protection since most chloride extraction operations run six-eight weeks. In contrast, the young EN treated specimens exhibited lower corrosion rates by a factor of 74 at the end of post saltwater exposure. These specimens had much less opportunity to absorb large quantities of chloride. Based on these observations, it appears that

the porosity and corrosion results indicated that the EN treatment was effective in sustaining an elevated pH while reducing the corrosion rates, presumably through a reduction in porosity.

4.1.4 Chloride Content Analysis

The chloride contents at various distances from the rebar are shown in Figure 4.9. The young and mature control specimens exhibited chloride contents of 0.16 and 0.21% by mass of cement. The allowable threshold chloride content as per ASTM C 1152 is 0.10%. In contrast, the chloride contents of 0.01% (mature EN treated) and 0.03% (young EN treated) were well below the allowable threshold level of 0.10% by mass of cement. In considering the chloride diffusion coefficients from Figure 4.4 together with these chloride contents, it is clear that the EN treatment was effective in retarding the ingress of chlorides during the post treatment saltwater exposure period.

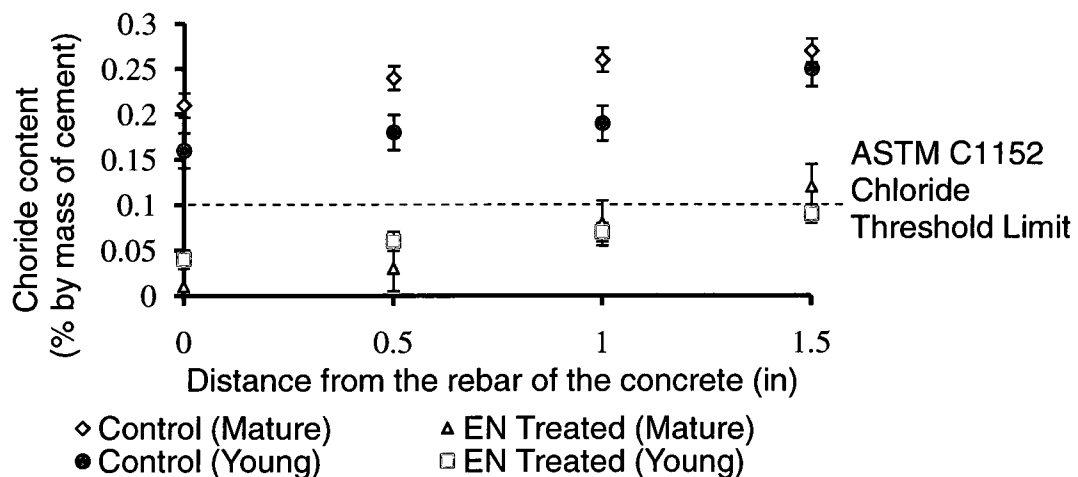


Fig 4.9 Variation of chloride contents with distance from the reinforcement

The chloride content for all the cases was higher at 1.5 in away from the reinforcement as compared to that adjacent to the rebar. It appears that the porosity at the rebar for EN treated specimens is reduced due to the particle packing and related porosity reduction. In the case of the controls the chloride content is much higher at the cover and the content decreases due to the tortuous path (twisted path) of the capillary pores. EN treatment appeared to cause porosity reduction and thus inhibited the ingress of the chlorides.

4.1.5 Microstructural Analysis

In Figure 4.10, scanning electron microscopy (SEM) conducted on the control specimens indicated the presence of ettringite needles in the vicinity of hexagonal shaped calcium hydroxide (Taylor, 1997). The further magnified image of ettringite is shown in Figure 4.10 B. Figures 4.11 A (Untreated) and B show an EN treated specimen with a dense morphology at the rebar concrete interface, as compared to the more porous control specimens. The dense morphology indicates that the EN treatment was effective in reduction of porosity and increasing strength.



Fig 4.10 A. Ettringite in the presence of calcium hydroxide of mature concrete. B. Ettringite needles in the mature concrete specimens

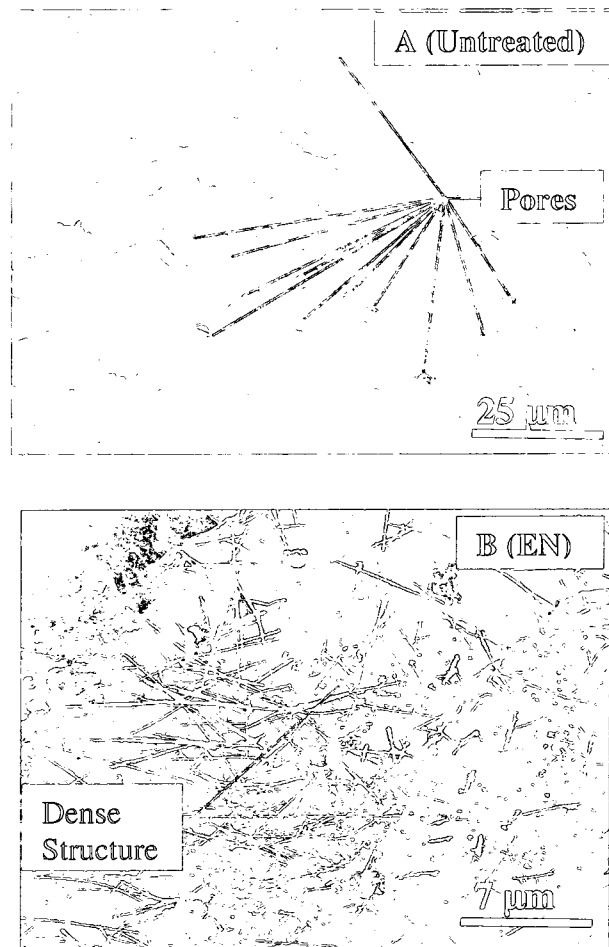


Fig 4.11 Morphology of untreated specimens compared to EN treated specimens that exhibited a more dense morphology

Figure 4.12 shows how the polished young EN treated specimen exhibited the presence of calcium silicate hydrate (C-S-H) inter-percolated with calcium carbonate (manifesting as a white powdery phase). The Energy Dispersive Spectroscopy (EDS) analysis indicates peaks of alumina, silica, calcium, chlorine, oxygen and carbon. This evidence together with the earlier noted pH value of 8.1 (which is below the threshold limit of 11 for corrosion initiation) further supports the suspected carbonation process.

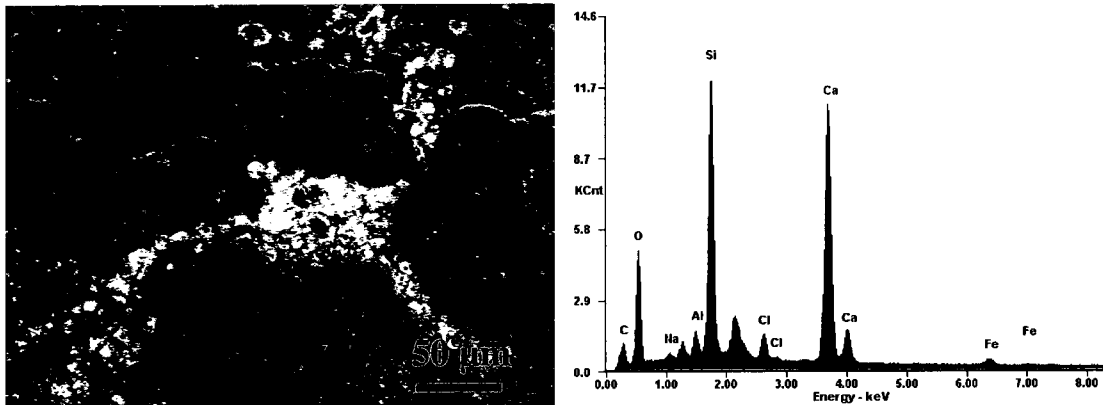


Fig 4.12 Backscattered electron image (BSE) of a young EN treated specimen. Brighter regions indicate C-S-H mixed with calcium carbonate

SEM micrograph of a polished untreated young control specimen shows the presence of chloride peaks but no aluminum peaks, as shown in Figure 4.13. Backscattered electron image (BSE) imaging confirms the presence of dicalcium aluminate hydrate (C_2AH_8) inside the pore (refer to Figure 4.14). The curving striated needles of dicalcium aluminate hydrate is shown at higher magnification in Figure 4.15. While the nanoparticles appear to act as pore blocking agents, they also appear to be forming strength increasing phases such as C_2AH_8 .

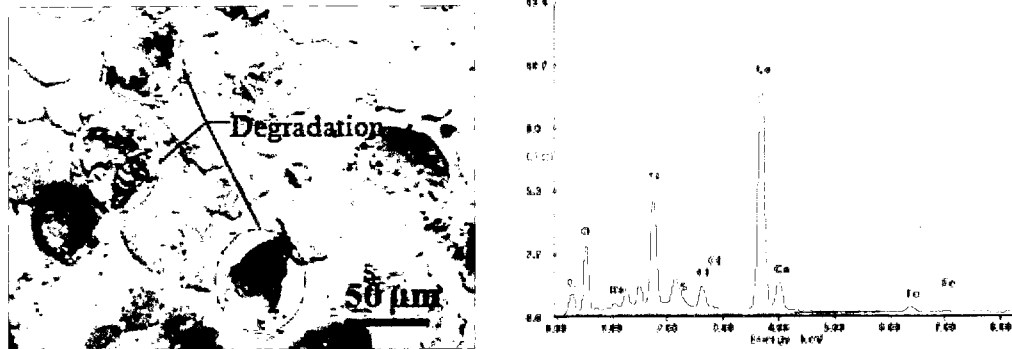


Fig 4.13 Backscattered electron image (BSE) of a young control specimen showing degradation and EDS spectrum

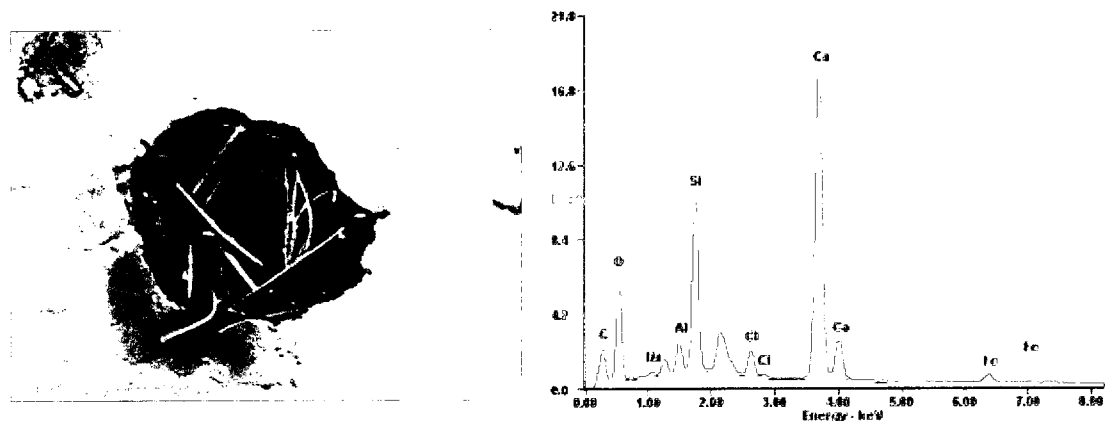


Fig 4.14 Presence of dicalcium aluminate hydrate (C_2AH_8) on young EN treated specimens



Fig 4.15 Magnified image showing striated needles of dicalcium aluminate hydrate (C_2AH_8)

4.1.6 FTIR and Raman Spectra Analysis

Fourier transform infra-red (FTIR) spectra are shown in Figure 4.16. The mature and young EN treated specimens exhibited strong broad peaks ranging from 3400 to 3600 cm^{-1} , which indicate calcium aluminate hydrate (C-A-H), while the untreated controls did not show any such peaks in this region (Fernandez-Carrasco et al., 2008; Yu et al., 1999). Based on these observations, it appears that the alumina coated silica nanoparticles reacted with the calcium hydroxide, forming C-A-H phases which can be metastable and strength enhancing phase.

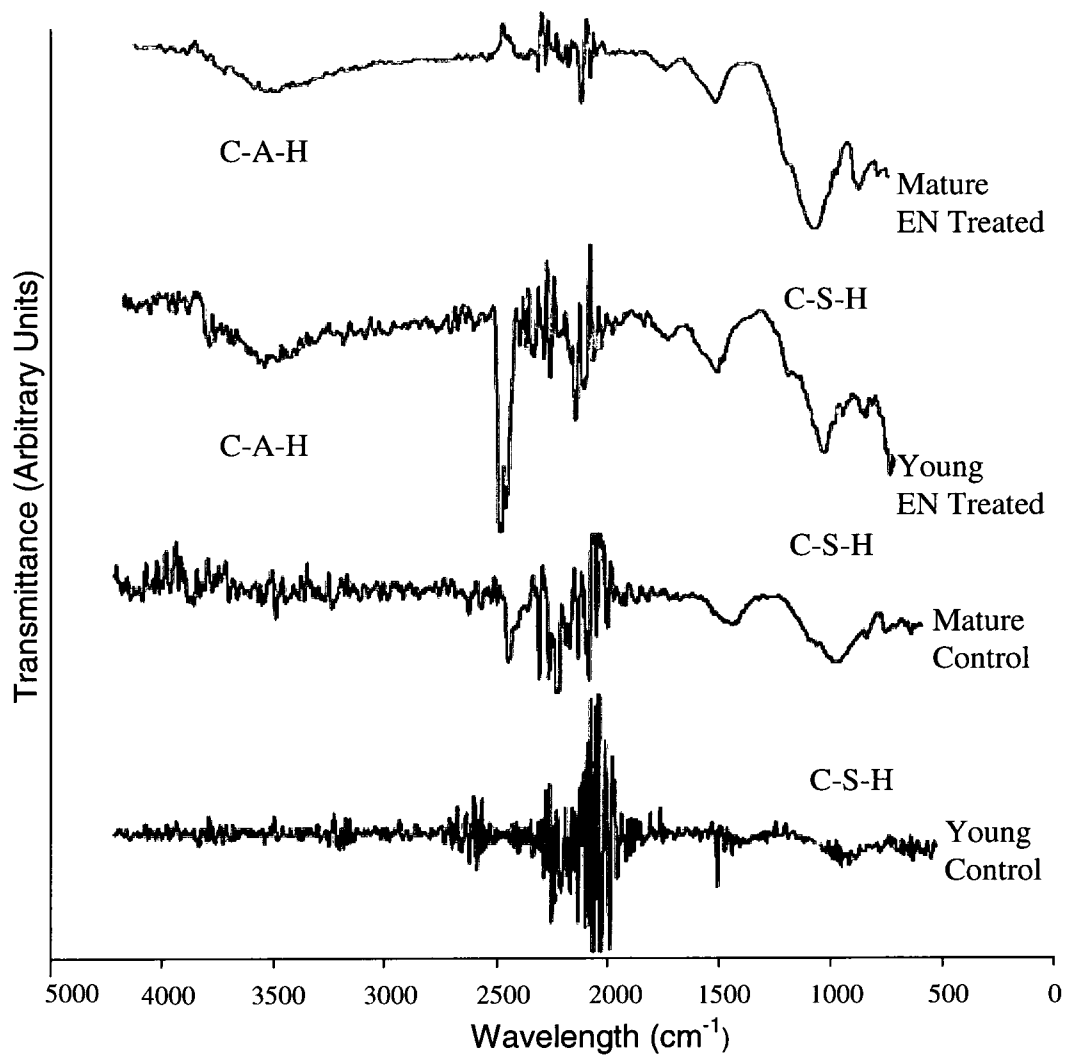


Fig 4.16 Fourier transform infrared spectroscopy (FTIR) of EN treated and control specimens

4.1.7 XRD Analysis

X-Ray diffraction results indicated the presence of gehlenite hydrate (C_2ASH_8) and C-S-H on the young EN treated specimens while both the young and mature EN treated specimens showed the presence of xonotlite, as shown in Figure 4.17. Gehlenite hydrate is formed by the reaction of silicate ions with the calcium aluminate hydrate phases (Taylor, 1997). Unidentified phases may also

be formed by the combination of C-S-H and aluminium rich gel. Further study is required to elucidate these phases. Xonotlite forms as a hydration product of semi-crystalline C-S-H (Nocun-Wczelik, 1999). Additionally, tobermorite can be gradually transformed into xonotlite at elevated temperatures. The EN treated specimens also exhibited ettringite ($6\text{CaO}\cdot\text{Al}_2\text{O}_3\cdot 3\text{SO}_3\cdot 32\text{H}_2\text{O}$). The untreated controls also exhibited the presence of C-S-H, calcium hydroxide and ettringite. Based on these observations, the EN treatment using alumina coated silica nanoparticles was successful in reducing reinforcement corrosion in concrete by blocking pores and by producing porosity reducing phases, such as calcium aluminate hydrate (C-A-H) and C-S-H.

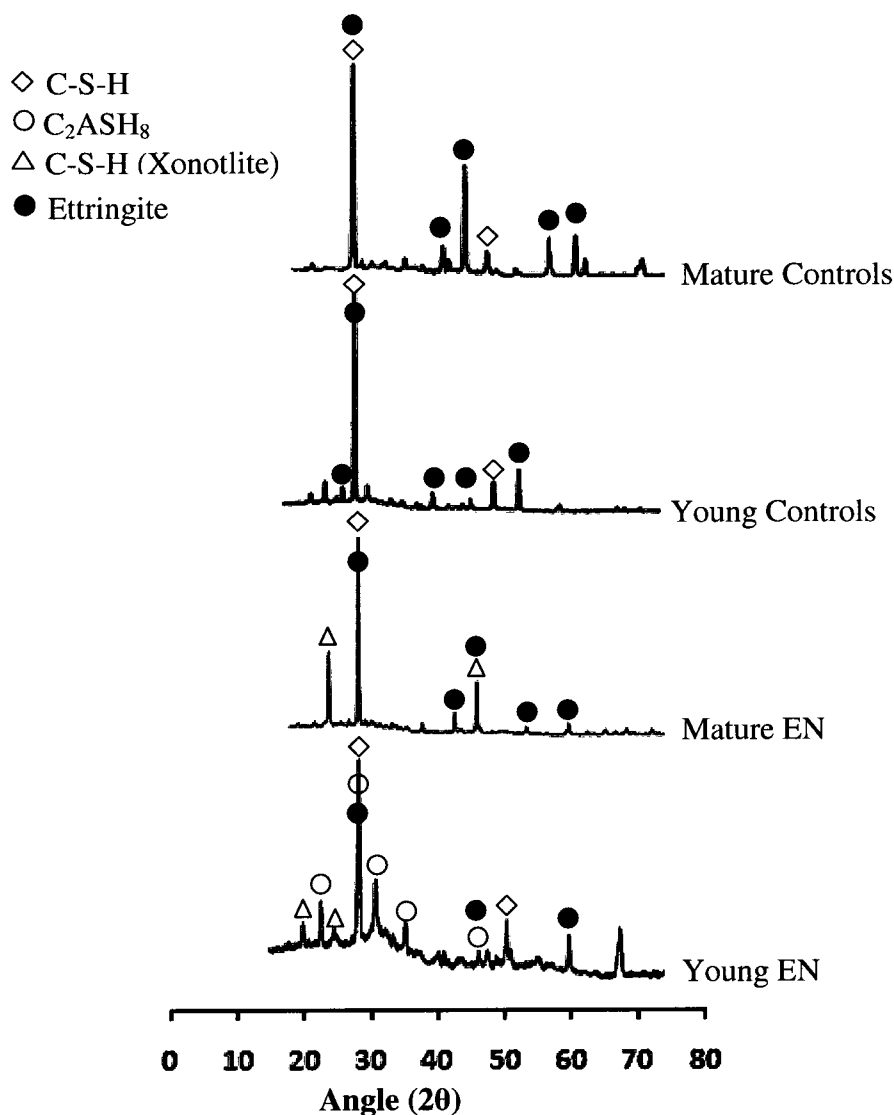


Fig 4.17 XRD data of EN treated and control specimens

4.1.8 Summary of Findings for Young and Mature RC Specimens

This section dealt with mitigation of corrosion in young and mature cylindrical reinforced concrete specimens. The mature and young EN treated specimens showed a reduction in corrosion rates by a factor of 8 and 74 as compared to their untreated controls. The corrosion potential of the EN treated specimens was also much lower as compared to their untreated controls. This

concept of inhibiting corrosion using nanoparticles was also applied to specimens whose geometry simulates a bridge deck. An experimental study was undertaken to examine the influence of EN treatment on dealing with the corrosion issues of bridge decks. Detailed conclusions from this section (4.1) are presented in Chapter 5.

4.2 EN Treatment of ASTM G109 Specimens

ASTM G109 specimens were used in this work as they simulate the configuration of the bridge deck. Nanoparticles were driven directly through the concrete matrix and to the reinforcement using an electric field (Kupwade-Patil and Cardenas, 2008). The intent was to use the nanoparticles as pore blocking agents that could prevent chlorides from re-entering and accessing the rebar. It was hypothesized that the particles could form a densified nanostructural barrier within the pores. ASTM G109 specimens were used in this work. These specimens tend to simulate the corrosion behavior of reinforcement in bridge decks when subjected to elevated chloride levels. In this study, corrosion behavior was evaluated using corrosion potentials, polarization resistance, and linear polarization techniques. The specimens were subjected to standard wet-dry cycles of saltwater exposure for 1 year. Following this period the nanoparticle treated specimens exhibited corrosion rates of 0.15 mils per year (mpy), 26 times lower than observed among the untreated specimens. Electrokinetic Nanoparticle (EN) treatment using alumina-coated silica nanoparticles (24 nm in size) was successful in mitigating reinforcement corrosion in concrete.

Section 4.2 was published by Kupwade-Patil and Cardenas, as “Corrosion mitigation in concrete using electrokinetic injection of reactive composite nanoparticles” in the Proceedings of International Conference on Advancement of Material and Process Engineering, Long Beach, CA, May 2008. The primary work was done by the author under the guidance of Dr. Henry Cardenas.

4.2.1 Corrosion Potential

Figure 4.18 contains a plot of the corrosion potential as observed during this study. The horizontal axis lists the time, and the vertical axis is the corrosion potential of the embedded steel. The corrosion potential measurements reported represent the average values for the three (one top and two bottom) bars among three specimens. A constant current density of one A/m^2 was maintained for the ECE and EN treatments. During the wet/dry saltwater exposure of the initial 60 days, the average corrosion potential dropped to -0.56 V. ECE treatment was carried out for a period of 14 days, causing the average corrosion potential to decrease to -1.05 V at the end of treatment. ECE treatment was also continued on the control specimens during this time since all the specimens (EN treated and control) held to matching time periods of chloride extraction and saltwater post exposure. During the ECE process, the chlorides were extracted from the specimen. Simultaneously, sodium, potassium and calcium ions residing in the concrete pore fluid were attracted to the rebar, causing it to behave somewhat like a sodium/potassium/calcium electrode, exhibiting a relatively negative corrosion potential as seen in Figure 4.18. EN treatment was carried out for 48 days. At the end of the EN treatment, a notable increase in the corrosion

potential was observed from -1.05 V to a peak of -0.29 V. At the end of the EN treatment period all the treatments were discontinued and the specimens were re-exposed to wet-dry cycles of saltwater for a period of 210 days.

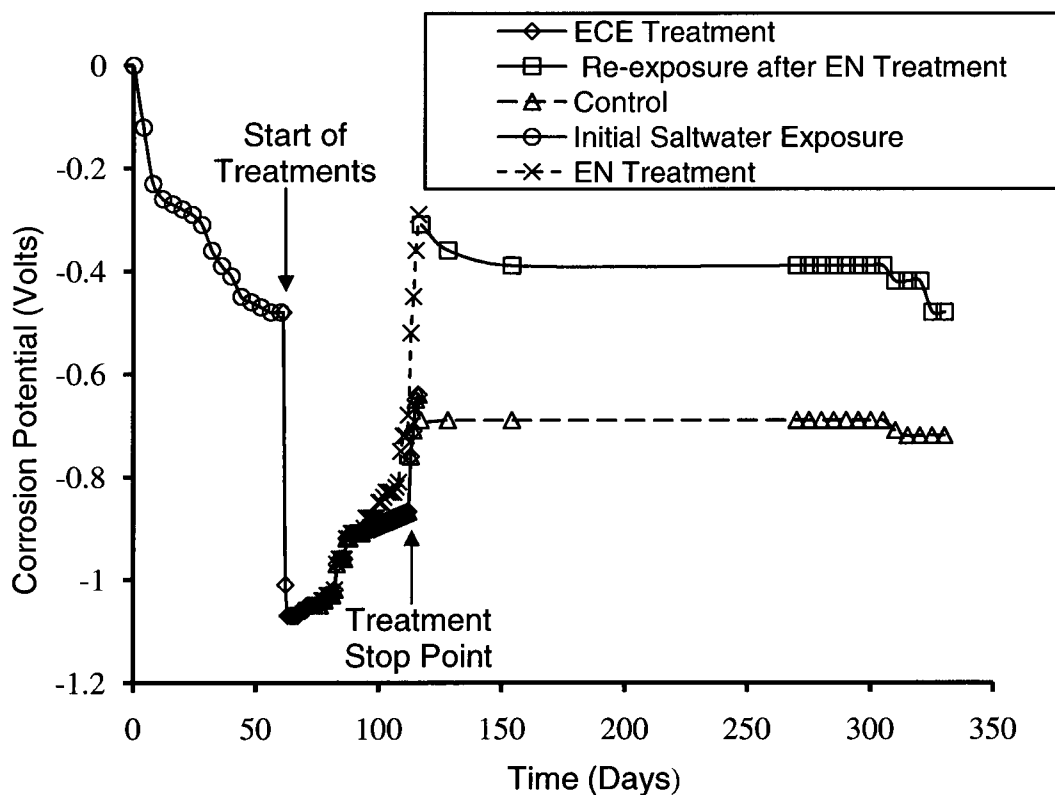


Fig 4.18 Corrosion potential plot of reinforced G109 specimens at different stages of the treatment

The increase in corrosion potential above the -0.4 V level may have been influenced by the increased alumina content provided by the EN treatment. Suryavanshi and others observed that elevated CAH content was associated with a relatively positive corrosion potential and the passivation of steel (Suryavanshi *et al.* 1998). One speculation is that the EN treatment may have induced a positive ionic precursor to CAH that could have contributed to the relatively

positive corrosion potentials (V_{corr}) observed during EN treatment. Such an ion would have exhibited some mobility to drift away from the steel after the treatment was discontinued, thus yielding a drop in corrosion potential. Further examination of this behavior is needed.

After the treatment was discontinued, the corrosion potential dropped back to -0.4 V. At this point, the influence of the Na^+ and K^+ ions that were drawn to the steel from the beginning of the treatment would be expected to resume their negative influence on the corrosion potential for some months. The controls exhibited a -0.70 V corrosion potential, as compared to the EN treated specimens (- 0.50 V) at the end of saltwater exposure. This implies that the EN treatment was effective in blocking the pores and impeding the chlorides from re-entering the specimen.

4.2.2 Corrosion Rates

The results obtained during the corrosion current density (I_{corr}) measurement of the rebars by linear polarization resistance are shown in Figures 4.19 and 4.20. An average I_{corr} of $2.6 \times 10^{-3} \mu\text{A}/\text{cm}^2$ for the EN treated top bars was observed as compared to the untreated controls ($0.7 \mu\text{A}/\text{cm}^2$). The bottom bars of EN treated specimens exhibited an I_{corr} of $1.3 \times 10^{-3} \mu\text{A}/\text{cm}^2$ while controls exhibited a rate of $0.13 \mu\text{A}/\text{cm}^2$. The severity of corrosion on the rebars was estimated based on the I_{corr} values using Table 4.1. The I_{corr} values of the EN treated specimens lie in the range of negligible corrosion. The I_{corr} values of the untreated controls exhibited moderate to high corrosion.

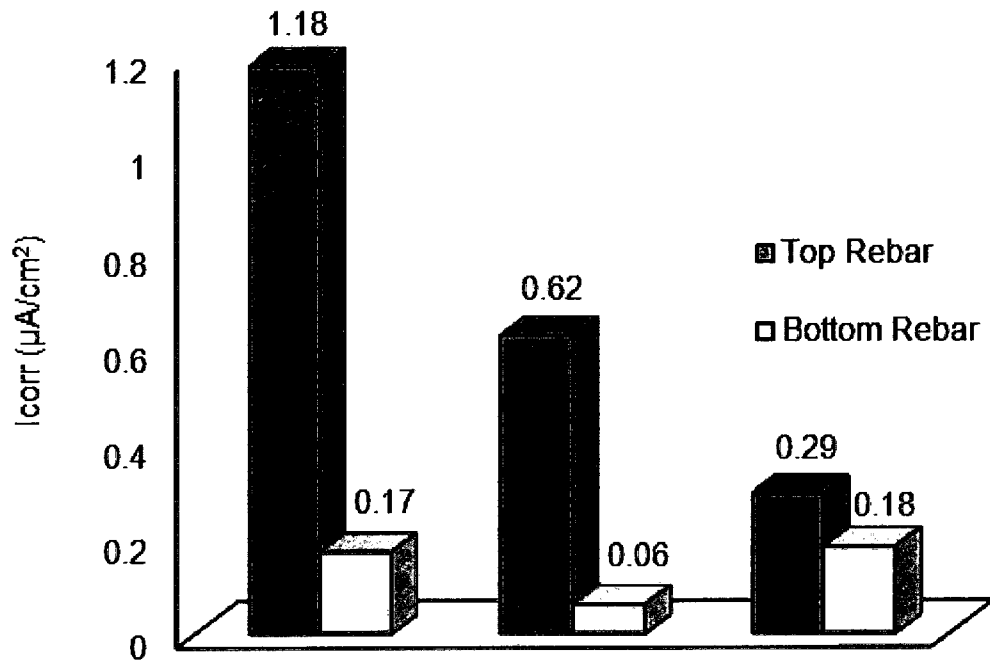


Fig 4.19 Corrosion current densities (I_{corr}) of control specimens

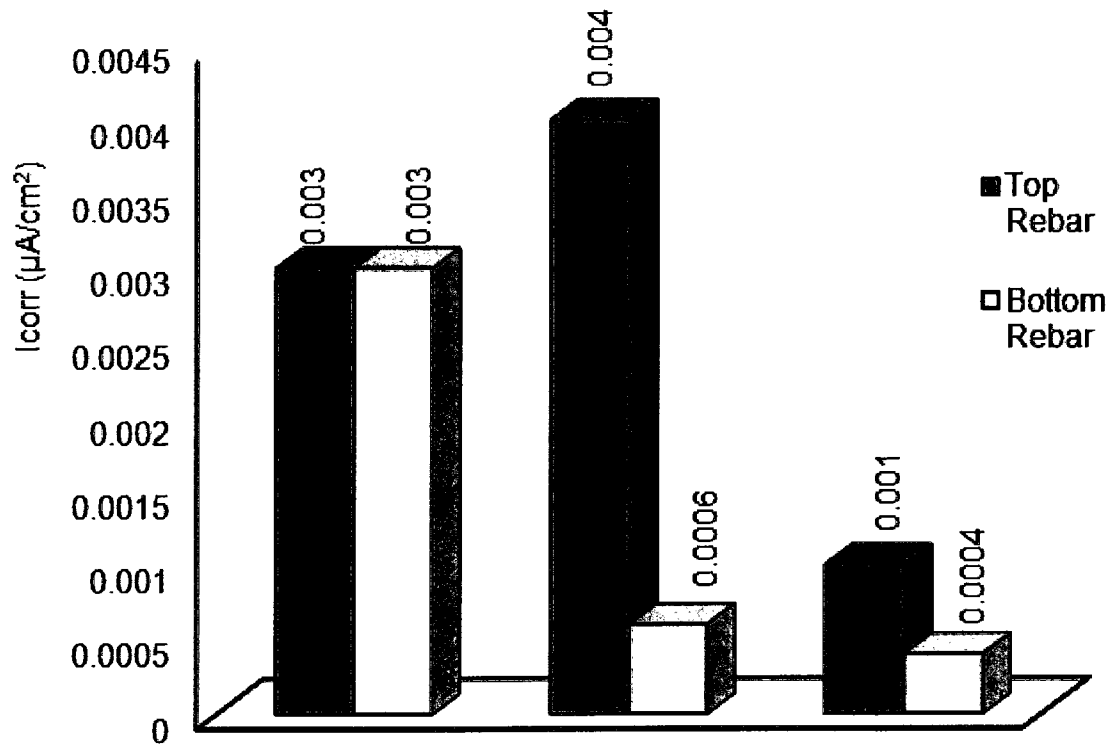


Fig 4.20 Corrosion current densities of EN treated specimens

The corrosion rates (top and bottom bars) using the LPR technique for the controls demonstrated a higher corrosion rate by a factor of 23 when compared to the treated specimens. Top bars exhibited 0.2 mpy while the bottom bars demonstrated 0.04 mpy for controls, as shown in Figure 4.21. For EN treated specimens, the top bars exhibited a slightly higher corrosion rate (0.005 mpy) compared to the lower bars (0.004 mpy). The chlorides likely maintained a higher concentration near the top because they were in the Plexiglass dam located at the top of the concrete specimen. It is thus not surprising that the top bars were surrounded by higher chloride content and higher corrosion rates.

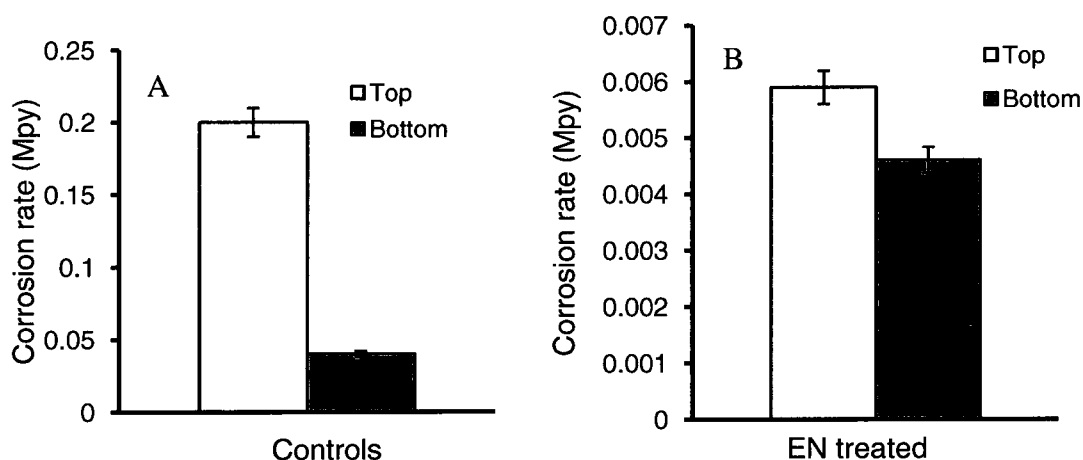


Fig 4.21 Corrosion rates of control (A) and EN (B) treated specimens

The mass loss rate (MR) data shown in Figure 4.22 was calculated using the value of I_{corr} . Average mass loss rates exhibited on the rebar of the controls was higher by a factor of 34 on the top bars and 20 for the bottom bars when compared to the EN treated specimens (see Figure 4.22). The upper bars of the controls thus appeared to have suffered significant mass loss compared to the bottom bars since they were more susceptible to chloride contact.

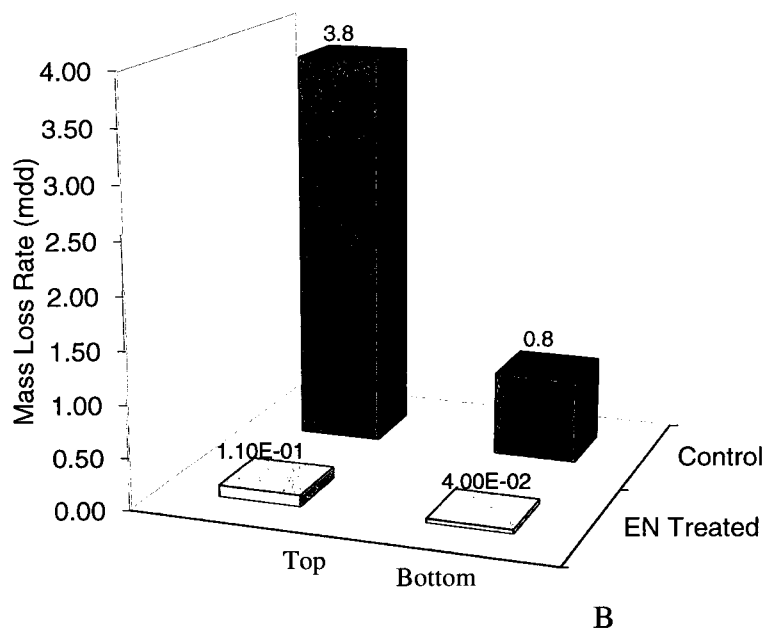


Fig 4.22 Mass loss rate of the top and bottom bars of control and EN treated specimens

The low corrosion current density (I_{corr}), corrosion rates, mass loss rate (MLR) values on treated specimens indicate that the reinforcement of the treated specimens was in a passive state and did not suffer corrosion damage due to the post saltwater exposure period.

4.2.3 Corrosion Plots

The total corrosion for the control and EN treated specimens are shown in Figures 4.23 and 4.24. The controls exhibited 1600 coulombs (average of three specimens) at the end of the 50th day of post saltwater exposure (refer to Figure 4.21). This value indicates low chloride ion penetrability while it moved up to 4209 coulombs after 100 days (refer to Table 4.3). Moderate chloride ion ingress was detected after 100 days and increased to high chloride ion penetrability mode at the end of 300 days (22867 coulombs).

Table 4.3 Guidelines for chloride-ion penetrability based on the charge passed as per ASTM C 1202

Charge passed (Coulombs)	Chloride-ion-penetrability
> 4000	High
2000 to 4000	Moderate
1000 to 2000	Low
100 to 1000	Very Low
< 100	Negligible

EN treated specimens exhibited 206, 330, 610 and 1832 coulombs after 50, 100, 150 and 300 days. EN treated specimens exhibited very moderate to low chloride ion penetrability as compared to the untreated control, which exhibited high chloride induced corrosion. These results indicate that the EN treated specimens may have the capability to hinder chloride ion transport by acting as a protective barrier.

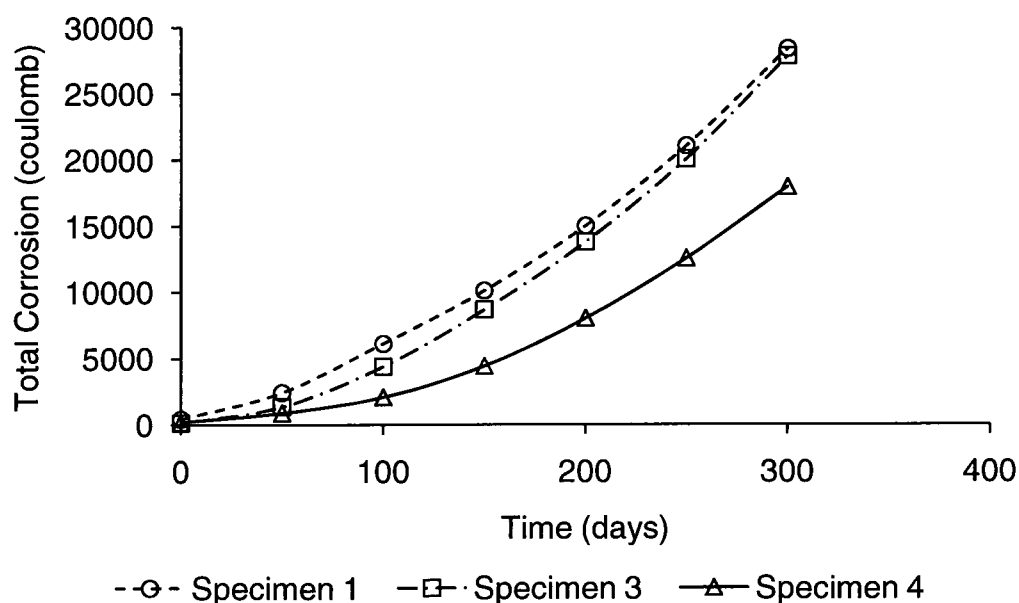


Fig 4.23 Total corrosion plot in terms of charge of coulombs for control specimens

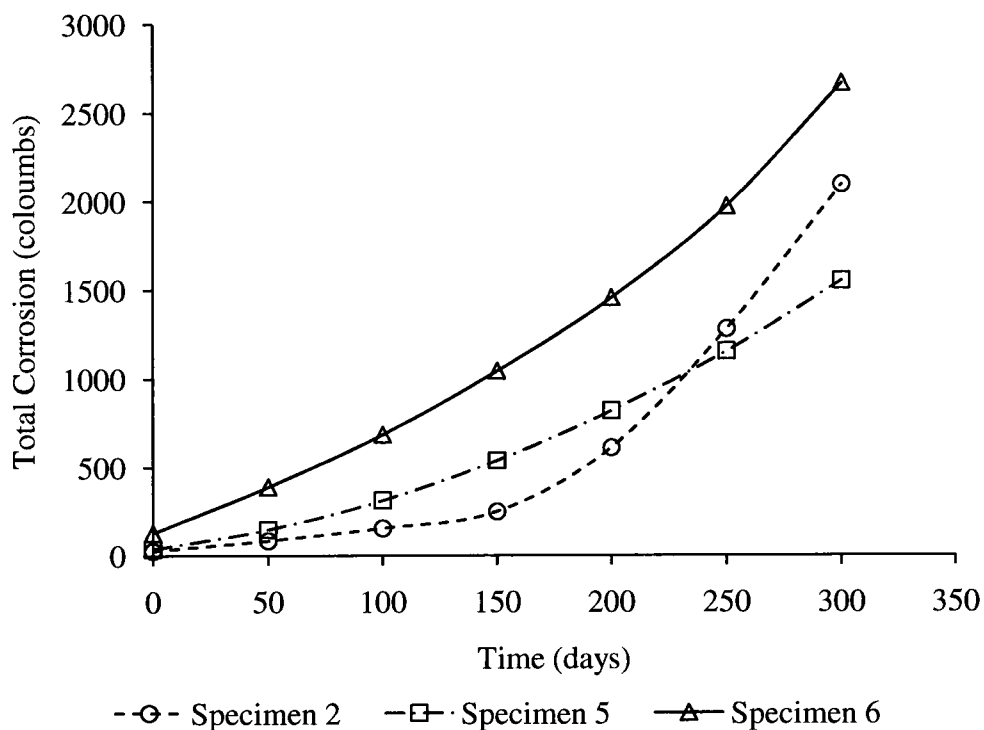


Fig 4.24 Total corrosion plot in terms of charge of coulomb for EN treated specimens

4.2.4 Electrochemical Impedance Spectroscopy

Corrosion analysis using electrochemical impedance spectroscopy (EIS) is discussed in this section. Nyquist plots of the control and EN treated specimens are shown in Figures 4.25 and 4.26. These plots consist of the real value of the impedance on the x axis and the imaginary value on the y axis. The EN treated specimens showed larger arc diameters as compared to the untreated controls, indicating relatively lower corrosion rates. In general the arc diameter decreases with, increase in corrosion rates (Zhang et al., 2001). The decrease in arc diameter indicates a lesser value of linear polarization resistance (R_p). The R_p is inversely proportional to the corrosion current density (I_{corr}). Thus the higher the

R_p value the lower will be the I_{corr} and corrosion rates, as shown in Equations 30 and 31.

A plot of the modulus of impedance versus resistance is shown in Figure 4.27. The controls demonstrated a flat curvature as compare to the EN treated specimens. The curves start to become flatter as corrosion increases (John et al., 1981; Wang et al., 1998; Zhang et al., 2001). Figure 4.28 represents the plot of frequency versus the phase angle. The drop in peak phase angle is attributed to the increase in corrosion rates. The controls exhibited a decrease in phase angle value by ~ 30 degrees indicating high active corrosion on the reinforcement.

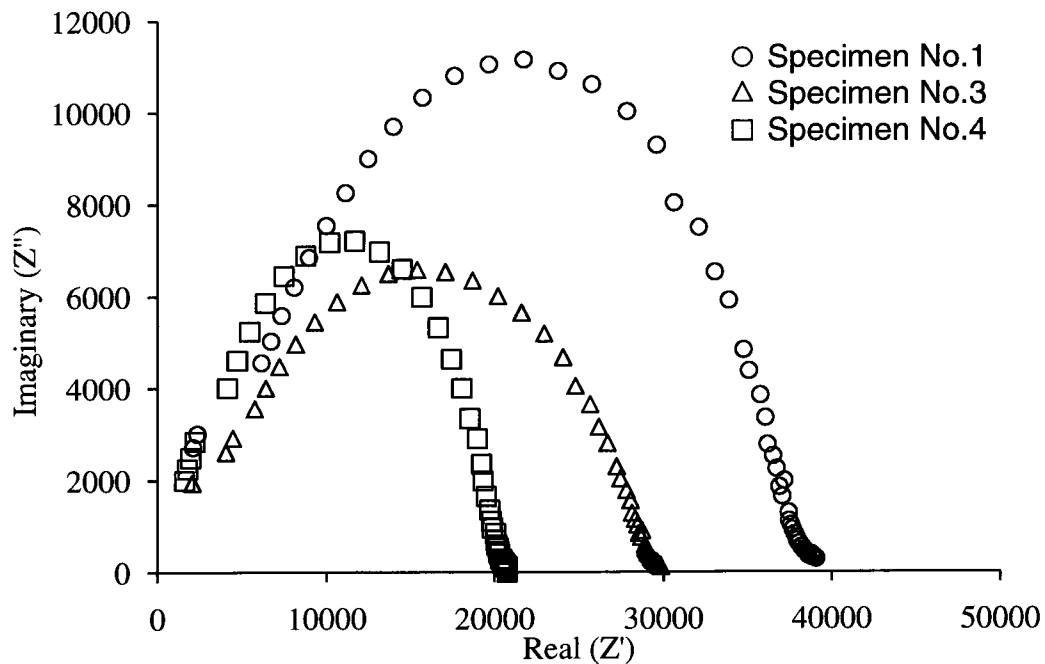


Fig 4.25 Nyquist plot of control specimens

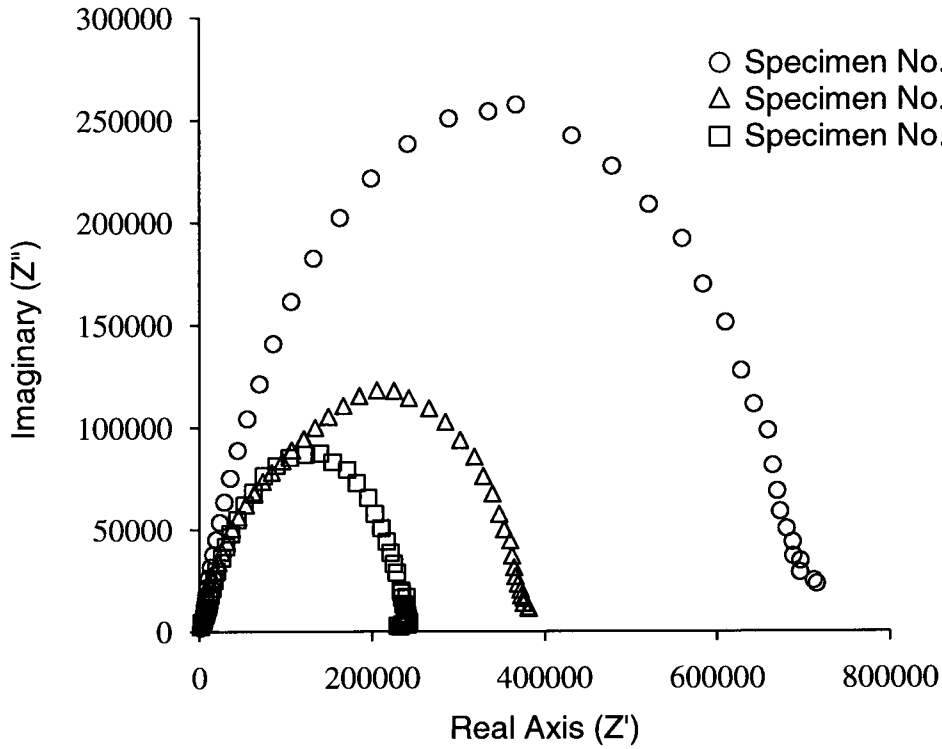


Fig 4.26 Nyquist plot of EN treated specimens

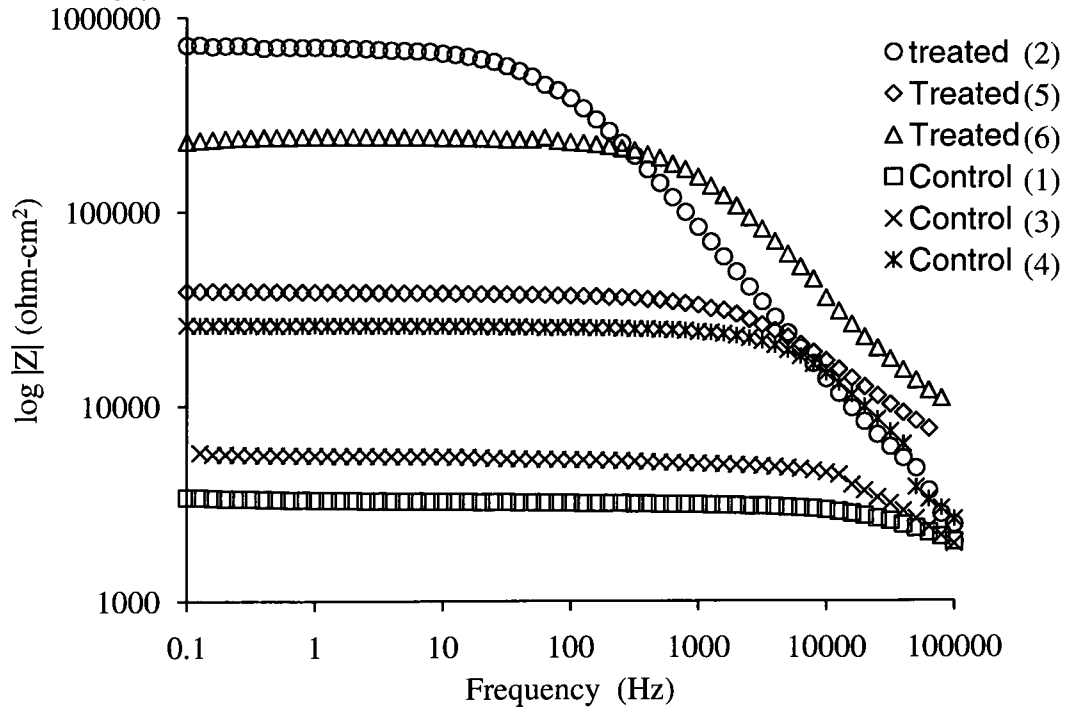


Fig 4.27 Resistivity spectra of $\log |Z|$ versus frequency (Hz)

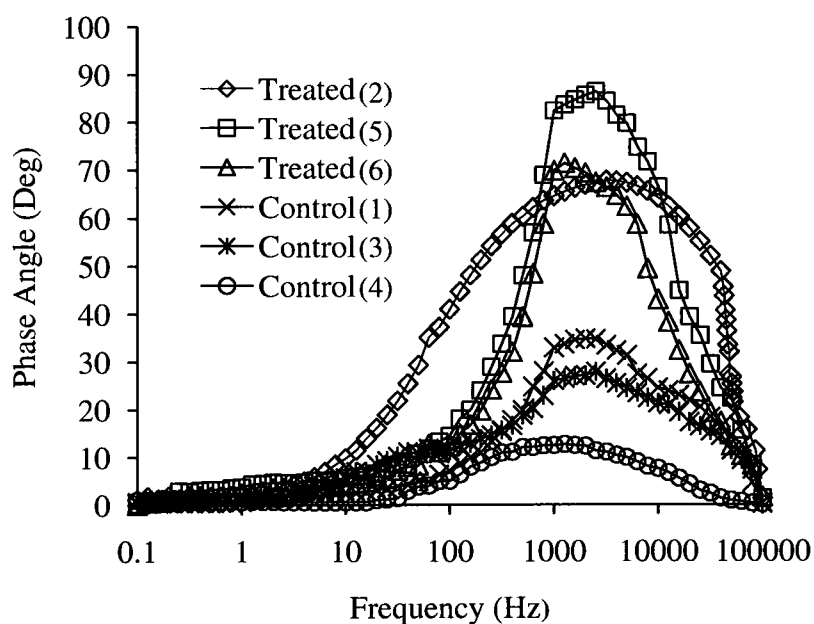


Fig 4.28 Phase versus log of frequency

4.2.5 Visual and Corrosion Product Analysis

Serious cracking in the concrete cover was observed on the control specimens after seven months of saltwater re-exposure (See to Figures 4.29. A and 4.29 C). No signs of cracks were observed on the EN treated specimens. This is in agreement with the results of corrosion potentials, corrosion rates and electrochemical impedance spectroscopy analysis as shown in Sections 4.21-4.24.

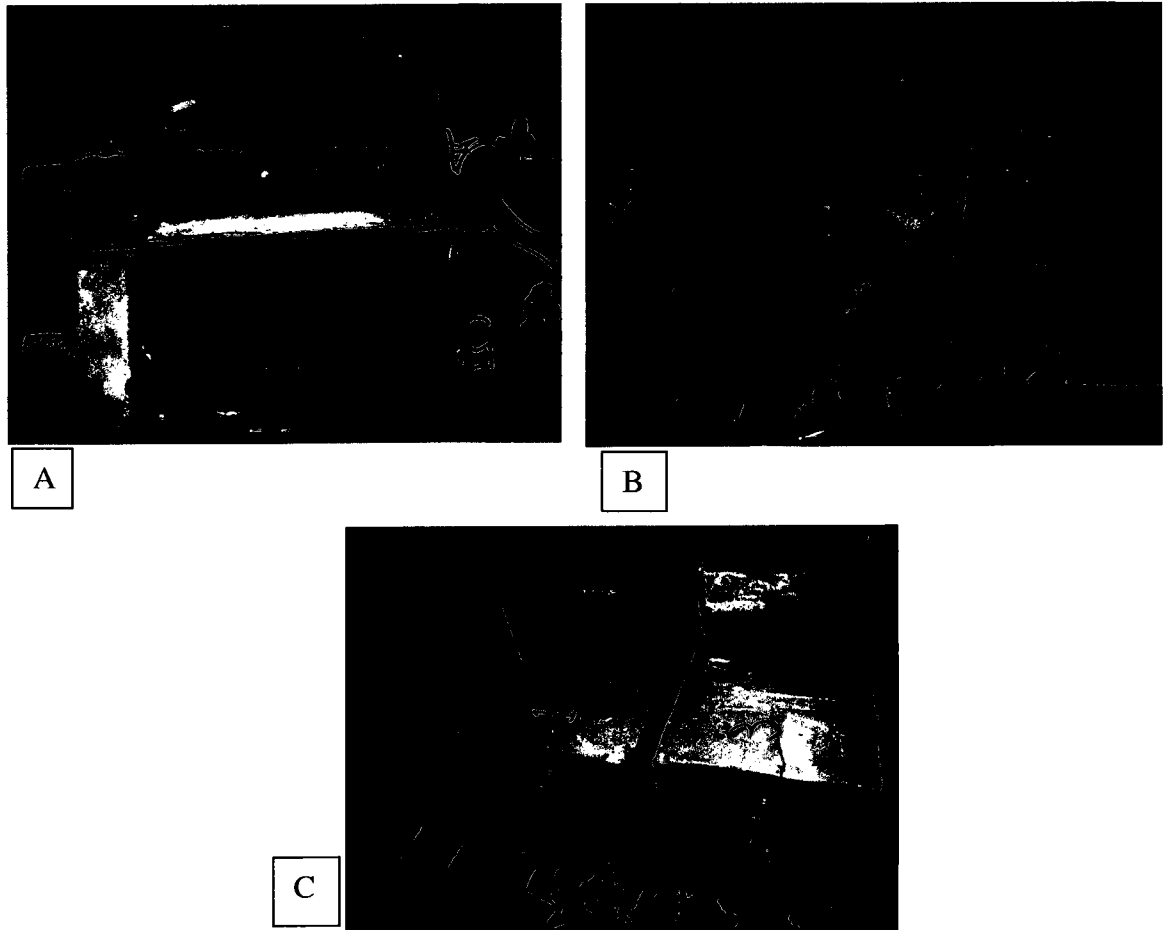


Fig 4.29 A. Top view of a cracked control and an un-cracked EN Treated specimen, B. EN treated specimens, and C. Cracked control specimens

The top and bottom reinforcements of EN treated and control specimens are shown in Figures 4.30 and 4.31. The clean EN treated rebars indicate no signs of corrosion products as compared to the controls (refer to Figure 4.30). The corrosion product analysis of the bottom and top rebars is shown in Figure 4.32. The top control and EN treated rebars showed 99% and 0.5% corrosion products respectively while the bottom reinforcements exhibited 52% and 1% coverage of corrosion products (See to Figures 4.30 and 4.31)



Fig 4.30 Digital image of top bars of controls and EN treated specimens

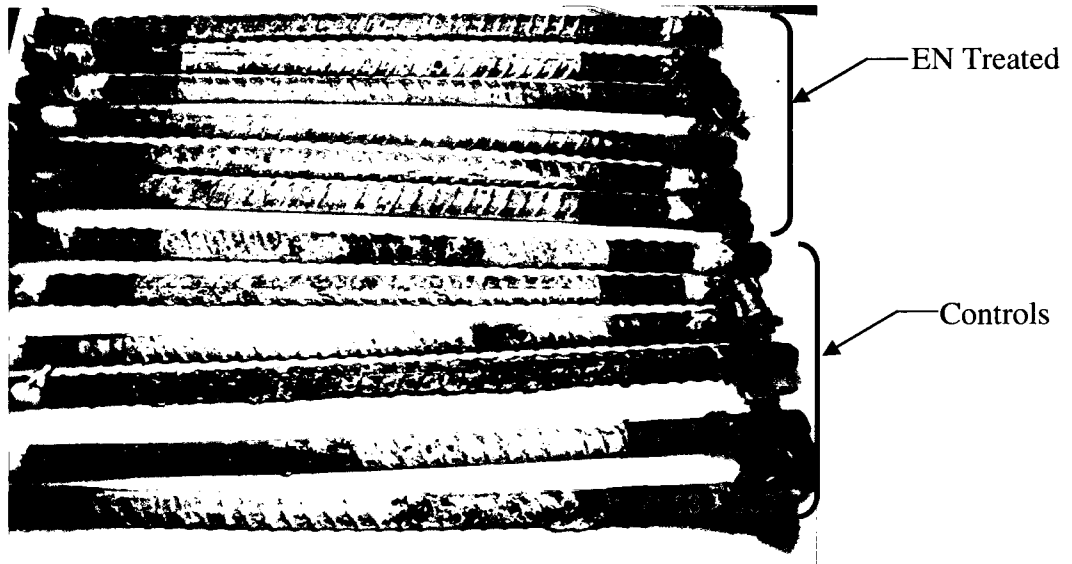


Fig 4.31 Digital image of bottom bars of controls and EN treated specimens

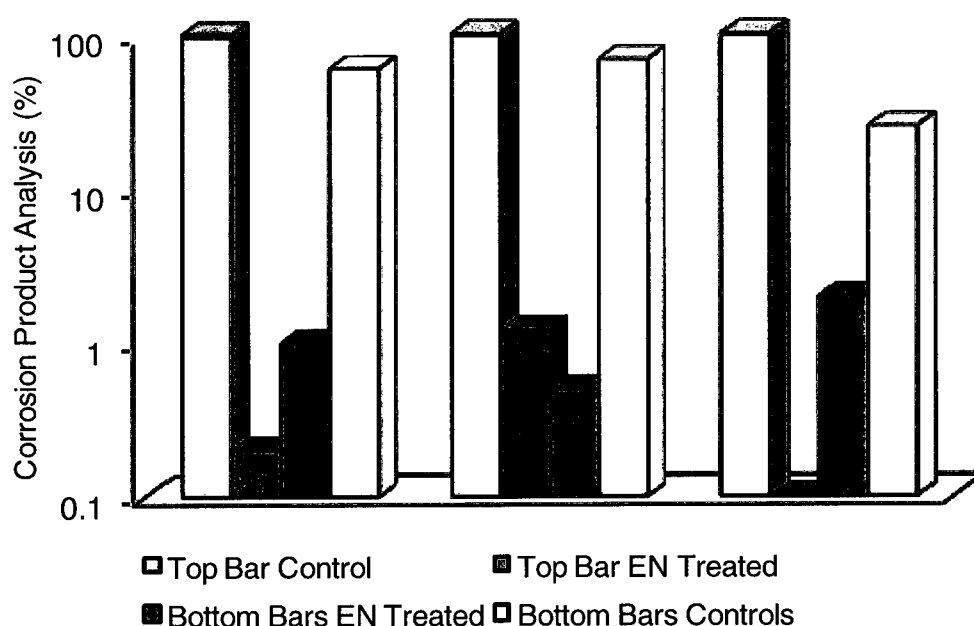


Fig 4.32 Corrosion product analysis of EN treated and controls of bottom and top rebars

The top rebar controls had one inch of concrete separating them cover from the chloride source as compared to the bottom rebars which had five inches of cover. High chloride exposure to the top rebars, correlates to higher corrosion on the upper reinforcement as compared to the lower bars. The EN treated specimens showed only 0.5% corrosion products as compared to the untreated controls exhibited 99% corrosion. These observations indicate that the nanoparticles may have created a barrier against chloride induced corrosion.

The amount of corrosion products clearly exceeded the minimum required to produce severe cracks. Based on these findings, it is clear that the EN treatment was successful at inhibiting chloride induced corrosion when the specimens were subjected to the wet and dry cycles of post saltwater exposure.

Results from the corrosion analysis indicate that the EN treatment was successful in preventing the formation of an oxygen concentration cell. Oxygen is essential for the onset of corrosion initiation and the formation of differential aeration cells in reinforced concrete (Ahmad, 2006). The porous nature of concrete is highly susceptible to the oxygen access leading to cathodic reduction of oxygen at the bottom rebar layer. The anodic reaction occurs due to the limited availability of oxygen but in this case the high chloride content on the top rebars caused the rust formation. The current study indicated that the EN treatment was successful in preventing access to chlorides on the top rebars, while simultaneously restricting the oxygen content to the bottom rebars. This prevented the formation of an oxygen concentration cell and thus reinforcement corrosion in concrete.

4.2.6 SEM Analysis

A scanning electron microscope analysis of control and EN treated specimens is shown in Figures 4.33 and 4.34. Severe macro cracks can be seen on the control specimens while the EN treated specimens exhibited a dense microstructure. EN treated specimens exhibited calcium silicate hydrate (C-S-H), along with large ettringite needles as shown in Figures 4.34 A and 4.34 B. The controls demonstrated corrosion products in the form of lepidocrocite (γ -FeOOH), a flowery like structure shown in Figures 4.35 A and B. Vacant space in the concrete due to leaching is shown in Figures 4.35 C and D.

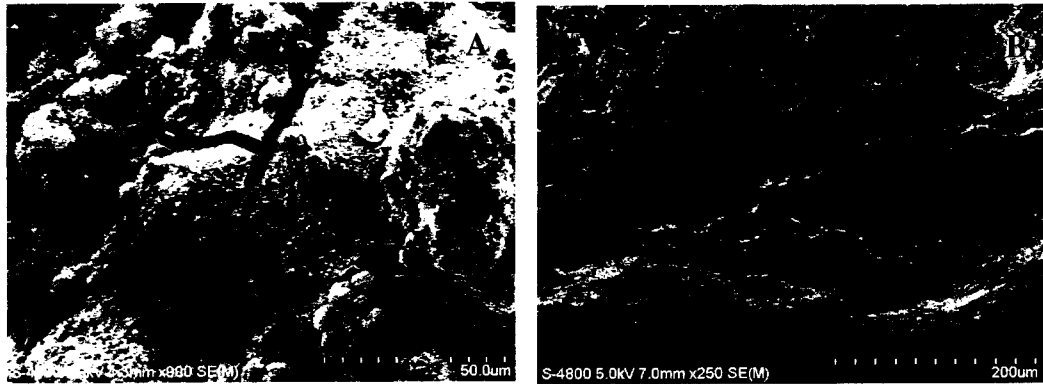


Fig 4.33 Control specimens (cracked specimen) and EN treated specimens showing dense microstructure

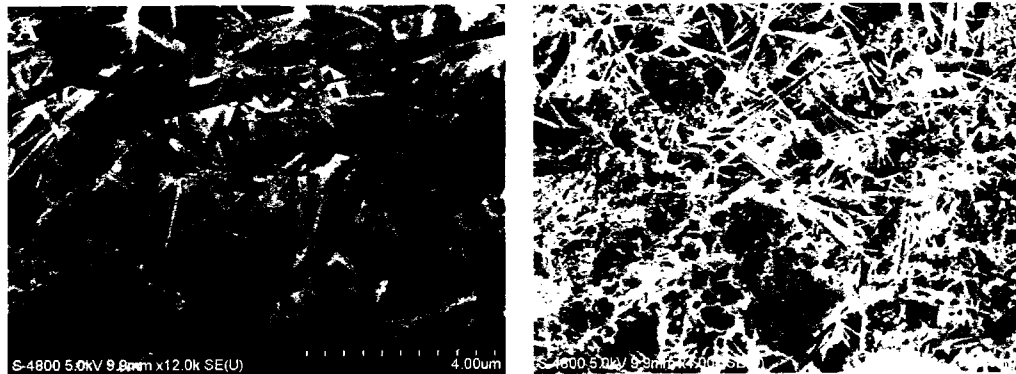


Fig 4.34 EN treated specimens depicting a microstructure of C-S-H

The wet and dry post saltwater exposure initiated the process of leaching. The process of leaching leads to higher porosity and can also lead to the formation of voids (refer to Figure 4.35). The EN treated specimens were exposed to similar saltwater exposure as the untreated controls. The treated specimens showed lower corrosion rates, relatively corrosion free rebars and virtually no signs of corrosion products or cracking. EN treatment exhibited densified microstructure as compared to the controls. The dense microstructure may have prevented the ingress of chloride ions from entering into the capillary

pores. Results demonstrate that the EN treatment was successful in mitigating reinforcement corrosion in simulated bridge deck specimens.

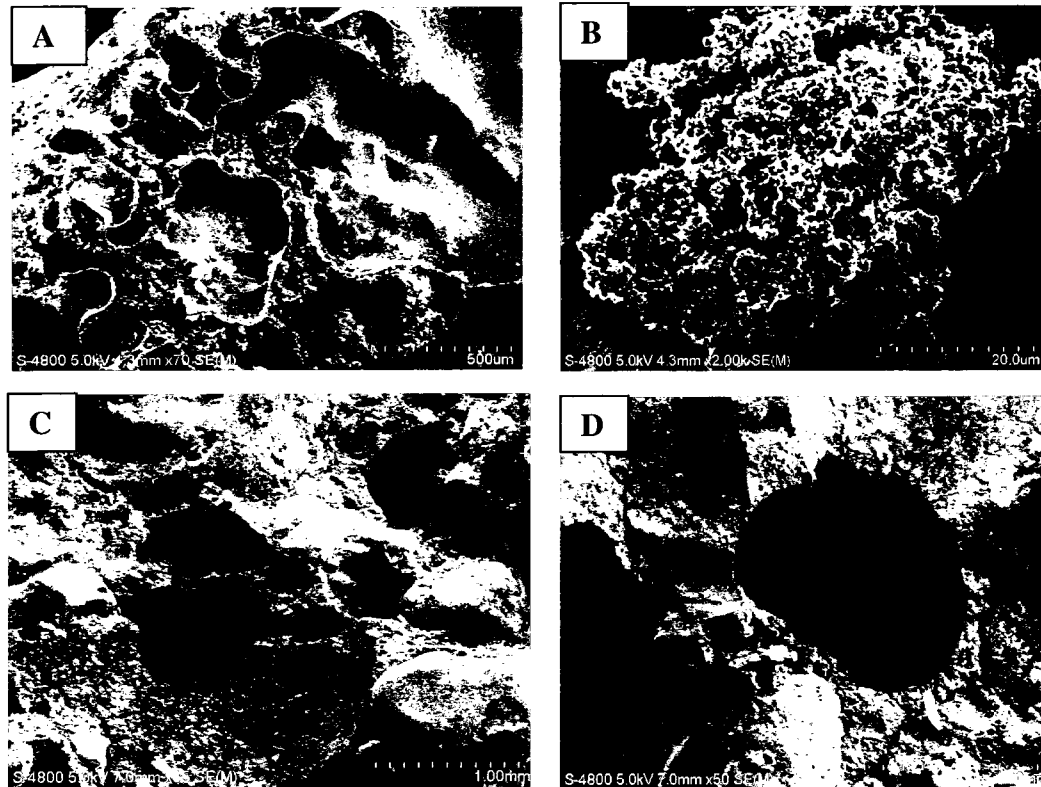


Fig 4.35 (A) Corrosion products in the form lepidocrocite, (B) Magnified image of corrosion products, (C) pores present in the control specimens and (D) Magnified image of corrosion products

4.2.7 Summary of ASTM G109 Simulated Bridge Deck Specimens

The untreated controls exhibited a higher corrosion rate by a factor of 23, as compared to the EN treated specimens. The EN treated specimens exhibited a reduction in the mass loss rate by a factor of 34 as compared to untreated controls. The EN treated specimens exhibited a dense microstructure and less chloride ion penetrability as compared to untreated controls. Based on the results of EN treatment on cylindrical reinforced concrete (refer to Section 4.1)

and those of ASTM G109 specimens, the treatments were found to enhance corrosion resistance in relatively small reinforced concrete specimens.

4.3 EN Treatment of Reinforced Concrete Beams

EN treatment was applied to full scale beams in order to simulate actual field conditions. This work evaluated the corrosion behavior of reinforced concrete beams when subjected to electrokinetic nanoparticle (EN) treatment (Kupwade-Patil et al., 2008). This treatment utilized a weak electric field to transport nanoscale pozzolans directly to the steel reinforcement. Each beam was batched with salt and subjected to saltwater exposure, followed by electrochemical chloride extraction (ECE) and EN treatment. The specimens were re-exposed to saltwater following treatment. Results from this test indicated significantly lower corrosion rates among the EN treated specimens (0.006 mils per year) as compared to the untreated controls (0.87 mils per year). Scanning Electron Microscopy (SEM) was used to examine the microstructural impact of the treatment process. A reduction in porosity (adjacent to the steel) of 40% was observed due to EN treatment. During the treatment application, the electric field also caused chlorides to be drawn away from the reinforcement and extracted from the concrete beam. After the chloride had been extracted, the nanoparticles apparently formed a physical barrier against chloride re-penetration.

The study presented in Section 4.3 was published by Kupwade-Patil, Gordon, Xu, Moral, Cardenas and Lee as "Corrosion mitigation in concrete beams using electrokinetic nanoparticle treatment" in the Proceedings of Excellence in Concrete Construction through Innovation on September 2008 in

London, UK. EN treatment, corrosion, microstructure, chemical analysis and MIP were conducted by the author. Kanielle Gordon conducted structural analysis under the supervision of Dr. Luke Lee. This portion of the work is not included in the dissertation. Dr. Karen Xu helped the author in scanning electron microscopy studies. Mr. Oner Moral constructed the treatment handling containers which were used in the study.

4.3.1 Corrosion Potential and Corrosion Rates

Corrosion potentials observed during this study are shown in Figure 4.36. The corrosion potential measurements reported represent the average values of two specimens for the control and ECE cases, and the average of six specimens for the EN treated case. During the initial saltwater exposure, the corrosion potential dropped to -536 mV. ECE was carried out for 14 days on all the specimens, causing the average corrosion potential to decrease to -1207 mV. During the ECE process, the chlorides moved away from the reinforcement, while sodium, potassium and calcium ions residing in the concrete pore fluid were attracted to the rebar, causing a negative trend in corrosion potentials. ECE was continued for an additional six weeks on two of the beam specimens while the other six were subjected to EN treatment over the same period.

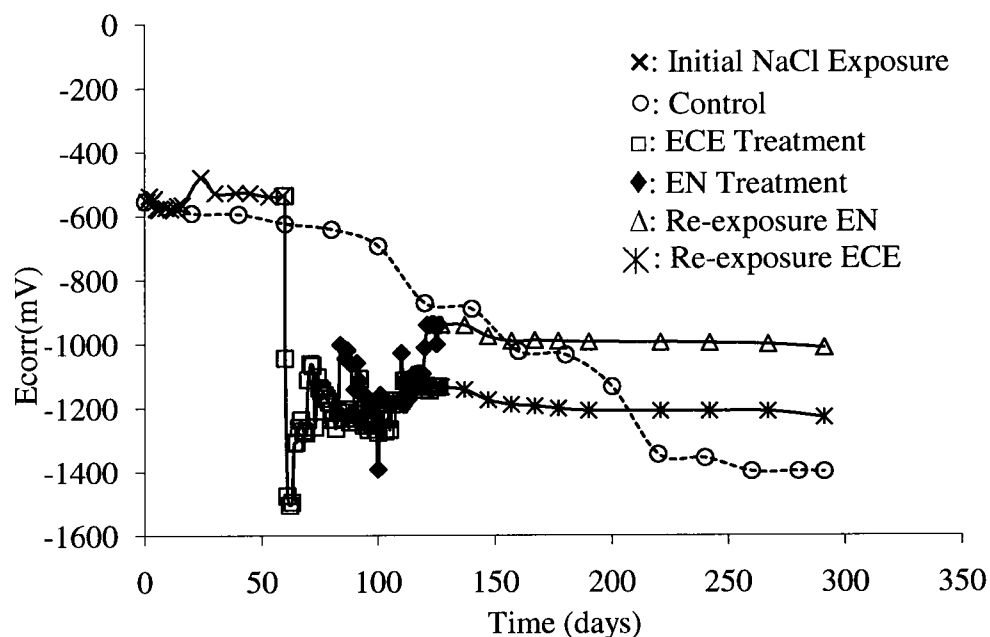


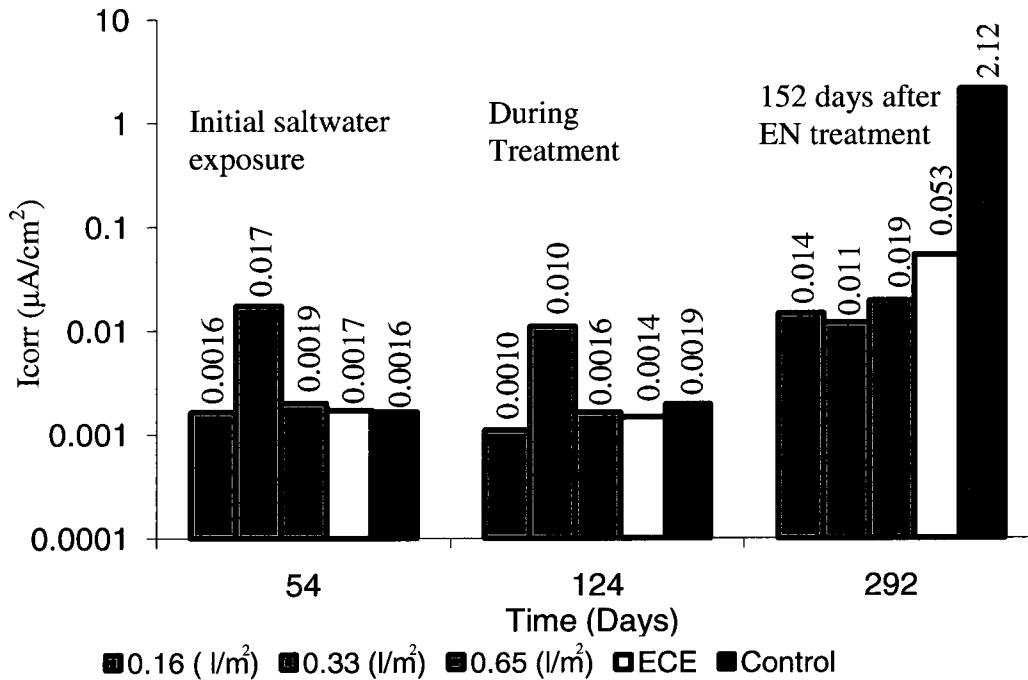
Fig 4.36 Corrosion potential data of reinforced concrete specimens

In the case of the EN treatments, a significant increase in corrosion potential was observed from - 1207 mV to - 940 mV. This increase in corrosion potential may have been influenced by the alumina content of the treatment. The control specimens exhibited a corrosion potential of -1399 mV at the end of post treatment saltwater exposure. Figure 4.36 shows that corrosion potentials of untreated specimens were more negative than the treated specimens. The average difference in corrosion potential between untreated and treated cases was 340 mV. As noted in an earlier section, studies conducted by Suryavanshi and others observed that elevated Calcium aluminate hydrate (C-A-H) content was associated with relatively positive corrosion potentials (Suryavanshi et al., 1998). As a point of speculation, the alumina content of the EN treatment may have produced C-A-H that could have induced the relatively positive corrosion potentials. Future work will need to examine this further.

Additional corrosion characterization was conducted by measuring the corrosion current density and polarization resistance. Corrosion current density (I_{corr}) and polarization resistance (R_p) values at 54, 124 and 292 days are shown in Figures 4.37 and 4.38. The I_{corr} were calculated from R_p values using the Equation 20. Corrosion current density (I_{corr}) of $0.014 \mu\text{A}/\text{cm}^2$, $0.011 \mu\text{A}/\text{cm}^2$ and $0.019 \mu\text{A}/\text{cm}^2$ was observed at the end of 292 days for the 0.16, 0.33 and $0.65 \text{ l}/\text{m}^2$ particle dosages, respectively. The ECE and control specimens exhibited 0.053 and $2.12 \mu\text{A}/\text{cm}^2$ at the end of 292 days. An average corrosion current density of $0.014 \mu\text{A}/\text{cm}^2$ for the EN treated specimens was observed, as compared to the untreated controls ($2.12 \mu\text{A}/\text{cm}^2$). The untreated controls exhibited a higher average corrosion current density I_{corr} by a factor of 151 as compared to the EN treated specimens. The corrosion current density (I_{corr}) values can be used directly to examine corrosion severity. Guidelines for evaluating the severity of corrosion are shown in Table 4.4. The corrosion rates were calculated using Equation 31. The average corrosion rate values of 0.87, 0.006 and 0.022 Mpy were observed for the control, EN treated and ECE specimens respectively at the end of post saltwater exposure. The controls exhibited a moderate to high corrosion rate, while EN treated and ECE specimens demonstrated a passive state.

Table 4.4 Guidelines for evaluating the severity of corrosion

Corrosion Current Density ($\mu\text{A}/\text{cm}^2$)	Corrosion Condition
< 0.1	Passive
0.1-0.5	Low to moderate
0.5-1	Moderate to high
> 1	High

Fig 4.37 Comparative plot of corrosion current density (I_{corr}) for EN Treated, ECE and Controls

The initial saltwater exposure of EN treated, ECE and control specimens depicted $0.0068 \mu\text{A}/\text{cm}^2$, $0.0017 \mu\text{A}/\text{cm}^2$ and $0.0016 \mu\text{A}/\text{cm}^2$. These values exhibit that all the specimens were in a passive state. During the treatment, I_{corr} values dropped for EN treated specimens and ECE specimens whereas the I_{corr} values of the controls increased from 0.0016 to $2.12 \mu\text{A}/\text{cm}^2$.

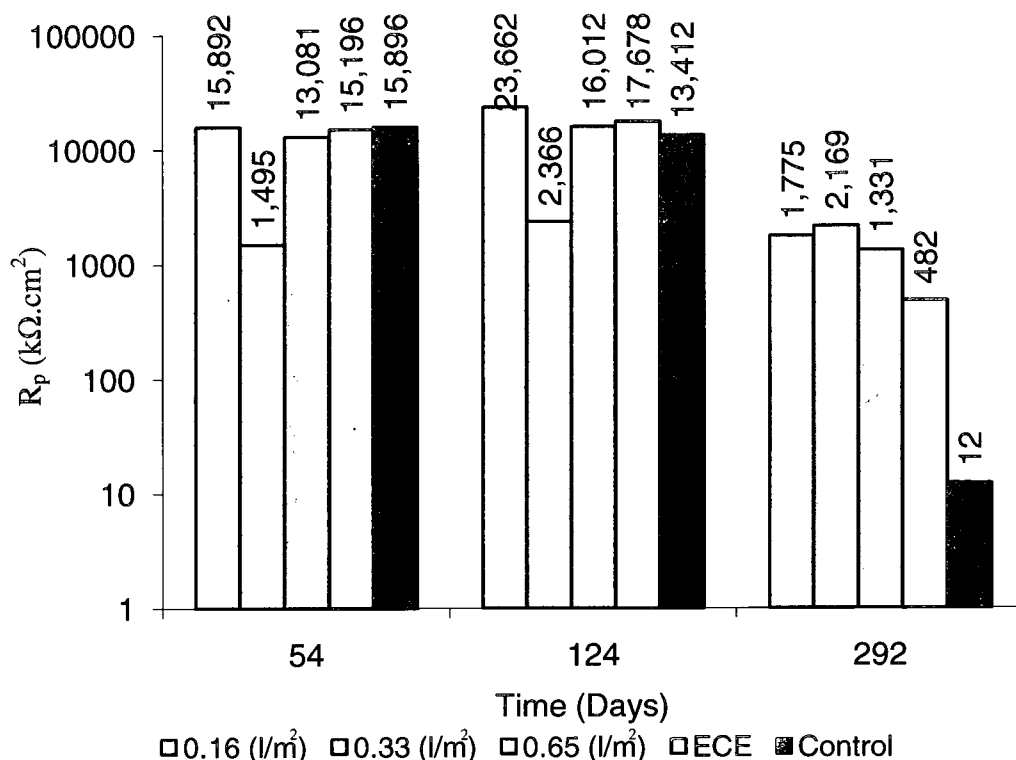


Fig 4.38 Comparative plot of polarization resistance (R_p) for EN treated, ECE and Controls

This appears to show that the alumina coated silica nanoparticles had formed a layer of protection on the 1018 steel reinforcement. The EN treated specimens exhibited a reduction in I_{corr} by a factor of 144 as compared to the untreated controls. The lower I_{corr} values after 152 days of EN treatment shows that EN treatment was effective in preventing the intrusion of chlorides by acting as a blocking agent. The high I_{corr} value ($2.12 \mu\text{A}/\text{cm}^2$) showed that the chlorides penetrated through the capillary pores of concrete and moved from a low to a high corrosion condition. This indicates that the chlorides were diffusing into the capillary pores and breaking down the passive layer of oxide on the reinforcing,

and initiating corrosion on the reinforcement. In the following section, detection of the chloride contents can be related to the corrosion rates.

4.3.2 Chloride Contents

The chloride content values at different distances from the reinforcement are shown in Figure 4.39. The control specimens exhibited chloride contents 0.12 (wt% of cement) at 1.5 in, 0.14 % at 1 inch and 0.14 at 0.5 in away from the rebar. Average chloride content values of 0.03 % at 2.5 in, 0.05 at 2 in, 0.04 at 1.5 in were detected by the EN treated specimens. ECE specimens demonstrated an average (over all locations) of 0.05 % of chloride content by weight of cement. The chloride content analysis showed that the controls exhibited higher chloride content by a factor of 4 as compared to EN treated specimens. Chloride content values above the threshold level (0.1 wt % of cement) for the controls indicated the initiation of reinforcement corrosion (ASTM C 1152). A trend with respect to the distance from the rebar could not be confirmed with respect to the distance from the rebar due to the presence of significant scatter in the data.

The controls exhibited an increase in chloride content above the threshold limit and I_{corr} values greater than one $\mu\text{A}/\text{cm}^2$, indicating a high corrosion condition. The EN treated specimens showed lower chloride contents near the reinforcement and lower I_{corr} . This indicates that the nanoparticles may have blocked the chlorides during their re-entry. This EN treatment was successful in preventing the ingress of chlorides during post saltwater exposure.

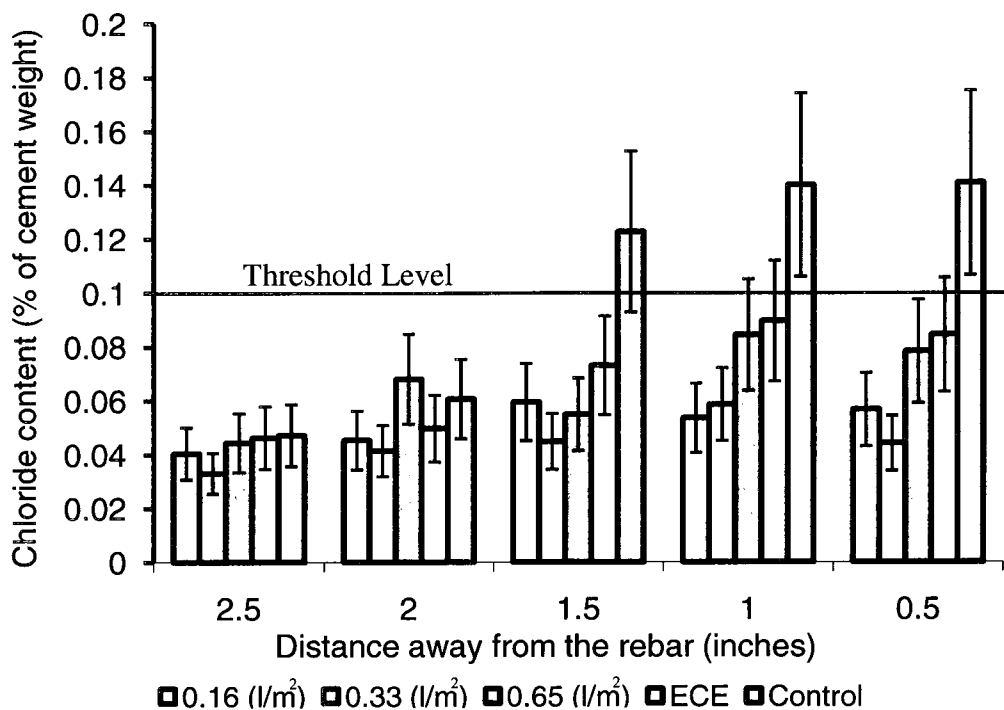


Fig 4.39 Chloride content values with the distance away from the reinforcement

4.3.3 Mercury Induced Porosimetry (MIP)

Mercury induced porosimetry (MIP) was used to characterize the threshold pore size entrances. These measurements are useful to provide the threshold diameters, which are used to provide information regarding the connectivity of the pores (Diamond, 2000). The largest pore diameter at which significant intruded mercury pore volume is detected is known as the threshold diameter. The critical pore diameter is one which allows maximum percolation throughout the pore system. Critical pore size helps to examine the effect of parameters such as water/cement ratio, transmissivity and temperature on the pore structure (Aligizaki, 2006). Graphical representation of the cumulative intrusion volume versus pore diameter of EN treated, ECE and controls specimens are shown in Figures 4.40 and 4.41.

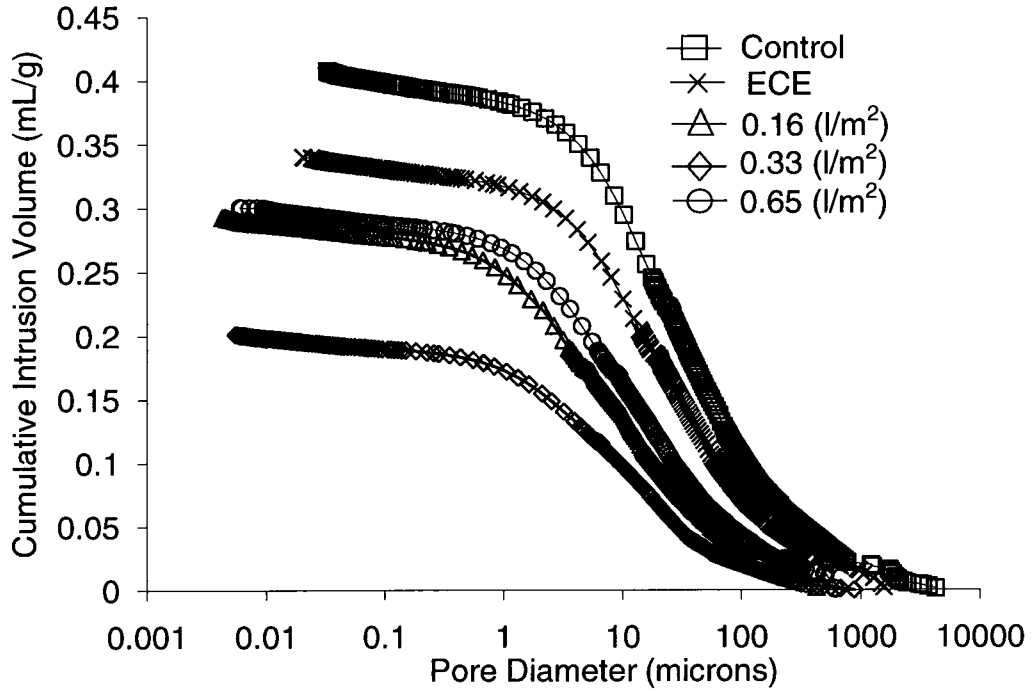


Fig 4.40 Mercury induced porosimetry (MIP) curves on powdered concrete adjacent to the rebar

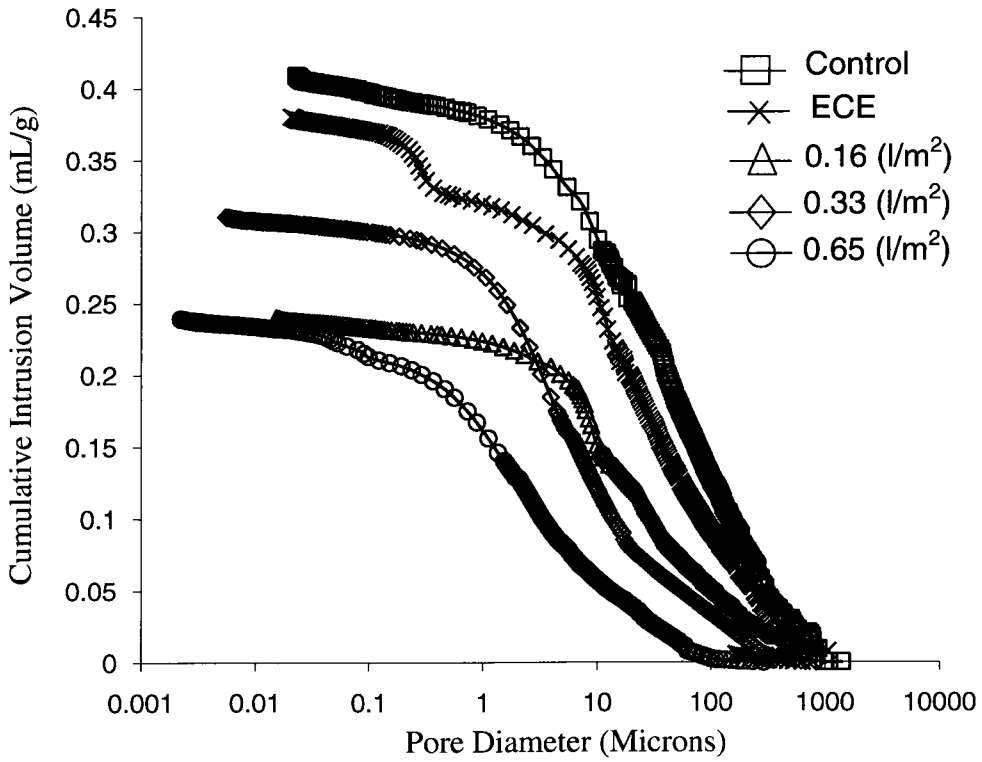


Fig 4.41 MIP curves on the powdered concrete two inches away from the rebar

The parameter values of threshold pore size, critical pore diameter, and bulk porosities obtained by MIP and weight loss reduction (WLR) method are assembled for comparison in Table 4.5.

Table 4.5 Porosity results using MIP and WLR methods

Treatment Type	MIP				Porosity			
	Threshold pore diameter (μm)		Critical pore Diameter (μm)		MIP (%)		WLR (%)	
	R/C interface	2 inch from R/C	R/C	2 inch R/C	R/C interface	2 inch from R/C	R/C interface	2 inch from R/C
Control	1725	773	29	18	11.4	15.3	8.9	12.9
ECE	401	482	19	12	9.4	10.4	13.8	9.1
0.16 (l/m^2)	119	352	6	11	7.2	8.4	5.2	4.9
0.33(l/m^2)	292	294	7	6	4.1	4.9	4.8	5.1
0.65(l/m^2)	184	64	10	2	3.01	2.8	5.3	6.4

R/C : Rebar concrete interface

The treated specimens exhibited a reduction in average threshold diameter (198 μm) by a factor of eight as compared to the control (1725 μm) and a factor of two for ECE specimens (401 μm). The particle dosage of 0.16 (l/m^2) exhibited the least threshold pore diameter (119 μm) at the rebar/concrete interface where as 0.65 (l/m^2) dosage showed the least value (64 μm) at two inches away from the reinforcement. The treated specimens exhibited a reduction in critical pore diameters by a factor of ~4 as compared to the controls and 2.5 for ECE specimens at the rebar concrete interface. The EN treated

specimens exhibited 74% porosity reduction at the rebar concrete interface and 82% at two inches away from the reinforcement, as compared to the controls.

The limited particle dosages exhibited a reduction in threshold pore diameters and porosity. The phenomenon of ionic conduction induced by ECE was expected to act concurrently with EN treatment. Ionic conduction consists of the combination sodium, potassium and calcium ions. This indicates that the fewer the number of particles the more the ions can be attracted, and thus can penetrate into smaller capillary pores. This shows that the combination of electrophoresis and ionic conduction provides better particle/ion packing efficiency. The larger the amount of particle/ion access the smaller the pore diameter is as shown in Figure 4.42.

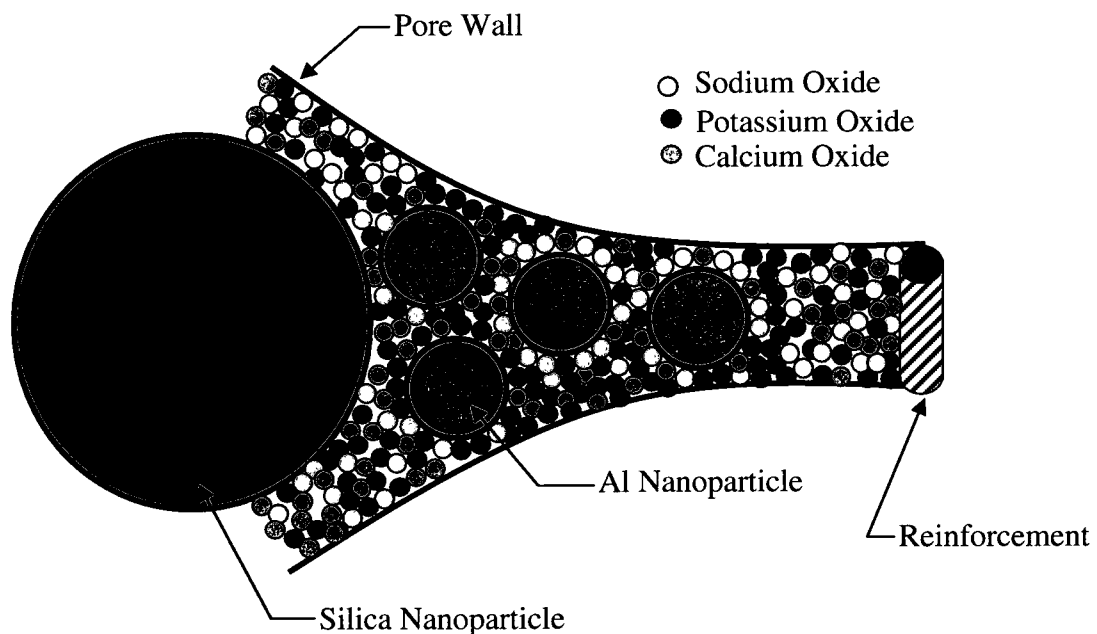


Fig 4.42 Concept of positive nanoparticles and negative ions into the capillary pore

Reduction in threshold pore diameters of treated specimens indicates that the nanoparticles were effective in blocking the capillary pores, hence acting as a

physical barrier preventing the ingress of the external chlorides. The chloride content and porosity studies showed that the nanoparticles which acted as blocking agents retarded the chloride content below the threshold level and retarding the re-entry of the chlorides. Micro structural characterization shown in the next section studies the phases formed due to the EN treatment.

4.3.4 SEM/BSE Analysis

Imprints of the rebar/concrete interface for the EN treated and control beams are shown in Figure 4.43. The corrosion products were observed on the rebar/concrete interface, whereas the EN treated specimens exhibited clean rebar/concrete interfaces, showing no trace of corrosion products. SEM micrographs of lepidocrocite (γ -FeOOH) in the form of (fine plates) flowery structures are shown in Figures 4.44 A and B (Antunes et al., 2003). The lepidocrocite was found on the interior and exterior of the pore, as shown in Figures 4.45 A and B. Lepidocrocite is an iron-oxide hydroxide formed in the early stage of corrosion. Lepidocrocite in later stages converts to goethite. The semicrystalline phase of goethite, which takes the form of cotton ball structures, is shown in Figure 4.46.

The rebar/concrete interface of EN treated specimens did not show signs of these corrosion products (refer to Figure 4.43). The controls demonstrated a reddish or brownish color of corrosion products. SEM microscopic analysis on the corroded R/C concrete interface exhibited the presence of lepidocrocite and goethite, which are iron-oxides. MIP results on the controls indicated large pores which were susceptible to chloride ingress, resulting in the initiation of corrosion.

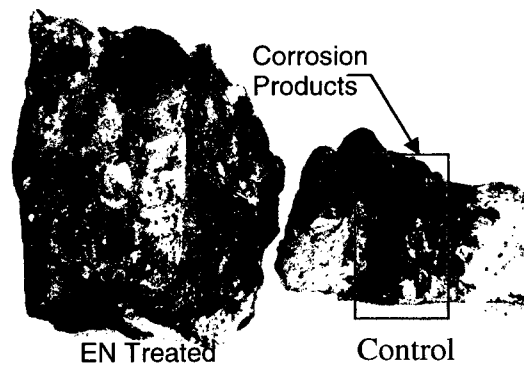


Fig 4.43 Imprints of corrosion products at the rebar/concrete interface for EN Treated and controls

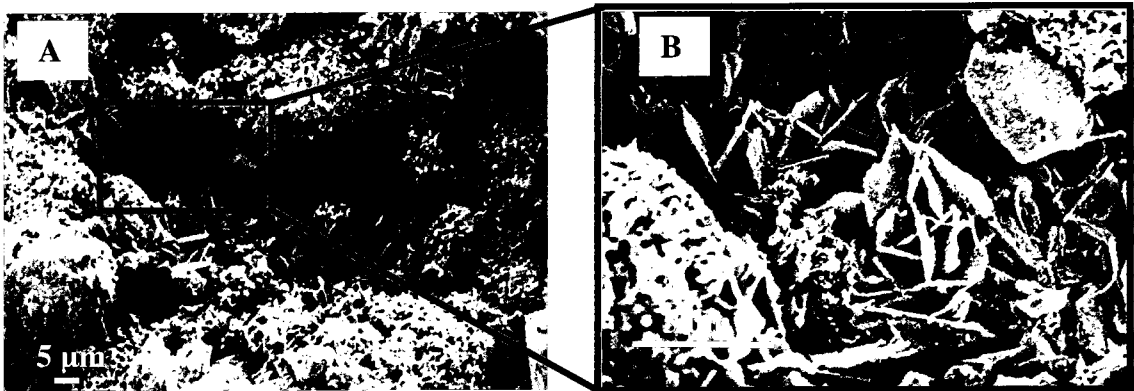


Fig 4.44 A: Presence of lepidocrocite which is exhibited as flowery structures. B: Magnified image of lepidocrocite on the control at R/C interface

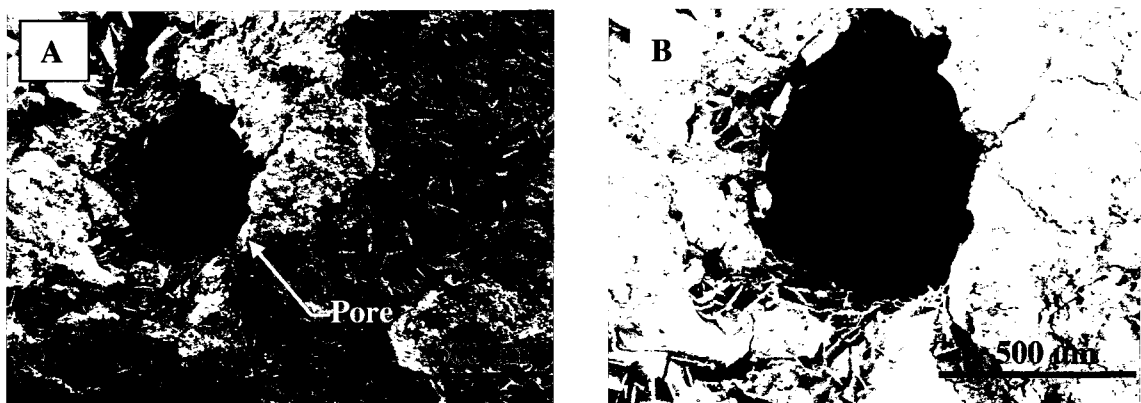


Fig 4.45 A: Lepidocrocite crystals depicting flowery pattern outside the pores. B: Presence of lepidocrocite crystals present in the inner layer of the pores

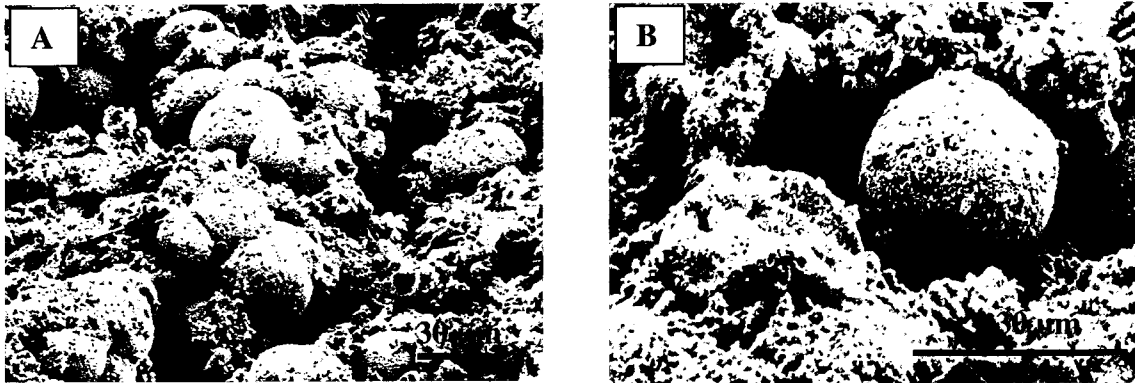


Fig 4.46 A: Cotton ball structures demonstrating the semicrystalline phase of goethite, B: Magnified image of goethite cotton ball

The corroded iron-oxide products have detrimental effect on the structure by inducing volume expansion and inducing tensile stress in the concrete, finally leading to cracking.

The EN treated specimens exhibited trigonal calcite while the controls showed the presence of hexagonal vaterite, as shown in Figures 4.47 A and 4.47 B. The combination of nanoparticles with calcium hydroxide (CH) led to the formation of stable orthorhombic shaped calcite. The combination of admixtures with calcium hydroxide (CH) leads to higher strength in the cement matrix (Mindess, 2001). The vaterite is considered to be the least stable, and it indicates that overall carbonation capacity is higher as compared to calcite (Skalny et al., 2001; Taylor 1997). Vaterite and calcite are transformed phases of calcium carbonate. Carbonated concrete transforms to vaterite and in later stages it transforms to aragonite (Wowra, 2002). Aragonite is orthorhombic in shape and is also less stable than calcite. This indicates that the EN treatment

may inhibit atmospheric carbonation, and therefore delay reinforcement corrosion in concrete.

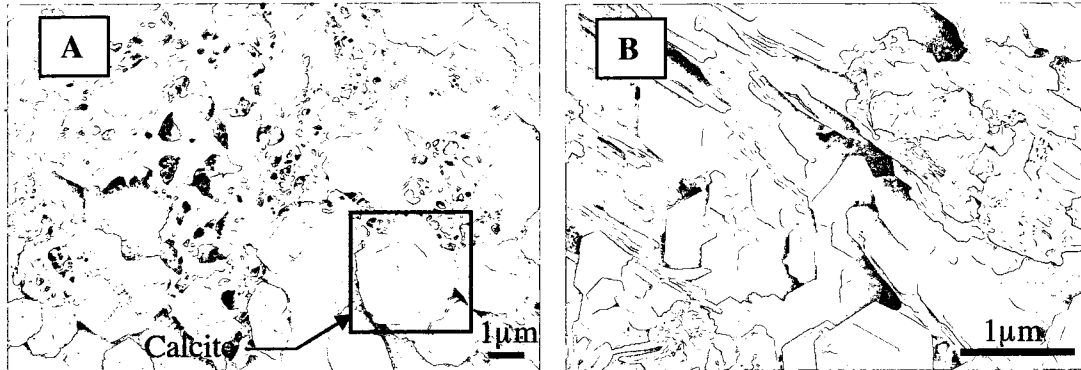


Fig 4.47 A: EN treated specimens indicating formation of stable trigonal calcite
 B: Control depicting sandwiched layer of unstable hexagonal calcium hydroxide (CH) crystals

Backscattered Electron (BSE) imaging of controls, EN treated and ECE specimens are shown in Figure 4.48. The presence of hollow cylindrical pores and the pores impregnated with dye are shown in Figures 4.48 A and B. The EN treated specimens exhibited a dense morphology as compared to the ECE and untreated controls. The treatment was effective in densifying the concrete as compared to the ECE and untreated controls. This dense microstructure, the reduced porosity and the reduced chloride contents observed in this work demonstrate that EN treatment was effective in inhibiting the re-entry of chlorides. BSE images, along with Energy Dispersive Spectroscopy (EDS), were obtained from polished controls and EN treated specimens. Figures 4.49 - 4.53 show that EN treated specimens exhibited lower average chloride content by weight of cement of 0.04% as compared to the ECE (0.45%) and control specimens (3.64%). This value can be compared to the ACI 22R-01 code,

which allows the threshold chloride content of 0.08% for non-pre-stressed concrete. These results show that EN treatment was effective in keeping the chloride contents below the ACI allowable values.

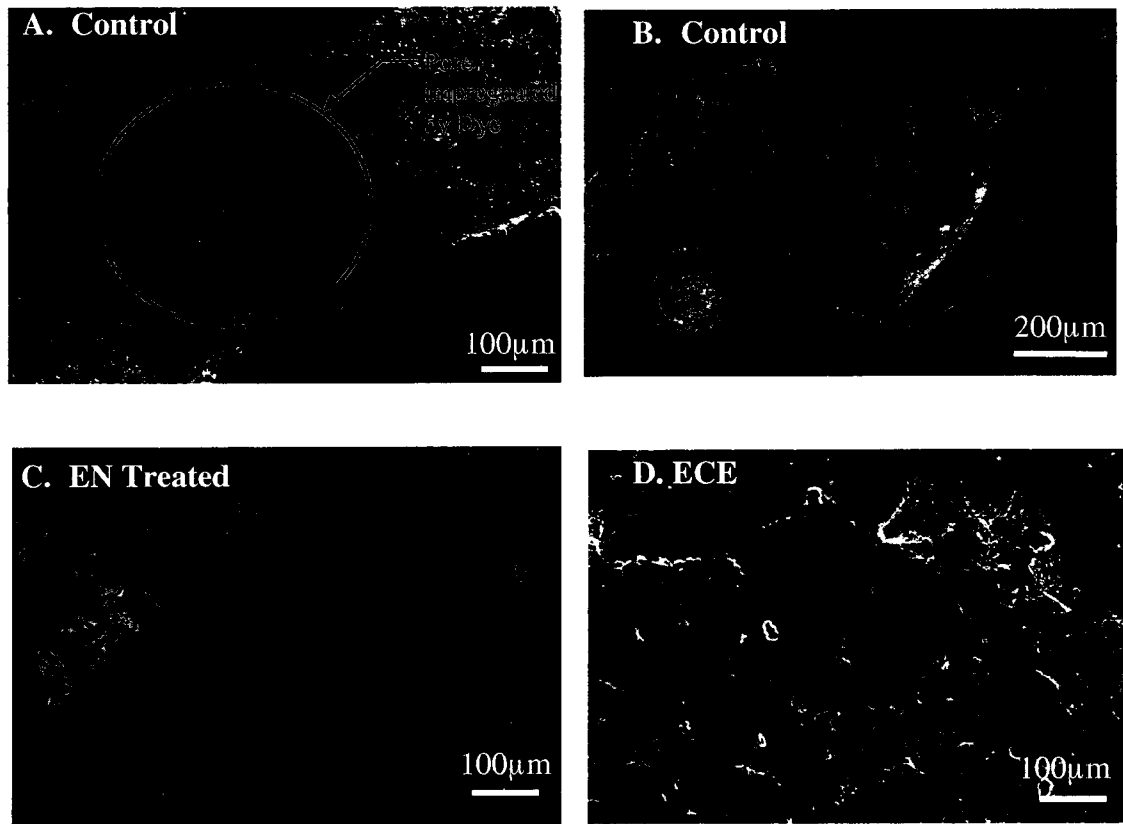


Fig 4.48 Backscattered electron (BSE) image of control (A and B), EN treated (C) and ECE specimen (D)

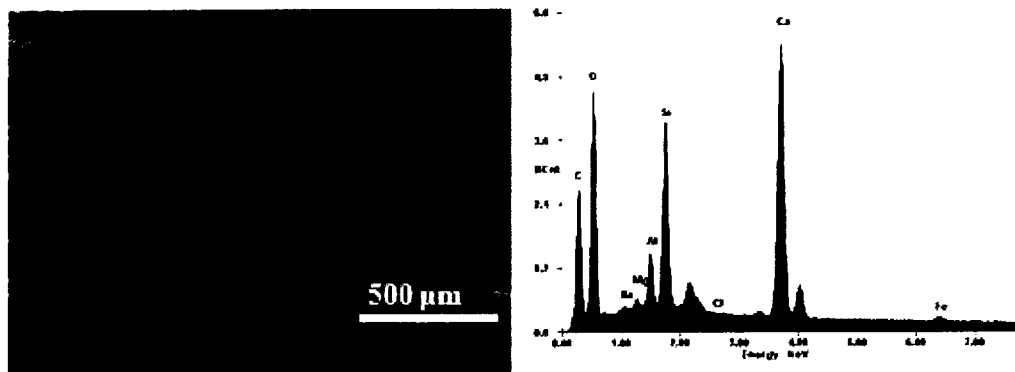


Fig 4.49 Quantitative EDS analysis of EN Treated specimen of $0.65 \text{ (l/m}^2\text{)}$

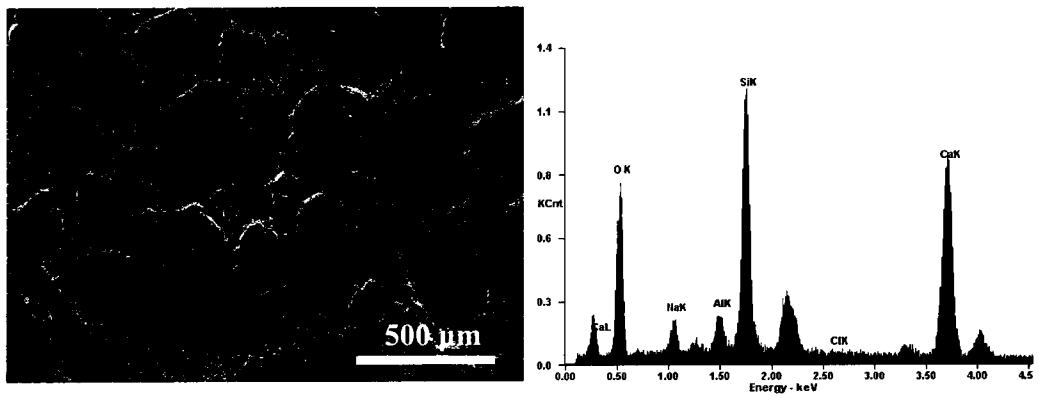


Fig 4.50 Quantitative EDS analysis of EN treated specimen of $0.33 \text{ (l/m}^2\text{)}$

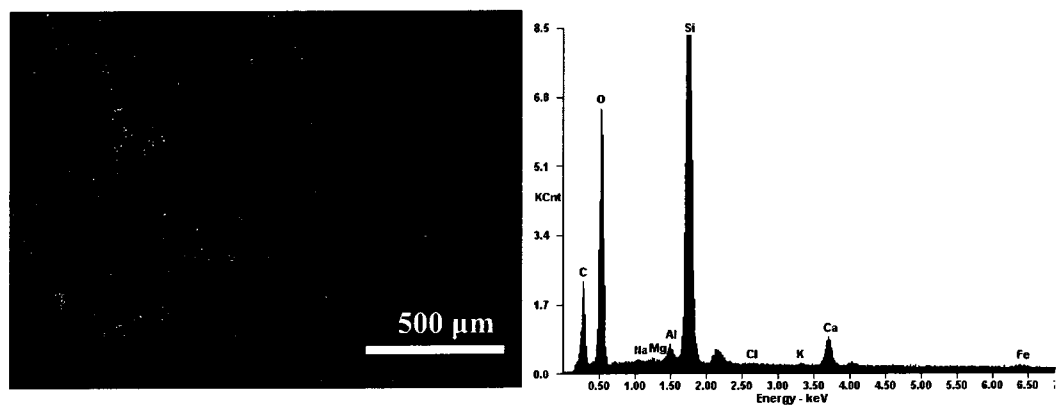


Fig 4.51 Quantitative EDS analysis of EN treated specimen of $0.16 \text{ (l/m}^2\text{)}$

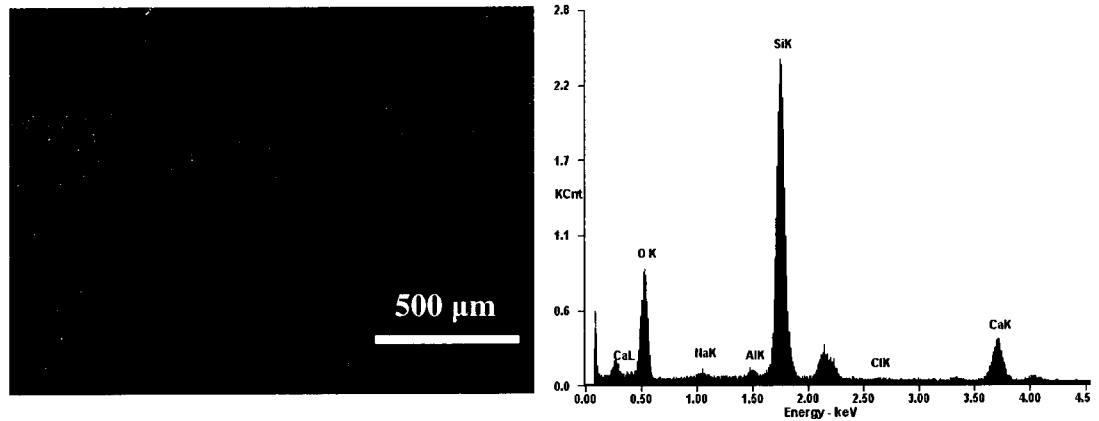


Fig 4.52 EDS analysis of ECE treated specimen

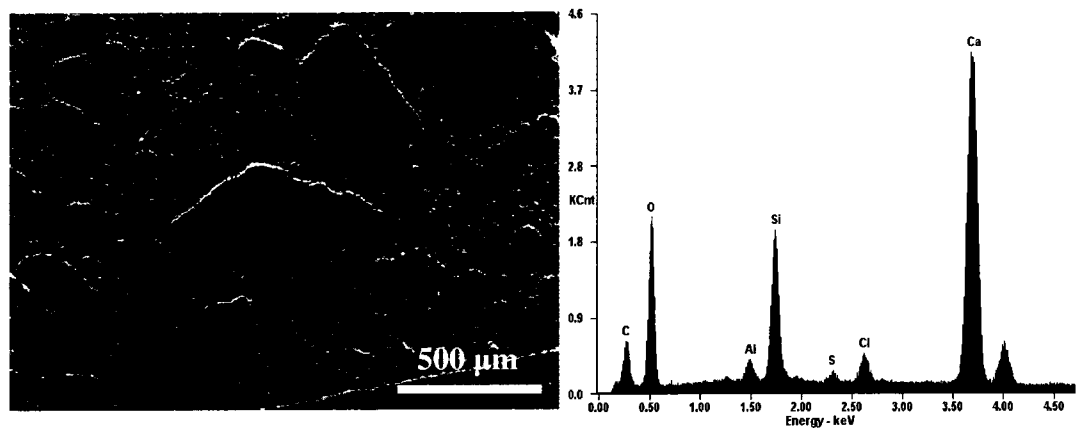


Fig 4.53 EDS analysis of the polished untreated control

4.3.5 Raman Spectroscopy

Raman Spectra of the EN treated specimens, the ECE and the control specimens are shown in Figure 4.54. The EN treated specimens exhibited sharp peaks of C-S-H in the range of $400-600\text{ cm}^{-1}$. The presence of weak C-S-H peaks on the controls and ECE specimens was due to the presence of initial hydration reaction (Mindess et al., 2002). The EN treated cases indicated formation of additional C-S-H as compared to ECE and control specimens. The

additional C-S-H formation was probably due to the reaction between the silica component of the nanoparticle and $\text{Ca}(\text{OH})_2$.

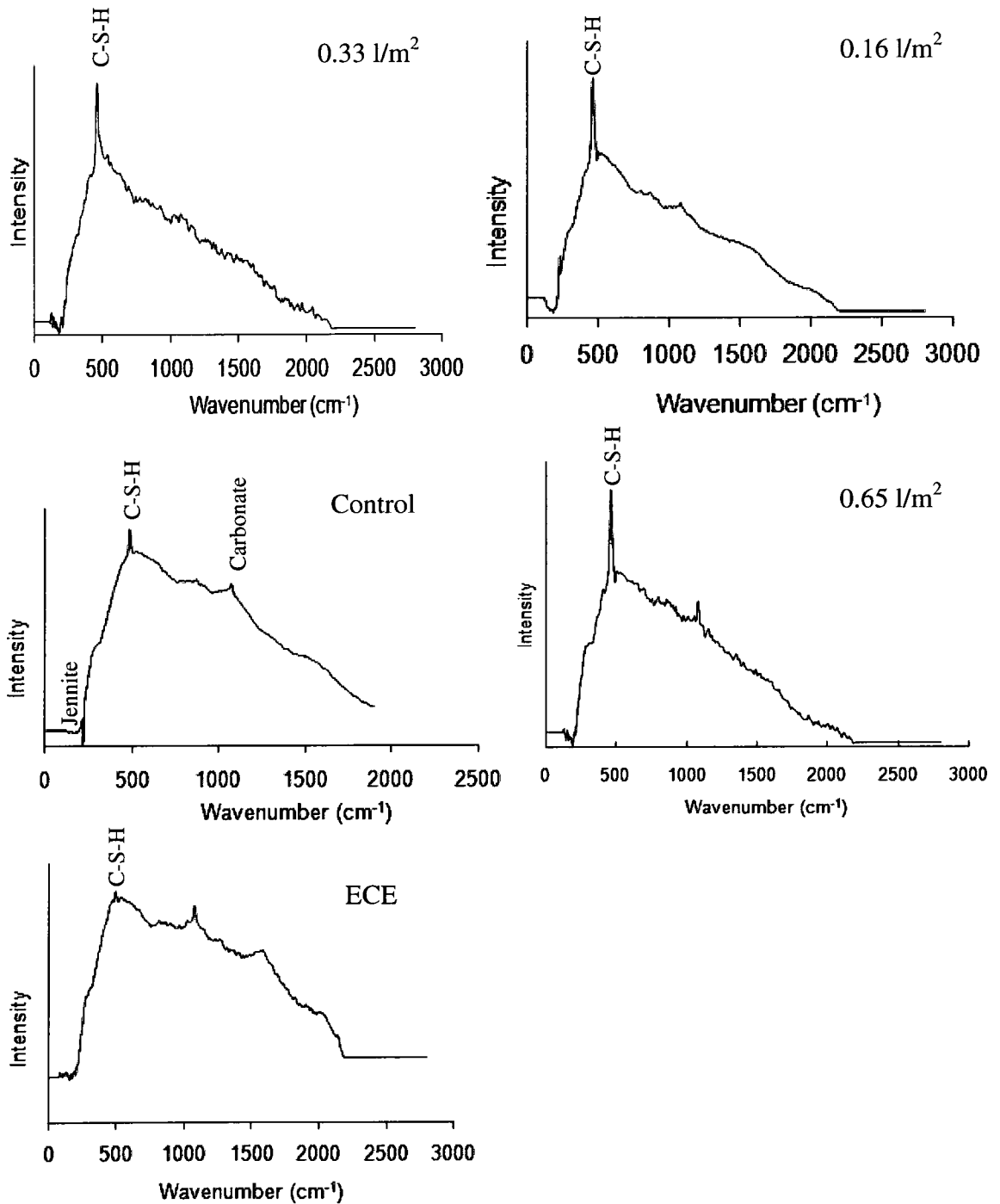
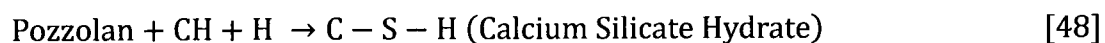
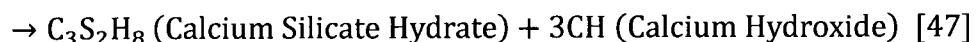
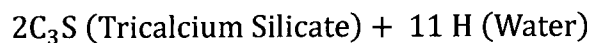


Fig 4.54 Raman spectroscopy of EN Treated (0.65 , 0.33 and 0.16 l/m^2) and control specimens

The initial hydration reaction led to some formation of C-S-H as shown in Equation 47. The ingress of the nanopozzolan into the concrete reacted calcium hydroxide and additional C-S-H was formed probably due to the pozzolanic reaction (Mehta and Monterio, 2006).



Raman spectroscopy analysis showed that the nanoparticle treatments were associated with strong C-S-H peaks on the EN treated specimens, as compared to the ECE and controls. The untreated control and ECE specimens showed very weak peaks of C-S-H and some presence of carbonation. C-S-H phases in the form of tobermorite and jennite were present when the alumina coated silica was mixed with excess calcium hydroxide, as shown in Figure 4.55 (Kirkpatrick et al., 1997). The SEM and MIP analysis also showed a formation of dense structure and a reduction in the threshold pore diameter (refer to Table 4.5), which can be related to the formation of additional C-S-H due to EN treatment. Un-reacted particles can also contribute to strength development in concrete. This indicates that the EN treatment was effective in the formation of the C-S-H, which is mainly responsible for the strength gain in the cement matrix.

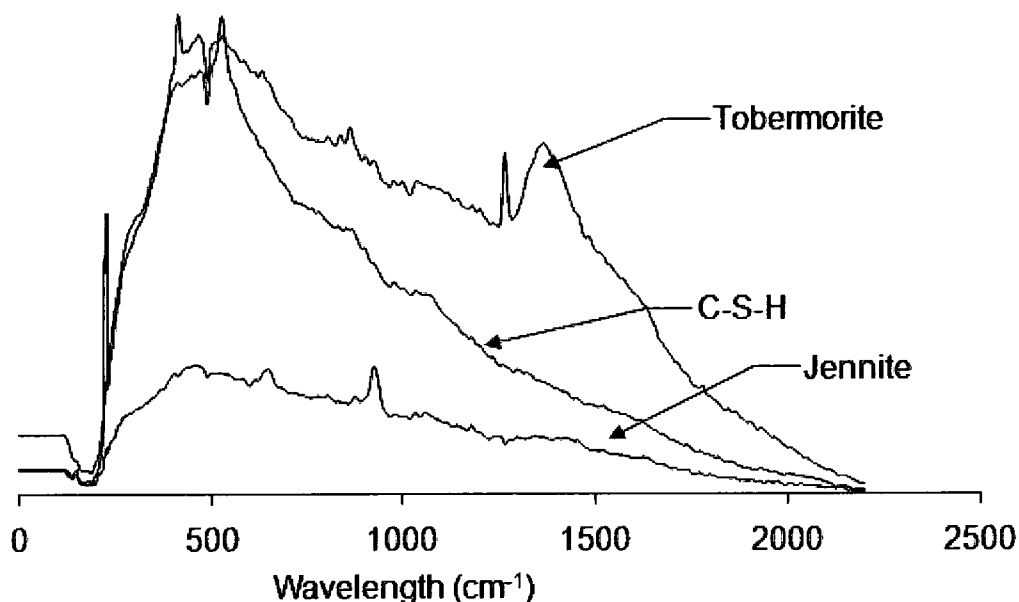


Fig 4.55 Raman spectra of simulated pore fluid (SMP) with alumina coated silica and excess calcium hydroxide

4.3.6 FTIR Spectral Analysis

FTIR transmittance spectra for simulated pore fluid (SMP) mixed with alumina coated silica as compared to ground concrete samples are shown in Figures 4.56 and 4.57. The EN treated specimens exhibited broad strong bands in the range of 3400-3600 cm⁻¹, indicating the presence of OH vibrations of water molecules in monocalcium aluminate hydrate, dicalcium aluminate hydrate and tri-calcium aluminate hexahydrate (Carraso et al., 2008). These are collectively referred to as C-A-H.

Complex spectras of calcium silicate hydrate were observed in the frequency range of 900-1100 cm⁻¹ and are shown in Figures 4.56 and 4.57 (Yu et al., 1999). The EN treated cases and the reaction products from nanoparticles mixed with SMP exhibited Si-O-Si bands of C-S-H in the range of 600-700 cm⁻¹

and Si-O band of C-S-H from 900-1100 cm^{-1} . Carbonate peaks at 1440 cm^{-1} frequency were also detected.

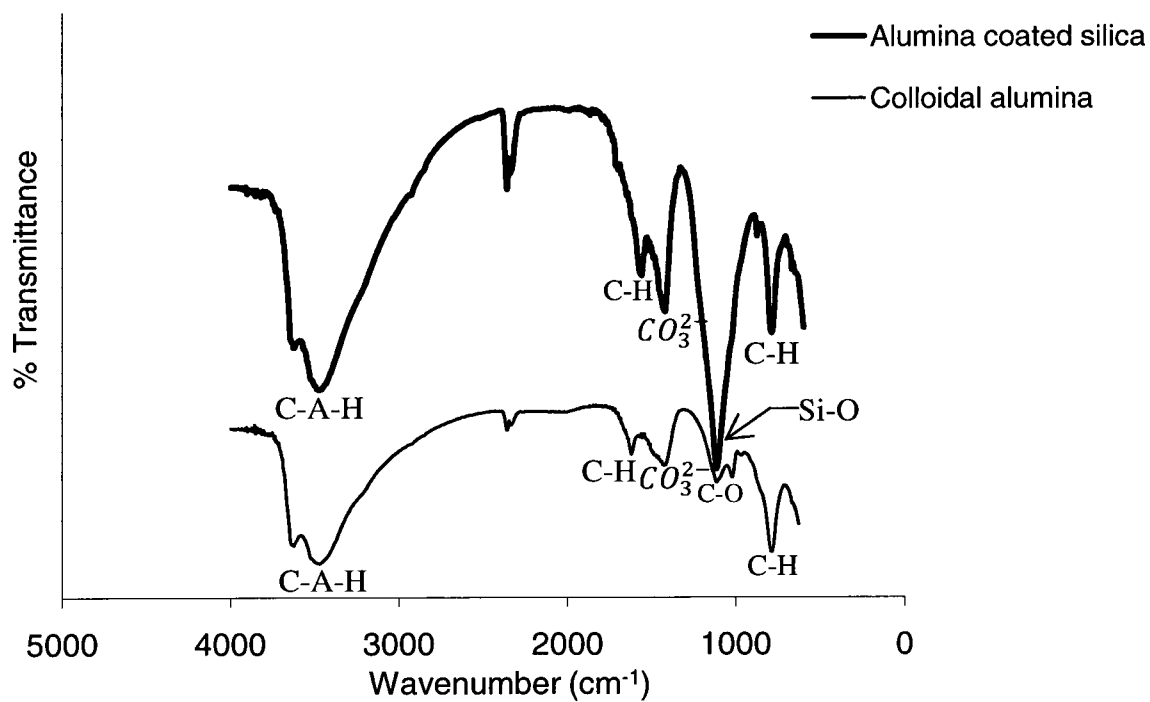


Fig 4.56 FTIR spectra of SMP mixed with alumina coated silica and colloidal alumina

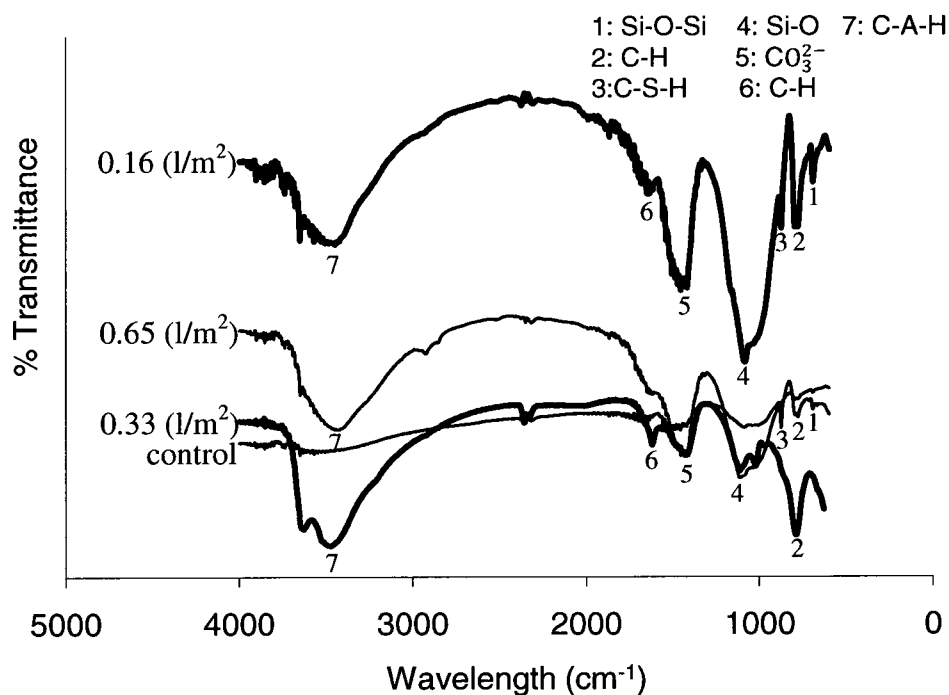


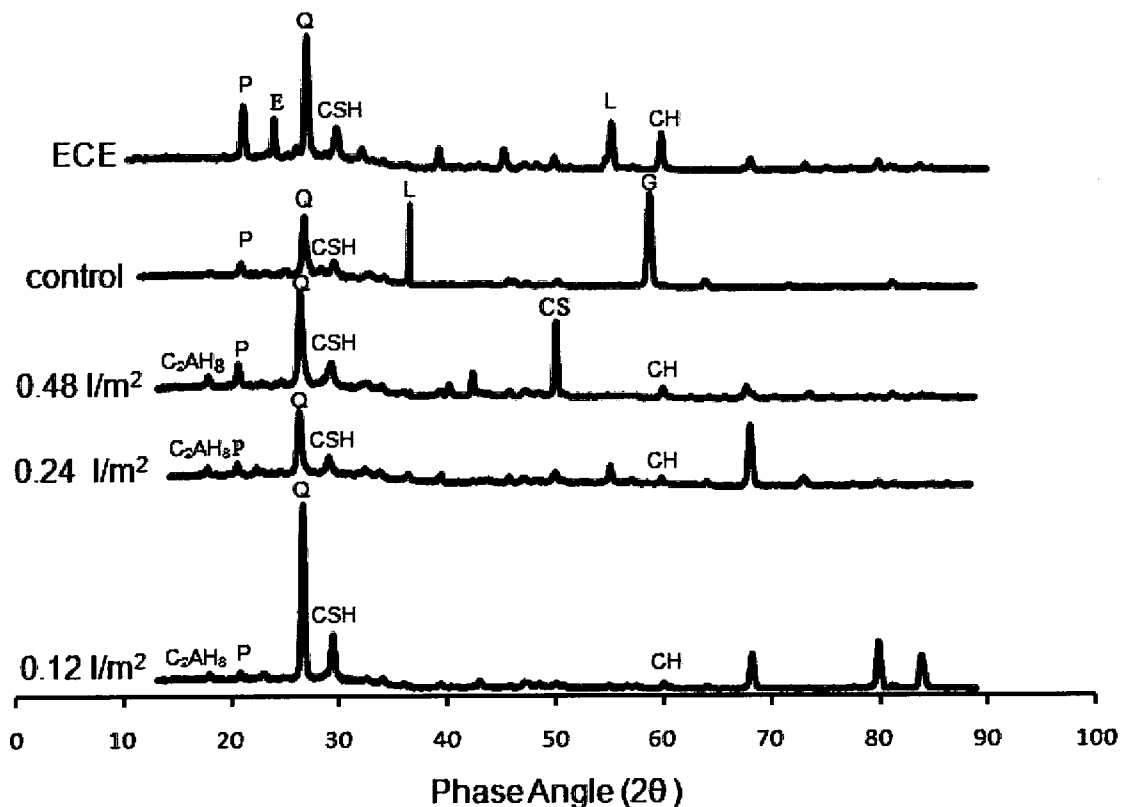
Fig 4.57 FTIR spectra of EN treated specimens and untreated control

4.3.7 X-Ray Diffraction (XRD) Analysis

Results of X-ray diffraction analyses are shown in Figure 4.58. The EN treated specimens showed minor peaks of monocalcium aluminate (CA) at 2θ of 18° , while no indications of such peaks were available on the ECE and control specimens. Peaks of portlandite, quartz and calcium silicate hydrate (C-S-H) were present among all the specimens at 20° , 27° and 30° . The control and ECE specimens exhibited the presence of lepidocrocite, while the peak of goethite was shown on the control specimen.

The CA phase among the EN treated specimens would indicate the possibility of strength enhancement. The alumina coated silica particles may have reacted with the available calcium hydroxide, leading to this phase. Phases of corrosion products in the form of lepidocrocite and goethite on the control

specimen indicate that the post saltwater exposure led to the initiation of corrosion. The EN treated specimen did not show any signs of corrosion product phases, as shown in Figure 4.58. The SEM, Raman, FTIR and XRD data confirm that EN treatment was successful in exhibiting additional C-S-H and C-A-H formation.



C_3AH_6 : Tricalcium Aluminate hexahydrate (CA), P: Portlandite, E: Ettringite, Q: Quartz, G: Goethite, L: Lepidocrocite, CS: Calcium Silicates (C_2S and C_3S),

Fig 4.58 XRD analysis of powdered concrete of beam specimens

4.3.8 Summary of the Beam Specimen Work

This section showed the experimental work conducted on beam specimens. EN treatment was applied on the beams, using dosages of 0.16, 0.33 and 0.65 liters of particles delivered per meters of beam length. The EN

treated specimens showed lower corrosion as compared to their untreated controls. Chemical analysis (XRD, FTIR and Raman spectroscopy) showed the presence of strength enhancing phases such as C-A-H and C-S-H. SEM microscopy exhibited a dense microstructure as compared to the ECE and untreated controls. Detailed conclusions of this work are described in Chapter 5.

4.4 Sulfate Attack in Concrete

Corrosion in a broad sense is the degradation of a material due to chemical attack. Sulfates like chlorides are deleterious species which enter the concrete and lead to the degradation of the cement matrix. This process is termed sulfate attack. EN treatment, when viewed as a pore blocking process from the corrosion study of Sections 4.1, 4.2 and 4.3, can be applied to mitigate sulfate attack in concrete. Section 4.4 exhibits the mitigation of an external sulfate attack using EN treatment. Section 4.4 presents to the work published by Kupwade-Patil and Cardenas in the International Conference on Advancement of Material and Process Engineering, Long Beach, CA, May 2008 and was titled "Composite nanoparticle treatments for mitigation of sulfate attack in concrete." This work was entirely conducted by the author under the supervision of Dr. Henry Cardenas.

Studies were conducted using alumina-coated silica nanoparticles to mitigate degradation due to sulfate attack (Kupwade-Patil and Cardenas, 2008). Initial sodium sulfate exposure on cylindrical concrete specimens was conducted for a period of 30 days. Extensive body cracking was observed during the exposure period. Treatments were applied to extract sulfates while nanoparticles

were being injected. The specimens were subjected to electrokinetic treatment using a constant current density of 1 A/m^2 for 7 days. Raman spectroscopy and FTIR analysis revealed significant sulfate content in the sulfate exposed specimens, which was not detected in the treated cases. A higher content of C-S-H was indicated by Raman spectroscopy. Treated specimens exhibited a 40% reduction in threshold pore size as compared to the sulfate exposed specimens. The treated specimens also exhibited a 33% increase in compressive strength and a 30% decrease in porosity. The nanoparticles appeared to act as pozzolanic porosity reducing agents that can inhibit the ingress of external sulfates, restore strength and thus mitigate early stages of sulfate attack.

4.4.1 Sulfate Exposure Results

Figure 4.59 contains images of cylinder specimens following 28 days of exposure to sodium sulfate. These specimens suffered from cracking and spallation. During this exposure period, specimen dimensions were monitored to observe expansion. Values for concrete expansion are shown in Figure 4.60. After a latent period of one week the specimens expanded by $\sim 1.25\%$. After this point, expansion continued at approximately 0.5% per week.

The sulfates were expected to react with monosulfoaluminate hydrates and also with residual unreacted phases (C_3A and C_4AF , tetracalcium aluminoferrite) (Neville, 1996; Rasheeduzzafar et al., 1994). As noted earlier, the products of these reactions tend to form the expansive phases of gypsum and ettringite. Some debate exists as to which product is most responsible for expansion related damage (Mehta, 1983; Bing and Cohen, 2000). The

expansion observed in this study could not be attributed to the formation of either ettringite or gypsum.

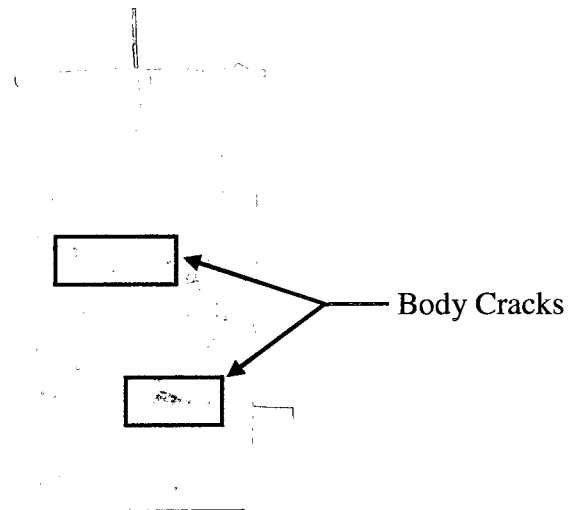


Fig 4.59 Damage due to sodium sulfate exposure

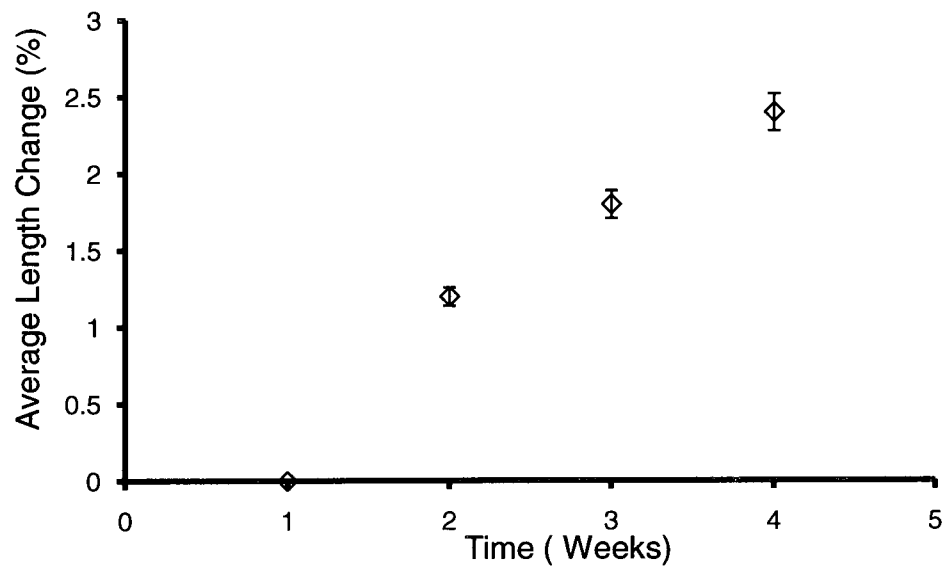


Fig 4.60 Sulfate induced expansion during the initial exposure applied to 12 specimens over a course of 4 weeks

4.4.2 Compressive Strength and Porosity Results

The progress of the sulfate attack was also evaluated by measuring the compressive strength of the cylinders. Average compressive strengths were measured at the end of each week through 4 weeks of sodium sulfate exposure (see Figure 4.61). The compressive strengths of the sulfate exposed specimens were compared to control specimens that were subjected to limewater curing. No difference in strength was observed after the first week of exposure. Differences in strength between sulfate exposed and limewater controlled specimens manifested at the end of the second week and continued to increase after the third and fourth weeks.

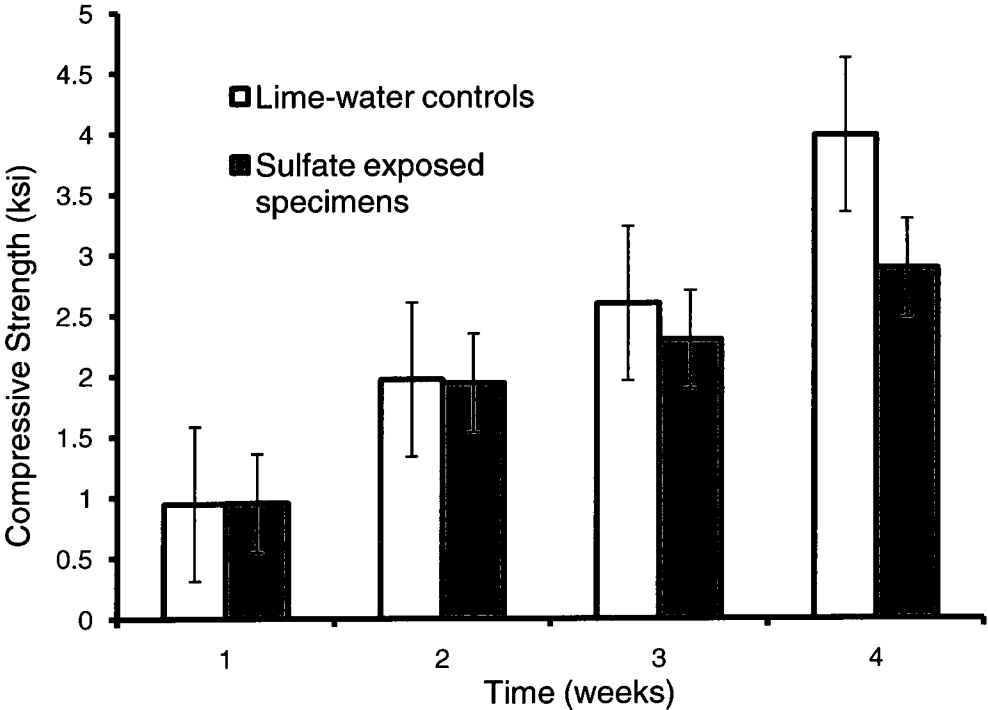


Fig 4.61 Influence of sodium sulfate exposure on compressive strength

For the control specimens, strength decrease of 13% was observed at the end of third week, and a total decrease of 38% was observed at the end of the fourth week. These results were similar to that of Boyd and Mindess who observed a 40% decrease in compressive strength when concrete was exposed to sulfate ions for 50 days (Boyd and Mindess, 2004). Nielsen demonstrated that ettringite crystals are generally responsible for formation of cracks, such as those shown in Figure 4.59 in this study (Nielsen, 1966). Each of these studies found that sulfate ingress appeared to cause significant cracking and therefore a decrease in the compressive strength. In the current work, the decrease in compressive strength among the sulfate exposed specimens was first observed after the second week of exposure. This suggests that some time passed before sufficient sulfate ions could start producing serious expansion. This delay is not surprising since time is required for the necessary diffusion and crystal growth to occur prior to causing damage.

In order to mitigate the damage from sulfate attack, the specimens were subjected to electrokinetic nanoparticle (EN) treatment. While these treatments were in progress, the control specimens were removed from sulfate exposure and placed in limewater. At six weeks all these controls as well as the treated specimens were subjected to strength testing. EN treated specimens exhibited a 33% higher compressive strength than the Na_2SO_4 exposed control specimens (see Table 4.6).

Table 4.6 Compressive strength and porosity analysis

Type of Exposure	Compressive strength (psi)	Porosity by WL (%)	Porosity by MIP (%)	Threshold Pore Diameter (μm)
Lime water	4000	33	31	123
Sulfate Exposed	2100	39	40	221
EN Treated	2800	26	29	58

Table 4.6 also shows porosity values obtained from simple capillary pore fluid evaporation as well as through MIP analysis. As a point of reference, pore diameters corresponding to different cementitious materials are shown in Table 4.7 (Winslow, 1989). Figure 4.62 shows the pore size distribution curves obtained in this study presented as the incremental intrusion volume versus pore diameter. The threshold pore diameter (d_{th}) represents the minimum diameter of the pores that form a continuous network throughout the cement paste and marks the commencement of percolation. Threshold diameters obtained from Figure 4.62 for sulfate exposed, EN treated and limewater control specimens are also shown in Table 4.6. The sulfate exposed specimens exhibited threshold pore size values of 221 μm , which lie within the typical range for concrete (Winslow, 1989). By comparison the treated specimens exhibited threshold pore size values of 58 μm .

Table 4.7 Typical pore diameter ranges for concrete materials

Material Type	Diameter (μm)
Cement Paste	0.001-1.4
Concrete	0.001-250
Aggregate	0.01-100
Concrete Block	0.01-750

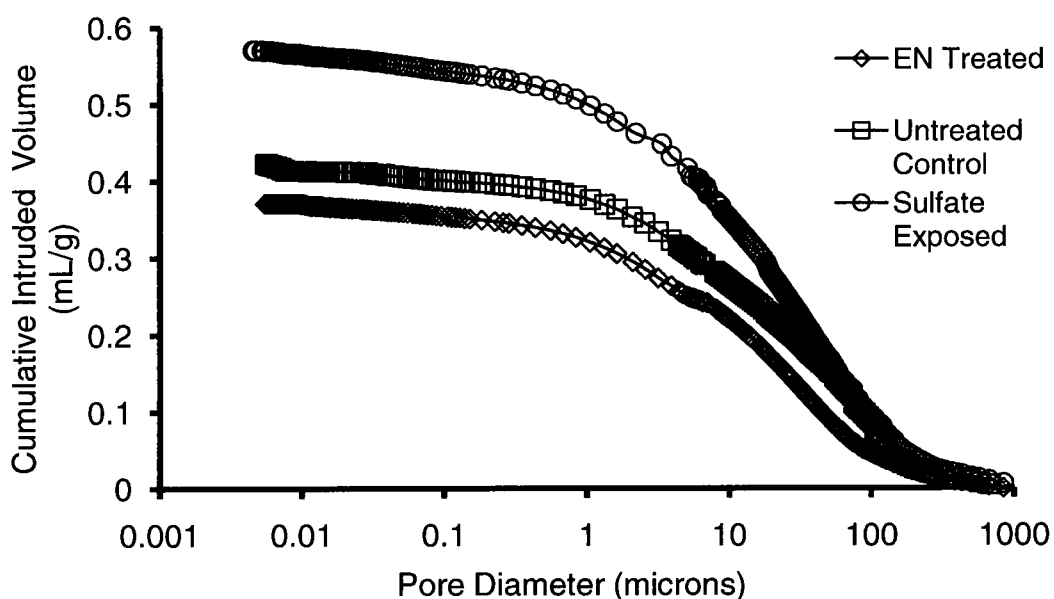


Fig 4.62 Pore size distributions using mercury intrusion porosimetry (MIP)

The extensive body cracks that formed due to ingress of sulfates and related ettringite formation clearly led to the concrete expansion and apparently resulted in large apparent pore sizes. EN treated specimens and lime water controls exhibited lower values of threshold pore diameter by a factor of ~4 and ~2 when compared with the sulfate exposed specimens.

As suggested by earlier work, the ingress of nanoparticles may have reduced the quantity of $\text{Ca}(\text{OH})_2$ by converting it to C-S-H, thus making it less available for reaction with sulfates. Simultaneous formation of C-A-H and C-S-H phases may have led to increases in strength. Even without these possible reactions, simple loading of pores with nanoscale pozzolans can reduce pore volume, and it is well recognized that a smaller pore volume tends to increase strength even if the new material is somewhat weaker than the surrounding solid phases (Neville 1996).

On average, Na_2SO_4 exposed specimens exhibited a 39% volume porosity and a compressive strength of 2100 psi as compared to the EN treated specimens, which showed a 26% volume porosity and a 2800 psi strength. The EN treated specimens thus exhibited a 33% higher compressive strength and a 13% lower porosity than the Na_2SO_4 exposed specimens (see Table 4.6). Electrokinetic nanoparticle treatment was successful in reducing the porosity of the sulfate damaged specimens and increasing the compressive strength.

Other pore structure parameters were also examined. Initially, the limewater control specimens exhibited a threshold pore size of 123 μm and an average volume porosity value of 31%. The specimens exposed to sulfates developed body cracks, probably due to ettringite crystal growth and gypsum formation. This exposure may also have led to a threshold pore size increase from 123 μm to 221 μm . The total volume porosity also increased up to 40% from the 31% value of the limewater controls. These observations indicate that sulfate attack expanded both the threshold pore size and volume porosity of the sulfate exposed specimens.

4.4.3 Microstructural Analysis

Scanning electron microscopy (SEM) was conducted on the sodium sulfate exposed specimens and the EN treated specimens. Figures 4.63 A and B (higher magnified image) show the needle-like ettringite crystals that were observed in abundance on the sodium sulfate exposed specimens. Gypsum veins were also observed along with the ettringite, indicating a significant alteration of the microstructure as shown in Figure 4.63 A. Aluminum, calcium

and small sulfur peaks were observed in both spectra, as shown in Figures 4.63 A and B (Mindess et al., 2003; Sahmaran, 2006).

As expected, the aluminum and especially the calcium peaks were relatively taller for the EDS spectrum that was focused on the section exhibiting classic ettringite needles. As shown in Figure 4.64, ettringite was also found associated with a highly porous region. It is conceivable that this apparent porosity may actually be damage induced by the growth of these needles. The specimens were initially exposed to sodium sulfate from an external source. This could have induced a conversion of monosulfate to ettringite, which would have provided a mechanism for the expansion and disintegration recorded in Figures 4.59, 4.60, and 4.64 (Skalny et al., 2001; Neville, 2004).

The expansion and damage induced by ettringite formation could explain the apparent increases in porosity and threshold pore diameters recorded in Table 4.6. Further evidence of this damage was observed in the strength reductions shown in Figure 4.61. Based on these observations, the sulfate exposure provided in this study caused the concrete to exhibit classic evidence of sulfate attack.

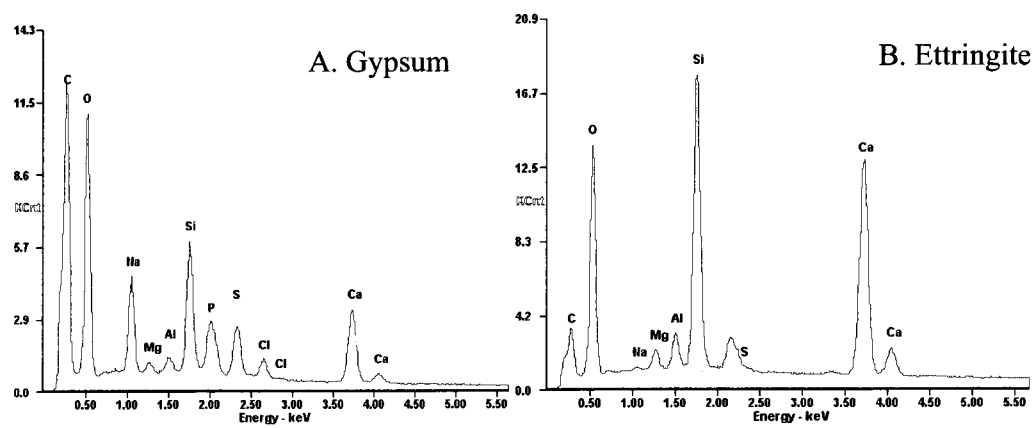
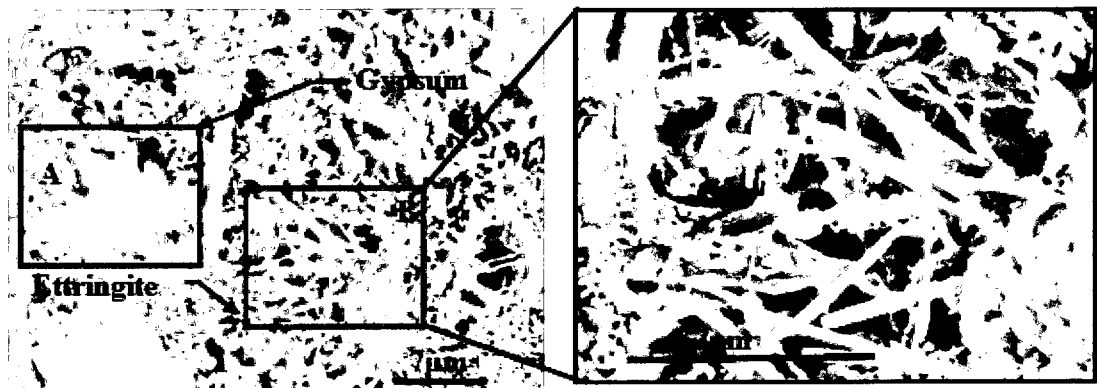


Fig 4.63 SEM micrograph of gypsum and ettringite

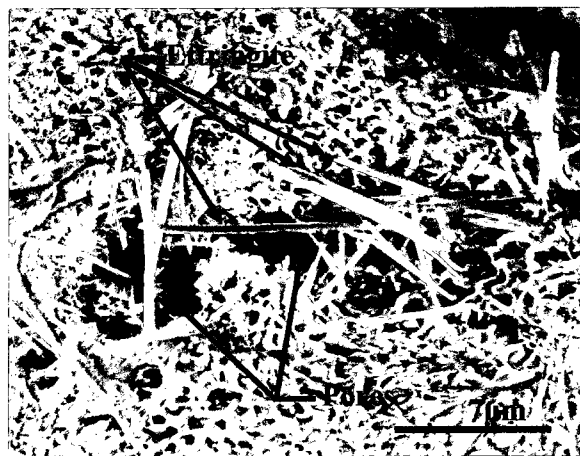


Fig 4.64 SEM micrograph of ettringite needles demonstrating porous volume

Backscattered electron (BSE) analysis was used to examine the impact of nanoparticle treatment. BSE images of concrete that was epoxy impregnated and polished were subjected to EDS analysis, as shown in Figures 4.65 A and 4.65 B. Large macro pore areas of apparent damage were observed on the sulfate exposed specimens (Figure 4.65 A), unlike the treated specimens which showed smaller and fewer pores (Figure 4.65 B).

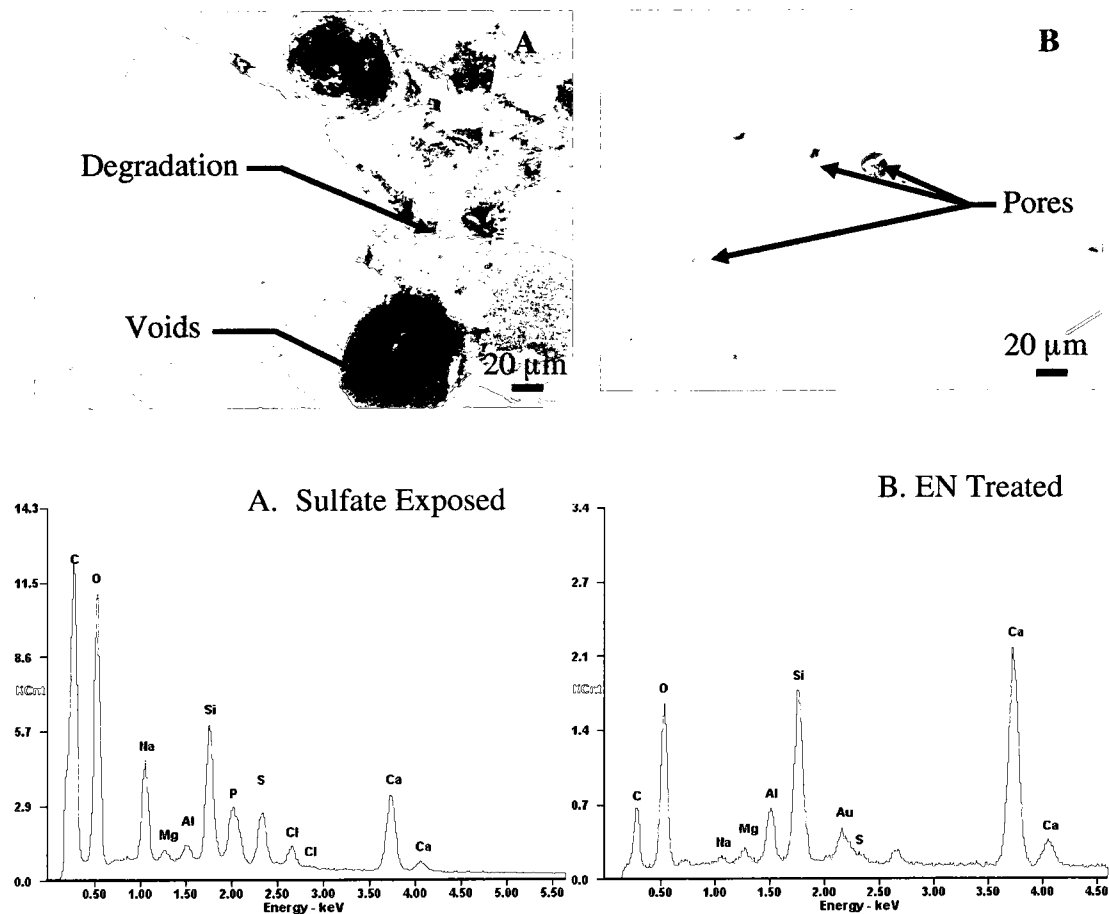


Fig 4.65 BSE image and EDAX micrograph of epoxy impregnated sulfate exposed and EN treated specimen indicating pores

The EDS analysis on the sulfate exposed specimens yielded a 2.9% weight content of sulfur and 4.8% sodium. The treated specimens exhibited

concentrations of sodium and sulfate that were both less than 1% . The different sulfate contents suggest that the electrokinetic treatment had removed some of these species from the concrete. It was not expected that the sodium would be diminished by the treatment. The reason why the sodium content was lower may be due to the fact that the electric field would have drawn the sodium ions to the titanium electrode, which was located further into the specimen than the locations examined via BSE. Based on these observations, it appears that the EN treatment was effective in reducing the sulfate content of the concrete specimens.

As noted earlier, limiting the alumina content of concrete is one way of increasing sulfate resistance. In this work, the amount of alumina present in the concrete was increased slightly while the sulfate content was being reduced. This increase in alumina content can lead to formation of various C-A-H and C-S-H phases as reported in the literature (Mindess, 2002). It is conceivable that Al^{3+} could form as an intermediate step in C-A-H formation. This availability of Al^{3+} could be problematic since this ion can facilitate the formation of ettringite and could thus worsen susceptibility to sulfate attack. In contrast, earlier work has shown that the alumina-coated silica nanoparticle tends to form C-S-H when it enters concrete. Other work has also shown that Al^{3+} incorporated into the C-S-H phase does not lead to ettringite expansion (Odler, 2000; Taylor, 1997). It is notable that a small amount of alumina was injected. It constituted approximately 7% by weight of each particle. Given the small amount of alumina that was injected, coupled with the removal of sulfate, it appears unlikely that the alumina

coating on these particles would significantly encourage sulfate attack. Removal of this alumina coating would be problematic since it would cause the particles to lose their positive charge and render the electrokinetic transport difficult to accomplish.

4.4.4 Raman Spectral Analysis

Raman spectra of sulfate exposed, limewater controls, and EN treated specimens are shown in Figures 4.66 A, B and C. The sulfate exposed specimens exhibited a sharp peak of S-O bond vibrations at 1083 cm^{-1} as shown in Figure 4.66 A (Kirkpatrick et al., 1997). A minor peak for C-S-H was also observed at 455 cm^{-1} . This peak generally lies within the broad bandwidth region of $400\text{-}600\text{ cm}^{-1}$ that is associated with C-S-H. Figure 4.66 B shows, a thaumasite peak that was observed at 1072 cm^{-1} . This peak is considered to be a combination of carbonate and sulfate group signatures (Potgieter-Vermaak et al., 2006; Brough and Atkinson, 2001). The EN treated specimens exhibited sharp peaks located at 459 cm^{-1} , indicating C-S-H as shown in Figure 4.66 C.

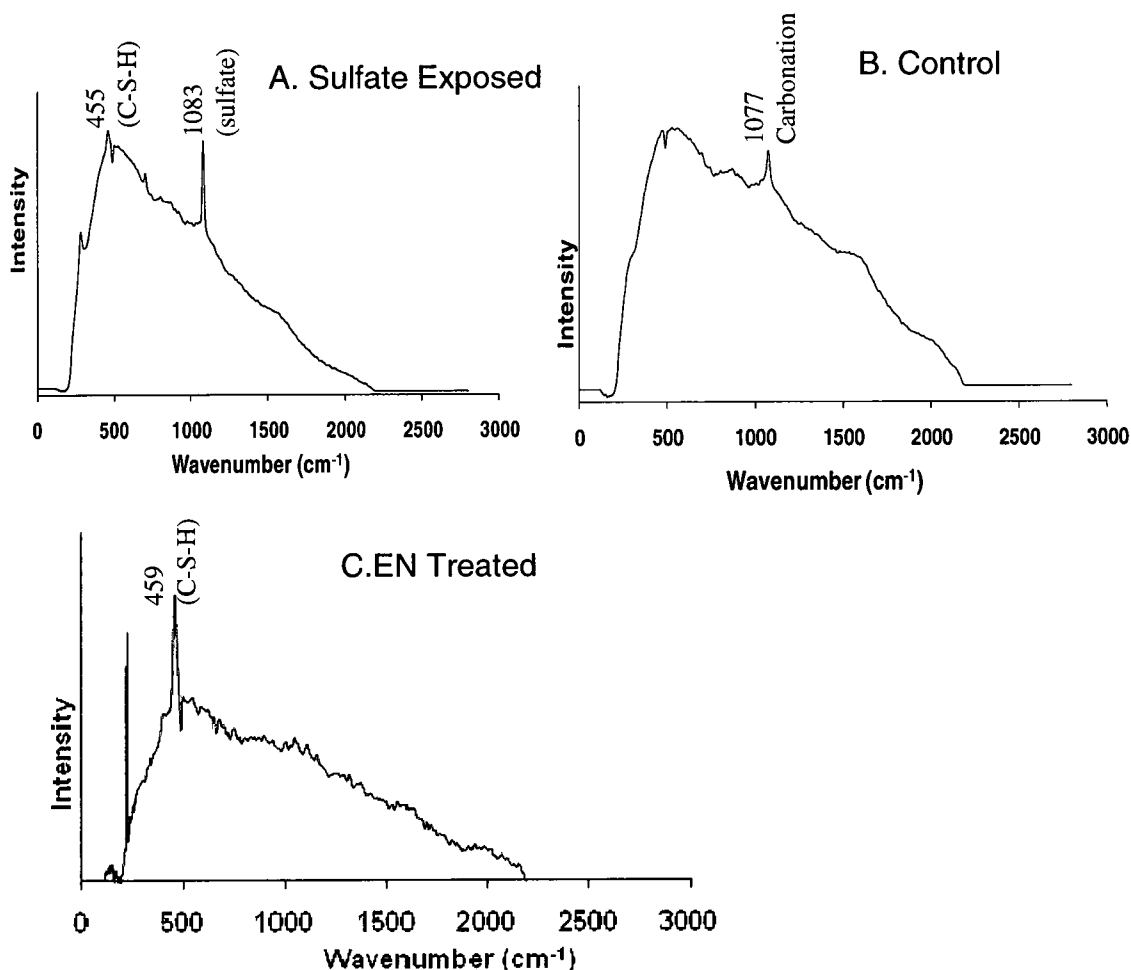


Fig 4.66 Raman spectroscopy of EN treated specimen depicting sulfate, carbonation and C-S-H phase

4.4.5 FTIR Analysis

Specimens were also subjected to FTIR analysis. The FTIR spectra of the sulfate-exposed and the EN treated specimens are shown in Figure 4.67. The treated specimens exhibited a broad band in the range of 3400-3600 cm⁻¹, indicating the OH vibrations of water molecules in monocalcium aluminate hydrate, dicalcium aluminate hydrate and tri-calcium aluminate hexahydrate (Carrasco et al., 2008). These specimens also showed the presence of C-H at

1527 cm^{-1} . The untreated specimens appeared to exhibit C-S-H as represented by Si-O-Si and Si-O peaks at 698 cm^{-1} and 1120 cm^{-1} . In addition, strong peaks of ettringite were observed on sulfate exposed specimens and untreated controls at 877 cm^{-1} (Pajares et al., 2003). The EN treated specimen exhibited relatively weak peaks for ettringite. CO_3^{2-} peaks at 1440 cm^{-1} indicated carbonate in the untreated controls (Carrasco et al., 2008) All the specimens exhibited SO_4^{2-} bonds at 680 cm^{-1} .

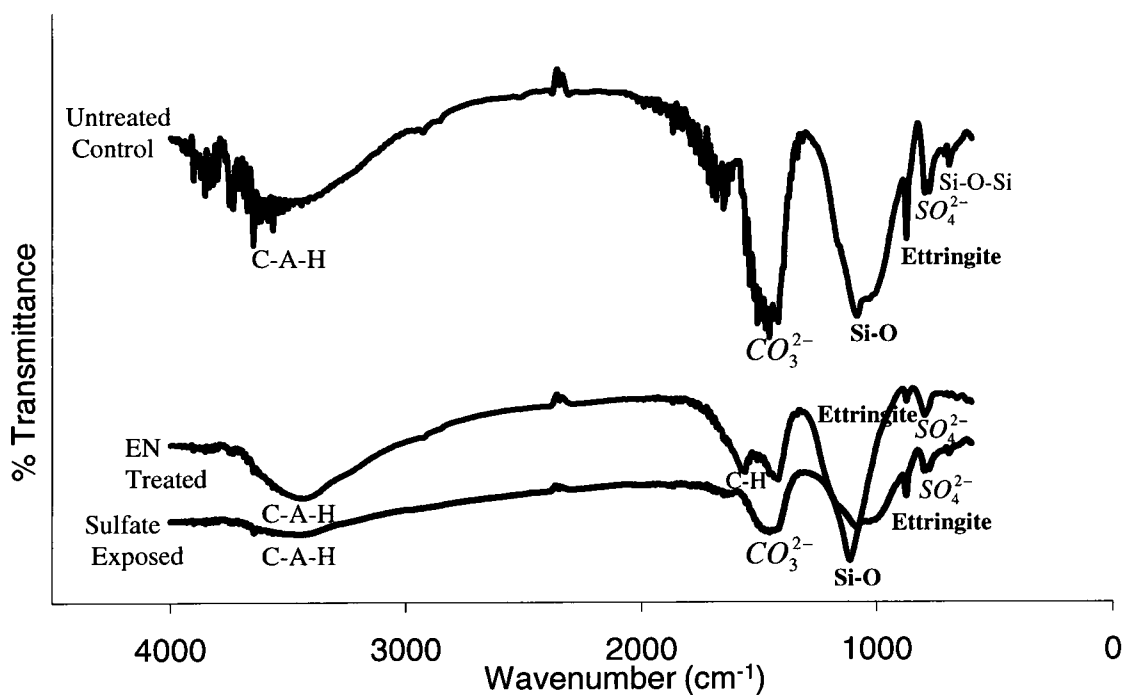


Fig 4.67 FTIR transmittance spectra of sulfate exposed, untreated control and EN treated specimen

FTIR spectra of precipitates formed from the mixture of nanoparticles and simulated pore fluids are shown in Figure 4.68. The alumina-coated silica mixture precipitates exhibited peaks at 777 cm^{-1} and 1525 cm^{-1} , indicating the presence of C-H associated with xylene (which was used to remove methanol

during the sample dewatering process) (Morrison and Boyd, 1992). Peaks observed at 1100 cm^{-1} were assigned to Si-O bonds in the C-S-H variant, jennite. Si-O peaks are expected to fall in the range of $900\text{-}1100\text{ cm}^{-1}$ and are considered to be silicon oxide bonds that are integral to the C-S-H structure (Yu et al., 1999). In contrast, the colloidal alumina mixture precipitate appeared to exhibit short peaks of possible C-O bonds at 1110 cm^{-1} . Both mixture precipitates also exhibited broad peaks of C-A-H in the range of $3400\text{-}3600\text{ cm}^{-1}$. Bonds of CO_3^{2-} were also located at 1410 cm^{-1} in both cases.

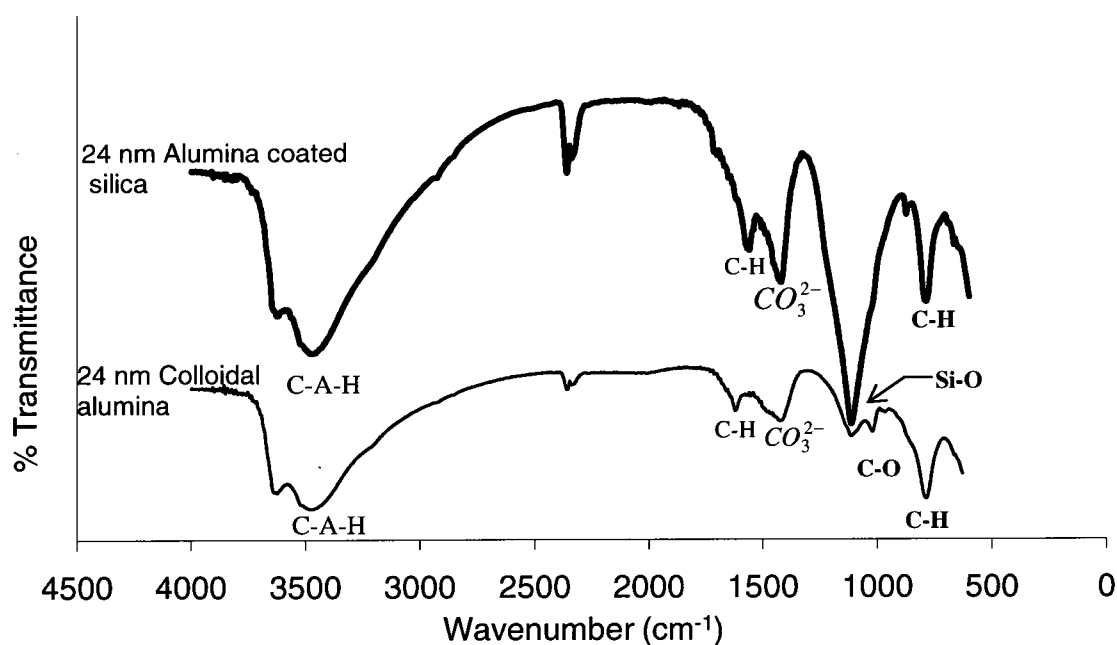


Fig 4.68 FTIR spectra of alumina-coated silica with colloidal alumina mixed with simulated pore fluid

As shown in Figure 4.67, FTIR analysis exhibited weaker peaks for ettringite as compared to the untreated controls and the sulfate exposed specimens. In addition, the Raman spectroscopy results of Figure 4.66 show no

sulfate peaks on the EN treated specimens while the sulfate exposed specimens indicated sulfate peaks. It is possible that the reduction of sulfate during the treatment period could have limited the extent of monosulfate conversion. These observations indicate that the sulfates were successfully extracted. It is also clear that this process was successful in mitigating the formation of ettringite.

The presence of the SO_4^{2-} bond (Figure 4.67) in the EN treated specimens indicates that the sulfate extraction aspect of the treatment did not fully remove all the available sulfates. Similar removal limitations have been observed in chloride extraction processes occurring over a 6-8 week period (Farjardo et al., 2006; Orellan et al., 2004; Marcotte et al., 1999). Since the sulfate ion is approximately three times larger than a chloride ion, it is clear that less extraction would be anticipated, especially for the relatively limited 14-day treatment conducted in this study. Future studies will explore the use of longer treatment periods. In the current study, the treatment resulted in a 33% strength increase that partially offset the 50% strength reduction suffered by the sulfate exposed concrete. This suggests that the EN treatments were successful in reducing the severity of sulfate attack despite the very limited duration of the extraction process.

EN treated specimens exhibited a porosity reduction of 13% compared to the sulfate exposed specimens (see Table 4.6). At the same time, these EN treated specimens exhibited a 33% increase in compressive strength. This reduction in porosity can be at least partially associated with the increase in strength (Mindess, 2001). In addition to the porosity and strength data, Raman

spectroscopy showed the presence of strong C-S-H peaks among the EN treated specimens. The pozzolanic reaction between the alumina-coated silica nanoparticles and calcium hydroxide within concrete was first observed in corrosion mitigation work conducted in 2007 (Mindess, 2001). It appears that this conversion was also manifested in the present study, yielding the enhanced C-S-H peaks observed in Figure 4.66. Mindess further noted in his work that calcium hydroxide conversion can “lead to considerable strengthening of the cement-aggregate bond, and hence of the concrete itself.” In the current work, this conversion may also have led to C-A-H formation. FTIR analysis detected broad C-A-H peaks (see Figure 4.67). Differences in peak strengths observed among the cases tested were not significant in the concrete samples, probably because of the relatively large population of C-A-H phases already present. In contrast, the mixture of both nanoparticle candidates combined with simulated pore fluid (see Figure 4.68) showed strong peaks generally associated with C-A-H formation. In any case, the low dosage of alumina was too low to yield a significant increase in C-A-H in the concrete itself (Mindess, 2001). Based on these observations, the 33% increase in strength among the EN Treated specimens may have been associated with both the simple reduction in porosity that comes from the injection of nanoparticles and the conversion of calcium hydroxide.

FTIR analysis of the untreated controls indicated the presence of carbonation as exhibited by relatively strong CO_3^{2-} bonding peaks at 410 cm^{-1} in Figure 4.67. This peak was much weaker for both the sulfate exposed and EN

Treated specimens. In the sulfate exposed specimens, the increased ettringite formation provided more opportunity for carbonate absorption since, as noted in the literature, it tends to form an ettringite analog (Ramachandran and Beaudoin, 2001). This activity would tend to reduce the population of CO_3^{2-} ions, leading to the weaker peak observed in Figure 4.67. In addition sulfate attack would take up calcium hydroxide for gypsum formation, leaving less available for carbonation. Similarly, a sharp carbonation peak (1077 cm^{-1}) was observed via Raman spectroscopy in the untreated controls, shown in Figure 4.66. Neither the sulfate exposed nor the EN treated specimens exhibited carbonation peaks via Raman spectroscopy. The tendency for carbonation has also been related to the pore structure of hardened cement paste. In the current study, the untreated control specimens exhibited higher threshold pore diameters than the EN treated cases by a factor of ~ 2.4 . This implies a difference in pore area by a factor of ~ 4.5 (see Table 4.6). This greater area of pore access probably facilitated the carbonation observed in the untreated controls. The sulfate exposed specimens exhibited an average threshold pore size that was larger than the EN treated cases by a factor of ~ 4 . These observations indicate that the EN treatment was useful in hindering carbonation by acting as a pore size reducing agent.

Porosity reduction effectiveness of the particle treatment can be analyzed by determining the number of particles that were supplied to fill the available pores. The following analysis explores this point.

The total volume of a cylindrical specimen is given by,

$$\pi (1.5\text{ in})^2 6\text{ in} = 42\text{ in}^3 = 700 \times 10^3\text{ mm}^3 \quad [49]$$

The porosity analysis in Table 4.6 indicated that 40% of the total volume (17 in^3) of this cylinder was occupied by pores. The total volume transport rate of particles that were available (from the treatment fluid) to fill the pores (when the fluid is refreshed every two days) is given by

$$\text{Particle Volume Transport Rate } (V) = \frac{f_p V_l}{t} \quad [50]$$

$$\frac{0.12 \times 30.5 \text{ in}^3}{2 \text{ day}} = 1.83 \text{ in}^3/\text{day} \quad (30 \text{ mm}^3/\text{day}) \quad [51]$$

where f_p is the volume fraction of fluid that contains particles for treatment, V_l is volume of treatment fluid used during a treatment, and t is time period of treatment. Comparing this value to the 17 in^3 ($280 \times 10^3 \text{ mm}^3$) volume of total available pores in the specimen indicates the amount of pore space that the particles could have filled during the seven day treatment period. The particle volume filled due to EN treatment for seven days was 12.8 in^3 ($210 \times 10^3 \text{ mm}^3$). This indicates that the available volume of particles over seven days could only have been able to fill 75% of the pore volume. Based on this particle volume transport rate, increasing the period of treatment by three more days would have filled the total estimated pore volume of 17 in^3 ($280 \times 10^3 \text{ mm}^3$). This could also have led to additional strength enhancement since the porosity could have been reduced by an additional 10%.

The porosity of the EN treated specimens was lower (26%) than the limewater exposed specimens (33%). This appeared to indicate that the porosity was reduced by the particle treatment. In contrast, the strength recovery was limited. The EN treated specimen strength only improved to 2800 psi as

compared to the 4000 psi strength of the limewater exposed specimens. This limited strength recovery had two possible origins. The first consideration stems from the fact that alumina was delivered to the concrete interior where it could have reacted to form an ettringite precursor that could combine with available sulfates to form ettringite. A more likely cause for the strength shortfall has to do with the macrocracking and spallation observed in Figure 4.59. The nanoparticle treatment would clearly be insufficient to fill in such large defects. The treatment could only be expected to “heal” micro-cracking as opposed to the macrocracking that can develop. Based on these observations, it appears that nanoparticle treatments are most suitable for restoring the strength that is lost from the accumulation of microcracks. From this standpoint, nanoparticle treatments are expected to be more beneficial before sulfate attack has reached an advanced stage.

Future research may indicate a negative impact due to the conversion of injected alumina into ettringite. This possibility may exist during the period prior to sufficient reduction of sulfate content. In addition, long after a given treatment, remaining macrocracks may allow continued soil or waterborne contact with sulfates, permitting the degradation to resume. Future work will focus on development of a coated-silica that carries a positive charge but does not have the potential for promoting ettringite.

CHAPTER 5

CONCLUSION AND FUTURE WORK

The conclusions from Sections 4.1 to 4.4 are categorized in four subdivisions, and a final conclusion is drawn from all these sections.

5.1 EN Treatment on Young and Mature Concrete

Based on the results of this investigation, the following conclusions are drawn:

1. Strength, porosity, and corrosion rate results indicate that the EN treatment was effective in keeping the pH and chloride content below threshold levels for both young and mature concrete.
2. SEM, FTIR and XRD examinations indicate that C-S-H and C-A-H were formed during treatment, which played a role in raising the tensile strength.
3. EN treatment was found useful in mitigating reinforcement corrosion in both relatively mature and young concrete.
4. Corrosion rates on the EN treated specimens increased due to the limited chloride extraction effectiveness. Diffusion of chloride species through the annulus of the particle-treated pore wall may have also permitted an increase in the corrosion rate.

5.2 EN Treatment on ASTM G109 Specimens

1. The EN treatment was successful in mitigating reinforcement corrosion and prevented concrete cracking over 300 days of the post treatment exposure.
2. The controls exhibited a higher corrosion rate by a factor of 23 when compared to the EN treated specimens.
3. Average mass loss rates exhibited on the rebar of the controls was higher by a factor of 34 on the top bars and by 20 for the bottom bars when compared to the EN treated specimens.
4. Electrochemical impedance spectroscopy (EIS) studies indicate that the EN treated specimens were in a passive state of corrosion as compared to their untreated controls.
5. EN treatment exhibited densified microstructure as compared to their controls. The dense microstructure may have prevented the ingress of chloride ions entering into the capillary pores.
6. EN Treatment prevented cracking in concrete as compared to the control specimens.

5.3 EN Treatment on Reinforced Concrete Beams

1. The EN treatment was successful in mitigating moderate to high reinforcement corrosion.
2. The controls exhibited a higher corrosion current density by a factor of 144 as compared to the EN treated specimens.

3. EN treated specimens exhibited a lower chloride content by a factor of 4 and a higher porosity reduction of 74% as compared to the untreated controls at the rebar/concrete interface.
4. Strong peaks of calcium silicate hydrate (C-S-H) and calcium aluminate hydrate (C-A-H) were detected by Raman spectroscopy, XRD and FTIR analysis on the EN treated specimens. The nanoparticles reacted with the available calcium hydroxide, leading to these strength enhancing phases.
5. This study showed that EN treatment was applicable to large structures.
6. Higher dosages lead to better porosity reduction as compared to limited dosage treatments.

5.4 EN Treatment to Mitigate Sulfate Attack in Concrete

1. An average decrease of 38% in compressive strength was observed among the sulfate exposed specimens when compared to the control specimens. The specimens that were EN treated following sulfate exposure exhibited a 33% increase in compressive strength and a 13% decrease in porosity when compared to the sulfate exposed specimens. It is clear from this work that a nanoparticle treatment can partially restore strength that has been decreased by sulfate attack.
2. EN treated specimens exhibited a reduction in threshold pore diameter by a factor of ~ 4 as compared to the sulfate exposed specimens. The impact of nanoparticle treatment on the pore structure is expected to significantly slow the return of sulfates and the resumption of sulfate attack.

3. Raman and FTIR observations indicated that sulfates were successfully extracted.
4. The nanoparticles acted as pore blocking agents that reduced porosity and increased strength, thus mitigating much of the prior damage.
5. For the first time, sulfates were successfully extracted from the sulfate damaged concrete.
6. Nanoparticle treatments are expected to be most beneficial before sulfate attack has reached an advanced stage.

5.5 Overall Conclusion Regarding EN Treatment

1. EN treatment was successful in mitigating both chloride and sulfate induced corrosion concrete.
2. EN treatment showed that the nanoparticles acted as pore blocking agents by packing the capillary pores and hindering corrosion.
3. EN treatment was successful in reducing porosity by forming a dense cement matrix.
4. Strength enhancement phases such as calcium silicate hydrate (C-S-H) and calcium aluminate hydrate (C-A-H) were detected in the EN treated specimens as compared to their untreated controls.
5. EN Treatments prevented cracking in reinforced concrete during a three year period exposure.
6. Effectiveness of the EN treatment depends on the particle dosage and length of the treatment.

5.6 Future Work

1. Studying the effectiveness of the treatment using the combination of macro and nanoparticles. This approach may be used to prevent cracking in concrete.
2. Characterization of the effectiveness of un-reacted nanoparticles and the influence of each phase (C-S-H or C-A-H) formed during the EN treatment.
3. Application of EN treatment at elevated temperature on reinforced concrete could be significant to study in the future.

APPENDIX A

MERCURY INTRUSION POROSIMETRY (MIP)

Mercury intrusion porosimetry (MIP) is a widely and commonly used method and a useful technique in characterizing the pore structure of hardened cement paste (Aligizaki, 2006; Winslow, 1978; Cook and Hover, 1993). This technique is used to study the internal porous structure of concrete, ceramics, clays and bones. This method predicts some of the parameters, like threshold pore diameter, critical pore diameter, total porosity, mean and median pore diameters. The concept is based on the principle of non-wetting liquids like mercury which can ingress into the porous material if only pressure is applied. Mercury poses a contact angle greater than 90° , which indicates if a porous specimen is in contact with mercury, then it will not intrude unless a certain pressure is applied.

The commercially available mercury porosimeters are widely used for characterization of pore structure (Aligizaki, 2006). The schematic layout of the MIP system is shown in Figure A.1. The system is mainly comprised of a specimen holder, high pressure vessel, vacuum apparatus, pressure generator, hydraulic fluid and equipment for process monitoring.

A penetrometer is used as a specimen holder and contains the mercury which is used for filling the pores (Aligizaki, 2006). A high pressure vessel the specimen cell is made of steel. A vacuum pump is used to take off air from the specimen cell and to inject the mercury upon release of the vacuum. Hydraulic fluid is used to initiate the pressure from the generator to the specimen holder (penetrometer).

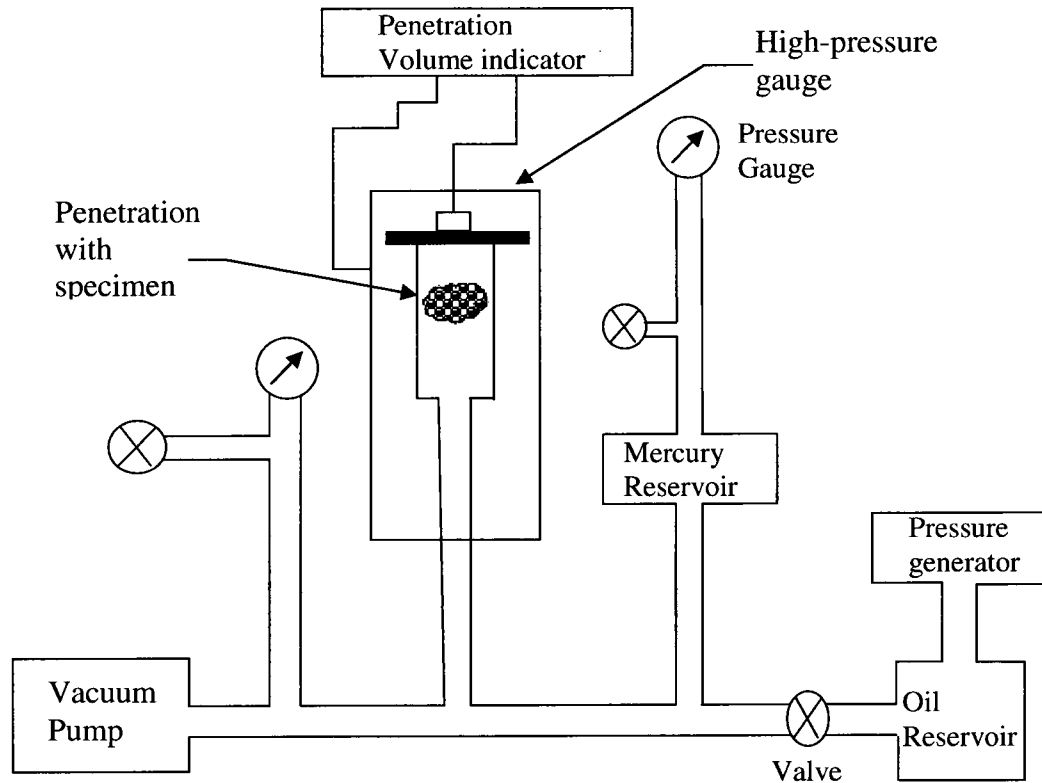


Fig A. 1 Schematic setup of MIP (Adapted from Aligizaki 2006, p.62)

An electronic pressure transducer is used to monitor the pressure as the mercury penetrates inside the capillary pores (Aligizaki, 2006). The testing procedure is comprised of low pressure followed by high pressure analysis. The low pressure analysis is initiated by pneumatic pressure up to two atm. The high pressure test is conducted by means of hydraulic pressure using the hydraulic fluid (oil).

Washburn proposed a relationship between pressure (ΔP) and radius of a cylindrical pore (r) that is valid for non wetting liquids as shown in Equation 52,

$$\Delta P = - \frac{2\sigma \cos \theta}{r} \quad [52]$$

where ΔP = pressure ($\Delta P >$ ambient pressure) necessary for mercury intrusion, r = radius of cylindrical pore being intruded, σ = surface tension of mercury, θ = contact angle between the pore wall and mercury (for wetting angles $< 90^\circ$, $\cos \theta$ is positive)

The forces developed due to the intrusion of mercury inside the pore wall are shown in Figure A.2 (Aligizaki, 2006). The forces originate due to the interfacial tensions acting along the normal plane and are the product of the surface tension of the mercury (σ) and the pore radius (refer to Equation 53). The reaction force due to the applied pressure that forces the mercury into the pore is given by Equation 54.

$$F_1 = -(2\pi r_p)\sigma \cos \theta \quad [53]$$

$$F_2 = (\pi r_p^2)P \quad [54]$$

where F_1 = force that drives the mercury out of the pore, r_p = the pore radius, σ = surface tension existing between the mercury and the pore wall, P = applied pressure.

The pore size distribution is related to the pore radius by

$$D_v(r) = -\frac{dV}{dr} \quad [55]$$

where $D_v(r)$ = pore size distribution function, dV = change in the pore volume and dr = change in pore radius. Differentiating Equation 53 and considering the surface tension (σ) and the contact angle (θ) constant we get

$$Pdr + r_p dP = 0 \quad [56]$$

where dP = change in applied pressure

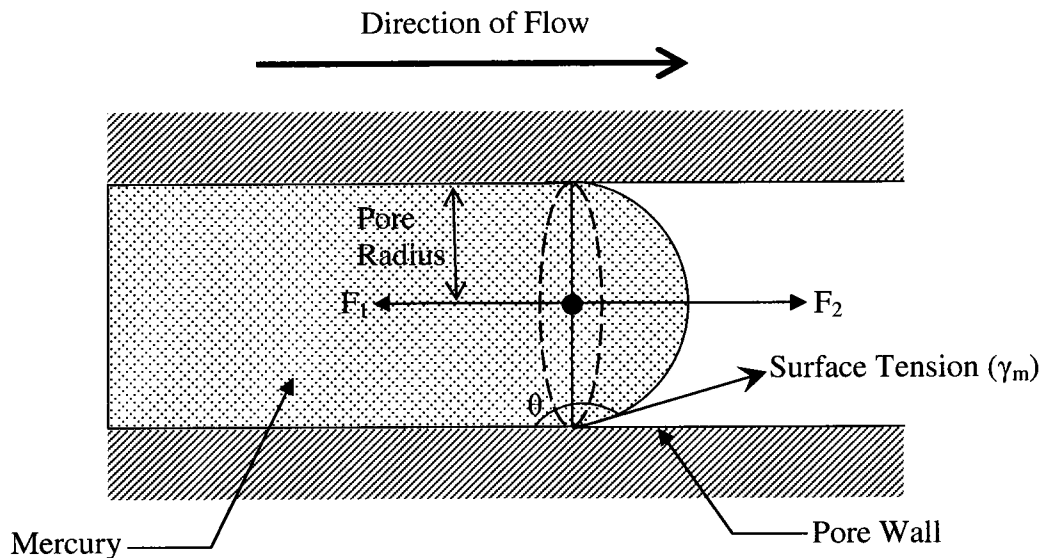


Fig A. 2 Forces inside a capillary pore (Adapted from Aligizaki, 2006, p.66)

Using the value of d_r from Equation 55 and substituting the value in Equation 56

$$D_v(r) = \frac{P}{r_p} \left(\frac{dV}{dP} \right) \quad [57]$$

This equation interprets that as the applied pressure to the mercury increases the amount of volume of mercury driven inside the pores also increases. (Aligizaki, 2006). Pore size distributions are analyzed by plotting a curve of pore volume (dV) versus the pore radius(dr). Specific surface area of the pores that are intruded with mercury is given by,

$$S = \frac{1}{\gamma_m \cos \theta} \int_0^v p dV \quad [58]$$

where S = pore surface area, γ_m is the surface tension between mercury and pore wall (N/m), P = applied pressure drive the mercury into the pore (m^2), $dV =$

change in pore volume (m^3), and θ is the contact angle between mercury and pore wall.

The plots that are commonly used to study the pore structure parameters are pore diameter versus cumulative intrusion volume, cumulative intrusion volume versus pressure and incremental surface area versus pore diameter (Aligizaki, 2006). The parameters that are drawn from the plots are total porosity, critical pore diameter and threshold pore diameter. The porosity is defined as the ratio of total intruded mercury volume to the total volume of the sample. Specimen volume is the volume of mercury filling the specimen cell when the sample is present.

Winslow and Diamond (1970) showed a significant difference between the threshold pore diameter and critical pore diameter, as shown in Figure A.3. The threshold pore diameter is the largest pore diameter at which significantly penetrated mercury pore volume is detected. At the threshold pore diameter, little mercury intrusion is possible as it represents the narrowest path that forms a continuous network through the cement matrix.

Threshold pore diameter is detected at the first inflection point on the curve of cumulative intruded pore volume versus the pore diameter. The point of the steepest slope on the curve represents the critical pore diameter (Aligizaki, 2006). The threshold pore diameter is the only valid parameter used in the analysis of MIP data (Diamond, 2000). The Washburn equation will only assist in detecting the relatively smaller pore while large pore diameters will not be detected. MIP technique is only useful if the cement pastes are vacuum mixed

and the intrusion process is done after the threshold pressure has been reached. Only then will large pore diameters be detected.

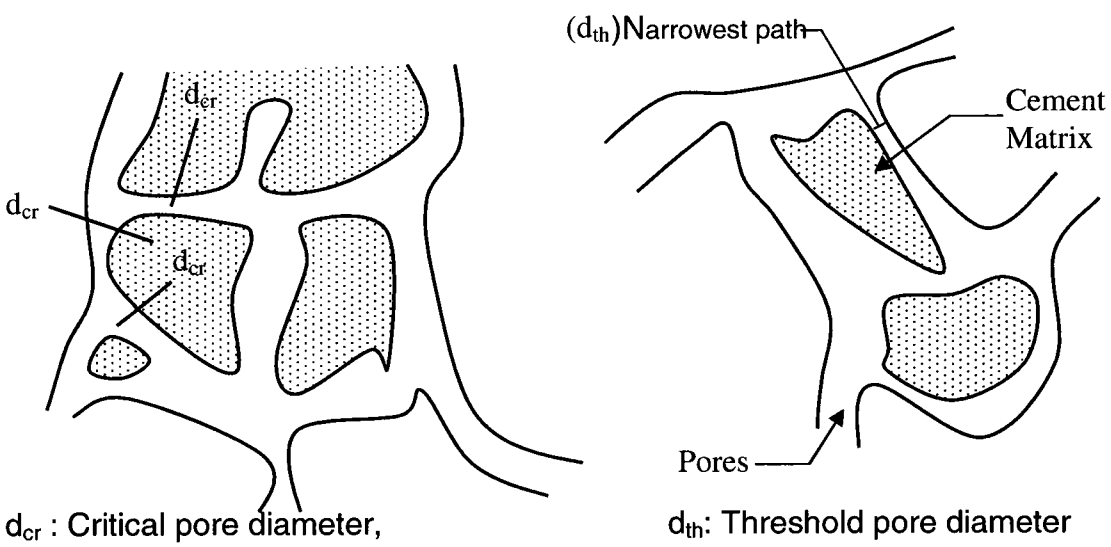


Fig A. 3 Critical and threshold pore diameter (Adapted from Aligizaki, 2006, p.74)

APPENDIX B

CHLORIDE CONTENT MEASUREMENTS

Preparation of 0.1 M AgNO₃ (Skoog et al., 1994; Christian, 1993)

1. Oven dry one gram of reagent grade NaCl and allow it to cool in a desiccator for 30 minutes.
2. 0.1 M AgNO₃ is prepared by dissolving about 8.5 g of AgNO₃ in 500 mL of deionized water. Store the solution in dark glass container.
3. Weigh 0.20 grams of oven dried NaCl into a 250 mL Erlenmeyer flask. Dissolve the sample in 60 mL of deionized water.
4. Add 5 drops of dichlorofluorescein indicator and roughly 0.1 grams of dextrin to the NaCl solution.
5. Rinse the burette at least three times with 0.1 M AgNO₃ and avoid bubble formation.
6. Titrate the sodium chloride solution with 0.1 M AgNO₃ solution until the first permanent appearance of the pink color of the dichlorofluorescein indicator. Calculate the average molarity of 0.1 M AgNO₃.

Titration of unknown sample

1. Weigh 0.30 grams of unknown sample to the nearest 0.0001 g.
2. Titrate the unknown sample using the steps 3 to 6 from the preparation of 0.1M AgNO₃.

Calculation of chloride content

The unknown grams of sodium chloride content in concrete are given by,

$$\text{Unknown grams of NaCl} = \frac{58.5 \left(\frac{\text{g}}{\text{mol}} \right) \times 0.1 \left(\frac{\text{mol}}{\text{L}} \right) \times x(\text{L})}{1000} \quad [57]$$

where the molecular weight of NaCl is 58.5 (g/mol), 0.1 is molarity of the AgNO₃ solution and x is the input value from the titration in mL.

60% is chloride from the sodium chloride

$$\% \text{ Chloride by mass of concrete} = \text{Unknown grams of NaCl} \times 0.60$$

17% of the total mass is cement from the concrete

$$\% \text{ Chloride by mass of cement} = \% \text{ chloride} \times 0.17$$

APPENDIX C

pH MEASUREMENT IN CONCRETE

Calculation of pH from concrete (Broomfield, 1997; Rasanen and Pentalla, 2004)

- Rinse the burette with 0.1 N HCl at least three times and fill the burette with 0.1 N HCl solution.
- Weigh 3 grams of oven dried concrete into a 250 mL Erlenmeyer flask. Dissolve the sample in 60 mL of deionized water.
- Add 5 drops of phenolphthalein indicator in the 60 mL flask containing concrete solution for measuring the transition range (pH) of 8.0 – 9.6. Titrate the concrete solution with 0.1 N HCl until it changes from red to colorless.
- Titrate the concrete specimens using pH alizarin yellow for measuring the pH range of 10.1-12.0. Titrate the solution with 0.1 N HCl until the first change from orange red to yellow is observed.
- The titrated value will be the concentration of hydroxide ions (OH^-) or alkalinity.
- The pH value is calculated

$$pH = 14 - p[OH^-] \quad [58]$$

APPENDIX D

CORROSION PRODUCT ANALYSIS

The corrosion products for the reinforcements are calculated based on ASTM G109- 99a. Figure D.1 exhibits the sectional view of the reinforcement with corrosion products. The total corrosion product coverage area is calculated by the summation of all the individual corrosion product area. The area includes both sides of the longitudinal and circular sections of the reinforcement.

$$\text{Individual Corrosion Product Area (in}^2\text{)} = x \text{ (in)} \times y \text{ (in)}$$

The total corrosion product coverage area (TCP) is calculated by,

TCP

$$= \left[\sum \{\text{Front sectional area of the rebar (in}^2\text{)}\} \right. \\ + \sum \{\text{Back sectional area of the rebar (in}^2\text{)}\} \\ \left. + \sum \{\text{Circular cross sectional area of the rebar (in}^2\text{)}\} \right] \quad [59]$$

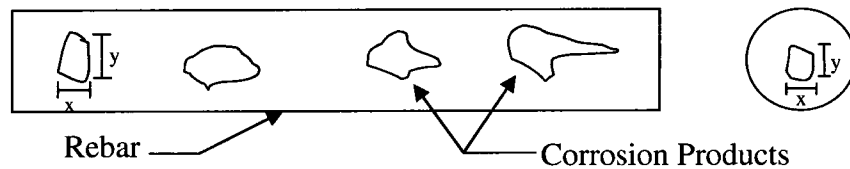


Fig D. 1. Schematic layout of corrosion products on the reinforcement

APPENDIX E

EN TREATMENT ON BEAMS

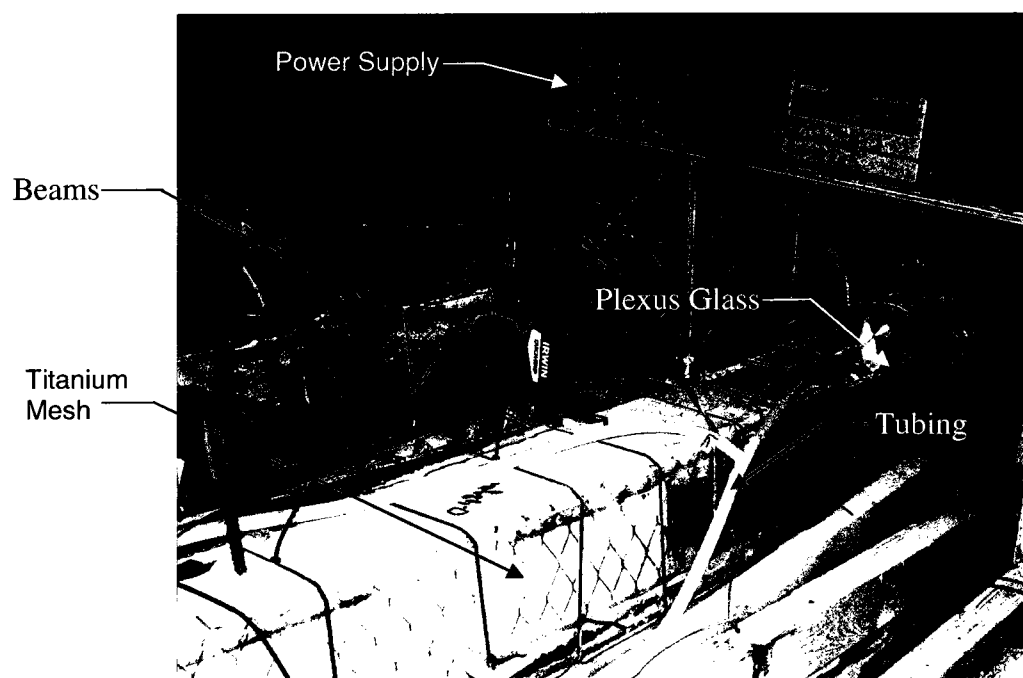


Fig E. 1. Configuration of EN treatment on beams

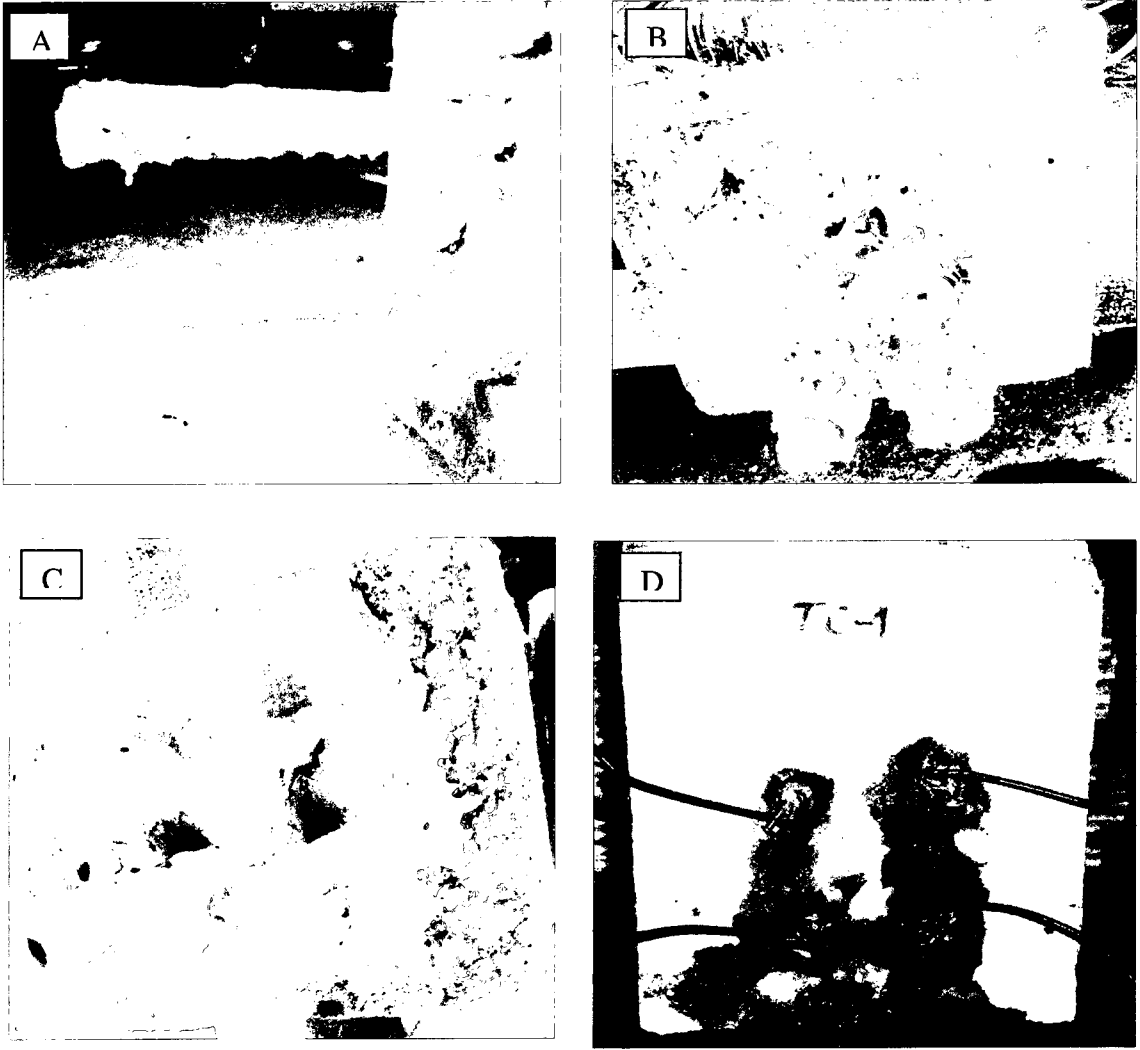


Fig E. 2 EN treated (A and B) and control reinforcements (C and D)

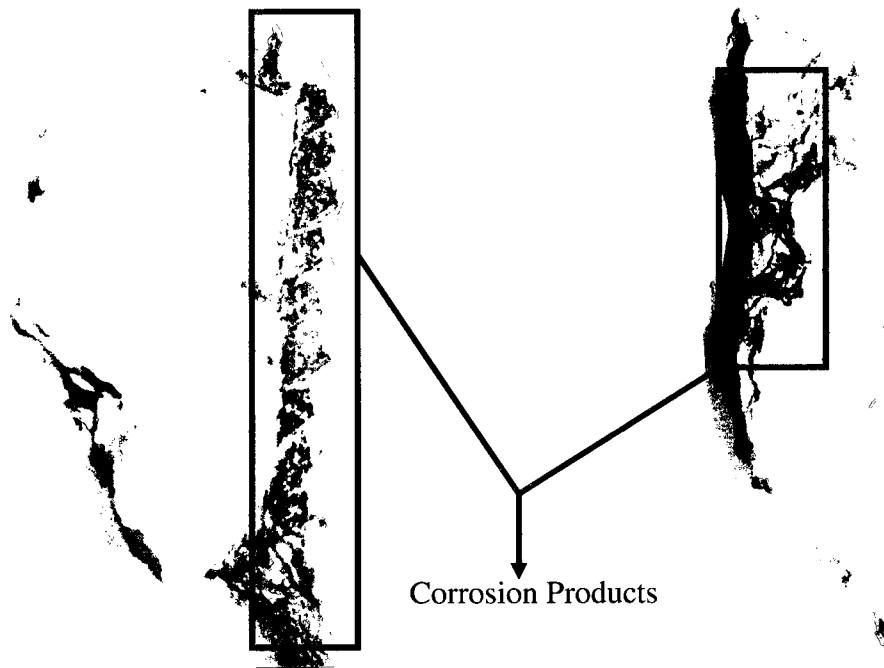


Fig E. 3. EN treated and control rebar/concrete interface

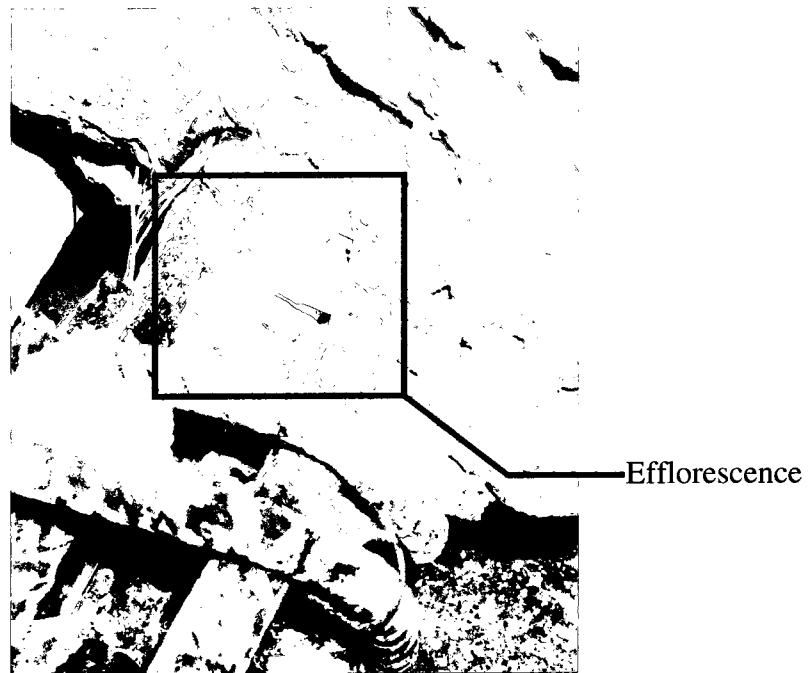


Fig E. 4. Efflorescence observed on the EN treated specimens

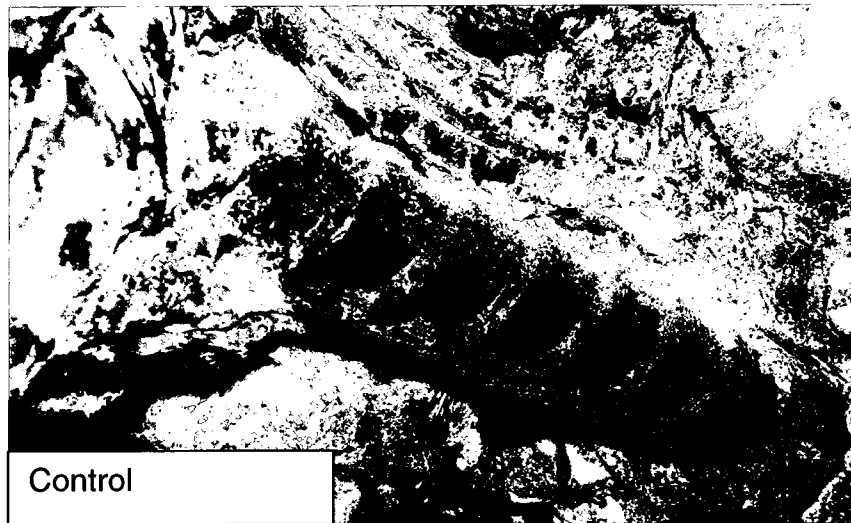
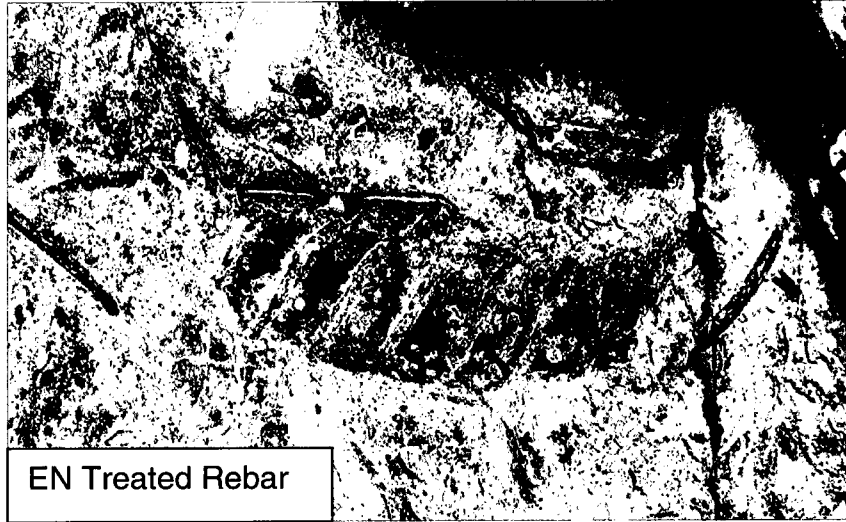


Fig E. 5. EN treated and control reinforcements after strength test

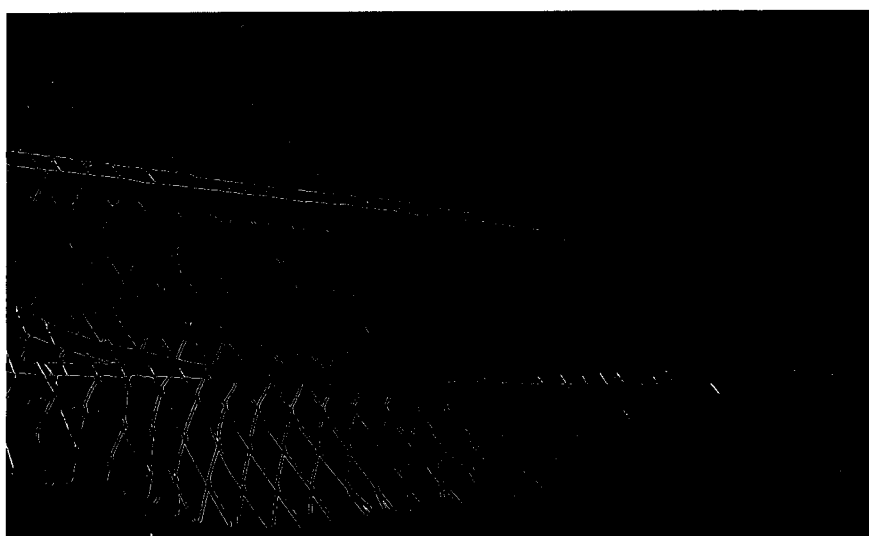


Fig E. 6 Sponge and titanium mesh used for EN treatment

APPENDIX F

ADDITIONAL IMAGES ON SULFATE ATTACK

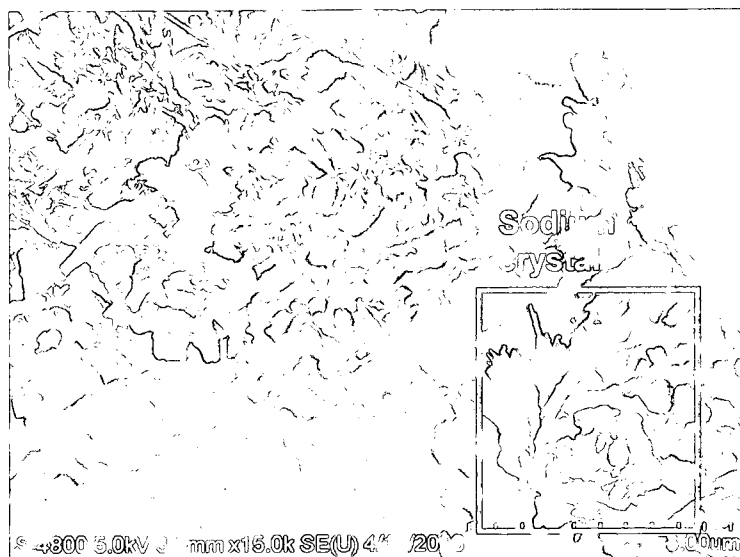


Fig F. 1 Sodium sulfate crystal on sulfate exposed specimen

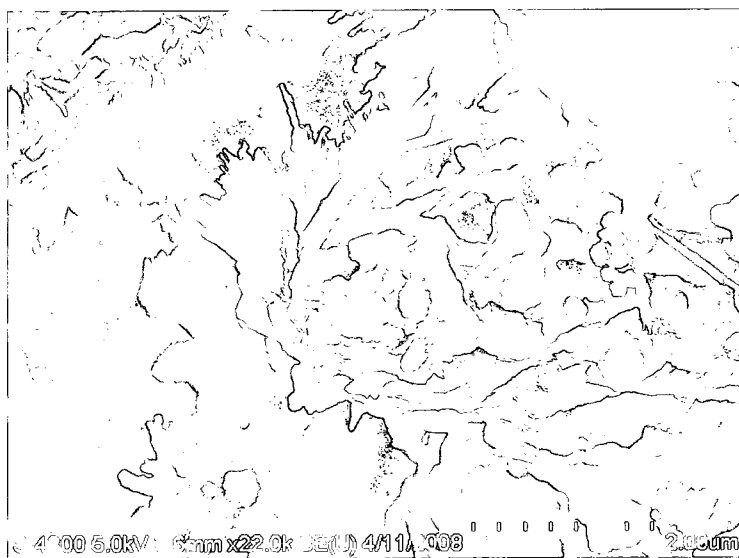


Fig F. 2 Magnified image of the sodium sulfate crystal

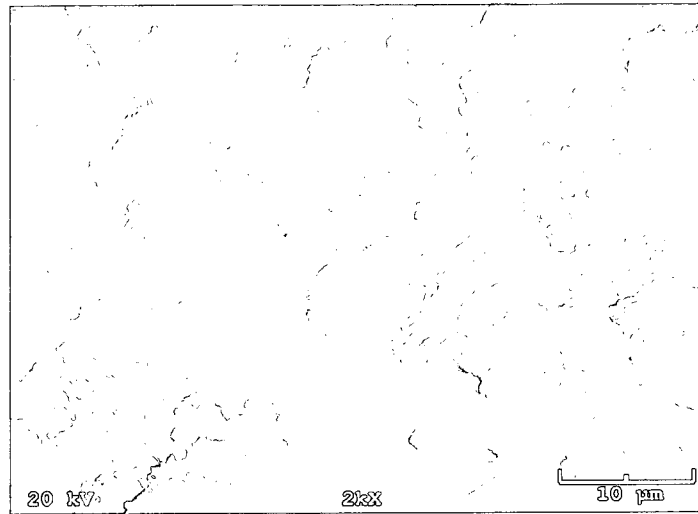


Fig F. 3 C-S-H II in the form of flakes on the EN treated specimens

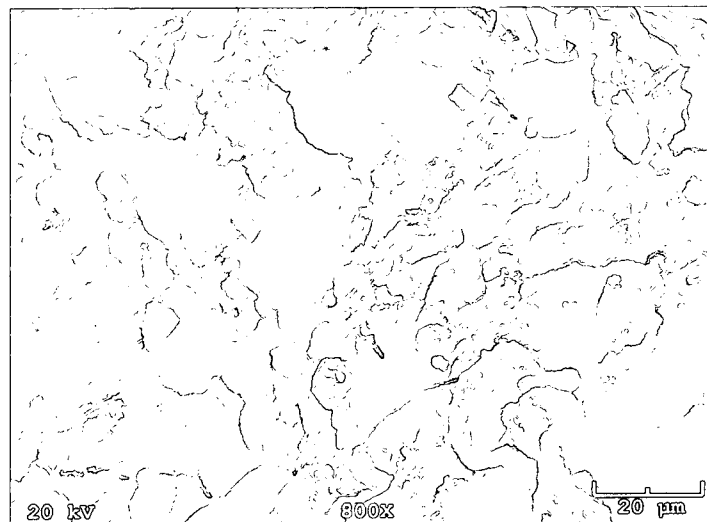


Fig F. 4 Type II C-S-H in the form of honeycomb flakes within EN Treated specimen

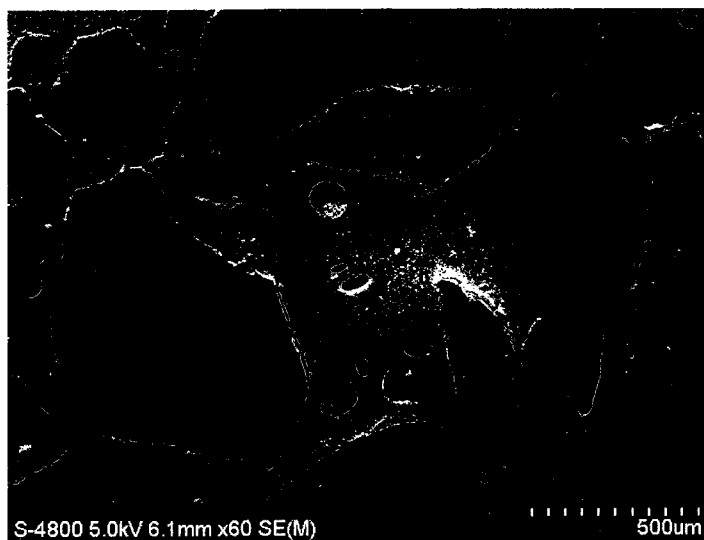


Fig F. 5 Pores within the control specimens

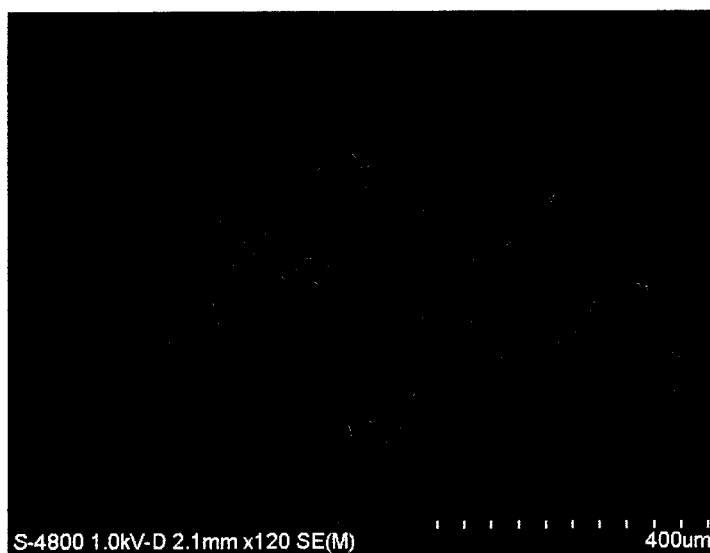


Fig F. 6 Micro-cracks within control specimens

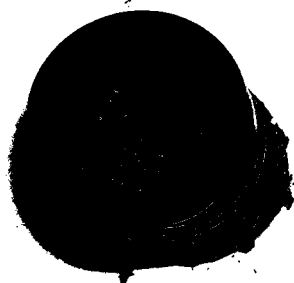


Fig F. 7 Concrete specimen cast in epoxy

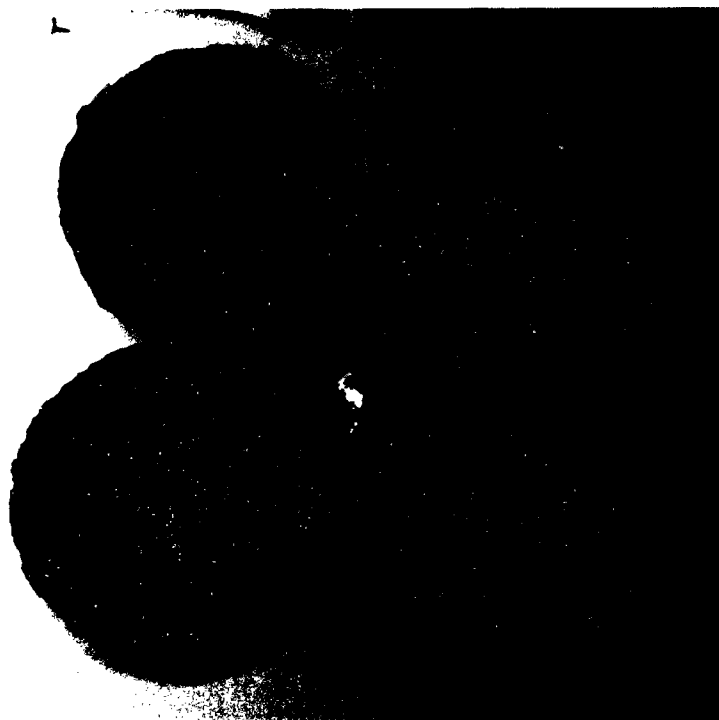


Fig F. 8 Degradation in the form of color change on sulfate control

APPENDIX G

ATOMIC FORCE MICROSCOPY (AFM)

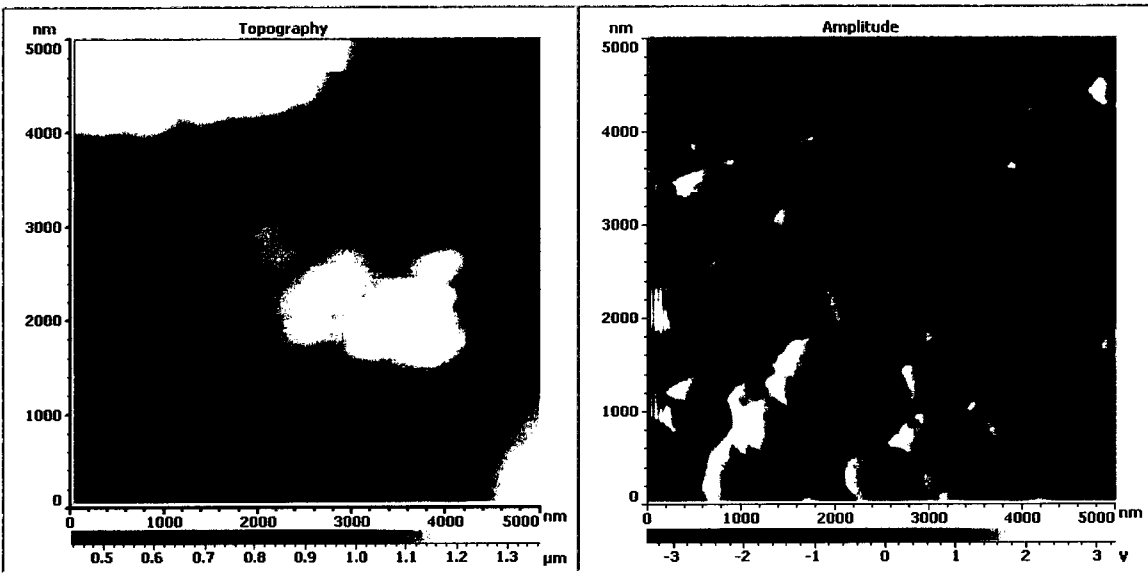


Fig G. 1 AFM image of C-S-H gel

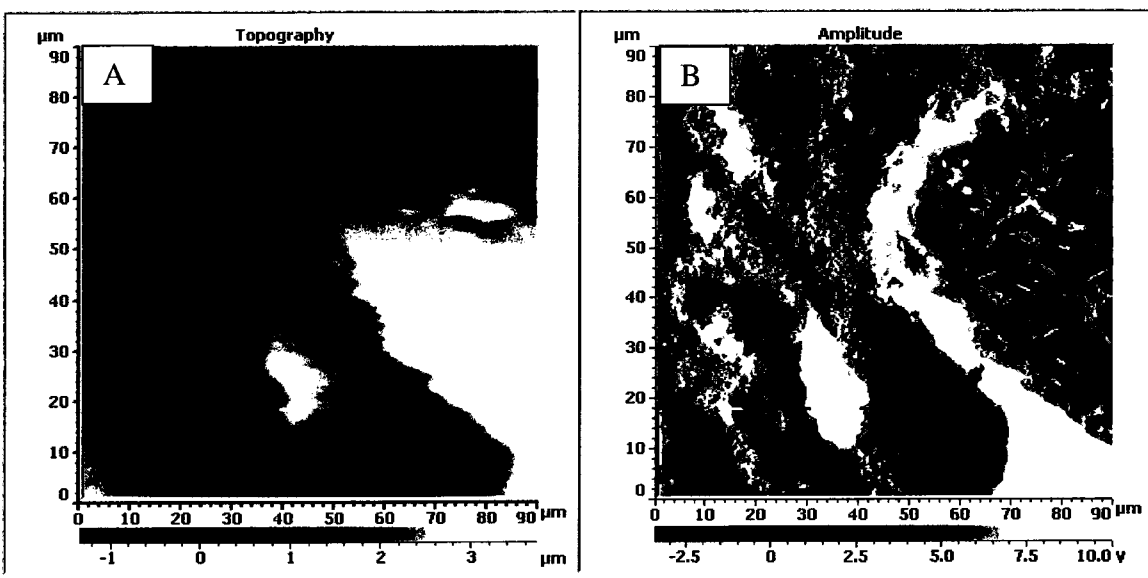


Fig G. 2 (A) AFM Image C-S-H gel (topography), (B) Change in amplitude

APPENDIX H

EQUIPMENT USED FOR MICROSTRUCTURAL ANALYSIS

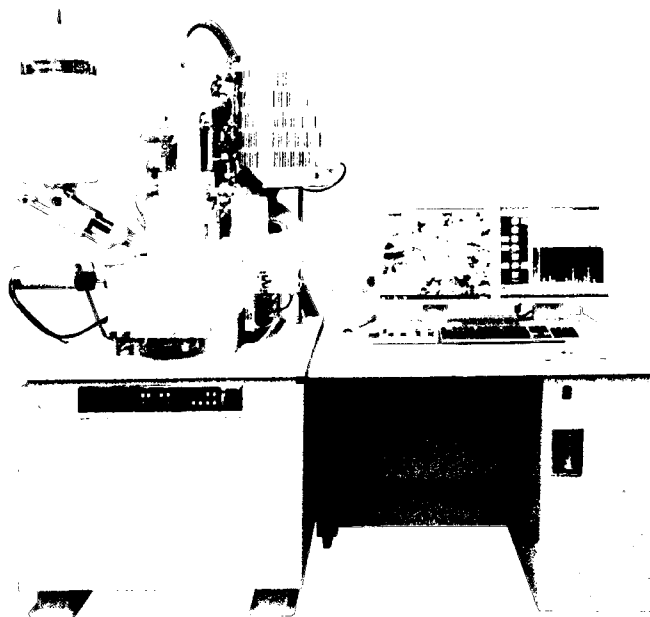


Fig H. 1 Hitachi S-4800 field emission scanning electron microscope



Fig H. 2 X-ray diffraction analysis (D8 Advance Bruker AXS Inc)

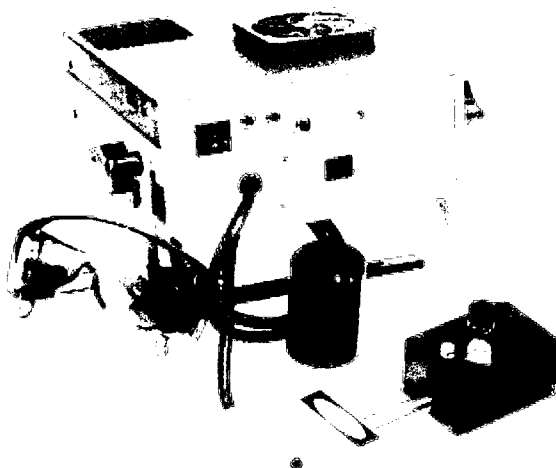


Fig H. 3 Raman Spectrometer (Raman Systems, Woburn, MA)



Fig H. 4 Mattson Genesis II Fourier Transform Infrared Spectroscopy (FTIR)

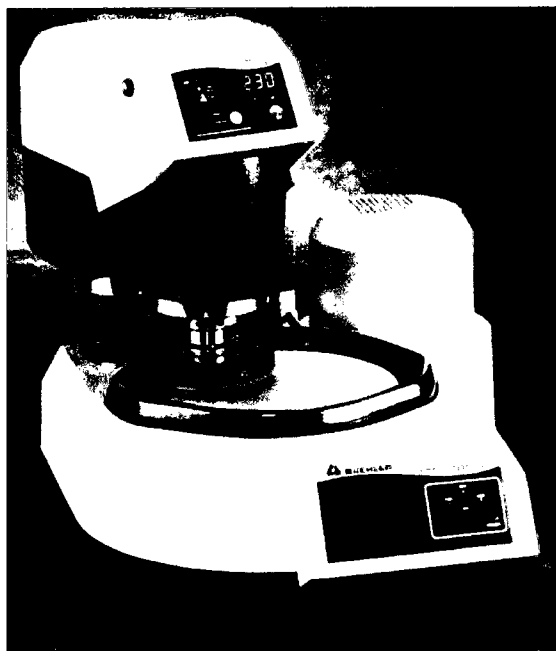


Fig H. 5 Alpha beta grinder used for polishing concrete (Buehler, Lake Bluff, IL)



Fig H. 6 Vacuum impregnation using castable vacuum system (Buehler, Lake Bluff, IL)

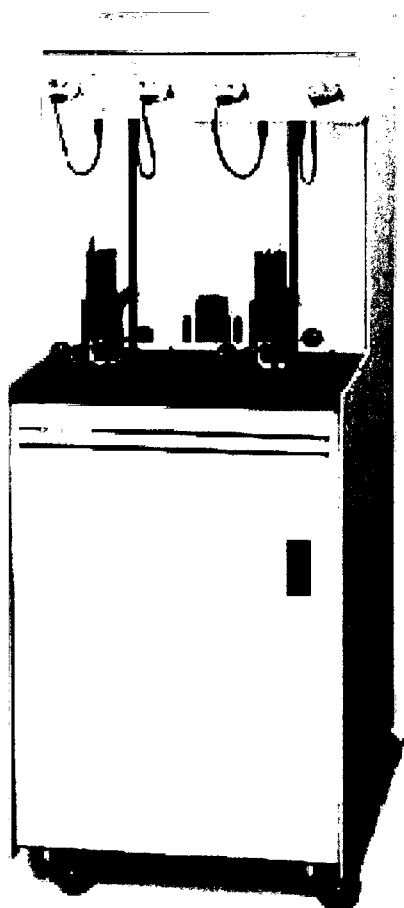


Fig H. 7 Mercury Intrusion porosimetry (Auto Pore 9500, Micromeritics, Inc, Norcross GA)

APPENDIX I

DATA OF YOUNG AND MATURE CONCRETE

Table I. 1 Corrosion potential data

Time (Days)	Corrosion Potential (mV)			
	Controls		EN Treated	
	Mature	Control	Mature	Young
1	-200	-243	-230	-214
50	-634	-453	-975	-345
100	-764	-634	-535	-355
150	-783	-648	-498	-345
200	-832	-657	-484	-435
250	-874	-689	-475	-453
300	-898	-698	-503	-465
350	-900	-702	-534	-467
400	-934	-893	-564	-502
450	-981	-1034	-657	-534
500	-987	-1094	-675	-563
550	-1034	-1135	-678	-573
600	-1039	-1235	-689	-579
650	-1055	-1259	-678	-589
700	-1067	-1345	-703	-591
750	-1034	-1456	-709	-599
800	-1089	-1467	-734	-601
850	-1103	-1489	-774	-619
900	-1109	-1504	-789	-634
950	-1235	-1538	-793	-723
1000	-1278	-1543	-796	-783
1050	-1249	-1544	-834	-803
1100	-1284	-1545	-845	-819

Table I. 2 Diffusion coefficients of young and mature reinforced concrete

Time (Days)	Diffusion Coefficients (m^2/s)			
	Control		EN Treated	
	Mature	Young	Mature	Young
250	8.69E-12	2.30E-13	6.50E-13	2.30E-14
500	7.90E-12	3.24E-12	7.80E-13	4.50E-14
750	5.37E-12	4.32E-12	1.76E-12	5.30E-13
1100	3.64E-12	3.00E-13	8.00E-13	2.10E-12

Table I. 3 Chloride content data

Distance from the R/C (inches)	Chloride Contents (% by mass of cement)			
	Control		EN Treated	
	Mature	Young	Mature	Young
1.5	0.27	0.25	0.09	0.12
1	0.26	0.19	0.07	0.08
0.5	0.24	0.18	0.06	0.03
0	0.21	0.16	0.04	0.01

APPENDIX J

DATA OF ASTM G109 SPECIMENS

Table J. 1 Corrosion rate measurements on control specimens

Specimen No	3		1		4	
Position	T	B	T	B	T	B
Tafel plot method						
Corrosion Rate (Mpy)	0.48	0.13	1.05	0.11	0.49	0.19
B _a (mV)	416	257	486	494	520	474
B _c (mV)	435	271	477	495	508	473
I _{corr} (μA/cm ²)	1.18	0.33	2.56	0.27	1.21	0.46
Linear polarization resistance calculation						
R _p , (kΩcm ²)	73	145	41	379	89	221
R _Ω (kΩcm ²)	0.03	0.05	0.45	0.06	0.01	0.68
I _{corr} μA/cm ²	1.18	0.17	0.62	0.06	0.29	0.17
E _{corr} , mV	- 627	- 545	- 571	- 573	- 689	- 618
Corrosion Rate (Mpy)	0.31	0.07	0.25	0.02	0.04	0.04

Note: T = top bar, B = bottom bars, B_a = slope of anodic tafel curve, B_c = slope of cathodic tafel curve, I_{corr} = corrosion current density, R_p = Linear polarization resistance, R_Ω = Ohmic resistance, E_{corr} = Half cell potential

Table J. 2 Corrosion rate measurements on EN Treated specimens

Specimen No	2		5		6	
Position	T	B	T	B	T	B
Tafel plot method						
Corrosion Rate (Mpy)	0.01	0.01	0.06	0.006	0.002	0.005
B _a (mV)	254	267	466	312	419	420
B _c (mV)	282	298	401	336	428	424
I _{corr} (μA/cm ²)	0.003	0.002	0.17	0.005	0.0006	0.001
Linear polarization resistance calculation						
R _p , (kΩcm ²)	524	822	574	4060	13800	5910
R _Ω (kΩcm ²)	0.06	0.97	0.75	1.97	0.75	7.65
I _{corr} μA/cm ²	0.001	0.003	0.004	0.0006	0.0001	0.0004
E _{corr} , mV	- 478	- 487	- 679	- 122	- 324	- 146
Corrosion Rate (Mpy)	0.007	0.01	0.01	0.002	0.0007	0.0018

Table J. 3 Total corrosion data of the control specimens

Time (Days)	Specimen No.1		Specimen No.3		Specimen No. 4	
	I_{corr} (μ A)	Charge (C)	I_{corr} (μ A)	Charge (C)	I_{corr} (μ A)	Charge (C)
0	0	432	0	159	0	203
50	200	2440	74	1382	96	911
100	730	6125	492	4410	234	2093
150	976	10113	910	8687	313	4432
200	870	15001	1070	13791	771	8024
250	1393	21044	1293	20051	893	12556
300	1405	28365	1605	27803	1204	17932

Table J. 4 Total corrosion data of the EN Treated specimens

Time(Days)	Specimen No. 2		Specimen No.5		Specimen No. 6	
	I_{corr} (μ A)	Charge (C)	I_{corr} (μ A)	Charge (C)	I_{corr} (μ A)	Charge (C)
0	0	26	0	38	0	128
50	12	84	17	148	59	388
100	14	155	32	313	61	686
150	18	249	43	539	76	1044
200	25	611	61	819	89	1456
250	142	1280	68	1154	101	1972
300	167	2094	86	1552	137	2666

APPENDIX K

ENERGY DISPERSIVE SPECTRUM ANALYSIS

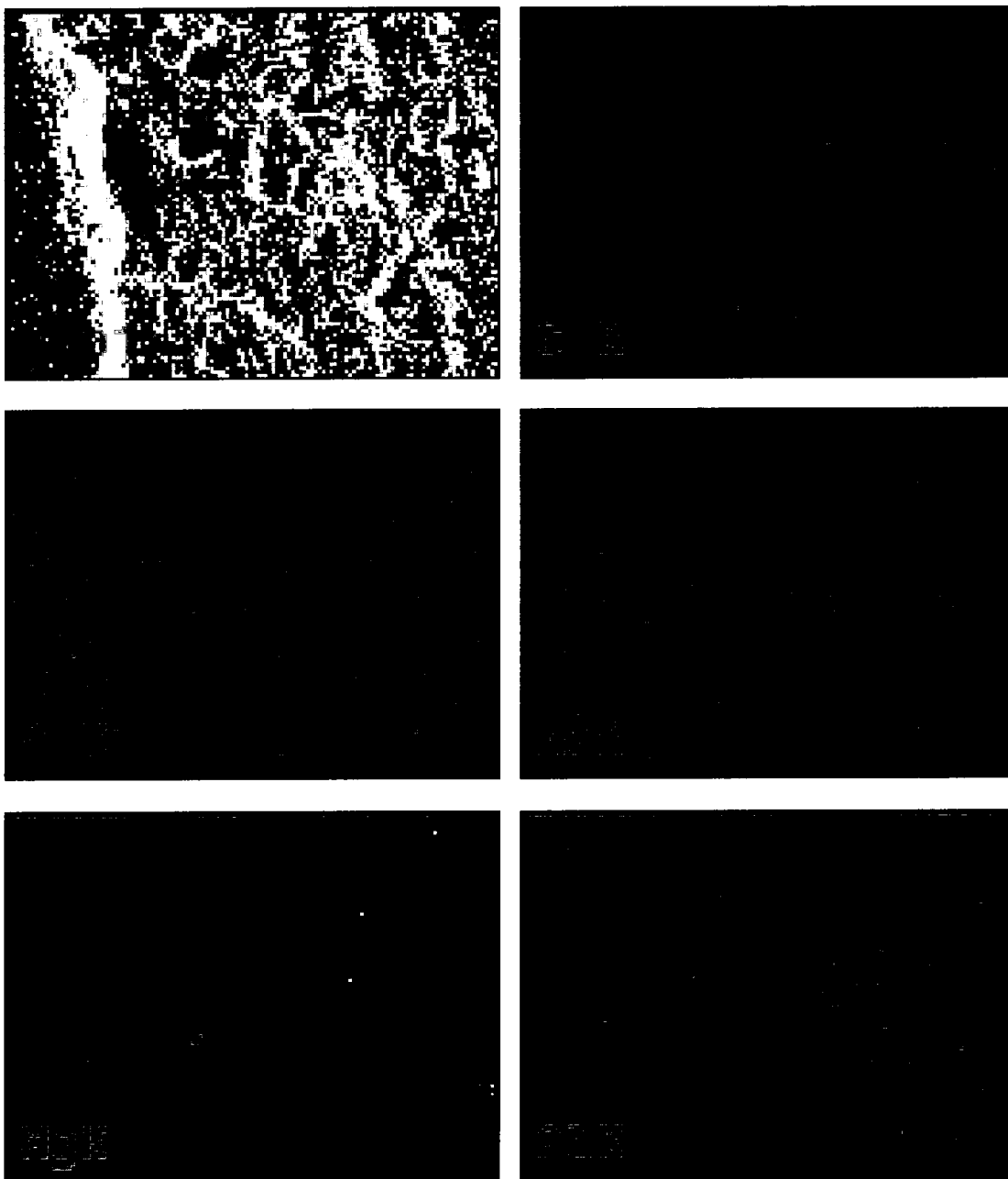


Fig K. 1 EDS spectrum with element mapping

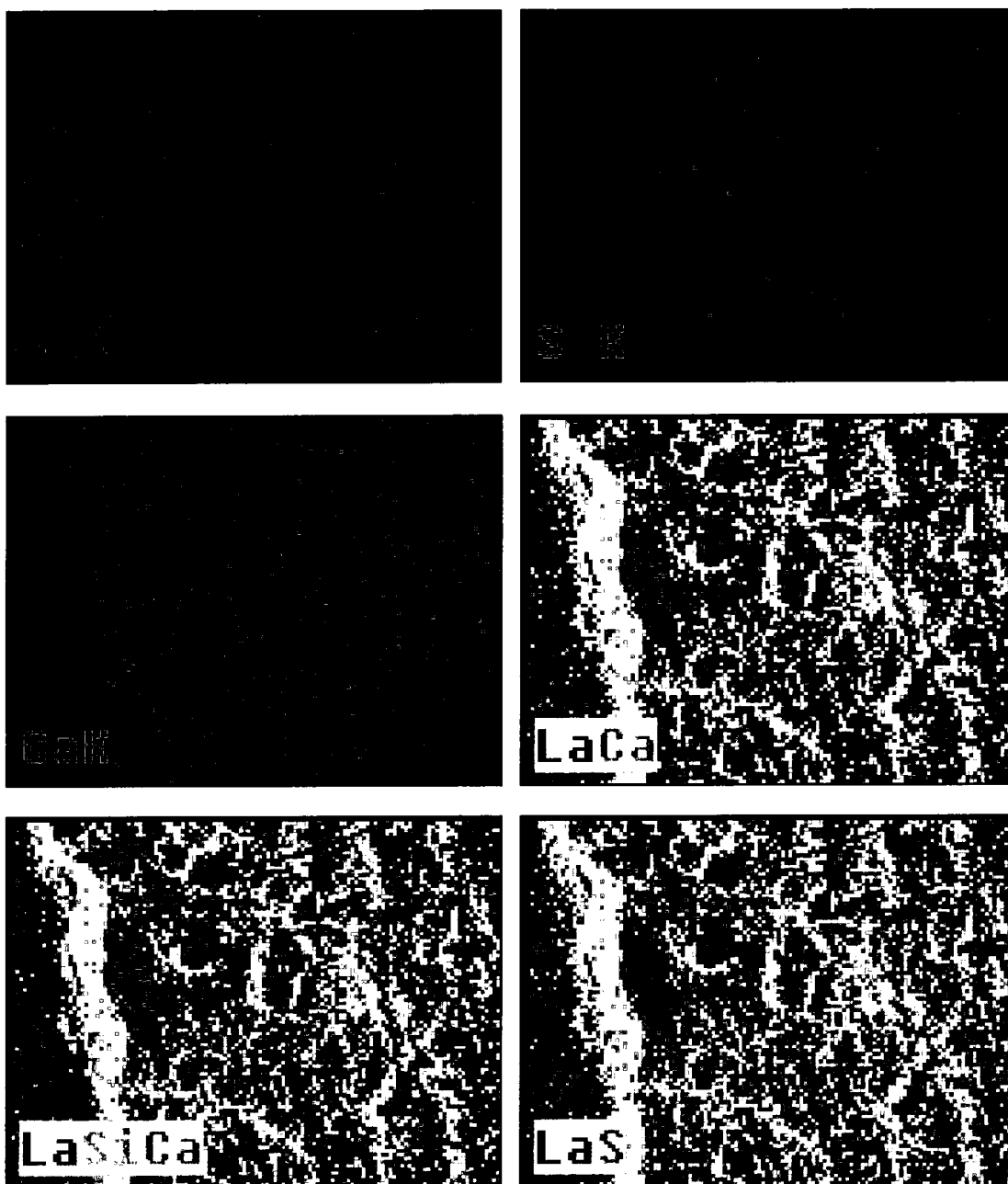


Fig K. 2 EDS spectrum with element mapping of SiK, SK, CaK, LaCa, LaSiCa and LaS

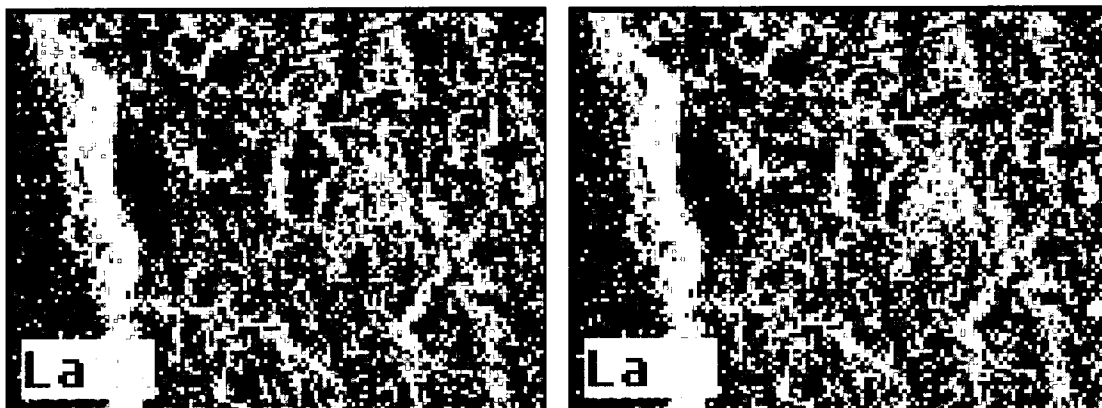


Fig K. 3 EDS spectrum with element mapping of LaAl and LaMg

REFERENCES

ACI 211.1-91, "Standard practice for selecting proportions for normal, heavyweight and mass concrete," *American Concrete Institute*, August 1991, pp. 277-279.

ASTM C 469, "Standard test method for static modulus of elasticity and poisson's ratio of concrete in compression," American Society of Testing and Materials, Philadelphia, 2002.

ASTM C 1152., "Standard test method for acid- soluble chloride in mortar and concrete," American Society of Testing and Materials, Philadelphia, 2002.

ASTM C 33, "Standard Specification for Concrete Aggregates," *American Society of Testing and Materials*, Philadelphia, January 2002.

ASTM C192M, "Standard Practice for making and curing concrete test specimens in the laboratory," *American Society of Testing and Materials*, Philadelphia, March 2002.

ASTM C 195, "Standard Specification for Mineral Fiber thermal insulating Cement," *American Society of Testing and Materials*, Philadelphia, March 2006.

ASTM C496-96, "Standard Test Method for Splitting Tensile Strength of Cylindrical Concrete Specimens," *American Society of Testing and Materials*, Philadelphia, March 2006.

ASTM G109-99a, " Standard Test Methods for Determining the Effects of Chemical Admixtures on the Corrosion of Embedded Steel Reinforcement in Concrete Exposed to Chloride Environments," *American Society of Testing and Materials*, Philadelphia, August 2000.

ASTM G 33-99, "Standard Practice for Recording Data from Atmospheric Corrosion Test of Metallic-coated Steel Specimens," *American Society of Testing and Materials*, Philadelphia, February 1998.

ASTM STP 1056, "The Measurement and Correction of Electrolyte Resistance in Electrochemical Tests," *American Society of Testing and Materials*, Philadelphia, July 1990.

ASTM C1012- 95a, "Standard test method for length change of hydraulic-cement mortars exposed to sulfate solution." *American Society of Testing and Materials*, Philadelphia, July 1990.

ASTM 1202, "Standard test method for electrical indication of concrete's ability to resist chloride ion penetration," *American Society of Testing and Materials*, Philadelphia, July 1997.

ASTM C 876-91, "Standard test method for half-cell potentials of uncoated reinforcing steel in concrete." *American Society of Testing and Materials*, Philadelphia, July 1990.

ASTM G106, "Standard practice for verification of algorithm and equipment for electrochemical impedance measurements," *American Society of Testing and Materials*, Philadelphia, July 1990.

ASTM C 873, "Standard test method for compressive strength of concrete cylinders cast in place in cylindrical molds." *American Society of Testing and Materials*, Philadelphia, July 1990.

ASTM C 684, Standard test method for making, accelerated curing, and testing concrete compression test specimens, Annual book of ASTM Standards, West Conshohocken, Pennsylvania, 2001.

ASTM G102, Standard Practice for calculation of corrosion rates and related information from electrochemical measurements, *American Society of Testing and Materials*, Philadelphia, 1999.

Aligizaki, K, Pore structure of cement based material: Testing Interpretation and Requirements, 1st Edn, Taylor and Francis Publications, London UK, 2006, pp.1-102.

Allen, A.; Thomas, J.; and Jennings, H., "Composition and density of nanoscale calcium-silicate-hydrate in cement," *Nature Materials*, Vol 6. April, 2007, pp. 311-316.

Al-Tayyib, A.; and Khan, M., "Corrosion rate measurements of reinforcing steel in concrete by electrochemical techniques," *ACI Materials Journal*, Vol. 85-M21, May 1998, pp.172-177.

Ahmad, Z, Principles of Corrosion Engineering and Corrosion Control, Elsevier Publications, New York, 2006, pp. 325-326.

Andrade, C.; Arteaga, A.; Lopez-Hombrados, C.; and Vazquez, A., "Test on bond of galvanized rebar and concrete cured in seawater," *ASCE Journal of Materials in Civil Engineering*, Vol. 13. No. 5, September/October, 2001, pp. 319-324.

Ann, K.; and Song, H., "Chloride threshold level for corrosion of steel in concrete," *Corrosion Science*, Vol 49. No. 11, May 2007, pp. 4113 - 4133.

Antunes, A.; Costa, I.; and deFaria, D., "Characterization of Corrosion Products Formed on Steels in the First Months of Atmospheric Exposure," *Revista Materia*, Vol. 28 No.1, 2003, pp. 27-34.

Basheer, P.; Basheer, L.; Lange, D.; and Long, A., "Role of thresholding to determine size of interfacial transition zone," *ACI Special Publication*, Vol. 189, January 2000, pp.165-186.

Barsoukov, E, and Macdonald, J, Impedance Spectroscopy Theory, Experiment, and Applications, Wiley Publications, New Jersey, 2005, pp.1-10.

Bentur, A.; Diamond, S.; Berke, N.; Steel Corrosion in Concrete, Spon Publications, UK, 1998, pp.24-38.

Bentur, A and Cohen, M, "Effect of condensed silica fume on the microstructure of the interfacial zone in Portland cement mortars," *Journal of American Ceramic Society*, Vol. 70 No.10, October 1987, pp.738-743.

Belaid, F.; Arliguie, G.; and Francois, R., "Effect of bar properties on bond strength of galvanized reinforcement," *ASCE Journal of Materials in Civil Engineering*, Vol. 13 No. 3, November/December 2001, pp. 454-458.

Bertolini, L.; Carsana, M.; Pietro, P., "Corrosion behavior of steel in concrete in the presence of stray current," *Corrosion Science*, Vol. 49, March 2006, pp. 1056-1068.

Bertolini, L.; Elsener, B.; Pedferri, P.; and Polder, R., Corrosion of Steel in Concrete: Prevention, Diagnosis, Repair, Wiley-VCH Publications, Weinheim, Germany, March 2004, pp. 326-366.

Bing, T.; and Cohen, M., "Does gypsum formation during sulfate attack on concrete lead to sulfate attack," *Cement and Concrete Research*, Vol. 30, No.1, January 2000, pp. 117-123.

Bird, R; Stewart, W; Lightfoot, E, Transport Phenomena, Wiley Publications, New York, July 2001, pp. 513-539.

Bockris, J; and Reddy, A., Modern Electrochemistry: An Introduction to an Interdisciplinary Area, Plenum Publishing Corporation, New York, 1970, p.840.

Boyd, A.; and Mindess, S., "The use of tension testing to investigate the effect of W/C ratio and cement type on the resistance of concrete to sulfate attack," *Cement and Concrete Research*, Vol.34 No.3, March 2004, pp.373-377.

Brandt, A., Cement-based composites: Materials, Mechanical Properties and Performance, 2nd Ed., Taylor and Francis, London, UK, 2009, p.193.

Broomfield, J. P., *Corrosion of Steel in Concrete: Understanding, Investigation and Repair*, Taylor and Francis, London UK, December 1997, pp.103-106.

Brough, A.; and Atkinson, A., "Micro-Raman spectroscopy of thaumasite," *Cement and Concrete Research*, Vol.31 No.3, March 2001, pp.421-424.

Cardenas, H; and Struble,L., "Electrokinetic Nanoparticle Treatment of Hardened Cement Paste for Reduction of Permeability," *ASCE Journal of Materials in Civil Engineering*, Vol. 18 No 4, August 2006, pp. 554-560.

Cardenas, H; and Struble, L., "Modeling Electrokinetic Nanoparticle Penetration for Permeability Reduction of Hardened Cement Paste," *ASCE Journal of Materials in Civil Engineering*, Vol. 20 No. 11, November 2008, pp. 683-691.

Cardenas, H; "Investigation of Reactive Electrokinetic Processes for Permeability Reduction in Hardened Cement Paste," Doctor of Philosophy Thesis, University of Illinois at Urbana-Champaign, 2002.

Cardenas, H; and Kupwade-Patil, K., "Corrosion remediation using chloride extraction concurrent with electrokinetic pozzolan deposition in concrete," *New solutions for environmental pollution*, 6th Symposium on Electrokinetic Remediation, June 2007, p.117.

Cardenas, H; Paturi, P.; and Dubasi, P., "Electrokinetic treatment for freezing and thawing damage mitigation with limestone," *First International conference on sustainable construction materials and technologies*, Coventry, UK, June 2007, pp. 603-609.

Cardenas, H; Kupwade-Patil, K; and Eklund, S., "Corrosion mitigation in mature reinforced using nanoscale pozzolan deposition." *Second international conference on sustainable construction materials and technologies*, Ancona, Italy, June 2010.

Carrasco, L.; Rius, J.; and Miravittles, C., "Supercritical Carbonation of Calcium Aluminate Cement," *Cement and Concrete Research*, Vol. 38 No. 8-9, August 2008, pp. 1033-1037.

Castellote, M.; Andrade, C.; and Alonso, C., "Electrochemical removal of chlorides: Modeling of extraction, resulting profiles and determination of the efficient time of treatment," *Cement and Concrete Research*, Vol. 30 No. 4, April 2000, pp. 615-621.

Cheng, P.; Lee, T.; Tsai, W., "Corrosion of Reinforcements in Artificial Sea water and Concentrated Sulfate Solution," *Cement and Concrete Research*, Vol. 20, May 1990, pp. 243-252.

Christensen, B.J.; Coverdale, R. T.; Olson, R. A.; Ford, S.J.; Garboczi, E.J.; Jennings, H. M., and Mason, T. O., "Impedance spectroscopy of hydrating cement-based materials: measurement, interpretation, and application," *Journal of the American Ceramic Society*, Vol.77, No.11, November 1994, pp. 2789-2804.

Christian, G., Analytical Chemistry, 5th Ed., John Wiley and Sons, 1993, pp.703-705.

Cohen, M.; and Bentur, A., "Durability of Portland cement silica-fume pastes in magnesium sulfate and sodium sulfate solutions," *ACI Materials Journal*, Vol. 85-M18, May 1988, pp.148-157.

Cohen, M.; and Mather, B., "Sulfate attack on concrete: research needs," *ACI Materials Journal*, Vol. 88-M09, January 1991, pp. 62-69.

Cook, R, and Hover, K., "Mercury porosimetry of cement-based materials and associated correction factors," *ACI Materials Journal*, Vol. 90-M16, March-April 1993, pp. 152-161.

Corr, D.; Monteiro, P.; Kurtis, K.; and Kiureghian, A., "Sulfate attack of concrete: reliability analysis," *ACI Materials Journal*, Vol. 98-M12, March-April 2001, pp. 99-104.

Crow, D., Principles and Applications of Electrochemistry, CRC Press, September 1994, pp. 78-83.

Delgado, A, Interfacial Electrokinetics and Electrophoresis, CRC Press, New York, December 2001, pp. 1-55.

- Dhouibi-Hachani, L.; and Ezzedine, T., "Comparing the steel-concrete interface state and its electrochemical impedance," *Cement and Concrete Research*, Vol. 26 No. 2, February 1996, pp. 253-266.
- Diamond, S.; and Bonen, D., "Microstructure of hardened cement paste-a new interpretation," *Journal of the American Ceramic Society*, Vol 76, No. 12, February 1993, pp. 2993-2999.
- Diamond, S., "Mercury Porosimetry: An inappropriate method for the measurement of pore size distributions in cement-based materials," *Cement and Concrete Research*, Vol. 30, October, 2000, pp.1517-1525.
- Elsener, B.; Molina, M.; and Bohni, H.; "The Electrochemical Removal of Chlorides from Reinforced Concrete," *Corrosion Science*, Vol. 35, March 1993, pp. 1563-1570.
- Fajardo, G.; Escadellias, G.; and Arliguie, G., "Electrochemical Chloride Extraction (ECE) from Steel Reinforced Concrete Specimens contaminated by Artificial Sea-Water," *Corrosion Science*, Vol 48, No.1, January 2006, pp.110-125.
- Ghafoori, N.; and Mathis, R., "Sulfate resistance of concrete pavers," *ASCE Journal of Materials in Civil Engineering*, Vol. 9, No. 1, 1997, pp. 35-40.
- Glasstone, S., An Introduction to Electrochemistry, Litton Educational Publishing, New York, 2008, pp. 521-523.
- Grantham, G., "An automated method for the determination of chloride in hardened concrete," Proceedings 5th International Conference on Structural Faults and Repair, 1993, pp. 2131-2136.
- Hearn, N.; and Figg, J., "Transport Mechanisms and Damage: Current Issues in Permeation Characteristics of Concrete," Materials Science of Concrete VI, edited by Mindess, S.; and Skalny, J., 2001, pp. 327-375.
- Hester, C.; Salamizavaregh, S.; Darwin. D.; McCabe, S., "Bond of epoxy-coated reinforcement: Splices," *ACI Materials Journal*, Vol. 90-S11, January 1993, pp. 89-102.
- Jones, A.J., Principles and Prevention of Corrosion, Prentice Hall, New Jersey, 2nd Ed, 1995, pp. 388-391.
- John, D.; Searson, P.; and Dawson, J., "Use of AC impedance technique in studies of steel in concrete in immersed conditions," *British Corrosion Journal*, Vol 95 No.6, 1981, pp.102-106.

Kanno, J.; Richardson, N.; Phillips, J.; Kupwade-Patil, K.; Mainardi, D.; and Cardenas, H., "Modeling and simulation of Electromutagenic processes for multiscale modification of concrete," *Journal of Systemics, Cybernetics and Informatics*, Vol. 7 No. 2, pp. 69-74.

Kelly, R.; Scully, J.; Shoesmith, D.; Buchheit, R.; Electrochemical Techniques in Corrosion Science and Engineering, Marcel Dekker, New York, 2002, pp. 125-149.

King, G.; Caldwell, W.; and Williams, M., College Chemistry, Van Nostrand Reinhold Company, New York, 1972, p. 421.

Kirkpatrick, R.; Yarger, J.; McMillan, P.; Yu, P.; and Cong, X., "Raman Spectroscopy of C-S-H, Tobermorite and Jennite," *Advanced Cement Based Materials*, Vol. 5, April-May, 1997, pp. 93-99.

Koch, G.K.; Brongers, P.M.; Thompson, G.; Virmani, P.; and Payer, J., "Corrosion Cost and Preventive Strategies in the United States," US Department of Transportation Federal Highway Administration, Report No FHWA-RD-01-156, March 2002, pp. 3-9.

Kurtis, K.; Monterio, P.; and Madanat, S., "Empirical models to predict concrete expansion in sulfate attack," *ACI Materials Journal*, Vol.97-M20, March 2000, pp.156-161.

Kupwade-Patil., "A new corrosion mitigation strategy using nanoscale pozzolan deposition," Master of Science Thesis, Louisiana Tech University, May 2007.

Kupwade-Patil.; and Cardenas, H., "Corrosion mitigation in concrete using electrokinetic injection of reactive composite nanoparticles." Proceedings of 53 International Conference on Advancement of Material and Process Engineering, Long Beach, CA, May 2008.

Kupwade Patil, K., and Cardenas H., "Composite nanoparticle treatments for mitigation of sulfate attack in concrete." Proceeding of 53 International Conference on Advancement of Material and Process Engineering, Long Beach, CA, May 2008.

Kupwade Patil. K.; Gordon. K.; Xu. K.; Moral O.; Cardenas. H.; and Lee. L., "Corrosion mitigation in concrete beams using electrokinetic nanoparticle treatment," Proceedings on Excellence in Concrete Construction through Innovation, September 2008, London, UK, pp. 365-371.

Li, G.; Bescop, P.; and Moranville, M., "The U-phase formation in cement-based systems containing high amounts of Na₂SO₄," *Cement and Concrete Research*, Vol. 26 No. 1, January 1996, pp. 27-33.

Liu, Y.; and Weyers, R., "Modeling the time-to-corrosion cracking in chloride contaminated reinforced concrete structures," *ACI Materials Journal*, Vol. 95-M 65, November-December, 1998, pp. 675-681.

Lyklema, J., *Fundamentals of Interface and Colloid Science, Volume II : Solid – Liquid Interfaces*, Academic Press, London, UK, 1995, p. 208.

Maage M., Helland S., Poulsen E., Vennesland O., and Carlsen J. "Service life prediction of existing concrete structures exposed to marine environment," *ACI Materials Journal*, Vol 93- M 68, Nov-Dec 1996, pp. 602-608.

Malvern Instrument, Zetasizer Nano Series User Manual, Malvern Instruments Limited, Worcestershire UK, 2004, pp.16.2.

Marcotte, T.; Hansson, C.; Hope, B., "The effect of the electrochemical chloride extraction treatment on steel-reinforced mortar Part I: Electrochemical measurements," *Cement and Concrete Research*, Vol. 29 No.10, October 1999, pp.1555-1560.

Marcus, P.; and Mansfeld, F., Analytical methods in corrosion science and engineering, CRC Press, Boca Raton FL, 2006, pp. 463-505.

Masliyah, J.; and Bhattacharjee, S., Electrokinetic and Colloid Transport Phenomena, Wiley-Interscience, New York, 2006, pp. 295-333.

Mays, G.C., Durability of Concrete Structures: Investigation, Repair, Protection, E & FN Spon Publications, London, 1990, pp.15-33.

Mehta, P.K.; and Monteiro, P.J., Concrete : Microstructure, Properties and Materials, 3rd Ed., McGraw-Hill Professional, New York, 2006.

Mehta, P.K.; and Gerwick, B.C., "Cracking-corrosion interaction in concrete exposed to marine environment," *Concrete International*, Vol. 4 No.10, October, 1982, pp. 45-51.

Mehta, P.K., Mechanism of sulfate attack on Portland cement concrete-another look, *Cement and Concrete Research*., Vol.13 No.3, May 1983, pp. 401-406.

Mehta, P.K., Sulfate attack in concrete separating myths from reality, *Concrete International*, Vol. 22 No. 8, August 2000, pp. 57-61.

Menzies, T.; "National Cost of Damage from Highway De-icing," in *Corrosion Forms and Control for Infrastructure*, ASTM 1137, 1992, pp. 30-45.

Mindess, S.; Young, F.; Darwin, D., Concrete, 2nd Ed., Pearson Education, Inc, New Jersey, 2003, pp.15-55.

Mindess, S., The Strength and Fracture of Concrete: The role of the Calcium Hydroxide in Material Science of Concrete: Calcium Hydroxide in Concrete, The American Ceramic Society, Ohio, 2001, pp. 143-154.

Mitsui, K.; Li, Z.; Lange, D.; and Shah, S., "Relationship between microstructure and mechanical properties of the paste-aggregate interface," *ACI Materials Journal*, Vol. No. 91-M4, January-February, 1994, pp. 30-39.

Mohammed, T.; Otsuki, N; Hisada, M; and Shibata, T., "Effect of crack width and bar types on corrosion of steel in concrete," *ASCE Journal of Materials in Civil Engineering*, Vol 13 No. 3, May/ June 2001, pp. 194-201.

Mohammed, T.; and Hamada, H., "Corrosion of horizontal bars in concrete and method to delay early corrosion," *ACI Materials Journal*, Vol. 103 - M33, September / October 2006, pp. 303-311.

Mohammed, T.; Otsuki, N.; and Hisada, M., "Corrosion of steel bars with respect to orientation in concrete," *ACI Materials Journal*, Vol. 96-M19, March-April, 1999, pp.154-160.

Mondal, P.; Shah, S.; and Marks, L., "Nanoscale characterization of cementitious materials," *ACI Materials Journal*, Vol. 105-M20, March-April 2008, pp. 174-179.

Monteiro, P.; and Kurtis, K., "Time to failure for concrete exposed to severe sulfate attack," *Cement and Concrete Research*, Vol. 33. No. 7, July 2003, pp. 987- 993.

Morrison, R.; and Boyd, R., Organic Chemistry, Prentice Hall, New Jersey, 1992.

Nagla, V.T.; Page, C.L.; Page, M.M., "Corrosion inhibitor systems for remedial treatment of reinforced concrete. Part 2: sodium monofluorophosphate," *Corrosion Science*, Vol 45 No. 7, 2003, pp. 1523-1537.

Naik, N.; Jupe, A.; Stock, S.; Wilkinson, A, Lee, P, Kurtis, K., "Sulfate attack monitored by microCT and EDXRD: Influence of cement type, water-to-cement ratio, and aggregate," *Cement and Concrete Research*, Vol. 36 No.1, January 2006, pp. 144-159.

Nemati, K.; and Gardoni, P., "Microstructural and statistical evaluation of interfacial zone percolation in concrete," *Strength, Fracture and Complexity*, Vol. 3 No. 2-4, 2005, pp. 191-197.

Neville, A.M., Properties of Concrete, 4rd Ed., Wiley, New York, 1996.

Neville, A. M., Neville on Concrete, Book Surge Publishing, Charleston SC, 2006, pp. 5-25.

Nielsen, J., "Investigation of resistance of cement paste to sulfate attack," Highway Research Record-113, 1966, pp. 114-117.

Odler, I., Special Inorganic Cements, E & FN Spon Publications, London, UK, 2000.

Orellan, J. C.; Escadellias, G.; and Arliguie, G., "Electrochemical Chloride extraction: efficiency and side effects," *Cement and Concrete Research*, Vol. 32 No. 2, February, 2004, pp. 227-234.

Pajares,I.; Ramirez, S.; and Blanco-Varela, M., "Evolution of ettringite in presence of carbonate, and silicate ions," *Cement and Concrete Composites*, Vol. 25 No. 8, December 2003, pp. 861-865.

Peterman, R.; Ramirez, J.; and Poston, R., "Durability assessment of bridges with full-span prestressed concrete form panels," *ACI Materials Journal*, Vol. 96-M2, January-February, 1999, pp. 11-19.

Potgieter-Vermaak,S.; Potgieter, J.; and Van Grieken,R., "The application of raman spectrometry to investigate and characterize cement, Part I: A review," *Cement and Concrete Research.*, Vol. 36 No. 4, April 2006, pp. 656-662.

Poulsen,E.; and Mejlbro, L., Diffusion of chloride in concrete : Theory and Application, Taylor and Francis, London, UK. December 2006, pp. 55-109.

Ramachandran, V.; and Beaudoin, J., Handbook of analytical techniques in concrete science and technology: principles, techniques and applications, 1st Ed., William Andrew Publishing, January 2002, pp. 441-497.

Rasanen, V.; and Penttala, V., "The pH measurement of concrete and smoothing mortar using concrete powder suspension," *Cement and Concrete Research*, Vol. 34 No. 5, 2004, pp. 813-820.

Rasheeduzzafar, O.; Al-Amoudi, O.; Abduljauwad, S.; and Maslehuddin, M., "Magnesium-sodium sulfate attack in plain and blended cements," *ASCE Journal of Materials in Civil Engineering.*, Vol. 6 No. 2, 1994, pp. 201-222.

Reinhardt, H.W., "Transport of Chemicals through Concrete," *Materials Science of Concrete III*, J.P. Skalny, Ed., American Ceramic Society, Westerville, 1992, pp. 209-241.

Richardson, I.G., "The nature of C-S-H in hardened cements," *Cement and Concrete Research*, Vol. 29 No. 8, August 1999, pp. 1131-1147.

Roberge, P.; and Revie, R., Corrosion Inspection and Monitoring, Wiley Interscience, February 2007, pp. 234-246.

Roy, D, M.; Brown, P. W.; Scheetz, B.E.; May, W., "Concrete Microstructure Porosity and Permeability," Strategic Highway Research Program, National Research Council, Washington DC, 1998, pp. 43-48.

Sahmaran, M.; Erdem, T.; and Yaman, I., "Sulfate resistance of plain and blended cements exposed to wetting-drying and heating-cooling environments," *Construction and Building Materials*, Vol. 21 No. 8, August 2007, pp. 1771-1778.

Samaha, H,R; and Hover, K,C., "Influence of microcracking on the mass transport properties of concrete," *American Concrete Institute Materials Journal*, Vol 89, April 1992, pp. 416-424.

Scannell,W.; Sohanchpurwala, A.; Islam, M., "Assessment of physical condition of concrete bridge components," US Department of Transportation Federal Highway Administration, July 1996, pp. 4.1-4.31.

Schwarz, A.J.; Contescu,C.; and Putyera, K., Dekker Encyclopedia of Nanoscience and Nanotechnology-Volume 3, CRC Press, March 2004, pp. 1998-1999.

Scrivener, K.; Crumbie, A.; and Laugesen, P., "The interfacial transition zone (ITZ) between cement paste and aggregate," *Interface Science*, Vol. 12 No.4, October 2004, pp. 411-421.

Siegwart, M; Lyness, J.; McFarland, B.; and Doyle, G., "The effect of electrochemical chloride extraction on pre-stressed concrete," *Construction and Building Materials*, Vol. 19 No. 8, January 2005, pp. 585-594.

Shamsad, A., "Reinforcement corrosion in concrete, its monitoring and severe life prediction: a review," *Cement and Concrete Composites*, Vol. 25 No. 4-5, May 2003, pp. 459-471.

Shazali, M.; Baluch, M.; and Al-Gadhib, A., "Predicting residual strength in unsaturated concrete exposed to sulfate attack," *ASCE Journal of Materials in Civil Engineering*, Vol. 18 No. 3, May/June, 2006, pp. 343-354.

Skalny, J.; Marchand, J.; and Odler, I., Sulfate Attack on Concrete, Taylor and Francis Publications, London, 2001, pp. 43-93.

Skoog, D.; West, D.; and Holler, J., Analytical Chemistry: An Introduction, Harper Collins Publications, New York, 1994, p. 112.

Sorenson, T., Surface Chemistry and Electrochemistry of Membranes, CRC Press, 1999, pp. 512-521.

Suryavanshi, A.K.; Scantlebury J.D.; and Lyon S. B., "Corrosion of Reinforcement Steel embedded in High Water-Cement Ratio Concrete Contaminated with Chloride," *Cement and Concrete Composites*, Vol. 20 No. 4, November 1998, pp. 263-381.

Talbot, D.; and Talbot, J., Corrosion Science and Technology, 2nd Edn, CRC Press, 2007, pp. 104-105.

Taylor, H.F.W., Cement Chemistry, 2nd Edn, Thomas Telford Ltd, 1997, pp. 123-131.

Tikal'sky, P.; and Carrasquillo, R., "Influence of Fly ash on the sulfate resistance of concrete," *ACI Materials Journal*, Vol. 89-M09, January 1993, pp. 69-75.

Thomas, J.; Jennings, H.; and Allen, A., "The surface area of hardened cement paste as measured by various techniques," *Concrete Science Engineering*, Vol. 1, March 1999, pp. 45-64.

Treece, R.; and Jirsa, J., "Bond strength of epoxy-coated reinforcing bars," *ACI Materials Journal*, Vol. 86-M17, March-April, 1989, pp. 167-174.

Tritthart, J.; Pettersson, K.; Sorensen, B., "Electrochemical Removal of Chloride from Concrete," *Cement and Concrete Research*, Vol. 26, January 1996, pp. 851-860.

Uhlig, H., Corrosion and Corrosion Control, John Wiley and Sons, Inc, New York, 1971, pp. 99-112.

Verbeck, G.J., "Corrosion of Metals in Concrete," SP-49 American Concrete Institute, 1975, pp. 21-26.

Wang, S.; Lin, W.; Ceng, S.; and Shang, J., "Corrosion inhibition of reinforcing steel by using acrylic latex," *Cement and Concrete Research*, Vol. 28 No. 5, 1998, pp. 649-653.

Weyers, R., "Service life model for concrete structures in chloride laden environments," *ACI Materials Journal*, Vol. 95-M 42, July 1998, pp. 445-453.

Wiegrink, K.; Marikunte, S.; and Shah, S., "Shrinkage cracking of high-strength concrete," *ACI Materials Journal*, Vol. 93-M46, September-October, 1996, pp. 409-415.

Winslow, D., "Some experimental possibilities with mercury intrusion porosimetry," *Proceeding on Pore Structure and Permeability of Cementitious Materials*, Materials Research Society, Warrendale, PA, Vol. 137, 1989, pp. 93-103.

Winslow, D., and Diamond, S., "Specific surface of hardened cement paste as determined by small-angle X-ray scattering," *Journal of American Ceramic Society*, Vol. 57 No. 5, January 1974, pp. 193-197.

Winslow, D.; and Diamond, S., "A mercury porosimetry study of the evolution of porosity in Portland cement," *Journal of Materials*, Vol. 5 No.3, 1970, pp. 564-585.

Winslow, D., "The validity of high pressure mercury intrusion porosimetry," *Journal of Colloid and Interface Science*, Vol. 67 No.1, October 1978, pp. 42-47.

Wowra, O., "Effect of carbonation to micro structure and pore solution," *Proceedings on Frost Resistance of Concrete*, Rilem Publishing, 2002, pp. 61-68.

Yang, R.H.; Liu, B.; and Wu, Z., "Study on the pore structure of hardened cement paste by SAXS," *Cement and Concrete Research*, Vol. 20 No.3, May 1990, pp. 385-393.

Yang, W.; Weiss, J.; and Shah, S., "Predicting shrinkage stress field in concrete slab on elastic subgrade," *Journal of Engineering Mechanics*, Vol. 126 No. 1, January 2000, pp. 35-42.

Yu, P., Kirkpatrick, J., Poe, B., Mcmillan, P.; and Cong, X., "Structure of Calcium Silicate Hydrate (C-S-H): Near-, Mid-, and Far-Infrared Spectroscopy," *Journal of American Ceramic Society*, Vol. 82 No. 3, March 1999, pp. 742-748.

Zhang, J.; Monteiro, P.; and Morrison, F., "Noninvasive surface measurement of corrosion impedance of reinforcing bar in concrete-Part 1: experimental results," *ACI Materials Journal*, Vol. 98-M14, March-April 2001, pp. 116-25.